THE JURASSIC METEORITE FLUX:
A RECORD FROM EXTRATERRESTRIAL CHROME-SPINELS

A DISSERTATION SUBMITTED TO THE GRADUATE DIVISION OF THE UNIVERSITY OF HAWAIʻI AT MĀNOA IN PARTIAL FULFILLMENT OF THE REQUIREMENTS FOR THE DEGREE OF

DOCTOR OF PHILOSOPHY

IN

EARTH & PLANETARY SCIENCE

December 2020

By

Caroline E. Caplan

Dissertation Committee:

Gary R. Huss, Chairperson
Kazu Nagashima
Hope A. Ishii
Greg Ravizza
Schelte J. Bus

Keywords: chrome-spinel, chromite, Jurassic, meteorites, oxygen isotopes

To my ten-year-old self who wanted this for so long, you did it!

ACKNOWLEDGMENTS

Graduate school will forever be one of my favorite times in life. Through its ups and downs I have become more knowledgeable, confident, and have found true joy in science. I am especially thankful to my advisor, Gary Huss, without whom none of this work would have been possible. He has guided me through graduate school to grow as researcher, including giving me the opportunities to explore new avenues of my work. I would also like to thank my committee members: Kazu Nagashima for always answering my questions with patience, Hope Ishii for work and life guidance, Greg Ravizza for his excitement and new perspectives, and Bobby Bus for help with statistics and his endless curiosity. Thanks to Birger Schmitz who allowed me to work on such a special project and for the incredible opportunity to travel to Sweden, Russia, and Italy to obtain a better understanding of my samples and the area of work.

I would also like to thank the HIGP and ERTH (GG) departments for fostering a productive and friendly environment. The faculty truly helped me learn and improve as a researcher and person, including Linda Martel, Julia Hammer, Eric Hellebrand, Ryan Ogliore, Jeff Taylor, Paul Lucey, Jeff Gillis-Davis, Patty Fryer, John Bradley, and Kenta Ohtaki. Graduate school was so enjoyable due to the friendships of other students (past and present), including Myriam Telus, Christine Jilly, Sarah Crites, Katie Robinson, Myriam Lemelin, Estelle Bonny, Erin Fitch, Elizabeth Shields, Laura Corley, Melissa Adams, Macey Sandford, Lingzhi Sun, Chiara Ferrari-Wong, Abbey Flom, Emily Costello, Colin Ferguson, Warren McKenzie, and Hannah Shelton. Special thanks to the graduate students who helped with defense and dissertation prep: Diamond Tachera, Brytne Okuhata, and Trista McKenzie.

Finally, I would like to thank my family. Thank you to my parents, for letting me live my dreams and for giving me every opportunity to succeed. Thank you to my grandparents for their support, and especially my grandfather, Calhoun Howard, for being a scientific inspiration throughout my life. Thanks to my sister, Anna, for always being my biggest supporter and reminding me that I am intelligent and worthy of great things. And thank you to my husband, Andrew, for always being by my side throughout the hardest and happiest parts of graduate school.

ABSTRACT

This dissertation focuses on the classification of extraterrestrial chrome-spinels to determine meteorite types and fluxes during the Jurassic time period and the techniques needed to achieve such classifications.

We know the relative abundances of meteorite types falling on Earth today, but we do not know what fell in the distant past. Abundances of the past are unknown because meteorites tend to only survive on Earth's surface for a few tens of thousands of years due to the weathering environment of the Earth. Fortunately, chrome-spinels from disaggregated meteorites and micrometeorites can be preserved in limestone and retain their characteristic compositions. In many instances, the parent meteorite type of each grain can be determined by comparing their chemical compositions and oxygen isotope abundances to those of chrome-spinels from modern day meteorites.

The goal of this dissertation is to classify chrome-spinel grains from the Jurassic period, determine the relative abundances of parent meteorite types, and compare these abundances to those of other time periods. This was achieved by ensuring we had a well-characterized database of chrome-spinel compositions from modern meteorites in order to reliably classify each remnant chrome-spinel. We also had to confirm that our chemistry and oxygen-isotope measurements of the Jurassic chrome-spinels were reliable. This was determined, in part, by taking new measurements of chrome-spinels from modern meteorites using the same electron and ion microprobes used for the remnant grains. It was also necessary to understand instrumental artifacts that may affect oxygen isotope abundances during ion probe measurements, such as the crystal orientation of chrome-spinel.

We confidently classified the remnant chrome-spinels of the Jurassic using the compiled database, and compared the meteorite abundances to other time periods. However, it was difficult to determine the subgroup for a few of the ordinary-chondrite-like grains using chemistry and isotopes alone. In this event, (scanning) transmission electron microscope techniques were implemented to study the silicate inclusions within these chrome-spinels to help determine their parent meteorite type. Overall, this work supports the use of chemistry, oxygen isotopes, and inclusions to classify remnant chrome-spinels and demonstrates that meteorite populations from the past are different than today.

TABLE OF CONTENTS

ACKNOWLEDGMENTS ..... **iii**

ABSTRACT ..... **iv**

LIST OF TABLES ..... **vii**

LIST OF FIGURES ..... **ix**

CHAPTER1. INTRODUCTION **1**

1.1 Background **2**

1.2 Jurassic Grains **3**

1.3 Classifications **4**

1.4 Technical Advancements **6**

1.5 Dissertation Outline **7**

CHAPTER 2. REMNANT EXTRATERRESTRIAL CHROME-SPINELS REVEAL METEORITE ABUNDANCES OF THE JURASSIC **8**

2.1 Abstract **8**

2.2 Introduction **9**

2.3 Methods **10**

2.3.1 Collection and Preparation 10

2.3.2 Analysis 12

2.3.3 Classification Schemes 24

2.4 Results **29**

2.4.1 Chemical Compositions 29

2.4.2 Oxygen Isotopic Compositions 31

2.4.3 Classification 34

2.5 Discussion **41**

2.5.1 Classification Limitations 41

2.5.2 Jurassic Grains 50

2.5.3 Time period comparisons 51

2.5.4 Jurassic Relative Abundances 62

2.6 Conclusions **64**

CHAPTER 3. THE CLASSIFICATION OF RELICT EXTRATERRESTRIAL CHROME-SPINELS USING STEM TECHNIQUES ON SILICATE INCLUSIONS **66**

3.1 Abstract **66**

3.2 Introduction **66**

3.3 Material and Methods **70**

3.4 Results **74**

3.4.1 Jurassic Grain 1 74

3.4.2 Jurassic Grain 2 78

3.4.3 Jurassic Grain 3 83

3.4.3 Brunflo Grain 87

3.5 Discussion **91**

3.5.1 SEM-EDS versus STEM-EDS 91

3.5.2 Compositions of Jurassic Inclusions 94

3.5.3 Rims 97

3.5.4 Lamellae 99

3.6 Conclusions **100**

CHAPTER 4. EXTRATERRESTRIAL CHROME-SPINEL DATABASE FOR THE CLASSIFICATION OF REMNANT GRAINS FROM THE SEDIMENTARY RECORD 102
4.1 Abstract 102
4.2 Introduction 102
4.3 Methods 103
4.4 Results 106
4.4.1 Search for chrome-spinels in modern meteorites 107
4.4.2 Chemical compositions of modern meteorite chrome-spinels 108
4.4.3 Oxygen Isotopes of modern meteorites 115
4.5 Discussion 117
4.5.1 Database Limitations 117
4.5.2 Extraterrestrial versus Terrestrial chrome-spinel abundances 121
4.5.3 Database Uses 122
4.6 Conclusions 125
CHAPTER 5. CRYSTAL ORIENTATION EFFECTS FOR OXYGEN-ISOTOPE MEASUREMENTS OF CHROME-SPINEL AND MAGNETITE 126
5.1 Abstract 126
5.2 Introduction 126
5.3 Methods 128
5.3.1 Samples and Preparation 128
5.3.2 Analysis 129
5.4 Results 131
5.4.1 Inverse Pole Figures 132
5.4.2 SIMS pit textures 135
5.5 Discussion 137
5.6 Conclusions 138
CHAPTER 6. CONCLUSIONS 139
APPENDIX A. COMPOSITIONS AND CLASSIFICATIONS OF JURASSIC CHROME-SPINELS 141
APPENDIX B. NEW MEASUREMENTS OF MODERN METEORITE CHROME-SPINELS 148
APPENDIX C. EXTRATERRESTRIAL CHROME-SPINEL DATABASE 164
REFERENCES 189

LIST OF TABLES

Table 2.1 Electron microprobe analysis of Stillwater chromite 12
Table 2.2 Electron probe settings of elements measured for Jurassic chrome-spinels 13
Table 2.3 Compositions of entries for the hierarchical clustering example of High-Al grains shown in Fig. 2.9 36
Table 2.4 Compositions of entries for the hierarchical clustering example of Ureilite-like grains shown in Fig. 2.11 38
Table 2.5 Compositions of entries for the hierarchical clustering example of Acapulcoite- and Lodranite-like grains shown in Fig. 2.12 39
Table 2.6 Classifications of extraterrestrial Jurassic chrome-spinel grains 40
Table 2.7 Number of chrome-spinels (Cr-sp) per gram of dissolved meteorite types 49
Table 3.1 Element compositions (wt%) of the lamella and surrounding chrome-spinel (Cr-sp) in Grain 2 obtained by STEM-EDS 81
Table 3.2 The average element compositions (wt%) of the Jurassic chrome-spinel grains obtained by electron microprobe 84
Table 3.3 Element compositions (wt%) for Jurassic Grain 3 chrome-spinel lamellae and surrounding chrome-spinel obtained by STEM-EDS 87
Table 3.4 Element compositions (wt %) of olivine inclusions from Brunflo grain measured by SEM-EDS 88
Table 3.5 Element compositions (wt %) of olivine and high-Ca pyroxene inclusions in Brunflo grain determined by STEM-EDS 91
Table 3.6 Element composition (wt%) comparisons of SEM-EDS and STEM-EDS measurements for olivine inclusions in Brunflo grain 94
Table 3.7 Element composition (wt%) comparisons of SEM-EDS and STEM-EDS measurements for inclusions in the Jurassic grains 95
Table 4.1 Chemical compositions (wt %) of chrome-spinel grains from modern meteorites 110
Table 4.2 Oxygen isotope abundances of chrome-spinels from dissolved meteorites and bulk samples of meteorites 119
Table A.1 Chemical compositions, oxygen isotopes, and classifications (first and second order) for Jurassic chrome-spinels 141

Table B.1 Chemical compositions of chrome-spinel grains from modern meteorites.....148
Table B.2 Ion microprobe spot measurements (oxygen isotopes) of chrome-spinel grains from modern meteorites.....159
Table C.1 Chemical composition database for chrome-spinels from modern meteorites 164
Table C.2 Oxygen isotope values for modern meteorites, chrome-spinel and bulk 187

LIST OF FIGURES

Figure 1.1 Bulk three oxygen isotope fields of modern meteorites 5
Figure 2.1 Steps of chrome-spinel grain extraction from limestone 11
Figure 2.2 Schematic of typical electron multiplier components and the corresponding transitions of an ion/event into a counted pulse 18
Figure 2.3 Schematics of the mass and intensity of ^{16}OH, ^{17}O, and ^{18}O peaks 20
Figure 2.4 Example of a drift correction to determine Final $\Delta^{17}O$ values 22
Figure 2.5 Dendrogram depicting hierarchical clustering of representative ordinary chondrite compositions (H, L, LL) 26
Figure 2.6 Chemical compositions of large- and small- size fraction chrome-spinel grains from Jurassic sediment 30
Figure 2.7 Distribution of $\Delta^{17}O$ for large and small fraction grains 31
Figure 2.8 Chemistry and oxygen isotope plots of Jurassic grains and chrome-spinel compositions from modern meteorites 33
Figure 2.9 Dendrogram subsection consisting of High-Al Jurassic grains and database entry matches 35
Figure 2.10 Chemistry and oxygen isotopes of entries from Figure 2.9 and Table 2.2 36
Figure 2.11 Dendrogram subsection consisting of Ureilite-like Jurassic grains and database entry matches 37
Figure 2.12 Dendrogram subsection consisting of Acapulcoite- and Lodranite-like Jurassic grains and database entry matches 39
Figure 2.13 Overlapping chemical compositions and oxygen isotope values for different meteorite types 42
Figure 2.14 Compositions for types 3-6 of H, L, and LL ordinary chondrites 44
Figure 2.15 Comparison between a large surface area with a time interval of 1 and a smaller surface area with a time interval of 10 45
Figure 2.16 Mass distribution of interplanetary bodies falling to Earth's surface per year 47
Figure 2.17 Marked time periods for which remnant chrome-spinel abundances have been measured 51

Figure 2.18 Relative abundances of H-, L-, and LL-chondrite origin chrome-spinel grains from different time periods 52
Figure 2.19 Abundances of H- and L-chondrite origin chrome-spinel grains relative to LL-chondrite origin chrome-spinels from different time periods 53
Figure 2.20 Relative abundances of ordinary chondrites and other extraterrestrial origin chrome-spinel grains from different time periods 55
Figure 2.21 Abundance of other extraterrestrial origin chrome-spinel grains relative to ordinary chondrite origin chrome-spinels from different time periods 56
Figure 2.22 Sediment-dispersed chrome-spinel V_2O_3 and TiO_2 abundances from different time periods 59
Figure 2.23 Sediment-dispersed chrome-spinel Al_2O_3 and TiO_2 abundances from different time periods 60
Figure 2.24 Abundances from extraterrestrial and terrestrial chrome-spinel databases 61
Figure 2.25 Chemical abundances of Jurassic grains and select modern day meteorite chrome-spinels 61
Figure 3.1 H, L and LL-type ordinary chondrites can be distinguished by oxygen isotope and silicate chemistry 68
Figure 3.2 The Fa content of olivine and Fs content of Ca-poor pyroxene in the matrix and inclusions of chrome-spinels in H-, L-, and LL-chondrites 69
Figure 3.3 FIB section preparation for representative inclusion 72
Figure 3.4 Secondary-electron image of Grain 1 74
Figure 3.5 Complex rim on Inclusion 6 from Grain 1 75
Figure 3.6 Characterization of iron oxide laths in rim on Inclusion 6 from Grain 1 76
Figure 3.7 HAADF STEM images of FIB section through Inclusions 2a and 2b in Grain 1 77
Figure 3.8 Bright field STEM image of the FIB section through Inclusion 1 from Grain 1 78
Figure 3.9 Secondary electron and backscattered-electron imaging of Grain 2 79
Figure 3.10 Bright-field STEM image of FIB section through Inclusions 1 and 2 in Grain 2 80
Figure 3.11 SEM-EDS map of Fe-Kα and Fe-Kα line scan extracted from the map and crossing from the interior of Inclusion 2 into the surrounding chrome-spinel of Grain 2 80
Figure 3.12 Overlaid STEM-EDS element maps of Si, Fe, and Ti in Inclusions 1 and 2 in Grain 2 with surrounding chrome-spinel 81

Figure 3.13 Diffraction patterns from two lamellae and surrounding chrome-spinel 82
Figure 3.14 Secondary electron and backscattered-electron imaging of Grain 3 83
Figure 3.15 HAADF STEM image of the FIB section through Inclusion 6 in Grain 3.....85
Figure 3.16 Backscatter electron images of the polished surface of Jurassic Grain 3 85
Figure 3.17 Lamellae in Jurassic Grain 3 86
Figure 3.18 HAADF STEM image of Jurassic Grain 3 chrome-spinel lamellae and surrounding chrome-spinel near Inclusion 6.....86
Figure 3.19 Backscatter electron image of olivine inclusions in a chrome-spinel grain from the Brunflo meteorite.....87
Figure 3.20 Cr and Si K-α X-ray signal from SEM-EDS line scans as a proxy for Cr and Si content in olivines 1-4.....89
Figure 3.21 HAADF image of the Brunflo chrome-spinel FIB section with olivine Inclusions 1 and 2.....90
Figure 3.22 Scanning electron image of Brunflo FIB section before lift out 90
Figure 3.23 Hypothetical line scans of inclusions with the same diameter at the surface but with varying depths in the chrome-spinel host grain 94
Figure 3.24 Ferrosilite compositions of Inclusions 1 and 2 from Jurassic Grain 2, determined by SEM-EDS before FIB sectioning and STEM-EDS after FIB thinning 96
Figure 3.25 FIB-SEM backscatter electron images of inclusions within Grains 1 and 2 98
Figure 4.1 Representative back-scattered electron and Cr Kα X-ray map of a modern meteorite section 104
Figure 4.2 Different types, classes, and groups of modern meteorites in the chrome-spinel database.....107
Figure 4.3 Representative chrome-spinel grain and corresponding composition spectrum 108
Figure 4.4 Representative grain from the Eagle (EL6) chondrite consisting of two phases.....108
Figure 4.5 Comparisons between literature and new measurement compositions of chrome-spinels from LL-chondrites.....109
Figure 4.6 Comparisons between literature and new measurement compositions of CM2 chrome-spinels 109
Figure 4.7 Compositions (Al_2O_3 and TiO_2) of chrome-spinels from modern meteorites.....111
Figure 4.8 Compositions (V_2O_3 and MgO) of chrome-spinels from modern meteorites 112

Figure 4.9 Compositions (Al_2O_3 and Cr_2O_3) of chrome-spinels from modern meteorites 112
Figure 4.10 Compositions (Fe_2O_3 and FeO) of chrome-spinels from modern meteorites.....113
Figure 4.11 Compositions of H, L, and LL ordinary chondrites (types 3-6) 114
Figure 4.12 Compositions of chrome-spinels from carbonaceous chondrites 114
Figure 4.13 Bulk oxygen-isotope fields show partial overlaps of various meteorite types 116
Figure 4.14 Oxygen isotope abundances of dissolved chrome-spinel grains from modern meteorites 116
Figure 4.15 Oxygen isotope values of chrome-spinels from modern meteorites and bulk modern meteorites 120
Figure 4.16 The FeO wt% versus the difference in $\delta^{18}O$ values of the chrome-spinels from dissolved meteorite samples and their respective bulk meteorite values 120
Figure 4.17 Chrome-spinel compositions from terrestrial and extraterrestrial sources 122
Figure 4.18 Cr Kα X-ray maps of modern meteorite sections 124
Figure 5.1 Possible crystal orientation effects that may occur during SIMS analysis 127
Figure 5.2 Chrome-spinel crystal orientations of favorable and unfavorable for focusing and channeling 128
Figure 5.3 Crystal structures (slightly offset from [100]) of chrome-spinel and magnetite 128
Figure 5.4 SEM backscatter electron montage images of the a) chrome-spinel and b) magnetite one-inch round sections 129
Figure 5.5 Representative chrome-spinel grain with an electron backscatter diffraction pattern and secondary electron image with small square SIMS pits of the same grain 130
Figure 5.6 Three dimensional crystal structure of a sample chrome-spinel before and after a 20° tilt to account for the SIMS reference frame 131
Figure 5.7 $\delta^{18}O$ values of chrome-spinel and magnetite grains in measurement order 132
Figure 5.8 Chrome-spinel inverse pole figures before rotation and after a 90° rotation 134
Figure 5.9 Magnetite inverse pole figures before rotation and after a 90° rotation.....134
Figure 5.10 Inverse-pole figures and orientations for representative magnetite grains.....135
Figure 5.11 SIMS pits of chrome-spinel grains are smooth and show little variation in $\delta^{18}O$ values 136
Figure 5.12 SIMS pits of magnetite grains contain small craters of varying intensities 136
Figure 5.13 SIMS pits in two magnetite grains with and without cracks 137

CHAPTER 1

INTRODUCTION

Meteorites have been falling to the terrestrial surface throughout Earth's history, but they only survive as recognizable meteorites for a few thousand to tens of thousands of years. Meteorites and micrometeorites primarily originate from collisions between bodies in the asteroid belt. These extraterrestrial rocks travel to Earth via gravitational interactions with the planets. Once on the Earth's surface, the meteorites begin to alter and weather away due to the Earth's oxidizing atmosphere and active hydrologic cycle. Fortunately, remnants of meteorites can be preserved in certain sediments allowing us the ability to study meteorite distributions throughout Earth's history.

The work in this dissertation is part of a larger, long-term effort to understand the collisional history of the asteroid belt and how that history has affected the material impacting Earth over its history. Meteorite remnants in the sedimentary record include extraterrestrial mineral grains and fossil meteorites (e.g., Schmitz, 2013). Some meteorites that fall to Earth may retain their original structure, but their minerals have been almost completely replaced by secondary minerals. These are called fossil meteorites. Other meteorites that fell in the past can become chemically altered and disaggregate via terrestrial weathering processes, causing their remnants to be dispersed throughout the sediment. The remnant chrome-spinels are referred to as sediment-dispersed grains. While we are not able to study the altered meteorite material, there are still some minerals that survive the terrestrial environment. Extraterrestrial chrome-spinel grains remain unaltered for millions of years in terrestrial sediments and retain their original compositions (Schmitz, 2013). The parent meteorite type of these grains can be determined using chrome-spinel compositions from present-day meteorites. The overall goal of classifying remnant grains is to map the distribution and abundance of extraterrestrial grains in various stratigraphic units around the world so as to construct a meteorite flux record throughout Earth's history. The main objective of this dissertation is to identify which meteorite types were falling during the Jurassic period, ~165 million years ago (Ma), and compare to the flux of other time periods to observe how meteorite populations have changed over time.

1.1 Background

Extraterrestrial meteorite remnants can be recovered and measured because they are preserved in pelagic limestone (deep sea). These sediments were originally in deep tranquil seas far offshore that were not exposed to destructive waves and storms. This calm environment preserves the layering in the sediments, allowing them to retain a detailed time record. The deep waters also have low sedimentation rates, which allows for high meteorite remnant concentrations within smaller volumes of sediment. Most meteorites that fell in the past did not become fossil meteorites, but instead weathered and disintegrated, leaving only very resistant minerals such as chrome-spinels behind.

Sediment-dispersed chrome-spinels can be used to investigate the types of meteorites that were falling on the Earth in various times of the past. There are many more micrometeorites arriving on Earth than meteorites large enough to be easily recognized; therefore, one can collect a representative sample of infalling material from a relatively small area, as long as terrestrial chrome-spinel grains do not obscure the sample. The infall rate of extraterrestrial material is relatively low; therefore very slowly deposited (highly condensed) limestones are ideal for retaining high chrome-spinel/limestone ratios. Highly condensed limestones are deposited at rates of a few mm per Kyr and form in relatively deep water, far from land. This environment keeps the abundance of terrestrial chrome-spinel contamination relatively low.

The study of fossil meteorites began with a sample from a Swedish limestone quarry in the early 1950s. Since then, over 100 fossil meteorites have been found, all of which date from the mid- Ordovician, ~466 Ma (Schmitz, 2013; Schmitz et al., 1996, 1997, 2001). Birger Schmitz and his team at Lund University, Sweden, led the classifications of these fossil meteorites. The fossil meteorites (except one, see below) were classified as L-chondrites using features like chondrule size, as well as the chemical and oxygen-isotopic compositions of chrome-spinels. The infall rate for L-chondrites in the Ordovician inferred from these fossil meteorites was ~100 times higher than the meteorite infall rate of today. Following this discovery, limestone samples were collected to study sediment-dispersed grains above and below the fossil meteorite layers of the quarry to establish the duration of the enhanced influx. A drastic increase in extraterrestrial chrome-spinel grains was discovered that spanned ~2 Myr of sediment deposition. Chrome-spinels from limestone sections of the same time interval in Russia and China were measured next to determine if this enhanced flux could be found elsewhere in the world (Cronholm and

Schmitz, 2010; Lindskog et al., 2012). Grains from these locations revealed the same large increase in material, thus demonstrating a worldwide event. The extraterrestrial grains from all sites were classified as originating from L-chondrites. This global increased flux has now been tied to the breakup of the L-chondrite parent body ~470 Ma (Schmitz et al., 2001, 2003, 2008).

The collection of fossil meteorites also uncovered a type of meteorite (Österplana 065) that is unlike the types we know today (Schmitz et al., 2016). Chromium and oxygen isotope abundances of chrome-spinels from this fossil meteorite show that the meteorite falls outside the fields of known meteorite types. Cosmic-ray exposure ages of Österplana 065 suggest that the meteorite may be from the impactor that broke up the L-chondrite parent body.

1.2 Jurassic Grains

This dissertation focuses on chrome-spinel grains from the Jurassic time period. Few time intervals have been studied, thus almost any period would provide useful information for understanding how meteorite populations have changed over time. The Jurassic time period was specifically chosen for the possibility of discovering remnants from the breakup of the Baptistina asteroid family ~160 Ma (plus 30, minus 20 Myr) (Bottke et al., 2007; See Section 2.5.4). The Jurassic samples were collected from limestone that formed during the upper Bathonian to Callovian (168-164 Ma; Reolid and Abad, 2019), approximately 280 km southwest near Carcabuey in Southern Spain. The Spanish sediments were deposited very slowly in a calm shallow sea in the Mediterranean region where little sediment from land was incorporated. The slow sedimentation rate and calm environment resulted in high abundances of extraterrestrial chrome-spinels (10-15 grains > 63 microns per 100 Kg).

Classifying remnant chrome-spinels may lead to different discoveries. It is likely that the chrome-spinels collected represent the background flux of micrometeorites. However, it is also possible that the sample collection recovers a surplus of grains from a local event (one large meteorite fall in the area of collection) or a global event (similar to the L-chondrites of the Ordovician). A local or global event can be distinguished by comparing the classifications of samples from multiple locations. If the surplus is observed in one location then there was likely a local event, but if the surplus is observed in multiple locations then it is likely a global flux of material. It is also possible that a new meteorite type is discovered within the sample collection. A new meteorite type must be shown to have distinct chemical and isotopic compositions compared to the meteorite types known today. Thus far, chrome-spinels from a fossil meteorite

that fell during the Ordovician (Österplana 065) have compositions that are unlike chrome-spinels from meteorite types we know today (Schmitz et al., 2016). Each of these types of discoveries leads us to a better understanding of what was occurring in the Solar System throughout the past.

1.3 Classifications

Remnant chrome-spinels are classified into parent meteorite types by comparing their compositions to those of grains from modern meteorites. In order to make the most reliable classifications, a database of compositions from all meteorite types is needed. Chapter 4 describes such a database, how it was constructed, and how it can be used to infer the changes in meteorite populations through time.

Chrome-spinel grains from meteorites have distinct chemical compositions for different meteorite types that are falling to Earth today (Bunch, T. E., Keil, K., & Snetsinger, K. G., 1967). We can use these distinct compositions to classify the extraterrestrial grains into parent meteorite types. However, chemical compositions of chrome-spinels from different meteorite types can overlap. The implementation of oxygen isotopes can help with the classification of remnant chrome-spinels.

Oxygen isotopes are used as a primary means of classifying meteorites because they can help discriminate amongst different meteorite types, as well as distinguish between extraterrestrial and terrestrial origins (Fig. 1.1; Clayton et al. 1991). Terrestrial samples fall along the Terrestrial Fractionation Line (TFL). Oxygen isotopes are commonly represented as delta values ($\delta^{17}O$, $\delta^{18}O$; Eq. 1.1), which give the deviation from a defined international measurement standard in parts per thousand (per mil, ‰). Vienna Standard Mean Ocean Water (VSMOW; Eq. 1.2) is commonly used as the oxygen standard composition for extraterrestrial samples (Fahey et al. 1987). Oxygen isotopes can also be represented in $\Delta^{17}O$ notation (Eq. 1.3), which gives the extent to which a sample deviates above or below the TFL. Many meteorite types are fractionated along the same slope as the TFL via physical, geological and environmental processes, as well as by instrumental fractionation effects, which give consistent $\Delta^{17}O$ values. The $\Delta^{17}O$ value often represents the material itself from which meteoritic components formed, which is the fundamental property that we focus on for the classification of remnant chrome-spinels. Chapter 2 uses oxygen isotope abundances in conjunction with chemical compositions to determine parent meteorite types of remnant chrome-spinels from the Jurassic time period.

$$\delta^{17or18}O = \left(\frac{\left(\frac{^{17or18}O}{^{16}O}\right)_{\text{sample}}}{\left(\frac{^{17or18}O}{^{16}O}\right)_{\text{VSMOW}}} - 1 \right) \times 1000 \qquad (1.1)$$

$$\left(\frac{^{18}O}{^{16}O}\right)_{\text{VSMOW}} = 0.0020052; \quad \left(\frac{^{17}O}{^{16}O}\right)_{\text{VSMOW}} = 0.00038288 \qquad (1.2)$$

$$\Delta^{17}O = \delta^{17}O - 0.52 \times \delta^{18}O \qquad (1.3)$$

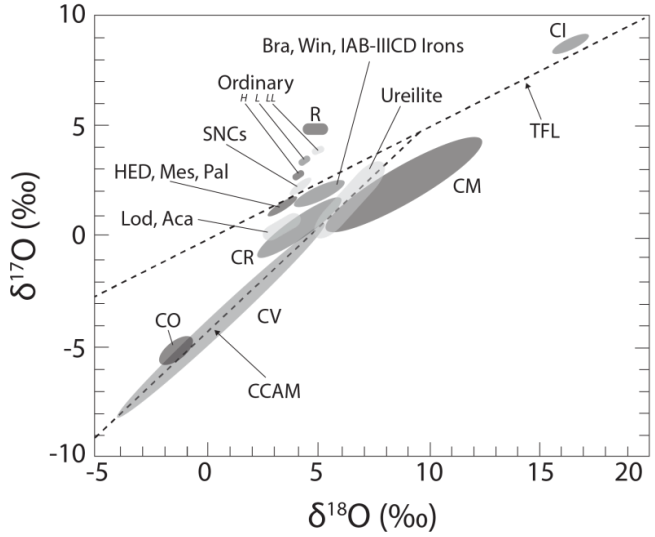

Figure 1.1. Bulk three-oxygen-isotope fields show the regions in which different meteorite types fall (after Clayton, 2004). TFL - Terrestrial Fractionation Line. CCAM - Carbonaceous Chondrite Anhydrous Mineral. Meteorite types: Bra – brachinite; Win – winonaite, R – R chondrite, SNCs – shergottite, nakhlite, chassignite; HED – howardite, eucrite, diogenite; Mes – mesosiderite; Pal – pallasite; Lod – lodranite; Aca – acapulcoite.

Silicate inclusions within extraterrestrial chrome-spinel grains can also be used to classify parent meteorite types. Studies have shown that inclusions in ordinary chondrites show a clear distinction between H, L, and LL chondrites based on the fayalite (Fa) content in olivine and the ferrosilite (Fs) content of Ca-poor pyroxene (Alwmark and Schmitz, 2009a). Large inclusions (> 3 μm) can be measured via electron microprobe. Smaller inclusions cannot be measured using the electron microprobe because the interaction volume of the measurement can incorporate

surrounding chrome-spinel compositions, thus giving an incorrect composition. In Chapter 3, I utilize focused ion beam (FIB) and (scanning) transmission electron microscope (S/TEM) techniques to measure small inclusions within Jurassic chrome-spinels to help determine the origin of grains that cannot be classified using chemistry and oxygen-isotopes alone.

1.4 Technical Advancements

As part of my work to study remnant chrome-spinels, I investigated several technical aspects to ensure reliable grain measurements. This includes mounting techniques, standard monitoring, and the possible effects of crystal orientation on $\delta^{18}O$ values.

The remnant chrome-spinels are mounted in epoxy because they are loose grains that must be held in place for polishing and measurements. Loose grains can be mounted in one-inch round pucks of epoxy, but large amounts of epoxy can degas into the vacuum chamber and release unwanted compounds that would negatively affect our measurements, such as causing high OH ion signals. To overcome this issue, we used quarter-inch-diameter stainless steel cylinders ("bullets") with small wells to contain the grains and a drop of epoxy. The grains are ground flat and polished to decrease topography effects on the grain surfaces and to uncover large enough surfaces within the grains for measurements.

This mounting technique also allowed us to improve standard measurement techniques. Stillwater chrome-spinel grains were also placed in the same bullet mounts as the Jurassic chrome-spinels to be used as an oxygen-isotope standard. This allowed us to keep the measurements consistent throughout a session. Otherwise, an unknown mount and standards mount would have to be switched multiple times a session, possibly causing instrument settings to be slightly different after each exchange. Placing standard grains in the same mount as the unknowns also allowed for multiple standard measurements throughout a session. The standards must be monitored throughout a session so the drift of the electron multiplier can be corrected during data reduction. The increased frequency and ease of standard measurements throughout a session provided reliable and robust chrome-spinel measurements for classifications.

We also investigated potential instrumental artifacts that could affect ion probe analyses. Huberty et al. (2010) reported a crystal-orientation fractionation effect for magnetite, and since chrome-spinel has a similar crystal structure as magnetite, it may be expected to show a similar fractionation. Thus far, a fractionation effect has not been observed in chrome-spinel samples (e.g., Valley and Kita, 2009). In Chapter 5, we carried out a set of measurements to examine

whether crystal orientation influences the oxygen isotopic ratios in chrome-spinel and magnetite grains.

1.5 Dissertation Outline

This dissertation focuses on the classification of extraterrestrial chrome-spinels to determine meteorite fluxes of the Jurassic time period and the techniques needed to achieve such classifications. This work is relevant to those studying chrome-spinels from different time periods, as well as those who study chrome-spinels in modern day meteorites.

Chapter 2 classifies extraterrestrial chrome-spinels from the Jurassic into parent meteorite types to help understand how meteorite fluxes (types and abundances) have changed over time. Chemical compositions from electron microprobe measurements and oxygen isotope abundances from ion microprobe measurements were used in conjunction with the compiled database (Chapter 4) to classify each remnant grain. The relative meteorite type abundances of the Jurassic were compared with those from other time periods.

Chapter 3 uses FIB/STEM techniques to help further classify remnant chrome-spinels by measuring the compositions of silicate inclusions. I also evaluated the use of STEM-EDS versus SEM-EDS for reliable compositional measurements based on inclusion size.

Chapter 4 compiles an extraterrestrial chrome-spinel database that is used for the classification of grains from the Jurassic (Chapter 2). I collected chemical and oxygen isotope compositions from literature searches and took new measurements to add additional entries to the database.

Chapter 5 investigates possible crystal orientation effects of chrome-spinel and magnetite grains on ion microprobe analyses. I determined the orientations of randomly oriented grains in thick sections of terrestrial magnetite and chrome-spinel samples. The orientations were compared with $\delta^{18}O$ values measured to determine if there are orientation effects that must be addressed for ion microprobe analyses.

CHAPTER 2

REMNANT EXTRATERRESTRIAL CHROME-SPINELS REVEAL METEORITE ABUNDANCES OF THE JURASSIC

2.1 Abstract

Remnant chrome-spinels from meteorites and micrometeorites provide insights into what meteorite types were falling throughout Earth's history. The chrome-spinels are preserved in terrestrial limestone and retain their characteristic chemical and oxygen isotope compositions. These abundances can be compared to those of modern meteorite chrome-spinels to determine the parent meteorite type of the grain. Chrome-spinels for this study were recovered from highly condensed Jurassic (~165 Ma) limestone in southern Spain and measured for element and oxygen isotope abundances. Grains were classified by comparing their compositions to a compiled database of modern meteorite chrome-spinels using hierarchical clustering techniques. Classifications were confirmed with oxygen isotope values. Approximately 88% of the 179 grains measured were classified as extraterrestrial, with likely ordinary chondrite, carbonaceous, diogenite, ureilite, and other possible meteorite type sources. A group of grains was also observed that had distinct compositions unlike the other Jurassic grains and meteorite types of the database. These grains were termed "High-Al" due to their Al content. The classification abundances of the Jurassic were also compared to the chrome-spinel abundances of other time periods to see how populations of meteorite types evolved over time. An abundance of ordinary chondrite-like grains is observed throughout all of the time periods, suggesting that this meteorite type is an abundant source of material in the solar system. However, ordinary chondrites may not have been as abundant throughout time compared to today due to the higher abundances of grains from other extraterrestrial sources observed in earlier time periods. Comparison of our Jurassic data to similar studies preceding and following our time period suggests drastic differences in relative meteorite abundances. However, it is more likely that differences in methodologies used for the classification of extraterrestrial grains are the underlying cause of abundance differences. This implies that methodologically dissimilar studies should be compared with caution. Updates to the modern meteorite chrome-spinel database and a thorough

understanding of meteorite compositions (chemical and oxygen) will provide more robust classifications in the future.

2.2 Introduction

Studying meteorites is vital to understanding the formation and evolution of the Solar System. Meteorites, which have been raining on Earth throughout its history, primarily originate from the breakup of asteroids. Pristine samples can provide key information, but meteorites quickly weather on Earth's surface and lose some of their original characteristics. Weathering is primarily due to the higher oxygen content on Earth, causing the iron metal of the meteorite to rust. Meteorites can also be altered when they come in contact with terrestrial water. Due to the unique environment of the Earth, meteorites tend to survive on Earth's surface for only a few thousand to tens of thousands of years. We know the relative abundance of the different types of meteorites falling on Earth today from found meteorites and witnessed falls (90.6% are ordinary chondrites). But we do not know about the material that fell in the distant past.

Fortunately, some components of meteorites can be preserved in certain sediments, giving us the ability to study meteorites from different time periods. "Fossil" meteorites have been preserved in thinly bedded limestone that was deposited slowly in relatively deep water. These areas are far from shore where there is very little contribution of sediments from the continents. These environments are not exposed to destructive waves and storms that would otherwise disturb the sedimentary time stamp of their arrival (Love and Brownlee, 1993). Fossil meteorites have been mostly transformed to calcite and clays, but some of the more resistant minerals survive, such as chrome-spinel. Recognizable fossil meteorites are extremely rare in the sedimentary record, but remnant chrome-spinel grains are found throughout sedimentary sections. They are referred to as "sediment-dispersed" chrome-spinels. Searching for sediment-dispersed chrome-spinel grains instead of whole fossil meteorites provides a way to investigate the mixture of meteorites falling on earth through time. Remnant chrome-spinels retain their original chemistry and oxygen isotopes (e.g., Schmitz et al., 2001, 2003; Heck et al., 2010). These characteristics can be measured and compared to modern day meteorite chrome-spinel compositions to determine what type of meteorite each grain originated from.

The overall objective of studying remnant chrome-spinel grains throughout Earth's history is to determine how meteorite populations have changed over time. The first time interval studied was the Ordovician (Schmitz et al., 1996, 1997, 2001). This period was dominated by an influx

of L-chondrite chondrite material that was observed in Sweden, Russia, and China, and lasted for a stratigraphic time period of ~2 Myr (Cronholm and Schmitz, 2010; Lindskog et al., 2012). This geographical distribution demonstrated a worldwide flux of material to the Earth's surface and was linked to the breakup of the L chondrite parent body ~470 Ma (Schmitz et al., 2001, 2003, 2008; Heck et al., 2010). The study of Ordovician remnant grains showed that it is possible to collect and classify extraterrestrial chrome-spinels found in terrestrial limestone throughout Earth's history (Schmitz, 2013).

Remnant chrome-spinel grains are essential to understanding abundances of different meteorites throughout history because they are the only extraterrestrial materials from ancient falls that are still accessible on Earth. Other time periods studied have shown the first glimpses into how the distribution of meteorites has changed over time. Time periods include: Ordovician (pre-LCPB 467 Ma, Heck et al., 2017; post-LCPB 466 Ma, Martin et al., 2018), Late Silurian (~426 Ma, Martin et al., 2018), Upper Devonian (~373 Ma, Schmitz et al., 2019), Early Cretaceous (~139 Ma, Schmitz et al., 2017), and Late Cretaceous (~91 Ma, Martin et al., 2019) (See Section 2.5.3). Sampling the Jurassic time period will continue to fill in the timeline. Here we report data for sediment-dispersed chrome-spinel grains from Jurassic limestone (~165 Ma) in Southern Spain, near Carcabuey.

2.3 Methods

2.3.1 Collection and Preparation

The Jurassic grains originate from a highly condensed sediment bed (Ammonitico Rosso type) sampled at Carcabuey, province of Córdoba, in southern Spain. The bed formed during the upper Bathonian to Callovian age (168-164 Ma; Reolid and Abad, 2019). The method to separate chrome-spinel grains from limestone samples was developed by Birger Schmitz and his team in their specialized lab at Lund University, Sweden (Schmitz, 2013). All of the Jurassic chrome-spinel grains were extracted in the lab at Lund University. Each sediment batch began with approximately 100 kg of limestone and hundreds of liters of HCl in a large container (Fig. 2.1a). After the rock was dissolved, the acid was removed and neutralized. The remaining material was clay, which accounts for approximately a tenth of the original rock. The clay was sieved to a large (63-355 μm) and small size fraction (32-63 μm), and the spinel grains were separated by hand using a picking scope (Figs. 2.1b and 2.1c). Every grain from the 32-355 μm fraction is

recovered. The fraction smaller than 32 µm is lost, and the fraction larger than 355 µm is saved, but nothing of interest has been found in this fraction. In some cases, the grains were covered in residue and had to undergo further cleaning treatment, such as HF, H_2SO_4, and HNO_3 (Schmitz, 2013).

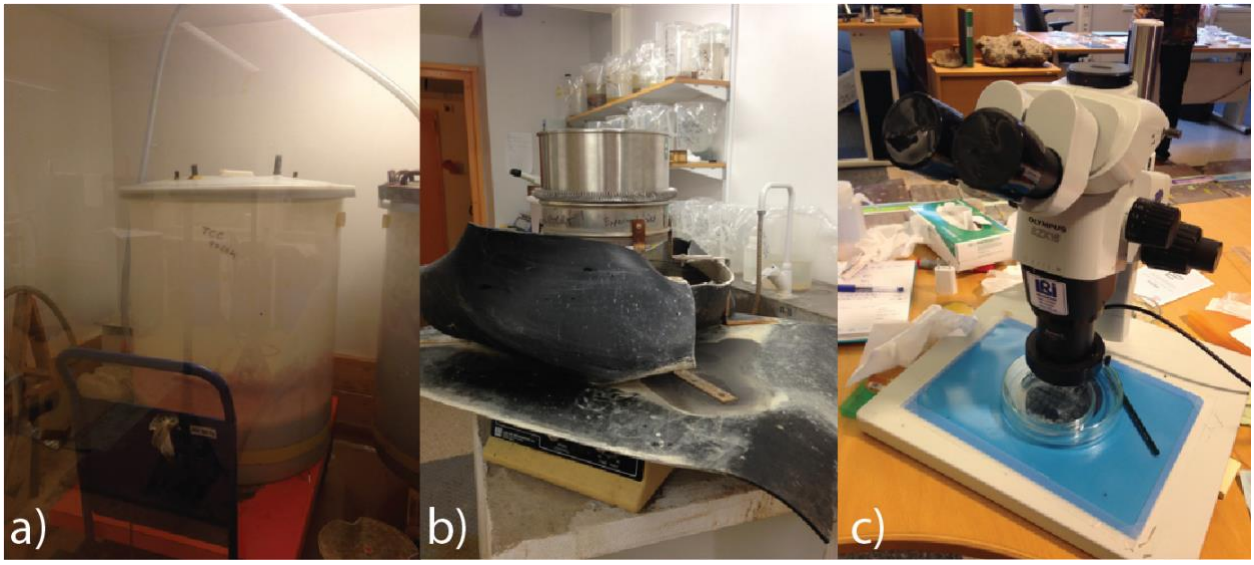

Figure 2.1: Steps of chrome-spinel grain extraction from limestone. A) The limestone was dissolved with acid in a large container, b) the remaining material was sieved, and c) the chrome-spinel grains were separated by hand using a picking scope.

After separation, the chrome-spinel grains were sent to the University of Hawai‘i (UH) to be mounted and analyzed. Ten to thirty Jurassic chrome-spinel grains and three Stillwater-chromite standard grains were mounted into each quarter-inch-diameter stainless steel cylinder (“bullets”) using epoxy (Beuhler EpoxiCure 2). Each bullet was ground flat and polished using diamond lapping papers with grit sizes ranging from 15 to 1 µm. The mounts were coated with ~20−25 nm of carbon using a Cressington 208 carbon coater. Stillwater chromite (Beartooth Mountains, Montana) was used as a standard for both electron probe and ion probe measurements. Stillwater compositions are reproducible in the electron probe (Table 2.1), and we have had the oxygen isotope composition independently measured at the Open University (I. Franchi).

Table 2.1. Electron microprobe analysis of Stillwater chromite.

	MgO	Al_2O_3	TiO_2	V_2O_3	Cr_2O_3	MnO	All FeO	FeO	Fe_2O_3	ZnO	SiO_2
Average (n=222)	10.13	17.60	0.51	0.17	43.18	0.22	26.52	19.35	7.97	0.05	0.00
2 SD	0.86	0.89	0.09	0.04	1.04	0.04	1.62	1.31	0.72	0.03	0.00

All FeO: all Fe assigned as FeO.
2 SD: 2 standard deviations.

Backscattered electron (BSE) and secondary-electron (SE) images of the grains were taken using a JEOL JSM-5900LV scanning electron microscope (SEM). Images were obtained both before and after isotope analyses in order to ensure that measurement spots were free from cracks and areas of alteration (see Schmitz, 2013 for more information on grain alteration). The SEM was also used to mark the grains so that a precise position on the grain can be measured by ion probe for oxygen isotopes. A focused, high-current electron beam will burn a hole in the carbon coat in a few minutes.

2.3.2 Analysis

Elemental Abundances

Grain compositions were determined using the JEOL JXA-8500F field emission electron microprobe at the University of Hawai‘i. This instrument bombards the sample with an electron beam, which causes the emission of x-rays at wavelengths that are characteristic to each element. Measurement parameters are given in Table 2.2. The measurements used an accelerating voltage of 20 keV, a beam current of 20 nA, and beam diameters of 1-10 microns. The beam diameter was adjusted to avoid cracks and alteration. All measurements used the ZAF matrix correction (CITZAF developed by Armstrong, 1995) embedded in the *Probe for EPMA* software. The ZAF correction takes into account the atomic number (Z), absorption (A), and fluorescence (F) in the sample. Interference corrections were applied to V for interference from Ti, and to Mn for interference from Cr. Standards were measured before, during, and after the Jurassic chrome-spinel grains to ensure that drift corrections for wavelength peak positions were not required. The UH electron probe lab standard Chromite USNM 117075 was also used as a standard for electron probe measurements.

Table 2.2. Electron probe settings of elements measured for Jurassic chrome-spinels.

Element	Crystal*	Time (s)	Standard+
Mg	TAPH	80	Chromite USNM 117075 (112)
Al	TAP	40	Chromite USNM 117075 (112)
Ti	PETH	80	Sphene Glass (111)
V	LIF	40	V_4O (142)
Cr	LIFH	20	Cr_2O_3 (Cameca 18-c) (159)
Mn	LIF	40	Garnet Verma (Mn) (102)
Fe	LIFH	20	Chromite USNM 117075 (112)
Si	TAP	40	Garnet Verma (Mn) (102)
Zn	LIFH	30	ZnO (Cameca 18-c) (156)

*Crystal: TAP – thallium acid phthalate; PET – pentaerythritol; LiF – lithium fluoride; H-crystals have limited range but higher count rate.
+The values in parentheses after each standard are the UH internal standard numbers.

Iron in chrome-spinel can be present as Fe^{2+} (tetrahedral site) and/or as Fe^{3+} (octahedral site, along with Cr^{3+}). The electron probe measures total Fe and cannot differentiate between Fe^{2+} and Fe^{3+}. Therefore further data reduction is needed to partition the cations between the tetrahedral and octahedral sites (Droop, 1987). The cation partitioning is based on the stoichiometry of a specified mineral, where the number of oxygens (X) and the number of cations (T) come from the mineral formula. In the case of chrome-spinel, X=4 oxygens and T=3 cations. For every Fe^{3+} ion in the spinel, there is a deficiency in the oxygen total of 0.5. Thus, the oxygen total tabulated in the electron-probe data (N) can be related to the number of Fe^{3+} ions present per X oxygens (F) by:

$$N = X - \frac{1}{2}F \qquad (2.1)$$

There is also a discrepancy between the measured cation abundance as reported by the electron probe (S) and the true cation value (T). The relationship between the cation and oxygen totals in the original and corrected compositions is given by:

$$\frac{S}{T} = \frac{X}{N} \qquad (2.2)$$

The combination of these two equations gives the general equation for determining the abundance of Fe^{3+}:

$$F = 2X(1 - \frac{T}{S}) \qquad (2.3)$$

The new values of FeO wt% (eq. 2.4) and Fe_2O_3 wt% (eq. 2.5) are calculated as follows:

1. If S > T, then equation (2.3) is used to determine the Fe^{3+} abundance (F).
2. The abundance of Fe^{2+} is the difference between F and the original cations of Fe.
3. Multiply Fe^{3+} and Fe^{2+} by T/S to normalize to T cations.
4. Calculate new oxide wt% values using the normalized values of Fe^{3+} and Fe^{2+}:

$$new\ FeO\ wt\% = old\ FeO\ wt\% \times \frac{Fe^{2+}}{Fe^{2+}+Fe^{3+}} \qquad (2.4)$$

$$new\ Fe_2O_3\ wt\% = 1.1113 \times old\ FeO\ wt\% \times \frac{Fe^{3+}}{Fe^{2+}+Fe^{3+}} \qquad (2.5)$$

Where 1.1113 is based on the ratio of Fe_2O_3 to FeO mass percentages (inverse of equation (4.3) in Section 4.3).

Oxygen Isotopes

The Cameca ims 1280 ion microprobe at UH was used to measure the oxygen isotopic compositions of the chrome-spinel grains in the polished mounts. The instrument setup was similar to that of Makide et al. (2009). A Cs^+ primary beam operated at +10 keV was used to sputter the sample surface, in which a small fraction of material is ionized to negative ions (secondary ions) that are accelerated into the mass spectrometer. The secondary-ion mass spectrometer was operated at -10 keV, giving impact energy of 20 keV. The transfer optics were tuned for high transmission. The energy window for the secondary ions was set to 40 eV. The normal incident electron gun was used for charge compensation.

The beam is centered at each new grain using Z-axis of the sample stage and primary beam Y-position deflector. The position(s) marked on the grains with the SEM are found using ion imaging (Nagashima et al., 2015). The imaging uses a small, low current beam (~1 μm, ~20 pA) and a large raster of 25 μm so as to not remove the carbon coating.

Each measurement began with a presputter to remove the carbon coat. The beam was rastered over a 7 μm area using a ~300 pA beam for 240 seconds. During the presputter, the Faraday cup backgrounds were measured. Next, the primary beam was increased to ~900 pA and the raster was reduced to a 3 μm area for the measurement. The spot size for this beam without rastering is ~8μm. The resulting pits were ~10x10 μm in size, sufficiently small to fit between areas of alteration and cracks on the grains. The secondary ions were measured simultaneously using the multicollector with $^{16}O^-$ on either the L'2 or L1 Faraday cup (FC) using an amplifier with a 10^{10}-ohm resistor and $^{18}O^-$ on the H1 FC with a 10^{11}-ohm resistor. The $^{17}O^-$ signal was measured on the monocollector electron multiplier (EM). The EM is used because the $^{17}O^-$ count rate from the relatively small spots is not high enough for the FC. The nuclear magnetic resonance (NMR) probe was used to control the magnetic field. Each measurement consisted of 30 cycles. During each cycle, the oxygen isotopes were measured for 4 seconds with ^{17}O on the EM, then for 10 seconds with all three oxygen isotopes on Faraday cups, and then for 2 seconds with $^{16}OH^-$ on the EM after switching from $^{17}O^-$ using the DSP2 deflector (located after the magnet). The $^{16}O^-$ and $^{18}O^-$ signals stayed on the same FCs for the 4s and 10s measurements. The $^{18}O/^{16}O$ ratio for each measurement was calculated from the 10s measurements and the $^{17}O/^{16}O$ ratio from the 4s measurements.

The mass resolving power (MRP) for $^{16}O^-$ and $^{18}O^-$ was ~2000 (M/ΔM, 10% definition) and for $^{17}O^-$ was ~5500. The MRP for $^{17}O^-$ is nominally enough to resolve $^{16}OH^-$ from $^{17}O^-$, but an abundance-sensitivity tail from $^{16}OH^-$ contributes to the $^{17}O^-$ peak. We correct for this tail using the peak-tail ratio of $^{16}OH^-$ and $^{16}OH^-$ count rate (Section 2.3.2 - ^{16}OH interference for ^{17}O). The abundance-sensitivity tail is a function of the tuning of the mass spectrometer, so the tail of $^{18}O^-$ is measured on the first day of each ion probe session. The peak-tail ratio should be relatively constant if the machine setup is not changed. The $^{16}OH^-$ peak is collected during the final 2s of each measurement cycle in order to be able to make a precise correction.

The gain of the EM decreases throughout the day due to aging of the first dynode in the EM. This is addressed in multiple ways. First, the $^{17}O^-$ signal is on the EM for the initial 4s of a cycle and is then switched to a FC to suppress the gain loss (originally proposed by Kita et al., 2007). Second, the pulse height distribution is checked at the beginning of each day and the EM high voltage is updated to keep the pulse height distribution consistent. The pulse height distribution can be checked throughout the day, but this method is time consuming and can be unreliable.

Instead, we set the gain at the beginning of the day and then monitor the gain drift by repeated measurements of standards (Section 2.3.2 - Drift correction in $\Delta^{17}O$). Approximately 8-10 unknown measurements are nested between 4-6 standard measurements. About 20 unknowns can be done in a 12-hour day including set up.

We typically made multiple measurements of each grain to determine reproducibility. Grains were re-polished to expose fresh surfaces for multiple measurements.

Detailed Data Reduction for Oxygen Isotope Analysis

1. Subtract Background

Signals from the Faraday cups had to be corrected for baseline count rate (background), which is an electronic offset in the electrometers. This offset varies depending on temperature of a feedback resistor used in the electrometer, and thus could be different among the measurements. We initially collected background measurements at the beginning and end of each day, but found that the background was not stable over the course of the days' measurements. The remaining ion probe sessions collected the background count rates on FCs used for ^{16}O and ^{18}O during the presputter of each measurement. In order to have enough background-collection time, the presputter timing was increased from 60s to 240s. The presputter raster size was increased from 5 μm to 7 μm and the beam current was reduced so as to not drill too far into the sample during presputter. The individual background measurements were used to create running average backgrounds for each day of data collection. The backgrounds were initially fit to a curve for each day, but we found that the running average was more appropriate because it tracks short period, irregular drifts and minimizes statistical variations in the background measurements. The running average for each measurement used the five nearby measurements. The first background measurement of each day could only be averaged with the two following measurements (average of three) and the second background was averaged with the previous and two following measurements (average of four). Similar averages were made for the last and second to last background measurements of the day. The corresponding running average for each measurement was subtracted from the raw counts to give background corrected values. The variation of Faraday cup background during a measurement could result in variations of measured ratios from cycles, and is partly reflected by the standard error of the mean of the ratios from the cycles.

The background counts for the electron multiplier are caused by stray ions that happen to hit the first dynode of the EM, occasional cosmic rays that hit one of the dynodes, and electronic noise in pre-amplifier. The background count rate was measured to be ~0.03 cps and is not significant compared to the ^{17}O count rates (~3×10^5 cps).

2. Deadtime Correction for the electron multiplier

The electron multiplier works by amplifying an incoming ion signal to produce a larger signal to be detected (Fig. 2.2). The ion hits the first dynode and several secondary electrons are emitted. These electrons are accelerated into the next dynode of the multiplier to produce more electrons and this is repeated for each of the multiplier dynodes (21 dynodes in our monocollection EM). This cascade of electron emission generates an amplified signal composed of 1.5 x 10^7 electrons. When the input signal exceeds the threshold voltage then the discriminator outputs a pulse that goes to a counter, which counts the number of pulses, i.e., the number of incoming ions. The output pulse width is determined by the discriminator and is known as the deadtime because the system cannot respond to additional input signal during the pulse width time (we use 30 ns). Figure 2.2 shows a single event versus two events in a nonretriggerable counting system. The nonretriggerable system uses a defined deadtime that does not change based on the size or duration of an input signal, i.e. the deadtime for a single-event signal is the same as for the longer two-event signal. A retriggerable counting system allows the deadtime to increase based on the input signal, i.e. a 30 ns deadtime would increase to a 60ns deadtime if the input signal were still above the threshold voltage at the 30 ns mark.

The count rates for ^{17}O must be corrected for electron-multiplier deadtime to account for ignored input signals. The UH Cameca ims 1280 has a nonretriggerable counting system, where the deadtime corrected ^{17}O counts ($^{17}O_{DT}$) is given by:

$$^{17}O_{\mathrm{DT}} = \frac{C_m}{1 - C_m \times T}, \qquad (2.6)$$

where C_m is measured ^{17}O count rate and T is deadtime. We measured the deadtime for our pulse counting system using the method described in Fahey (1998) and was determined to be 30±1 ns. This measured deadtime is slightly longer than the electronic deadtime (24 ns) set by the discriminator, but it is very reproducible. Given a measurement with 250,000 cps for ^{17}O, the

uncertainty in the deadtime correction would be approximately 0.26 per mil. The same corrections are applied to the standards so the errors are effectively cancelled out during instrumental mass fractionation corrections.

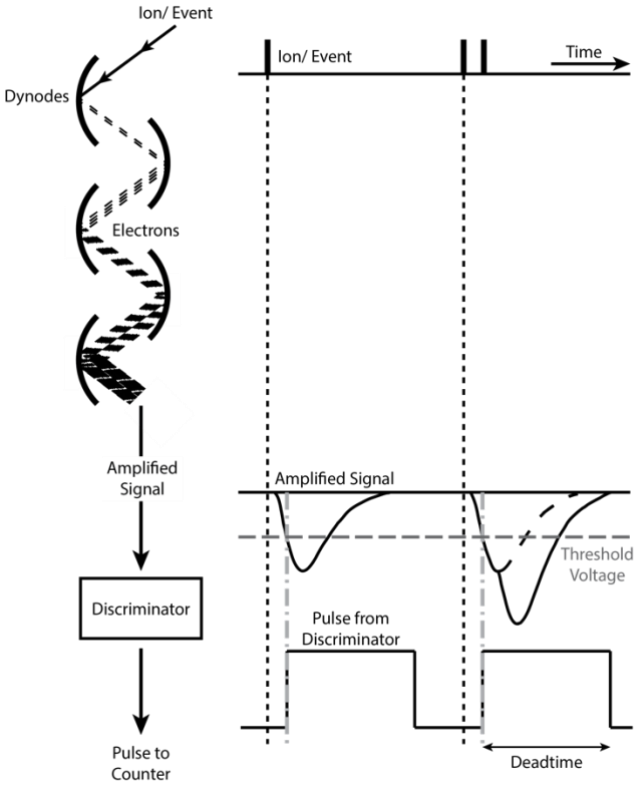

Figure 2.2. Schematic of typical electron multiplier components (left) and the corresponding transitions of an ion/event into a counted pulse (right). An event begins with an ion hitting a dynode resulting in a cascade of secondary electrons that produces an amplified signal. If the input signal is larger than the designated threshold voltage then the discriminator outputs a pulse to be counted. The output pulse from the discriminator does not begin until the input signal meets the threshold voltage (light grey dashed and dotted line). The duration (deadtime) and intensity of the discriminator output pulse is independent of the input signal strength and number of events. Any additional events/signals that arrive during the deadtime are ignored.

3. ^{16}OH interference for ^{17}O

An ^{16}OH correction must be done to remove the contribution from the ^{16}OH tail on the ^{17}O peak. While the $^{16}OH^-$ contribution can be corrected to first order, the size of the $^{16}OH^-$ peak can vary. For example, our work has shown that areas that experienced aqueous alteration can have a much larger $^{16}OH^-$ contribution and result in measured $^{17}O/^{16}O$ ratios higher than their true values. If the peak is small, the tail correction is insignificant, but if the $^{16}OH^-$ peak is much

larger than the $^{17}O^-$ peak, then the correction is significant and the uncertainty in the correction adds to the uncertainty of the final result.

The ^{16}OH interference on ^{17}O is illustrated in Figure 2.3a below. The black dashed line is the approximate continuation of the ^{16}OH curve, where at point b_1 the ^{16}OH signal is adding to the peak counts of the ^{17}O curve. The peak of ^{16}OH (b_2) is measured at the end of each cycle. The peak-tail ratio (a_1/ a_2) is measured on the ^{18}O curve because it has negligible interference; the peak of ^{17}OH relative to ^{18}O is eight times smaller than that of ^{16}OH relative to ^{17}O. The peak of ^{18}O is also used as a proxy for ^{16}OH because we assume their peak shapes are identical (Fig. 2.3b). The ^{18}O peak-tail ratio is measured at the beginning of an ion probe session. The masses 17.99, 17.9952, 17.99545, 17.99555, 17.99563 were measured on the electron multiplier (EM) and 18 was measured on a faraday cup (FC2). Other conditions were the same as those used for isotope measurements. The peak-tail ratio is calculated using signals at the 17.99555 and 18 masses (a_1/ a_2). The remaining masses were used to help determine variation and uncertainty in the measurement. The ratio (a_1/ a_2) is multiplied by the ^{16}OH peak (b_2) and gives the ^{16}OH interference (b_1). The ^{16}OH interference is subtracted from the ^{17}O count rate for each cycle of the measurement.

The ^{16}OH interference correction has a statistical uncertainty and an uncertainty due to the stability of the magnet. The statistical uncertainty is not taken into account because of the following reasons. The statistical uncertainty on the ~8 ppm peak-tail ratio measured for ^{18}O is 0.24-0.44 ppm. This uncertainty is translated to ~0.004 ‰ of OH correction with typical ^{16}OH count rate. Thus this uncertainty is negligible. The uncertainty for the magnet stability takes into account the maximum variation (±5 ppm) of the magnetic field controlled by the NMR probe. This is because the tail has a slope against mass and so the fluctuation of the magnet changes the ^{16}OH contribution on ^{17}O. This uncertainty can be approximated by the difference of two measured points on either side of a_1 (Fig. 2.3b - two orange dots, c_1 and c_2 corresponding to ±5 ppm of a_1). The tail correction uncertainty is ~8% of the tail correction.

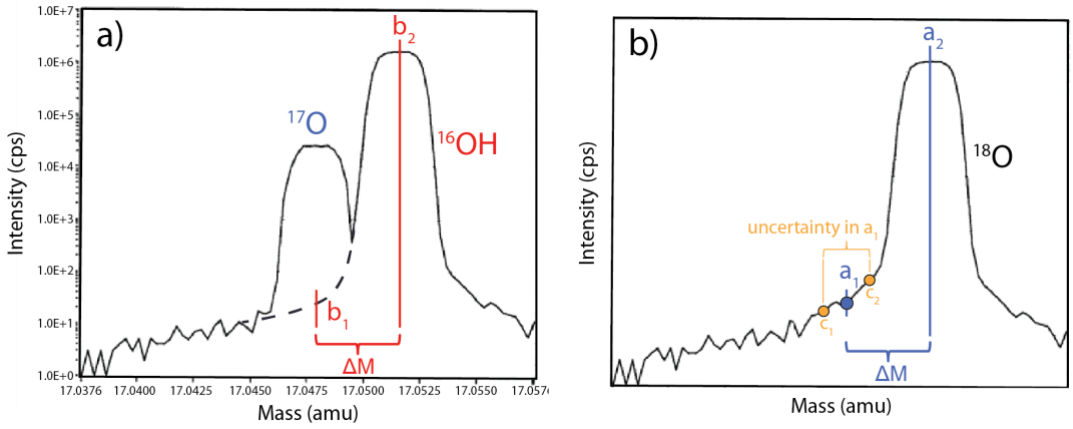

Figure 2.3. Schematics of the mass and intensity of ^{16}OH, ^{17}O, and ^{18}O peaks. A) The interference of the ^{16}OH tail on the ^{17}O peak (b_1) must be taken into account to determine the true value of ^{17}O. B) The curve of ^{18}O is measured as a proxy for the ^{17}O correction. Positions c_1 and c_2 are also measured to provide an uncertainty for the correction.

4. Ratios

The isotopes of each measurement are represented as ratios ($^{18}O/^{16}O$ and $^{17}O/^{16}O$) and are the average of the 30 cycles for each ratio. The measurement (internal) errors of the ratios are the standard error of the 30 cycles. Standard error is used because multiple cycles are being measured of the same sample under the same conditions.

$$Standard\ Error = \frac{standard\ deviation}{\sqrt{N}} \qquad (2.7)$$

5. Standardization

Standards are used to determine how the ion probe fractionates the isotopes. Since the true oxygen isotope values of the standards are known, we can use the difference between the measured and true values of the standards to determine the true values of the unknowns. The measurements for the unknown Jurassic grains were bracketed by standard measurements of Stillwater chromite. The delta values for Stillwater chromite relative to VSMOW were measured using the laser fluorination technique by Ian Franchi of Open University (e.g., Greenwood et al., 2007) and they are $\delta^{18}O = 2.67 \pm 0.30$ (2σ), $\delta^{17}O = 1.38 \pm 0.14$ (2σ), and $\Delta^{17}O = -0.011 \pm 0.016$ (2σ) (I. Frachi, personal communication).

The measured ratios for the unknowns are corrected using a Factor determined by dividing the true Stillwater ratios by the mean of the standard Stillwater measurement ratios from that

session, which corresponds to the instrumental mass fractionation from the ion probe (Equation 2.8). This Factor is multiplied by the measured ratios of the unknowns to give the standard-corrected (st corr) values for the unknowns under an assumption that the degree of mass fractionation obtained on the standard is exactly the same as those to unknowns (Equation 2.9).

$$Factor = \frac{\left(\frac{^{17}O \text{ or } ^{18}O}{^{16}O}\right)^{\text{Stillwater}}_{\text{true}}}{\left(\frac{^{17}O \text{ or } ^{18}O}{^{16}O}\right)^{\text{Stillwater}}_{\text{mean of measurements}}} \quad (2.8)$$

$$\left(\frac{^{17}O \text{ or } ^{18}O}{^{16}O}\right)_{\text{st corr}} = Factor \times \left(\frac{^{17}O \text{ or } ^{18}O}{^{16}O}\right)_{\text{measured}} \quad (2.9)$$

The uncertainty (σ) for the standard-corrected ratio is given in Equation 2.10, which takes into account the measurement (internal) ratio error and the standard deviation (SD) of the standard ratios.

$$\sigma\left(\frac{^{17}O \text{ or } ^{18}O}{^{16}O}\right)_{\text{st corr}} = \sqrt{\left(\sigma\left(\frac{^{17}O \text{ or } ^{18}O}{^{16}O}\right)_{\text{internal}}\right)^2 + \left(\sigma\left(\frac{^{17}O \text{ or } ^{18}O}{^{16}O}\right)^{\text{Stillwater}}_{\text{SD}}\right)^2} \quad (2.10)$$

At this point, the ^{18}O corrections are complete. More corrections are needed for ^{17}O.

6. Delta Values

The $\delta^{17or18}O$ values (Chapter 1) are calculated using the standard-corrected ratios and the known ratios of VSMOW. The uncertainty for ^{17}O and ^{18}O in delta notation are calculated through a similar conversion from ratio to delta notation (Equation 2.11). The calculations, corrections, and errors for ^{18}O are complete at this step. The calculations of ^{17}O continue with the conversion to $\Delta^{17}O$ ($= \delta^{17}O - 0.52 \times \delta^{18}O$).

$$\sigma\delta^{17or18}O_{st\ corr} = \left(\frac{\sigma\left(\frac{^{17}O \text{ or } ^{18}O}{^{16}O}\right)_{\text{st corr}}}{\left(\frac{^{17}O \text{ or } ^{18}O}{^{16}O}\right)_{\text{VSMOW}}}\right) \times 1000 \quad (2.11)$$

7. Drift correction in $\Delta^{17}O$

The gain of an electron multiplier degrades with time under an intense beam, causing count rate to decrease as the gain drops (Fig. 2.4). If left uncorrected, the gain drop for ^{17}O would cause the $^{17}O/^{16}O$ ratio to change over a set of measurements. The drift of the electron multiplier is shown by the trendline of the standard measurements (orange circles in Fig. 2.4) that are measured before and after the unknowns (blue triangles) in $\Delta^{17}O$ notation. When a trendline of the standard measurements does not have a slope, then it would mean there is no drift. But the negative slope in Fig. 2.4 as an example shows that a drift occurred during these measurements. Since this trend line is constructed by measurements of the standard with $\Delta^{17}O=0$, this trendline defines the TFL ($\Delta^{17}O=0$ by the definition); therefore the difference between the trendline and a specific unknown measurement will give the final $\Delta^{17}O$ value of the unknown.

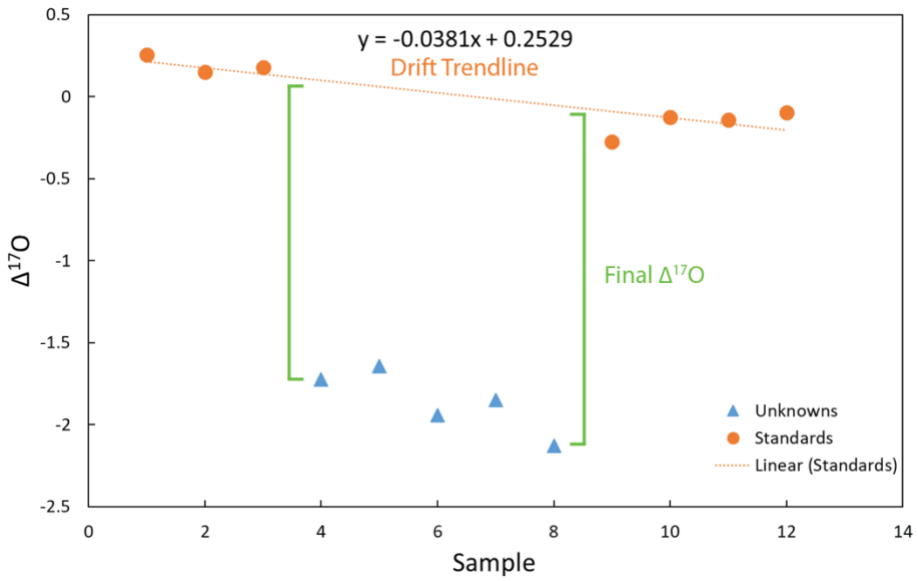

Figure 2.4. Example of $\Delta^{17}O$ values of standards (orange circles) and unknowns (blue triangles) used in drift correction. The drift trendline is a regression through the standard data and shows the degree of drift during the measurements. The vertical distance between an unknown and the drift trendline is the Final $\Delta^{17}O$ value for the specified unknown.

The uncertainty of the Final $\Delta^{17}O$ value for each measurement includes the variation of the standards (standard deviation) after the drift correction and the standard error for $\Delta^{17}O$ over the 30 cycles for the individual measurement (Equation 2.12). The average uncertainty (2SD) for the Jurassic grains is 0.60 ‰.

$$\sigma\,\Delta^{17}O = \sqrt{(\sigma Final\,\Delta^{17}O_{SD}^{standards})^2 + (\sigma\Delta^{17}O_{st\ error}^{30\ cycles})^2} \quad (2.12)$$

8. Final $\delta^{17}O$

Once the final $\Delta^{17}O$ values are generated, the Final $\delta^{17}O$ values can be calculated using the reverse of previous equations:

$$Final\ \delta^{17}O = Final\ \Delta^{17}O + (0.52 \times \delta^{18}O_{st\ corr}) \quad (2.13)$$

The uncertainty for the Final $\delta^{17}O$ values uses the variations of the standard measurements after the drift correction in small delta format and the variation in the 30 cycle measurement of the unknown (Equation 2.14).

$$\sigma\,\delta^{17}O = \sqrt{(\sigma Final\,\delta^{17}O_{SD}^{standards})^2 + (\sigma\delta^{17}O_{st\ error}^{30\ cycles})^2} \quad (2.14)$$

9. Cycle Cuts

Cycles from some measurements were cut due to dramatic variations in the ^{16}OH intensities. Variations include a jump in ^{16}OH for a single cycle, a gradual increase in ^{16}OH, or a sharp increase in ^{16}OH that continued for multiple cycles. These changes in ^{16}OH intensities were most likely due to the exposure of alteration or a crack beneath the surface that could not be foreseen.

Each measurement was reviewed and cycles with a jump in the OH correction were flagged. The data for measurements containing flagged cycles were reduced again with the flagged cycles removed from the data reduction process. The same cycles were also removed for the standards used in the measurement session in order to have identical measurement conditions between the standards and unknowns.

10. Measurement Screening

Each measurement must be screened for reliability before the grain can be classified into a parent meteorite type. The grains were imaged before electron and ion microprobe analyses using the SEM in SE and BSE imaging modes. The images helped establish appropriate locations for electron probe and ion probe measurements to avoid cracks and alteration. Images were also taken after measurements to ensure the correct positions were sampled. Cracks are an

issue because extra oxygen can be trapped within the crack, thus shifting the isotopic composition toward terrestrial oxygen. Rims and patches of alteration are fairly common amongst the grains. In altered areas, Fe can be replaced by Zn and Mn (Schmitz, 2013). Areas of alteration may also incorporate terrestrial water, which shifts the oxygen-isotope composition toward terrestrial compositions. Incorporated water can also affect the OH tail correction for a measurement. We are confident that OH corrections smaller than 1.0‰ are reliable. If the correction is larger than that, the uncertainty in the tail correction begins to significantly increase the total uncertainty for the measurement. For example, the uncertainty in the tail correction is ~8% of the tail correction (Section 2.3.2 - ^{16}OH interference for ^{17}O), which corresponds to a 0.08‰ uncertainty for a 1.0‰ tail correction. This 0.08‰ uncertainty minimally affects the final Δ^{17}O uncertainty for a Jurassic grain (average final uncertainty is 0.60 ‰, Section 2.3.2 - Drift correction in Δ^{17}O).

We created a class system to determine the reliability of a measurement based on the level of cracks, alteration, and OH correction:

- Class 1 – no cracks, no alteration, OH correction < 0.5‰ (Low correction)
- Class 2 – very minor cracks or cracks near edges of measurement, moderate alteration, OH correction 0.5 - 1.0‰ (Moderate correction)
- Class 3 – large crack, all alteration, OH correction > 1.0‰ (High correction)

2.3.3 Classification Schemes

Old Scheme

We developed an initial classification scheme for this data set to gain a first order view of the compositional groupings of the Jurassic grains (Caplan et al., 2018). The scheme incorporated a small selection of published data on chrome-spinels from various meteorite types and is based on elemental and oxygen-isotope compositions.

The initial subdivision of the grains was based on Fe_2O_3 content because we thought that all iron oxide in extraterrestrial chrome-spinels would be FeO. We soon found that this is not the case, based on our samples (Caplan et al., 2018) and Fe_2O_3 contents of modern meteorite chrome-spinels (Chapter 4). The following subdivisions were made based on Δ^{17}O values (Δ^{17}O > 0, Δ^{17}O ~ 0, and Δ^{17}O < 0) and element compositions. A grain was classified into a meteorite group if at least 5 out of 8 elements (Cr, Fe, Mg, Al, Ti, V, Mn, Zn) matched the composition of

a chrome-spinel from a modern meteorite. Elements were considered to be a match if their abundances were within error of one another.

Using these criteria, the Jurassic grains were organized into 5 groups: Ordinary Chondrites, Terrestrial, Ambiguous, Classifiable Meteorite types, and Unknown Extraterrestrial. Ordinary chondrite-like grains had positive $\Delta^{17}O$ values (~0.5 to ~1.5‰), no Fe_2O_3, and element abundances that matched known ordinary chondrite chrome-spinel abundances. Some grains had positive $\Delta^{17}O$ values with no Fe_2O_3, but their element abundances were unlike chrome-spinels from ordinary chondrites; we referred to them as "Ambiguous". Terrestrial-like grains had ~0‰ in $\Delta^{17}O$ and Fe_2O_3 up to ~18 wt.%. Grains that had negative $\Delta^{17}O$ and met the minimum element criteria for a meteorite type match were classified into known meteorite types (Classifiable Meteorites). Grains with negative $\Delta^{17}O$ values that did not meet the minimum element requirement were termed Unknown Extraterrestrial. The Unknown Extraterrestrial grains were unclassified, in part because our database was incomplete at the time.

Clustering Methods

Through our systematic addition of entries to the chrome-spinel chemistry database from modern meteorites, the database became large enough (700+) that unknown grains could not be classified by manual methods alone. A hierarchical clustering method (e.g. Nielsen, 2016) was incorporated into the classification process to determine the closest matches to the chemistry of the Jurassic chrome-spinels using the compiled database. This method clusters data into a multilevel hierarchy where groupings at the lowest level have the closest matches and the higher levels are less related. The degree of "closeness" of the matches and levels are shown in a dendrogram (Fig. 2.5).

Hierarchical clustering uses a series of functions to create the final dendrogram. First, the similarities of each entry in the dataset are determined by calculating the distance (d) between the entries (Matlab function: pdist):

$$d = \sqrt{(\delta MgO)^2 + (\delta Al_2O_3)^2 + (\delta TiO_2)^2 + (\delta V_2O_3)^2 + (\delta Cr_2O_3)^2 + \left(\delta(FeO + MnO + ZnO)\right)^2} \qquad (2.15)$$

Where δ represents the difference between any pair of oxides for each pair of chrome-spinel entries. Normalizations and oxide sums were performed before hierarchical clustering input (further explained below).

Next, the pair of entries that are in close proximity are linked using the distance information previously determined (Matlab function: linkage). The entries are continuously paired into larger clusters until all entries are added. Finally, the hierarchical groupings are shown using a Dendrogram (Fig. 2.5). The horizontal axis gives the entry identification number, which is based on the order of the data entry. The lines show which entries are linked and how they are linked to other entries. The height of the lines gives the distance between the entries. Therefore, similar entries are grouped closer together and have shorter vertical lines that attach. For example, grains (entries) 6 and 7 are the closest matches in Figure 2.5 because they have the shortest vertical lines that are attached to one another. The next closest matches for grains 6 and 7 are 10, 8, and 5, respectively. Grains 14 and 17 are closest matches for one another, but they are not as closely matched as grains 6 and 7 because the vertical lines that attach 14 and 17 are longer than the vertical lines of grains 6 and 7. While grains 6, 7, 10, 8, 5, 14, 17, and other grains are grouped into H-chondrites, there are still smaller subsets amongst the group, e.g. 6, 7, 10, 8, and 5 versus 14 and 17. The dendrogram allows a visual representation of all possible subgroups and the ability to define a group based on the focus level. The subgroups may help determine petrologic types, groupings of grains from the same meteorite, or it may show the variability within a single sample.

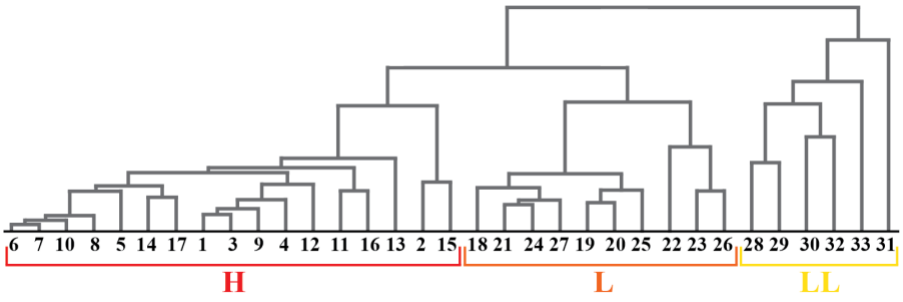

Figure 2.5. Dendrogram depicting hierarchical clustering of representative ordinary chondrite compositions (H, L, LL). Entries in dendrogram are our new grain measurements for Kernouve (H6, entries 1-17), Bruderheim (L6, entries 18-27), and Cherokee Springs (LL6, entries 28-33) (Chapter 4 and Appendix B).

The input of the clustering program contains entries (grains) with multiple dimensions (chemical abundances). The program simultaneously compares all of the dimensions in each entry from the meteorite database and the Jurassic grains to determine the closest matches. The current database is a compilation of 700+ entries from literature and our new measurements of chrome-spinel grains from modern day meteorites (Chapter 4). The elements measured for the Jurassic grains were used as the basis for the input of the clustering program, but some database entries did not have one or more of the elements (e.g., MnO, V_2O_3, ZnO, or FeO differentiated as Fe^{2+} and Fe^{3+}). The clustering initially used all of the elements to find the best matches, but some grains were not matched due to alteration. This was resolved by combining FeO (all Fe as FeO), MnO, and ZnO into a single dimension (FeO+MnO+ZnO). More grains were reliably matched using this approach. Finally, the chemical abundances of each grain and database entry were normalized so each entry total equals 100 wt%. The entries were normalized to see if the totals for the measurements had an effect on the matches. The summation of FeO, MnO, and ZnO into a single dimension was the most useful adjustment for reliable matches, but normalizing the entries also helped with classifications.

The final step was to compare the hierarchical clustering matches to the oxygen isotope values to provide independent evidence for a parent meteorite match. The reported oxygen isotope abundances of the closest 3-10 hierarchical matches were compared to the oxygen isotope value of the specified Jurassic chrome-spinel. The oxygen isotopes can confirm or refute a match, or narrow the options if multiple meteorite types matched the Jurassic grain.

The Jurassic grains were classified as originating from a specific meteorite type (e.g., ordinary chondrites), as part of a group not found in the database (e.g., the High-Al group), as Extraterrestrial, or Unclassified. A grain was determined to originate from a specific meteorite type if there was a close chemical and oxygen isotope match between a Jurassic grain and a database entry. High-Al grains were given their own classification group because they cluster separately from the other Jurassic grains and database entries (Section 2.4.3). Grains labeled "Extraterrestrial" had too many meteorite-type matches or they did not match a database entry closely enough based on chemistry and oxygen, but their $\Delta^{17}O$ values are not close to the terrestrial value. "Unclassified" grains did not match the chemistry of a database entry closely and oxygen isotopes were not discriminatory enough to determine an extraterrestrial origin, i.e. $\Delta^{17}O$ values are within errors of 0 ‰. The unclassified grains could be terrestrial or an outlier

composition from a known meteorite type whose oxygen isotopes are within errors of terrestrial ($\Delta^{17}O = 0$ ‰).

Compositions for each grain were screened before final classifications. Oxygen isotope values were put into different class groups based on cracks, alteration, and OH corrections (Section 2.3.2 - ^{16}OH interference for ^{17}O). Grains with Class 3 data were removed from the dataset. The chemical compositions were screened for low sums, high Fe_2O_3 and high ZnO contents. The high Fe_2O_3 and ZnO contents suggest terrestrial alteration of the original grain composition. Grains with Fe_2O_3 > 10 wt%, ZnO > 4 wt%, and Sums < 95 wt% were flagged. A grain with multiple flags suggested unreliable data and was classified based on oxygen isotopes alone. The Fe_2O_3 and ZnO ranges are based on compositions of chrome-spinels from modern day meteorites (Chapter 4). Modern meteorite chrome-spinels have ZnO contents < 4 wt%. Most modern day chrome-spinels have Fe_2O_3 contents less than 4 wt%, but type 3 ordinary chondrites go up to 5 wt%, carbonaceous chondrites and others up to 10 wt%, and R chondrite grains reach values much higher than 10 wt% Fe_2O_3. Since there is no strict composition for all meteorites, possible classifications are compared with flagged chemistries before determining a final classification.

Inclusions

Some grains that fit the criteria for ordinary-chondrite grains could not be sub classified as H, L, or LL chondrites, but some of the grains contained inclusions. Fayalite (Fa) and ferrosilite (Fs) contents of olivine and Ca-poor pyroxene inclusions within chrome-spinel grains can potentially help distinguish between the subclasses of ordinary chondrites (Alwmark and Schmitz, 2009a). The inclusions in Jurassic chrome-spinels are too small (2-4 μm) to collect reliable compositions using the electron microprobe and ion microprobe. Fortunately, sections of the inclusions can be extracted using the focused ion beam (FIB) and analyzed using the scanning transmission electron microscope (STEM) instruments. Inclusions found in ordinary chondrite-like grains were extracted and measured to help classify the chrome-spinels (Chapter 3; Caplan et al., 2020).

2.4 Results

2.4.1 Chemical Compositions

Chemical compositions of unknown extraterrestrial chrome-spinels and modern day grains are necessary for the classification of chrome-spinel grains into parent meteorite types. A total of 179 Jurassic chrome-spinel grains from two size fractions (large: 63-355 μm; small: 32-63 μm) were measured. Grains from the large and small size fractions have similar ranges in composition (Fig. 2.6). This is not surprising because the sieves available defined the size fractions, not by a fundamental property of the grains. The compositions of the Jurassic grains also have a similar range to that of chrome-spinel grains from modern meteorites as compiled in our database (Fig. 2.6). The overlap of compositions suggests that most of the Jurassic grains should be classifiable into their parent meteorite type using the current compiled chrome-spinel database.

Chemical features of the Jurassic grains show well-defined groups and trends (Fig. 2.6). First, there is a defined cluster with low Al_2O_3 and TiO_2 between 1.5 and 3.5 wt% (Fig. 2.6a). The same cluster appears on the Al_2O_3 vs MgO plot with MgO of ~1.5-5 wt%, on the Al_2O_3 vs Cr_2O_3 plot with Cr_2O_3 of 55-62 wt%, and the V_2O_3 vs TiO_2 with high V_2O_3 and TiO_2 of 1.5 and 3.5 wt%. A comparison with the modern meteorite database indicates that these grains are from ordinary chondrites. Second, the negative trend on the Al_2O_3 vs Cr_2O_3 plot (Fig. 2.6d) occurs because these elements share the same structural site; therefore one must decrease in content as the other increases. The positive trend on the Al_2O_3 vs MgO plot (Fig. 2.6b) reflects the contribution of the Mg-Al spinel end member ($MgAl_2O_4$) to the composition. Finally, high contents of ZnO and MnO can be attributed to terrestrial aqueous alteration that occurred while extraterrestrial chrome-spinel grains resided on the seafloor for millions of years (Schmitz et al., 2001). Most of the Jurassic grains have low MnO and ZnO contents, but there are many small size fraction grains with ZnO contents larger than 4 wt% (Fig. 2.6e and 2.6f). The replacement of FeO with ZnO can be observed in Figure 2.6h where the grains with the highest ZnO values have lower FeO contents. Understanding of defined chemical groupings and effects of alteration are necessary for the classification of extraterrestrial chrome-spinel grains.

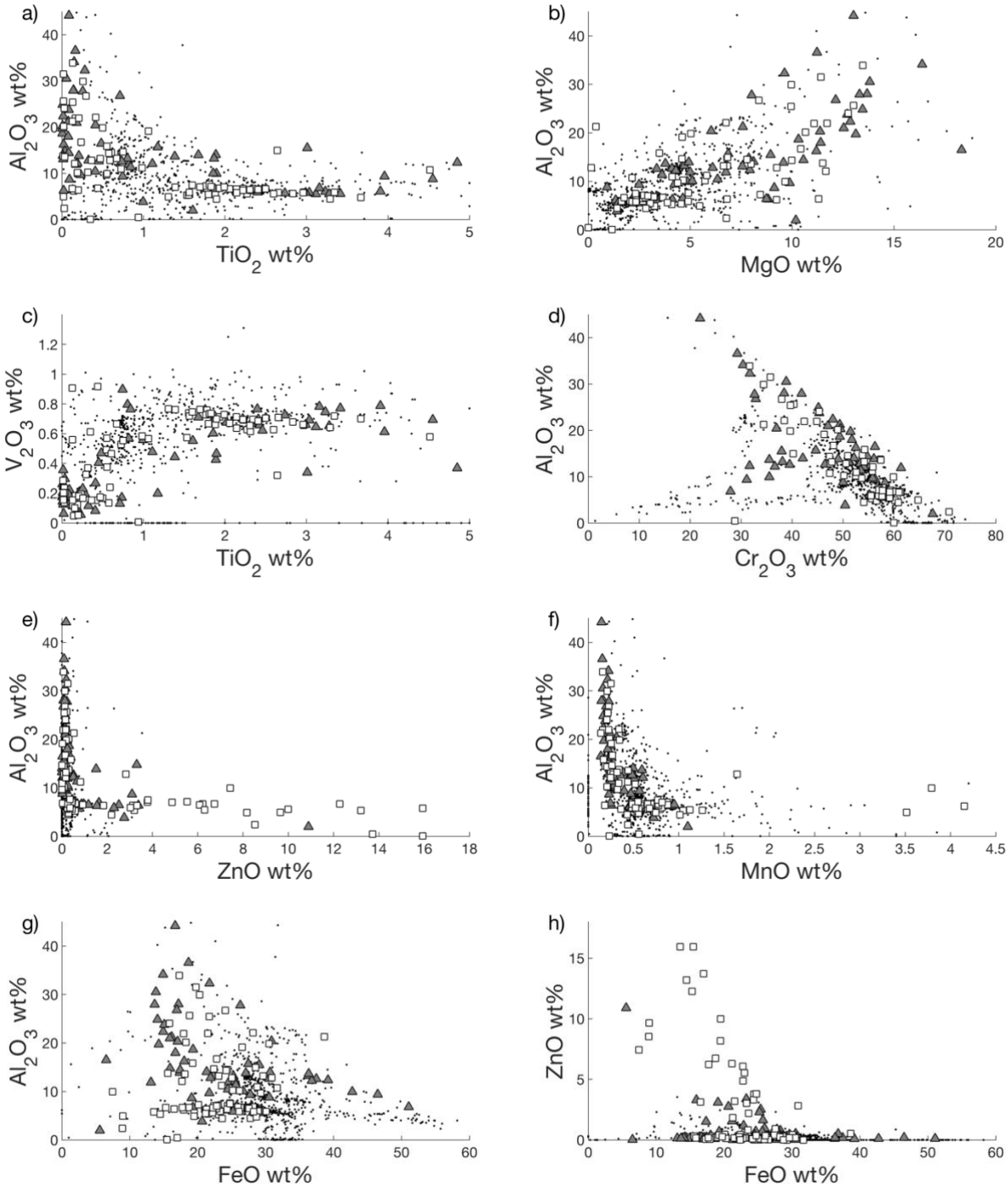

Figure 2.6. Chemical compositions of large- (grey triangles) and small- (white squares) size fraction chrome-spinel grains from Jurassic sediment. Compositions of chrome-spinel grains from modern meteorites are also plotted in the background (black dots; Chapter 4). Not all database entries have ZnO or V_2O_3 data. FeO represents all iron as FeO. For detailed plots of modern meteorite data, see Figs. 2.7-2.10 in Chapter 4.

2.4.2 Oxygen Isotopic Compositions

Oxygen isotopes also help determine the parent meteorite type of a chrome-spinel grain and can help discriminate between a terrestrial or extraterrestrial source. The $\Delta^{17}O$ values of most of the Jurassic chrome-spinels are between -1‰ and +2‰ (Fig. 2.7). The large and small size fractions generally cover the same range of oxygen isotope values, but the smaller size fraction has more grains with the lowest $\Delta^{17}O$ values. The $\Delta^{17}O$ values of the Jurassic grains also overlap with the observed ranges for modern meteorites (bars below the histogram). This overlap shows that the Jurassic chrome-spinels can also be classified into parent meteorite types using oxygen isotopes.

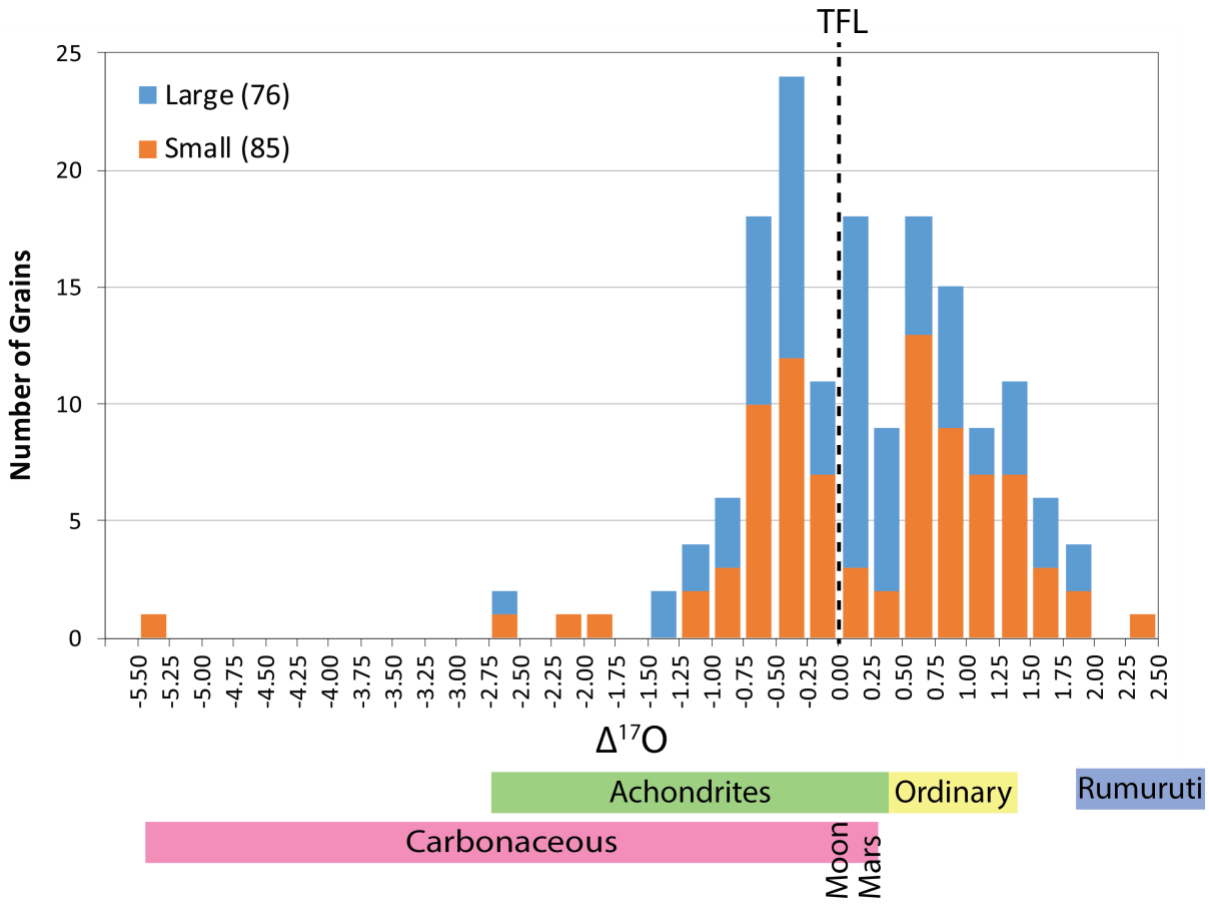

Figure 2.7. Distribution of $\Delta^{17}O$ for large and small fraction grains. The labeled bars below the histogram indicate approximate $\Delta^{17}O$ ranges of modern meteorite groups (Clayton and Mayeda, 1996, 1999). The vertical dashed line at $\Delta^{17}O = 0$ represents the Terrestrial Fractionation Line.

The combination of chemistry and oxygen isotopes can be used to define distinct groupings and uncover unique grains from the Jurassic time period (Fig. 2.8). Chrome-spinel grains in ordinary chondrites form well-defined groupings between H, L, and LL chondrites based on chemical compositions (previously discussed; e.g. Bunch et al., 1967; Wlotzka, 2005). Oxygen isotopes in type 4-6 ordinary chondrites also have distinctive compositions between H, L, and LL chondrites (Clayton et al., 1991). Jurassic chrome-spinel grains that likely come from ordinary chondrites appear in red in Figure 2.8. There is also a clustering of grains with high Al_2O_3, low TiO_2, and negative $\Delta^{17}O$ (lime green/yellow). These grains, referred to as High-Al below, also have high MgO and low V_2O_3. There is also an oxygen isotope trend in Figure 2.8 that has a connection with chemical compositions. The $\Delta^{17}O$ values tend to go from positive to negative $\Delta^{17}O$ values as TiO_2 and V_2O_3 decreases and as Al_2O_3 and MgO increases. This trend is supported by the tendency of chrome-spinels in ordinary chondrites to have lower Mg-Al contents (red), while spinels in carbonaceous chondrites and achondrites tend to have higher Mg-Al contents (Goodrich et al., 2014; Biebe, 2009).

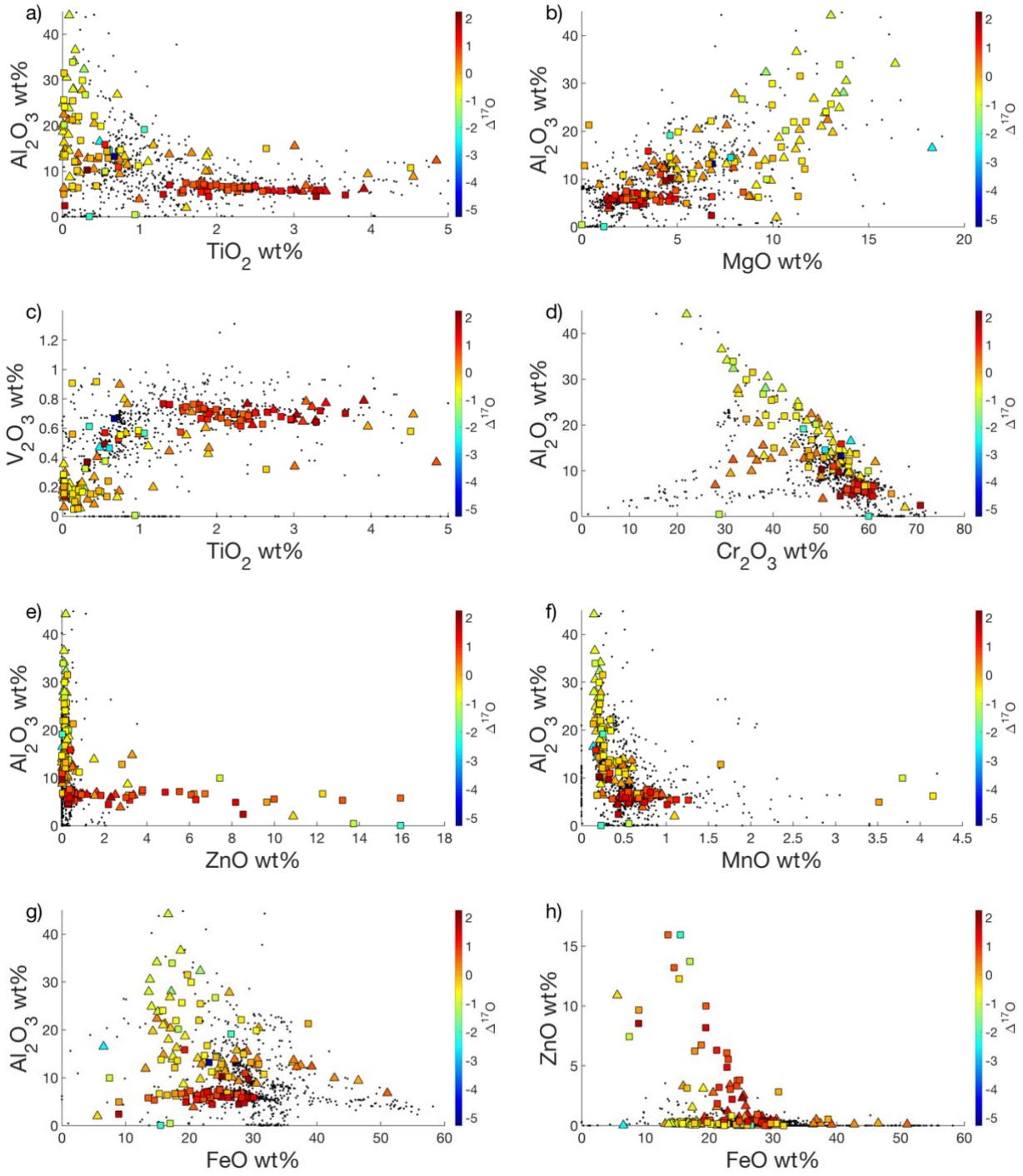

Figure 2.8. Chemistry and oxygen isotope plots of Jurassic grains (large fraction-triangles; small fraction-squares) and chrome-spinel compositions from modern meteorites (black dots) (same axes as Fig. 2.6). The color bar gives the of $\Delta^{17}O$ values for the Jurassic grains. Not all database entries have ZnO or V_2O_3 data. FeO represents all iron as FeO.

2.4.3 Classification

Hierarchical clustering was used to match the chemistry of each Jurassic grain with the chemistry of a known extraterrestrial chrome-spinel composition. The current database is a compilation of 700+ entries from literature and our new measurements of chrome-spinel grains from modern day meteorites (Chapter 4). After a chemical match was found, oxygen isotope compositions were considered in order to better finalize a classification. The Jurassic grains were classified as originating from a specific meteorite type, as part of a group not found in the database (e.g., the High-Al group), as Extraterrestrial, or Unclassified (Section 2.3.3).

The matches for the Jurassic and modern meteorite entries were determined using a visual output of the hierarchical clustering program, called a dendrogram. The dendrogram shows the distance linkages between chemical data entries and places the closest matches next to one another. The plot can show how Jurassic grains, modern meteorites, and the combination of the two clusters amongst the entire data entry. The calculations that are the basis of this diagram are discussed in Section 2.3.3.

Examples

The dendrogram is best illustrated with an example. The subsection of the entire dendrogram containing the High-Al grains (lime green/yellow in Fig. 2.8) and their database matches are shown in Figure 2.9 and Table 2.3. The numbers on the x-axis of Figure 2.9 are the identification labels for the data entries, which are based on the order of the data input. The entry numbers for the High-Al grains range from 95-109. (The clustering program analyzed the Jurassic grains before the database entries were added.) The red numbers and lines are the Jurassic grains and the black numbers and lines are database entries. The horizontal lines connect matches and the heights of the vertical lines give the degree to which the compositions match. Shorter vertical lines represent closer matches. Figure 2.9 and Table 2.3 show that closely plotted grains have very similar compositions (e.g., 96, 711, 97), and grains that plot on opposite ends of the figure are less similar (e.g., 95 and 109). There are also subgroups of grains, such as 99-109, that do not immediately match database entries, but these grains are eventually matched to a lesser degree with other subgroups containing database matches. Overall, this High-Al group still forms a defined cluster compared to the remaining Jurassic and database entries.

The database entries most similar to the High-Al grains are mostly from H, L, and LL chondrites of types 3 to 6, with one entry from an R chondrite and one entry from Österplana O65 (Ordovician fossil meteorite) (Fig. 2.9 and Table 2.3). The High-Al grains have $\Delta^{17}O$ values from -0.18 to -1.45, which fall below the terrestrial fractionation line (blue in Fig. 2.10), while H, L, and LL and R chondrites have positive $\Delta^{17}O$ values. The single database sample that has a negative $\Delta^{17}O$ is Österplana O65 (Schmitz et al., 2016), which is a unique sample that does not have an analogue among modern meteorite falls. Taken together, the chemical clustering from the hierarchical analysis and the oxygen isotopes indicate that the High-Al grains are a unique type of meteorite not found in our database of modern meteorites.

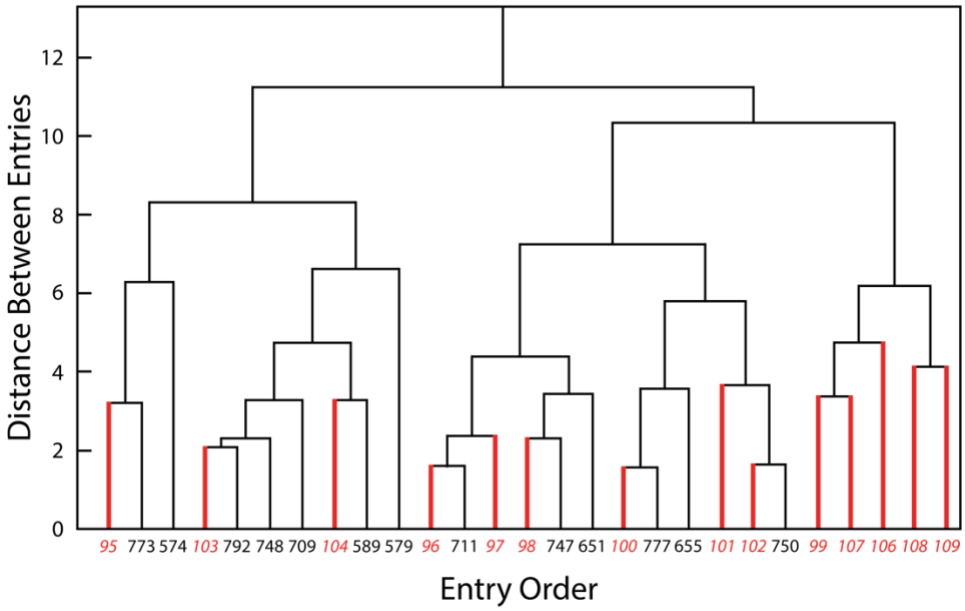

Figure 2.9. Dendrogram subsection consisting of High-Al Jurassic grains (red lines) and database entry (black lines) matches. The numbers on the horizontal axis are the entry identification numbers based on the order of the entries input into the Matlab program. The vertical axis shows the distance between the matched entries.

Table 2.3. Compositions of entries for the hierarchical clustering example of High-Al grains shown in Fig. 2.9.

Entry #	Reference	Name	MgO	Al_2O_3	TiO_2	V_2O_3	Cr_2O_3	FeO+ZnO+MnO	MnO	All FeO	ZnO	Total	$\Delta^{17}O$	2 SD	Class
95	measurement	m7_G11	8.39	29.04	0.27	0.24	34.12	27.95	0.24	27.47	0.23	100.00	-0.18	0.64	High-Al
773	Johnson and Prinz 1991	Sharps	10.39	29.11	0.35	0.25	34.43	25.47	0.23	25.14	0.09	100.00	0.73	0.18	H3.4
574	Bischoff et al 2011	PRE 95411	4.31	29.33	1.13	0.00	35.08	30.15	0.00	30.15	0.00	100.00	2.69	0.43	R chondrite
103	measurement	sm3_G28	10.22	26.11	0.14	0.16	40.77	22.61	0.22	22.28	0.11	100.00	-0.37	0.45	High-Al
792	Kimura et al 2006	Wells	9.07	25.19	0.61	0.41	42.14	22.58	0.25	22.17	0.16	100.00	1.26	0.24	LL3.3
748	Wlotzka et al. 2005	Richardton	8.64	25.99	0.56	0.25	40.49	24.07	0.59	23.00	0.48	100.00	0.73	0.18	H5
709	Kimura et al 2006	Krymka	10.58	27.40	0.50	0.52	39.86	21.15	0.31	20.84	0.00	100.00	1.26	0.24	LL3.2
104	measurement	sm1_G10	8.53	27.25	0.30	0.33	38.68	24.88	0.23	24.51	0.14	100.00	-0.99	0.66	High-Al
589	Kimura et al 2006	ALHA77260	8.61	29.88	0.36	0.31	37.08	23.77	0.26	22.84	0.67	100.00	1.26	0.24	LL3.5
579	Schmitz et al. 2014	Al-rich chrome	4.76	26.01	0.61	0.52	40.94	27.16	0.49	25.98	0.69	100.00	-1.08	0.21	Ost 065
96	measurement	sm4_G34	11.52	31.80	0.02	0.16	36.08	20.42	0.25	19.90	0.26	100.00	-0.25	0.91	High-Al
711	Kimura et al 2006	Krymka	12.26	31.91	0.55	0.50	35.42	19.36	0.27	19.09	0.00	100.00	1.26	0.24	LL3.2
97	measurement	sm4_G17	10.45	31.37	0.27	0.17	36.09	21.62	0.22	21.26	0.14	100.00	-0.68	0.62	High-Al
98	measurement	m7_G04	10.01	33.55	0.29	0.20	32.94	23.00	0.22	22.57	0.21	100.00	-1.30	1.04	High-Al
747	Wlotzka et al. 2005	Richardton	10.76	32.88	0.47	0.21	34.27	21.42	0.49	20.42	0.51	100.00	0.73	0.18	H5
651	Wlotzka et al. 2005	Dar al Gani 925	9.39	31.87	0.95	0.12	32.77	24.89	0.26	24.35	0.28	100.00	1.07	0.18	L6
100	measurement	m8_G04	11.64	37.97	0.17	0.15	30.37	19.60	0.16	19.34	0.10	100.00	-0.70	0.55	High-Al
777	Wlotzka et al. 2005	Simmern	11.70	36.69	0.27	0.29	30.59	20.46	0.84	19.29	0.33	100.00	0.73	0.18	H5
655	Wlotzka et al. 2005	Daraj 020	12.39	34.34	0.34	0.32	30.82	21.79	0.54	20.75	0.50	100.00	0.73	0.18	H5
101	measurement	m7_G12	16.98	35.36	0.16	0.14	31.47	15.78	0.23	15.44	0.11	100.00	-0.84	0.51	High-Al
102	measurement	sm1_G18	13.90	34.99	0.14	0.12	32.69	18.06	0.17	17.83	0.07	100.00	-0.98	0.75	High-Al
750	Kimura et al 2006	Semarkona	14.18	35.27	0.66	0.40	32.88	16.61	0.36	16.25	0.00	100.00	1.26	0.24	LL3.00
99	measurement	m7_G08	13.49	29.80	0.79	0.15	36.52	19.11	0.22	18.82	0.07	100.00	-0.48	0.50	High-Al
107	measurement	m4_G03	13.97	28.63	0.15	0.17	39.25	17.76	0.17	17.52	0.07	100.00	-1.45	0.58	High-Al
106	measurement	sm1_G20	13.22	26.05	0.02	0.24	40.95	19.52	0.21	19.09	0.22	100.00	-0.64	1.15	High-Al
108	measurement	m7_G09	14.17	31.29	0.06	0.15	39.85	14.50	0.17	14.18	0.15	100.00	-0.88	0.54	High-Al
109	measurement	m8_G10	13.67	28.71	0.14	0.14	43.03	14.30	0.15	14.02	0.14	100.00	-0.90	0.51	High-Al

The data input for the clustering program included the normalized values of MgO, Al_2O_3, TiO_2, V_2O_3, Cr_2O_3, FeO+MnO+ZnO for each entry. The remaining normalized elements were manually compared.
The Jurassic grains have measured $\Delta^{17}O$ values and the database entries show $\Delta^{17}O$ values based on bulk measurements (H, L and LL (finds) - Clayton et al., 1991; R chondrite - Schulze et al., 1994; Ost 065 - Schmitz et al., 2016).
All FeO: all Fe assigned as FeO.

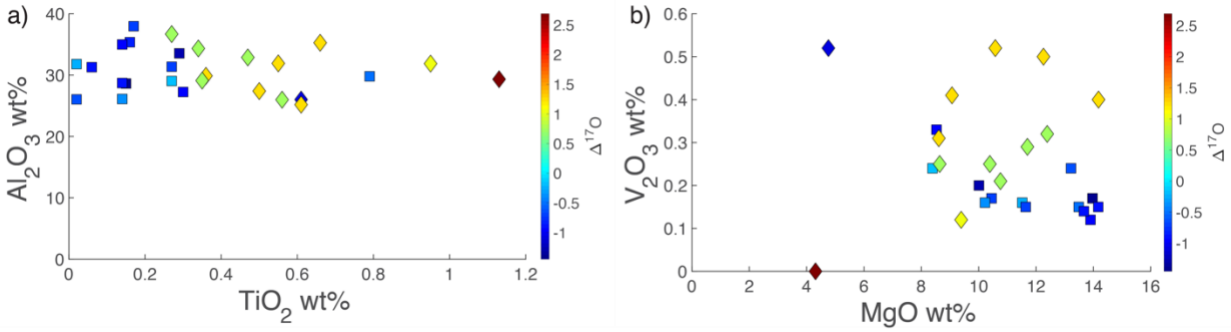

Figure 2.10. Chemistry and oxygen isotope (color bar) contents of entries from Figure 2.9 and Table 2.3. The diamonds are the database entries and the squares are the High-Al Jurassic grains. The red diamond is the R chondrite entry, the blue diamond is Ost 065, and the other diamonds are ordinary chondrites. The figures show that the High-Al Jurassic grains match the chemistry but not the $\Delta^{18}O$ values of the database entries.

Another subsection of the dendrogram shows matches to Ureilite database entries (Figure 2.11 and Table 2.4). Most of the Jurassic grains (red lines) have immediate matches to other Jurassic grains or to a database entry (black). The database matches include three Ureilite entries

and one LL chondrite entry. Five of these Jurassic grains were classified as originating from Ureilites because the unknown grains fall within the bulk oxygen isotope range of ureilites, $\Delta^{17}O$ = -0.23 to -2.45‰ (Clayton and Mayeda, 1996). The sixth Jurassic grain in this clustering (entry 85) has the largest distance for a match. This grain has a similar composition to the other entries, but contains slightly higher Al_2O_3 and lower MgO contents. The oxygen isotope value for this grain is just within 2 standard deviations of the ureilite range. The chemical match for the grain suggests a ureilite origin, but the oxygen isotope value does not definitively classify the grain as originating from a ureilite. In this case, the entry 85 grain is classified as having an Extraterrestrial origin with the possibility of a ureilite origin.

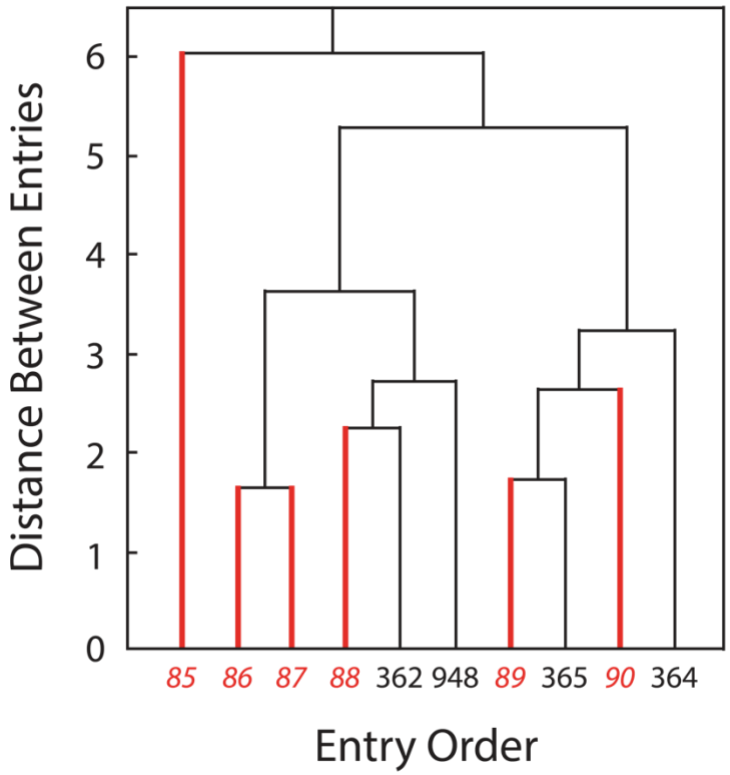

Figure 2.11. Dendrogram subsection consisting of Ureilite-like Jurassic grains (red lines) and database entry (black lines) matches. The numbers on the horizontal axis are the entry identification numbers based on the order of the entries input into the Matlab program. The vertical axis shows the distance between the matched entries.

Table 2.4. Compositions of entries for the hierarchical clustering example of Ureilite-like grains shown in Fig. 2.11.

Entry #	Reference	Name	MgO	Al_2O_3	TiO_2	V_2O_3	Cr_2O_3	FeO+ZnO+MnO	MnO	All FeO	ZnO	Total	$\Delta^{17}O$	2 SD	Class
85	measurement	m3_G15	7.99	22.36	0.08	0.19	52.01	17.37	0.17	17.03	0.18	100.00	0.28	0.56	Ext-Ur
86	measurement	m5_G06	11.51	20.54	0.01	0.19	50.08	17.66	0.24	17.22	0.20	100.00	-0.10	0.50	Ureilite
87	measurement	sm1_G05	10.79	20.40	0.02	0.24	49.53	19.01	0.24	18.47	0.31	100.00	-1.07	0.67	Ureilite
88	measurement	m4_G04	10.47	18.96	0.01	0.27	50.13	20.18	0.25	19.60	0.32	100.00	-0.66	0.53	Ureilite
362	Goodrich et al. 2014	NWA 766	9.47	17.83	0.70	0.41	49.91	21.68	0.39	20.88	0.41	100.00	-1.20	1.14	Ureilite
948	Kimura et al 2006	Y-790448	9.76	19.98	0.46	0.39	48.18	21.24	0.24	21.00	0.00	100.00	1.26	0.24	LL3.2
89	measurement	m4_G05	11.32	16.43	0.02	0.25	53.12	18.85	0.26	18.21	0.39	100.00	-0.44	0.50	Ureilite
365	Goodrich et al. 2014	HaH 064	10.82	16.75	0.61	0.43	51.81	19.57	0.50	18.71	0.36	100.00	-1.20	1.14	Ureilite
90	measurement	m6_G01	11.57	18.24	0.08	0.21	52.48	17.40	0.22	16.94	0.24	100.00	-0.49	0.59	Ureilite
364	Goodrich et al. 2014	EET 96328	11.96	16.28	0.40	0.52	54.28	16.55	0.49	15.78	0.27	100.00	-1.20	1.14	Ureilite

The data input for the clustering program included the normalized values of MgO, Al_2O_3, TiO_2, V_2O_3, Cr_2O_3, FeO+MnO+ZnO for each entry. The remaining normalized elements were manually compared.
The Jurassic grains have measured $\Delta^{17}O$ values and the database entries show $\Delta^{17}O$ values based on bulk measurements (LL (finds) - Clayton et al., 1991; Ureilite – Clayton & Mayeda, 1996).
Ext-Ur: classified as an extraterrestrial grain with the possibility of a ureilite origin.
All FeO: all Fe assigned as FeO.

Subsections of the dendrogram can also show how similar some meteorite type chemistries are to one another. Figure 2.12 shows two mini clusters that match at a higher level. The left cluster contains Acapulcoites and the right cluster contains Lodranites. The chemical compositions in Table 2.5 show how close the matches are for the Jurassic grains and their respective database entry. The dendrogram also shows the similarity between the Acapulcoite and Lodranite database compositions, which is consistent with their clan relationship (Clayton and Mayeda, 1996; Weisberg et al., 2006; Keil and McCoy, 2018). These Jurassic grains are classified as "Extraterrestrial" with the likelihood of an Acapulcoite or Lodranite classification because the oxygen isotope abundances for the Jurassic grains do not match the bulk oxygen close enough for a definitive match (Table 2.5).

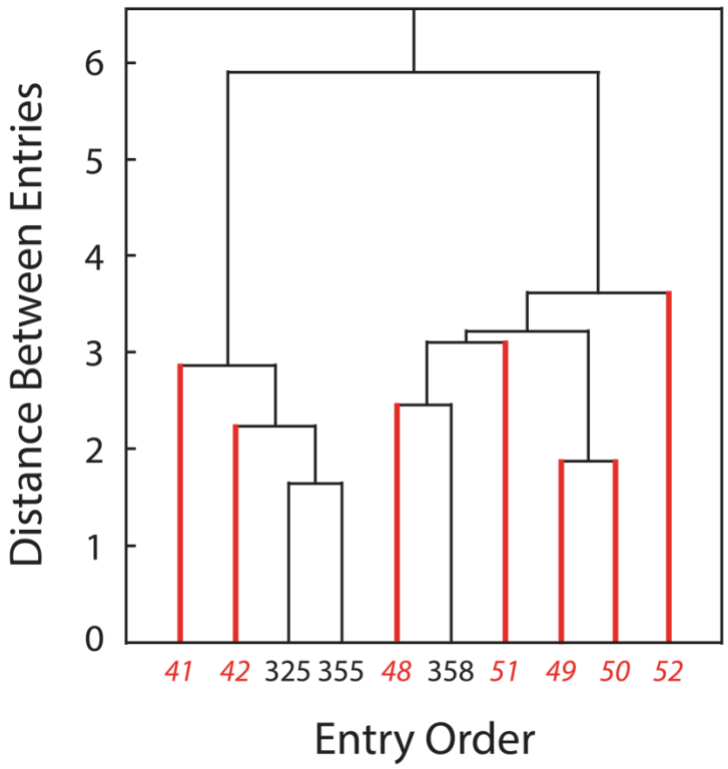

Figure 2.12. Dendrogram subsection consisting of Acapulcoite- and Lodranite-like Jurassic grains (red lines) and database entry (black lines) matches. The numbers on the horizontal axis are the entry identification numbers based on the order of the entries input into the Matlab program. The vertical axis shows the distance between the matched entries.

Table 2.5. Compositions of entries for the hierarchical clustering example of Acapulcoite- and Lodranite-like grains shown in Fig. 2.12.

Entry #	Reference	Name	MgO	Al_2O_3	TiO_2	V_2O_3	Cr_2O_3	FeO+ZnO+MnO	MnO	All FeO	ZnO	Total	$\Delta^{17}O$	2 SD	Class
41	measurement	m5_G14	10.10	9.89	0.24	0.06	57.01	22.62	0.29	22.16	0.16	100.00	-0.37	0.44	Ext-Ac
42	measurement	m6_G05	9.24	8.78	0.09	0.23	58.95	22.68	0.23	19.32	3.13	100.00	-0.60	0.54	Ext-Ac
325	Keil and McCoy 2018	FRO 95029 6	8.22	9.41	1.28	0.00	59.63	21.46	1.86	19.60	0.00	100.00	-1.04	0.24	Acapulcoite
355	measurement	NWA 8287	8.12	9.68	1.40	0.64	58.23	21.93	1.22	19.81	0.90	100.00	-1.18	0.47	Acapulcoite
48	measurement	sm4_G13	11.90	12.35	0.16	0.10	57.01	18.48	0.25	18.05	0.17	100.00	-0.26	0.60	Ext-Lo
358	measurement	NWA 10265	10.01	12.05	0.14	0.81	58.35	18.64	0.50	18.08	0.07	100.00	-1.68	0.49	Lodranite
51	measurement	sm3_G06	11.61	13.87	0.01	0.29	57.85	16.37	0.34	15.72	0.31	100.00	-0.47	0.68	Ext-Lo
49	measurement	m6_G04	9.69	14.04	0.01	0.21	56.72	19.33	0.24	17.56	1.53	100.00	-0.48	0.50	Ext-Lo
50	measurement	m7_G07	10.79	14.74	0.09	0.20	55.94	18.23	0.22	17.78	0.23	100.00	-0.72	0.48	Ext-Lo
52	measurement	sm3_G23	8.15	13.87	0.03	0.21	58.62	19.11	0.45	18.49	0.17	100.00	-0.33	0.73	Ext-Lo

The data input for the clustering program included the normalized values of MgO, Al_2O_3, TiO_2, V_2O_3, Cr_2O_3, FeO+MnO+ZnO for each entry. The remaining normalized elements were manually compared.
The Jurassic grains have measured $\Delta^{17}O$ values and the database entries show $\Delta^{17}O$ values based on bulk measurements or our own measurements (Acapulcoite and Lodranite measurement – Chapter 4; Acapulcoite - Clayton and Mayeda, 1996).
Ext-Ac or Ext-Lo: classified as an extraterrestrial grain with the possibility of an acapulcoite or lodranite origin.
All FeO: all Fe assigned as FeO.

All of the Jurassic chrome-spinels were assigned to parent meteorite types utilizing hierarchical clustering of compositional data supplemented by oxygen isotope data. Most of the grains were classified as having an extraterrestrial origin, including ordinary chondrite, High-Al, carbonaceous, diogenite, and ureilite (Table 2.6 and Appendix A). Almost half of the extraterrestrial grains have an ordinary-chondrite origin, with ~43% of them subtyped into H-chondrite. The remaining ordinary-chondrite-like grains could not be subtyped because their chemistry and oxygen isotopes did not align with a single subtype, but their oxygen isotopes confirmed an ordinary-chondrite origin. The grains classified as "Extraterrestrial" include possible matches to pallasites, acapulcoites, lodranites, brachinites, howardites, chassignites, ureilites, eucrites, diogenites, and irons.

Table 2.6. Classifications of extraterrestrial Jurassic chrome-spinel grains.

	Number of Grains with Matching Compositions	Fraction of Total Grains (%)
H-chondrite	29	18
L-chondrite	18	11
LL-chondrite	6	4
Ordinary - Not Subtyped	14	9
Ordinary	**67**	**42**
CM2	2	1
CR2	6	4
Diogenite	2	1
Ureilite	6	4
High-Al	15	9
Extraterrestrial*	60	38
Others	**91**	**58**
Total**	**158**	**100**

*Possible classifications are given in Appendix.
**Total does not include Unclassified grains (n=21).

2.5 Discussion

2.5.1 Classification Limitations

Compositions and Clustering

Identification of the parent meteorite type of remnant chrome-spinels relies on knowledge of chrome-spinel compositions from modern day meteorites. Well-characterized chemical and oxygen isotope compositions make it possible to reliably classify the parent meteorites of chrome-spinels from the past. A database of chrome-spinel compositions from modern meteorites was created for this project from published data and from new measurements. While the compiled database contains grain compositions from many types of meteorites, it is not yet comprehensive. Chrome-spinel is rare and small in some meteorites, particularly carbonaceous chondrites (Heck et al., 2017). Chrome-spinel is also unlikely to be found in highly reduced meteorites such as enstatite chondrites and aubrites (Rubin, 1997). For example, enstatite chondrites have chromium sulfide instead of chrome-spinel (Chapter 4). The current database does not have enough samples from aubrites, angrites, and CH and CK chondrites. Meteorite types that do not contain chrome-spinels are not viable classification options. This must be taken into account when comparing abundances to the present day.

The database includes bulk oxygen-isotope compositions for meteorite types, but contains few oxygen isotope measurements for chrome-spinels. Oxygen-isotope measurements of chrome-spinels would provide more reliable classification matches because bulk oxygen-isotope measurements do not consistently represent less abundant chrome-spinels. A difference in isotopic compositions among minerals can be due to the partitioning of isotopes among co-existing phases at equilibrium. For example, different degrees of mass-dependent fractionation have been observed between chrome-spinels and silicates of the same meteorite (e.g., McCoy et al., 2019). Small degrees of mass-dependent fractionation are expected from equilibrium fractionation between forsterite and chromite (end member); they are in the range of ~ 2.97-0.41‰ in $\delta^{18}O$ at 600-1200 °C (Chiba et al., 1989; Zheng, 1991). However, the fractionation differences observed in ion probe measurements for these minerals are significantly larger. These shifts are not fully understood, but are likely due, in part, to matrix-effects in the ion probe. A mineral must be standardized with a similar composition for the best results; therefore, a chrome-spinel cannot be successfully standardized with a silicate mineral or with chrome-spinels of different compositions. Stillwater chromite is the chrome-spinel standard for our Jurassic

measurements, but this composition does not closely match the various chemical compositions of extraterrestrial chrome-spinels. Our own measurements of the Hessle H5 meteorite show a mass-dependent shift between chrome-spinel and silicates with a difference of ~7.7‰ in $\delta^{18}O$. A similar shift is also observed between chrome-spinels and silicates of the Milton pallasite as ~3.8‰ in $\delta^{18}O$ (McCoy et al., 2019). Ion probe measurements of Ordovician chrome-spinels from the breakup of the L-chondrite parent body give a shift in $\delta^{18}O$ of ~6.8‰ compared to the bulk $\delta^{18}O$ of L-chondrites (Heck et al., 2016; Clayton et al., 1991). These effects mean that bulk-meteorite $\delta^{18}O$ values do not reliably represent the chrome-spinels. Fortunately, $\Delta^{17}O$ can be used for the classification of remnant chrome-spinels because it does not depend on shifts in mass fractionation. It would be beneficial to obtain accurate oxygen isotope values for chrome-spinels from modern day meteorites so that the combination of $\delta^{18}O$ and $\Delta^{17}O$ can be used to identify parent meteorites of chrome-spinel grains.

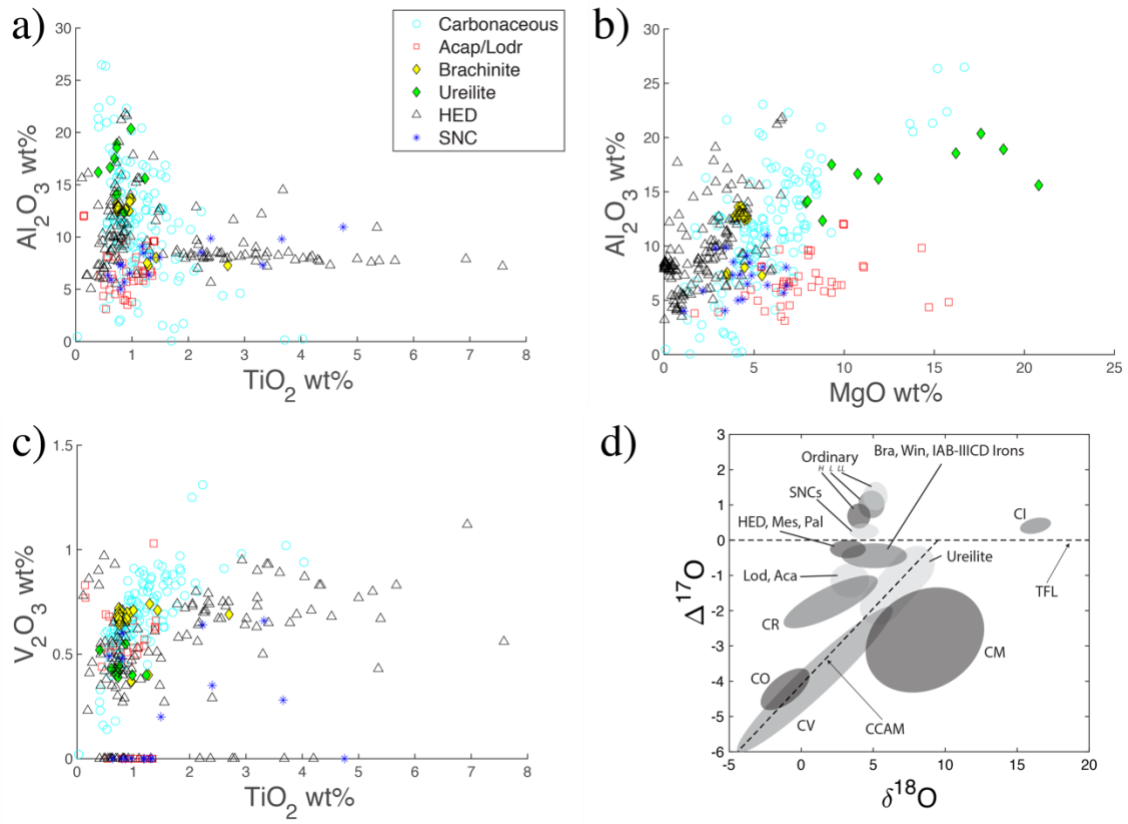

Figure 2.13. a-c) Overlapping compositions for different meteorite types (carbonaceous, acapulcoite/lodranite, brachinite, ureilite, HED, SNC; Appendix C). d) Oxygen isotope plot of meteorite types shows partial overlaps of oxygen-isotope fields (data from Clayton et al., 1991, Clayton and Mayeda, 1996, 1999).

Chemical compositions and oxygen isotopes are necessary for reliable classifications of chrome-spinels grains, but there are still limitations to the process. Each meteorite type occupies a region in composition space. Some meteorite types are unique and have well-defined compositions (e.g. equilibrated ordinary chondrites), whereas some types overlap in chemistry and oxygen isotopes (Fig. 2.13). Fortunately, there are eight elements in chrome-spinel that are sufficiently abundant to help resolve some compositional overlaps (e.g., Figs. 2.13a-c). There is also the issue of outlier compositions. Outlier compositions must be included in the database and clustering process in case a remnant chrome-spinel has an outlier composition, as they may not be classified correctly if a generalized or averaged composition is used. For example, equilibrated ordinary chondrites (types 4-6) tend to have well defined chemistry clusters with consistent Al_2O_3 and V_2O_3 abundances (grey toned markers), whereas unequilibrated ordinary chondrites (type 3) have larger ranges of the same elements (white markers) (Fig. 2.14). These different petrologic types generally have different ranges in compositions, but they still contain outlier compositions that fall within the ranges of other petrologic types. Such outliers include the types 3-6 ordinary-chondrite compositions that matched with the Jurassic High-Al grains (red circles; Fig. 2.14) (also see Fig. 2.9 and Table 2.3). In the event oxygen isotopes are not measured to confirm a chemical match, a remnant chrome-spinel with an outlier ordinary chondrite composition may not be classified as originating from a generalized ordinary-chondrite composition. We attempt to circumvent the outlier issue by including all compositions and measurements, which has produced a database with 700+ entries. The combination of chemistry and oxygen isotope compositions can help discern between possible matches, but large ranges and uncertainties of compositions can make it difficult to identify a unique parent meteorite type for each Jurassic grain. This is the case for some of the Jurassic grains that are classified as Extraterrestrial, which can have multiple possible classifications (Appendix A). It can also be difficult to differentiate between terrestrial and extraterrestrial grains because our oxygen isotope measurements cannot resolve some achondrites from the TFL ($\Delta^{17}O = 0$ ‰). Terrestrial grains also span the entire spectrum of extraterrestrial compositions (Barnes and Roeder, 2001); therefore the use of chemistry alone is not necessarily reliable for the classification of terrestrial versus extraterrestrial. Collecting highly condensed limestone sediments that were deposited far from shore help minimize the number of terrestrial spinel grains, such as the case for the Jurassic sediments. However, known compositions of terrestrial chrome-spinels in the region where the

limestone was collected could be compared to the remnant grains to see if there is a terrestrial source in the sample collection.

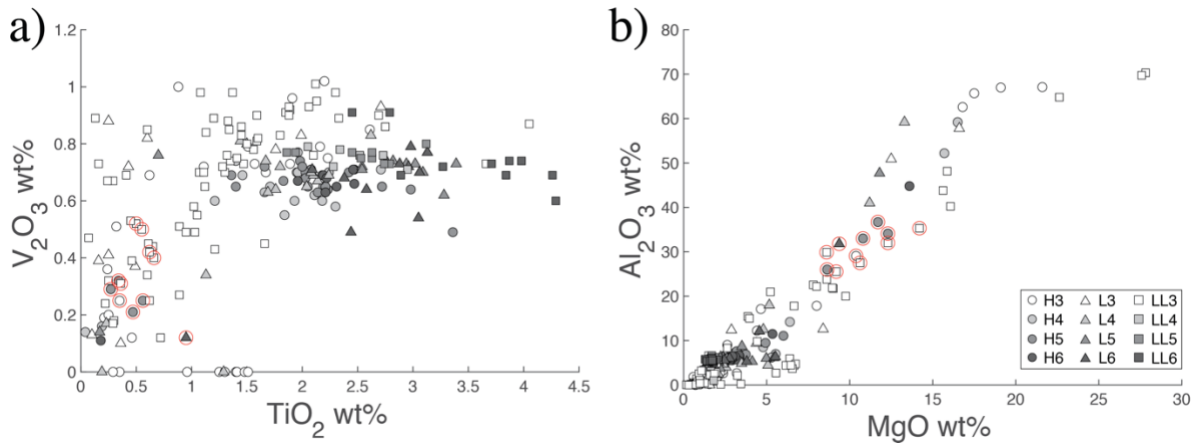

Figure 2.14. Compositions for types 3-6 of H, L, and LL ordinary chondrites (Bunch, 1967; Johnson and Prinz, 1991; Kimura et al., 2006; Snetsinger, 1967; Wlotzka et al., 2005; Chapter 4). The red circles show the entries that matched with the Jurassic High-Al grains with negative $\Delta^{17}O$ values in Fig. 2.9 and Table 2.3.

Hierarchical clustering was successfully implemented to help with the classification of Jurassic chrome-spinels, but possible improvements may provide more robust classifications. This technique provided comparisons of the Jurassic grains to a massive modern-meteorite database in a multi-dimensional space. Hierarchical clustering also lowered the number of manual chemical comparisons by ignoring compositions in the database that did not match a Jurassic chrome-spinel grain. The oxygen isotope values were compared to the matches separately in order to give a greater weight to the oxygen data. While the amount of manual comparisons was manageable for the Jurassic dataset, an increase in remnant grains and additions to the modern meteorite database may make the manual aspect of hierarchical clustering obsolete. The addition of oxygen isotopes into the clustering program would remove an additional manual step, however these values need to be weighted differently than the individual chemical compositions because isotopes are a distinct classification step. The reliability of classifications could be improved with a few additions. The inclusion of uncertainties in the grain compositions would provide more robust matches for the clustering output (Kumar and Patel, 2007). Posterior probability could provide the probability of a match if there are multiple matches. Principle component analysis could be used to determine the

diagnostic elements for classifications. These possible improvements were not made for the Jurassic clustering because they were not necessary for this number of unknowns, but more advanced techniques, such as those mentioned, would be needed for a larger dataset.

Mass Distribution

Enough chrome-spinel samples deposited on the Earth's surface in the past can be collected from small areas because the samples integrate large intervals of time. The area of collection and time accumulated must be understood to determine how many meteorites of a given size are likely to have accumulated in any given sediment sample (Fig. 2.15). Collecting over ten times more area would give ten times more meteorites of a given size. Ten times more meteorites would also be collected from a ten times longer time period. Similarly, a tenth the number of meteorites would be collected from a tenth of the area or a tenth of the time period. Time and area are interchangeable. In this case, we assume that meteorites fall uniformly over the Earth and that the flux over the time interval is approximately constant.

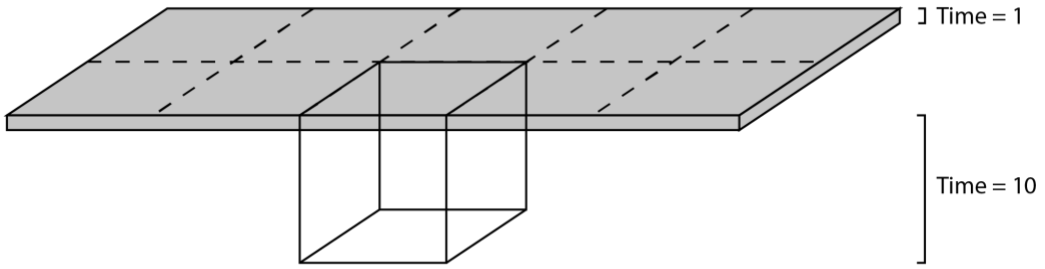

Figure 2.15. Comparison between a large surface area with a time interval of 1 (grey surface) and a smaller surface area with a time interval of 10 (white box). The grey region contains 10 times more surface area as the white box, but the white box contains 10 times more time. The grey region and the white box contain the same amount of material because time and surface area are interchangeable in this case, as long as the meteorite flux over that period is constant.

Meteorites and micrometeorites falling on Earth have a power-law mass distribution, with many more micrometeorites (red oval) falling than typical sized meteorites (blue oval) (Fig. 2.16). Figure 2.16 shows the relationship between the frequency and size of a meteorite falling to Earth's surface in one year. For example, the light grey dashed arrows show that approximately one 10^7 kg meteorite falls on Earth's surface in a year. If the area or time interval changes for Figure 2.16 then the likelihood of one meteorite falling (light grey horizontal dashed line) in a

specific size range changes. If samples are collected from a smaller region or over a shorted amount of time then the light grey horizontal dashed line will shift upwards, changing the likelihood of one meteorite falling from the 10^7 kg size to a smaller sized meteorite. For the Jurassic, the sample collection area was ~5 m^2. The surface area of the Earth is ~5.1 x 10^{14} m^2, so the collection area was ~10^{14} times smaller than the surface of the Earth. However, the collected limestone accumulated over about a million years (10^6 yr). The effective collection area of ~5 m^2 and ~10^6 yr translates to about 10^8 times smaller collection area than the Earth's surface over one year. The overall smaller area of the Jurassic sample causes the light grey horizontal dashed line to shift upward by eight orders of magnitude (dark grey dashed lines; Fig. 2.16). The time/area shift for this study changes the likelihood of one meteorite to fall from 10^7 kg to ~10^{-4} kg (~0.1 grams) (light grey and dark grey dashed lines, respectively), assuming the same infall rate as today. This shift moves the mass distribution of our sample collection into the region of micrometeorites.

It is possible, but unlikely, that a much larger meteorite could contribute chrome-spinels to the limestone collection. A large meteorite would likely contribute many chrome-spinels and skew the observed background flux of the limestone sample. Over a large enough time interval the chrome-spinel contribution of the large meteorite would dissipate and convolve into the background flux. We can identify large meteorite contributions by comparing different collection sites that sample the same time period but are outside the range of an average strewn field. A large object would dominate the chrome-spinels in one site, but not both. If we find a high abundance of one type of meteorite in multiple areas from the same time period then there was likely a global increase in the flux of that type, much like the break-up of the L-chondrite parent body observed in the Ordovician.

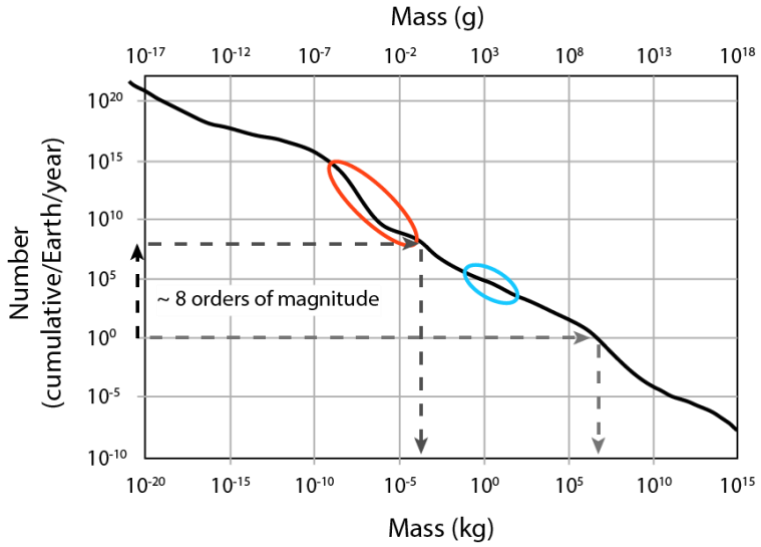

Figure 2.16. Mass distribution of interplanetary bodies falling to Earth's surface per year (solid black line; after Ceplecha et al., 1998). Blue oval represents typical recovered meteorites and the red oval shows the range for micrometeorites (10^{-9} to 10^{-4} kg; 10^{-6} to 0.1 g). Light grey dashed arrows show likelihood of 1 meteorite falling in a year for a 10^{7} kg body. Black dashed arrow shows the ~8 orders of magnitude shift needed for the time/area interval of the Jurassic samples. The dark grey dashed arrows show the Jurassic sample shift, where the likelihood of 1 meteorite falling is changed to a 10^{-4} kg body. The time interval for the Jurassic limestone collection limits the likely size distribution of meteorite collection to the mass of micrometeorites.

Grains to Meteorites

Populations of infalling meteorites derived for different time periods in the past can be directly compared because the chrome-spinels from each time period come from the same part of the mass distribution, the micrometeorites. It is not so straightforward to compare meteorite population from the past with modern meteorites, because modern abundances are not based on micrometeorites. In the case of modern meteorites, one chrome-spinel does not equate to one meteorite. Some meteorite types contain many chrome-spinels whereas other types contain a few chrome-spinels per volume of host material. Also, the grain sizes of chrome-spinels are not the same for all meteorite types. Additionally, some meteorite types contain grains that are smaller than what is sampled by our studies (smaller than 32 μm). In these cases, the meteorite type is under counted. The differences in grain sizes and abundances means that not all samples and meteorites can be treated the same way when converting from single chrome-spinels to relative meteorite abundances.

Initial steps have been taken to understand the issue of grain size and abundance. Heck et al. (2017) dissolved samples of various meteorites to determine the number of grains per gram of material (Table 2.7). Dissolving different meteorite types showed that some types contain many more chrome-spinel grains compared to others. For example, ordinary chondrites have among the highest abundances and carbonaceous chondrites have relatively low abundances. At this time, the grain abundances are only determined for the large size fraction (> 63 μm). It is unknown if the smaller size fraction of grains will show the same abundances, so we cannot yet make reliable assumptions for small size fraction grains. An issue with dissolved meteorites is sampling because meteorite types are heterogeneous to different degrees. For example, four different winonaite meteorite samples were dissolved, and they have 216, 880, 80, and 0 grains per gram (Heck et al., 2017). This variability is most likely due to the heterogeneous textures of winonaite samples (Benedix et al., 1998). Ordinary chondrite samples also showed ranges amongst petrologic type, where types 5 or 6 can contain ~1000-1500 chrome-spinel grains per gram and type 4 can contain 50-150 grains per gram (Heck et al., 2017). These disparities can make it difficult to determine the best representation for a specific meteorite type. However, the grains per gram of these dissolved samples can help with first order assumptions of meteorite abundances. The high abundance of chrome-spinels in ordinary chondrites suggests that a high abundance of grains does not necessary translate to a high influx of falling host material compared to other meteorite types. Also, the very low abundance of large-size-fraction grains in carbonaceous chondrites suggests that they will be a rare find unless they are from a large or abundant source. The analysis of more dissolved samples in the future will provide more reliable conversions to understand meteorite abundances.

Table 2.7. Number of chrome-spinels (Cr-sp) per gram of dissolved meteorite types.

Type	Cr-sp/g	1 SD
Carbonaceous (5)	0.2	0.3
CR6	718.0	-
Eucrite	59.0	-
Diogenite	896.0	-
Ureilite	371.0	-
Winonaite (4)	294.0	400.7
Lodranite	788.0	-
Acapulcoite	314.0	-
Brachinite	1258.0	-
H4	120	-
L4	73	-
H5	61	-
L5	79	-
L5	1231	-
H6	1236	-
L6	1104	-
L6	1628	-

All values are from Heck et al. (2017).
1 SD: 1 standard deviation.
Grain abundances are from the > 63 μm size fraction.
Parentheses show the number of samples in the average Cr-sp/g.
Carbonaceous contains dissolved samples of CV3, CM2, CO3.4, CR2, and CK4 types.

Many of these issues can be overcome by comparing the distributions of dispersed chrome-spinels of the past with those of modern day micrometeorites. Micrometeorites are dominated by material from carbonaceous chondrites (>70–90%; Love and Brownlee 1993; Beckerling and Bischoff 1995; Brownlee et al. 1997; Yada et al. 2005; Rudraswami et al. 2015). However, this high abundance of carbonaceous chondrite micrometeorites cannot be directly compared to abundances of the past because chrome-spinels are relatively rare in carbonaceous chondrites (Table 2.7). Rudraswami et al. (2019) analyzed chrome-spinels in micrometeorites from Indian Ocean deep-sea sediments (0-50,000 years old) and the South Pole water well (~1000 years old). Based on chemistry and oxygen isotope abundances, most of the chrome-spinel-bearing micrometeorites appear to originate from ordinary chondrites (~70%) with some from carbonaceous chondrites (~30%). Some of these chrome-spinel-bearing micrometeorites contain more than one chrome-spinel or some chrome-spinels are too small for oxygen isotope measurements and silicate proxies were measured. Most of the chrome-spinel grains studied in

Rudraswami et al. (2019) are from a smaller size fraction (< 32 μm) than the other time periods studied, which may represent a different distribution of meteorite types. Rudraswami et al. (2019) defined chrome-spinel grains with $\Delta^{17}O < 0$ ‰ to likely originate from carbonaceous chondrites, but they did not discuss the possibility of the grains originating from achondrites. The classification of these chrome-spinel-bearing micrometeorites into achondrite types would change the relative meteorite abundances.

A more direct comparison between the chrome-spinel abundances of the past and today is needed to move beyond first order assumptions of meteorite abundances. This may be overcome by using a similar method of chrome-spinel grain collection for today. The collection of material from the sea floor would provide an equivalent measure of modern abundances because similar methods of grain collection and measurements would be used. This method of collection would be similar to that of Rudraswami et al. (2019), but chrome-spinels that are not solely within micrometeorites would also be considered. While the work of Rudraswami et al. (2019) provides initial modern day abundances, more deep-sea sediment collections are needed from multiple regions to obtain a representative abundance of modern meteorite chrome-spinels that include grains from larger size fractions.

2.5.2 Jurassic Grains

Classifications

The Hierarchical clustering method helped to classify 88% of the Jurassic grains as originating from a specific meteorite type or as generally extraterrestrial, with the remaining grains unclassifiable at this time (Table 2.6). Grains classified as "Extraterrestrial" have $\Delta^{17}O$ values that are distinct from terrestrial ($\Delta^{17}O \cong 0$‰). Some of these grains matched too many types of meteorites in the database and oxygen isotopes were not able to determine the best match. There is also the case where the oxygen isotope values did not support a chemical match (e.g., High-Al grains). The inability to classify the extraterrestrial grains into a specific parent meteorite type may reflect gaps in the database or suggest new types of meteorites (e.g., High-Al group).

Ordinary-chondrite-like grains constituted 42% of the classified Jurassic grains (Table 2.6). Most of the grains that were classified as Ordinary were subtyped as H, L, or LL. The remaining grains could not be subtyped for various reasons. First, some grains matched database entries from multiple Ordinary subtypes or the grains did not reliably match an Ordinary entry. Oxygen

isotopes could not help distinguish between subtype matches, but isotope values did support an Ordinary chondrite origin. Second, the oxygen isotopes did not support the chemistry match. For example, a grain had H-chondrite-like chemistry but the oxygen isotopes were not within error of H chondrites.

The grains classified as carbonaceous-chondrite-like make up 5% of the Jurassic grains. This includes CR2-like and CM2-like grains. Other carbonaceous chondrites matched the unknown Jurassic grains based on chemistry but the $\Delta^{17}O$ values were not in the prescribed $\Delta^{17}O$ range for most carbonaceous chondrites (Appendix A). Chrome-spinels from carbonaceous chondrites tend to be small and rare (Johnson and Prinz, 2001; Bjarnborg and Schmitz, 2013). They are predominantly found in type II chondrules, and most type II chondrules have $\Delta^{17}O$ values of approximately -2 ‰ (based on olivine and pyroxene; Tenner et al., 2018). However, CR2 meteorites have a larger range of $\Delta^{17}O$ values from approximately -2.0 to 1.4 ‰ (based on olivine and pyroxene; Connolly and Huss, 2010; Schrader et al., 2013, 2014; Tenner et al., 2015).

2.5.3 Time period comparisons

Chrome-spinel abundances of the past

We can begin to understand how meteorite abundances have changed throughout time by comparing chrome-spinel abundances of different time periods. Time periods that have been studied thus far include: Ordovician (pre-LCPB 467 Ma, Heck et al., 2017; post-LCPB 466 Ma, Martin et al., 2018), Late Silurian (~426 Ma, Martin et al., 2018), Upper Devonian (~373 Ma, Schmitz et al., 2019), Jurassic (~165 Ma, this study), Early Cretaceous (~139 Ma, Schmitz et al., 2017), and Late Cretaceous (~91 Ma, Martin et al., 2019) (Fig. 2.17).

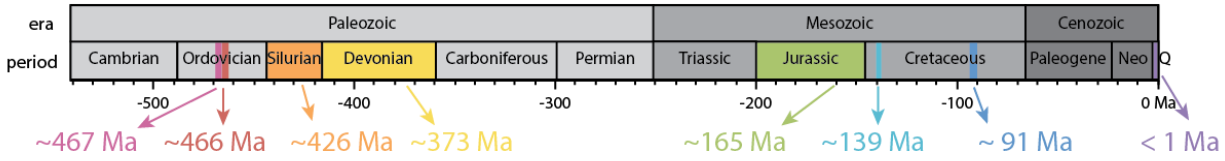

Figure 2.17. Marked time periods for which remnant chrome-spinel abundances have been measured (excluding Today, < 1 Ma). The abundances of Today (< 1 Ma) are based on whole meteorite samples (Meteoritical Bulletin). There are four time periods in the early to mid Paleozoic, and three periods in the mid to late Mesozoic. There is a gap of ~ 200 Myr between the Devonian and the Jurassic collections. These times periods are referenced in Figs. 2.18-2.21.

The ordinary chondrites provide a good point of comparison because ordinary-chondrite chrome-spinel grains are abundant throughout the geologic record and they are relatively straightforward to classify (Fig. 2.18). The most noticeable abundance anomaly in the record is the spike in L chondrites during the Ordovician (~466Ma). This spike represents a ~100-fold higher number of L chondrites falling to Earth than is observed today, and apparently reflects the breakup of the L-chondrite parent body (Schmitz et al., 2001, 2003, 2008; Heck et al., 2010). This high flux of L chondrites depresses the apparent abundances of H and LL chondrites at this time (Fig. 2.18) because the sum of the abundances of the three types is normalized to 100%. The increased number of L-chondrite-like grains during the post-LCPB period becomes distinct when the H- and L-chondrite-like grain abundances are shown relative to the LL-chondrite-like grains (Fig. 2.19). Later time periods show how this influx decreased over time. Relative increases in H-chondrites compared to other types can be seen in the Jurassic and Cretaceous samples. Overall, the L- and H-chondrite-like grains are the most abundant subtypes and LL-chondrite-like grains were consistently the least abundant throughout most of Earth's history.

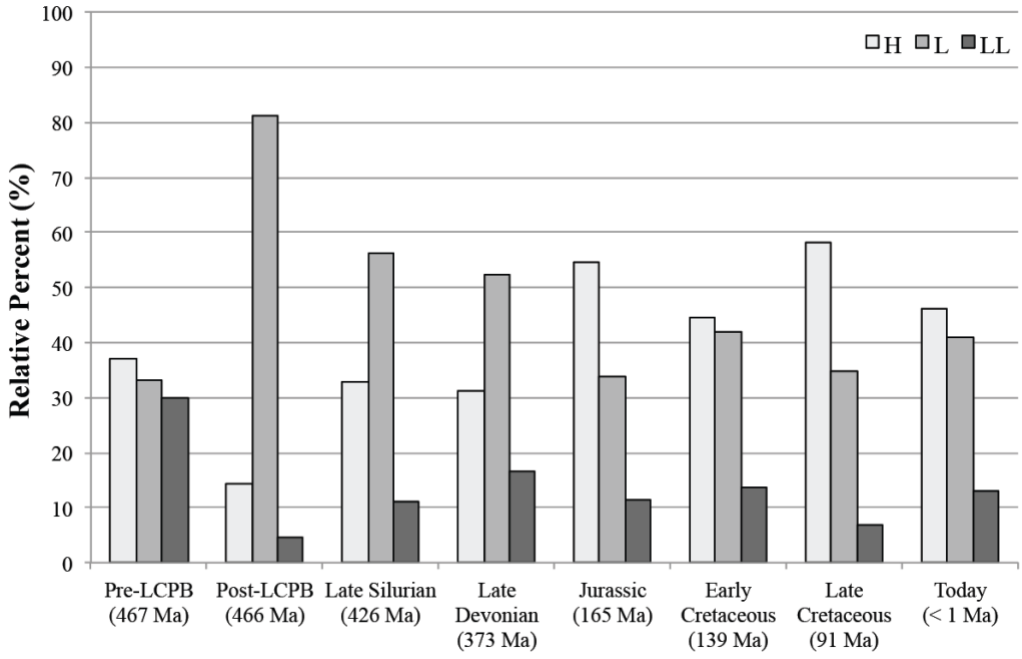

Figure 2.18. Relative abundances of H-, L-, and LL-chondrite origin chrome-spinel grains from different time periods. The abundances of Today (< 1 Ma) are based on whole meteorite samples (Meteoritical Bulletin). Abundances from each time period were determined using their respective classification methodologies. The peak in L-chondrites during the post-LCPB is due to the breakup of the L-chondrite parent body.

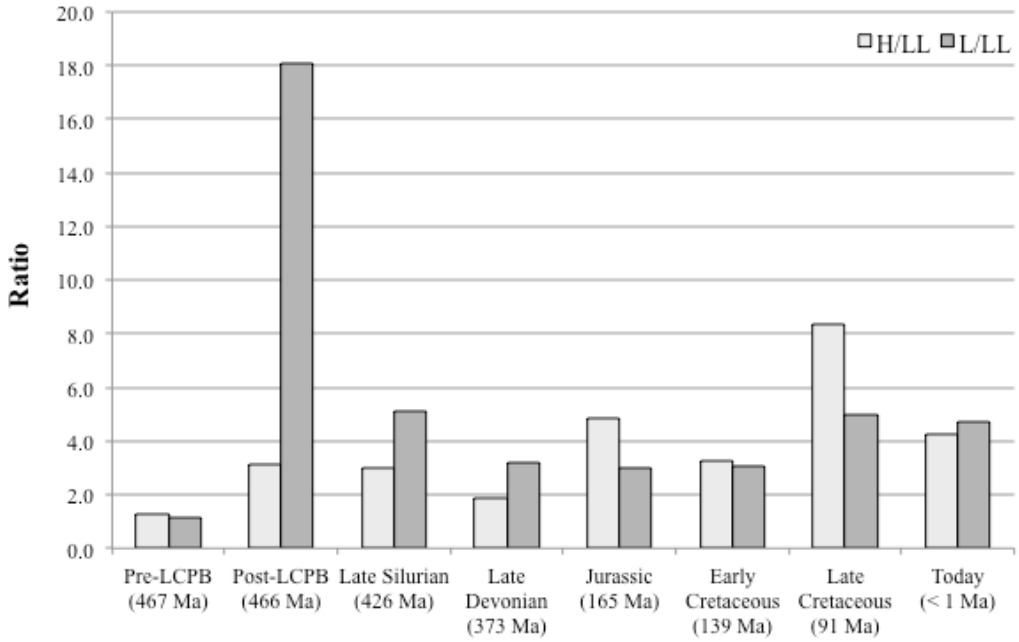

Figure 2.19. Abundances of H- and L-chondrite origin chrome-spinel grains relative to LL-chondrite origin chrome-spinels from different time periods. The increased magnitude of L-chondrite-like grains during the post-LCPB period is distinct when abundances are relative to the steady abundances of the L-chondrite-like grains. The abundances of Today (< 1 Ma) are based on whole meteorite samples (Meteoritical Bulletin). Abundances from each time period were determined using their respective classification methodologies.

The change in the relative abundances of ordinary chondrites and other meteorite types is illustrated in Figure 2.20. The ordinary chondrite peak of the Ordovican is due to the breakup of the L-chondrite parent body (Schmitz et al., 2001, 2003, 2008; Heck et al., 2010). Figure 2.20a shows an overall decrease in the abundances of ordinary chondrites from the Ordovician peak to the Jurassic followed by a gradual increase in ordinary chondrite abundances. The gradual changes in meteorite types through time are also observed when the abundances of other extraterrestrial origin grains are shown relative to ordinary-chondrite-like grains (Fig. 2.21). Figures 2.20a and 2.21a show a spike in the abundance of other extraterrestrial origin grains in the Jurassic. This spike requires some discussion and is likely due to the different classification methodology used in this study compared to previous studies.

Chrome-spinels from different time periods were classified using chemistry, with some periods including oxygen isotopes. Our treatment of the Jurassic time period uses hierarchical clustering to match chemistry and oxygen isotopes of the unknown grains to chrome-spinel

compositions from modern day meteorites. This method takes all extraterrestrial chrome-spinel compositions into account and does not define compositional ranges for different meteorites types. Grains from the pre-LCPB period were classified by matching chemistry and oxygen isotope abundances to modern meteorite chrome-spinel compositions; the methodology was similar to our study (Heck et al., 2017). The other time periods used a chemical scheme that classified the grains into four major groups (see Schmitz et al., 2019 for most recent details). Grains from equilibrated ordinary chondrites (EC; types 4-6) were defined to have oxide weight percentages (wt %) within the ranges of Cr_2O_3 ~53.0-62.0, FeO ~23.0-32.0, Al_2O_3 ~4.5-8.5, MgO ~1.3-4.5, V_2O_3 ~0.55-0.95, and TiO_2 ~1.40-4.50. The EC grains are further subtyped into H, L, and LL based on TiO_2 content (≤ 2.50 %, 2.51-3.39%, and ≥ 3.40%, respectively). Grains that significantly deviated in one or several oxides, but were still considered an EC grain were classified as Outlier EC grains. This group is further classified into low MgO content (< 1.0 wt%) or high MgO content (> 6.0 wt%). Other chrome-spinel grains (OtC-V) that are likely meteoritic in origin do not have the typical equilibrated ordinary chondrite composition, but they contain ≥ 0.45 wt% V_2O_3 and a Cr_2O_3/FeO ratio ≥ 1.45. The final group is defined as likely terrestrial (OtC) in origin and has V_2O_3 < 0.45 wt% or V_2O_3 ≥ 0.45 wt% with a Cr_2O_3/FeO ratio < 1.45. The time periods that used this chemical methodology contained ~ 3% (post-LCPB), ~ 8% (Late Silurian), ~ 85% (Late Devonian), and ~ 48% (Early Cretaceous) OtC grains (terrestrial grains in Figs. 2.22-2.23).

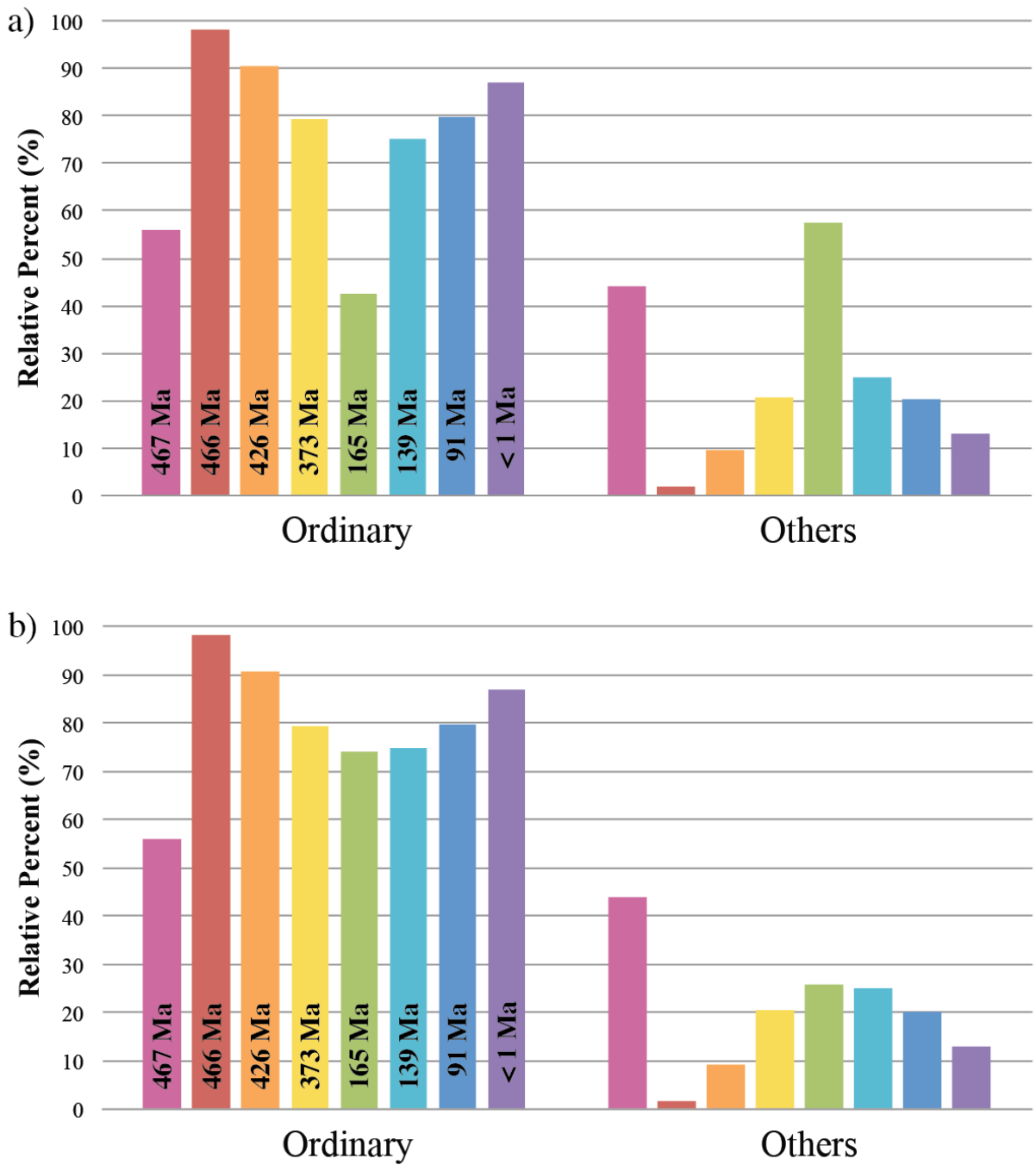

Figure 2.20. Relative abundances of ordinary chondrites (ordinary) and other extraterrestrial (others) origin chrome-spinel grains from different time periods. The abundances of Today (< 1 Ma) are based on whole meteorite samples (Meteoritical Bulletin). The Jurassic grains are classified using a) chemistry and oxygen isotopes with hierarchical clustering, or with b) the chemistry methodology of Schmitz et al. (2019).

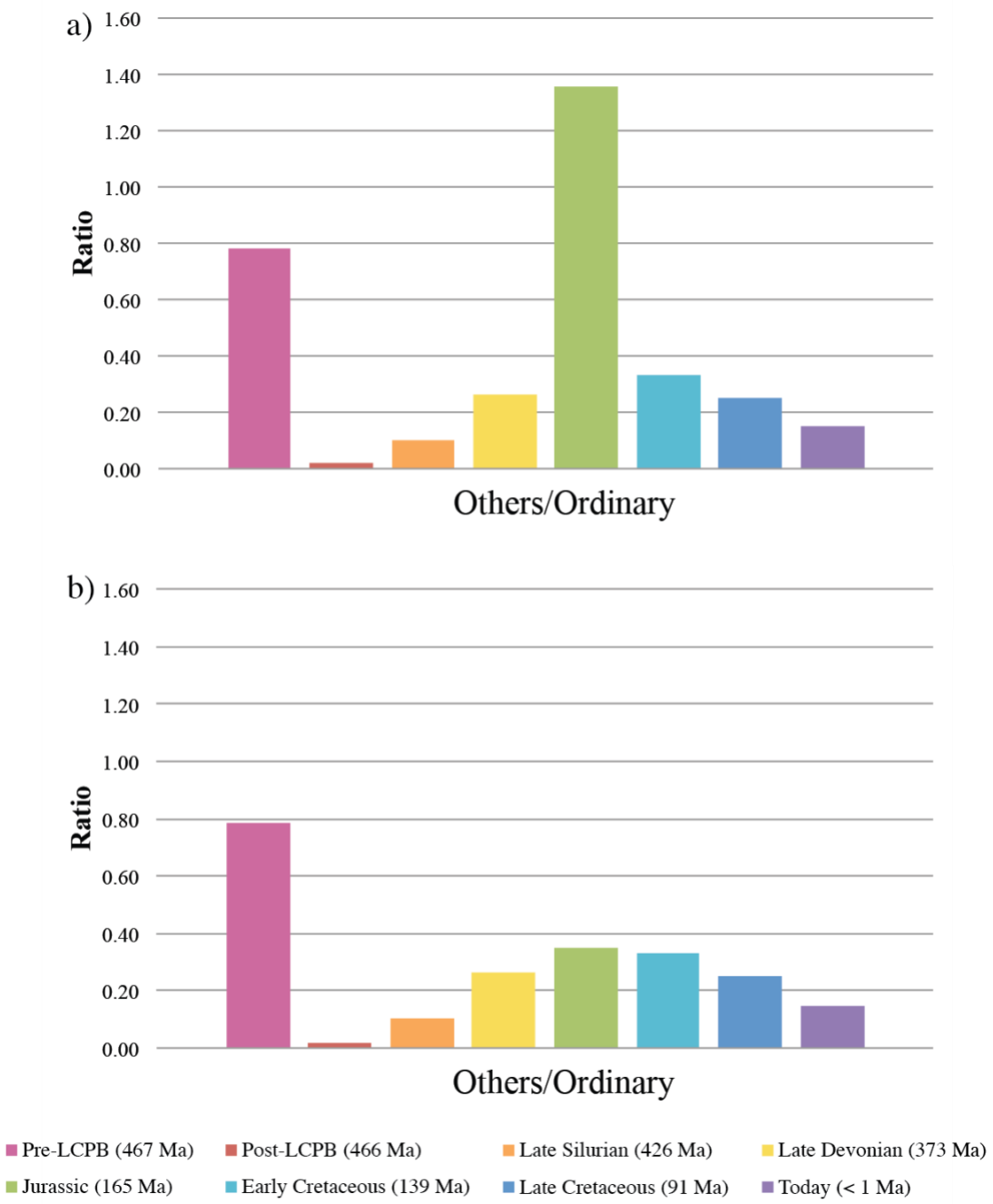

Figure 2.21. Abundance of other extraterrestrial origin chrome-spinel grains (others) relative to ordinary chondrite origin chrome-spinels (ordinary) from different time periods. The ratio of others to ordinary grains demonstrates the gradual changes in meteorite types throughout time. The abundances of Today (< 1 Ma) are based on whole meteorite samples (Meteoritical Bulletin). The Jurassic grains are classified using a) chemistry and oxygen isotopes with hierarchical clustering, or with b) the chemistry methodology of Schmitz et al. (2019).

In order to test the difference classification outcomes between our scheme and the common chemical scheme, we applied the above chemical methodology to our Jurassic grains. The results are shown in Fig. 2.20b. The chemical methodology gives a vastly different outcome when applied. This method increased the relative abundance of the Jurassic ordinary chondrites and caused the abundances to align more with the nearby time periods (Fig. 2.20b). The OtC chemistry ranges deemed ~ 50% of the Jurassic grains as "likely terrestrial", which is why the relative abundance of ordinary chondrites increased. Such a large number of terrestrial grains are unlikely for the Jurassic because most of these "likely terrestrial" grains have oxygen isotope values that support extraterrestrial origins. These excluded grains include the High-Al chrome-spinels that have similar compositions to the outlier ordinary chondrite grains discussed previously (Fig. 2.14). We also applied the OtC guidelines to the compiled chrome-spinel database of modern meteorites (Chapter 4), which resulted in the classification of 35% of the entries as "likely terrestrial". Finally, OtC ranges were applied to the terrestrial chrome-spinel database from Barnes and Roeder (2001), and 91% of the entries were determined to be "likely terrestrial". This common chemical method uses defined ranges for reliable ordinary chondrite classifications, but it is likely biased towards ordinary chondrites and can remove a number of grains that, based on oxygen isotopes, are likely extraterrestrial in origin. Oxygen isotope measurements are beneficial for the classifications of sediment-dispersed chrome-spinels, even if just a few grains from the cluster are measured. In depth analyses of modern meteorite chrome-spinels could also help us better understand the trends of individual meteorite groups to create an appropriate methodology.

Different classification methods can create abundance discrepancies, but the direct comparisons of compositions can show the true differences between periods (Figs. 2.22 and 2.23). The chemical distributions of the chrome-spinels show that all periods have a clustering of ordinary-chondrite-like chrome-spinel grains, suggesting that ordinary chondrites are a constant meteorite type throughout Earth's impact history. Each period shows a clustering of extraterrestrial chrome-spinels, mostly with TiO_2 contents less than the ordinary chondrite range. Many of the time periods do not contain grains identified as extraterrestrial below 0.5 wt% V_2O_3, except for the Jurassic and pre-LCPB. This difference may be due to what was falling during those time periods, but it is likely due to the classification methodology discussed previously. The Jurassic and pre-LCPB used oxygen isotopes to confirm extraterrestrial origins, whereas the

other periods relied on the assumption that grains poor in V are terrestrial and grains rich in V are likely extraterrestrial (Schmitz et al., 2017). While this is generally true (Fig. 2.24), it may be beneficial to focus on oxygen isotope measurements for low V_2O_3 grains to determine if they are truly terrestrial or not. This is even more apparent with the terrestrial classifications of the Late Devonian. This period had a high abundance of terrestrial grains so a screening was needed to remove unwanted samples. There appear to be two terrestrial groupings with low and high TiO_2 content, but similar V_2O_3 contents. The high TiO_2 cluster is likely terrestrial because this region is an uncommon composition for extraterrestrial grains (Fig. 2.24). However, the low TiO_2 cluster may represent extraterrestrial grains based on the distributions of the pre-LCPB and Jurassic (Figs. 2.22a and 2.22e). Both of these periods confirmed that grains within this chemical range were extraterrestrial based on oxygen isotope measurements. Another major difference between the time periods is the lack of high-Al chrome-spinels classified as extraterrestrial (Fig. 2.23). The source of these grains may be exclusive to the Jurassic, or they may have been classified as "likely terrestrial" due to their unique compositions. This could be confirmed for the Late Devonian and Early Cretaceous with oxygen isotope measurements of the grains in the High-Al region. Comparing the elemental and isotopic chemistry of individual grains of each time period can reveal true similarities and differences between the time periods that are currently obscured by classification methods.

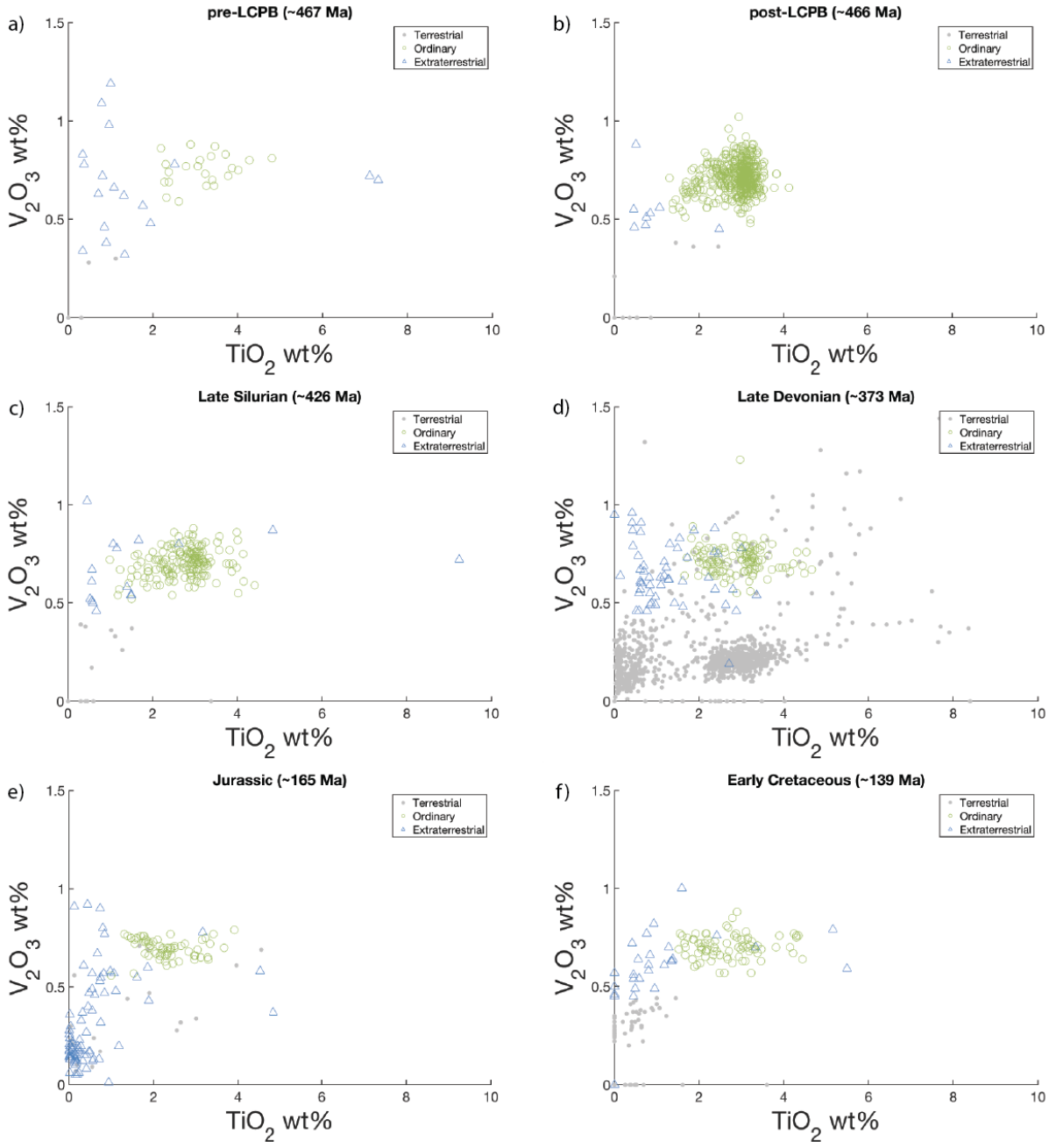

Figure 2.22. Sediment-dispersed chrome-spinel V_2O_3 and TiO_2 abundances from different time periods. Each period was classified as such: pre-LCPB - chemistry and oxygen isotopes compared manually with chrome-spinel compositions from modern meteorites (Heck et al., 2017); Jurassic - chemistry matched with modern meteorite chrome-spinels using hierarchical clustering then manually confirmed with oxygen isotopes; other periods - classifications based on defined chemical ranges (see Schmitz et al., 2019 for most recent methodology). Data: pre-LCPB 467 Ma - Heck et al., 2017; post-LCPB 466 Ma - Martin et al., 2018; Late Silurian ~426 Ma - Martin et al., 2018; Upper Devonian ~373 Ma - Schmitz et al., 2019; Jurassic ~165 Ma - this study; Early Cretaceous ~139 Ma - Schmitz et al., 2017; Late Cretaceous ~91 Ma - Martin et al., 2019.

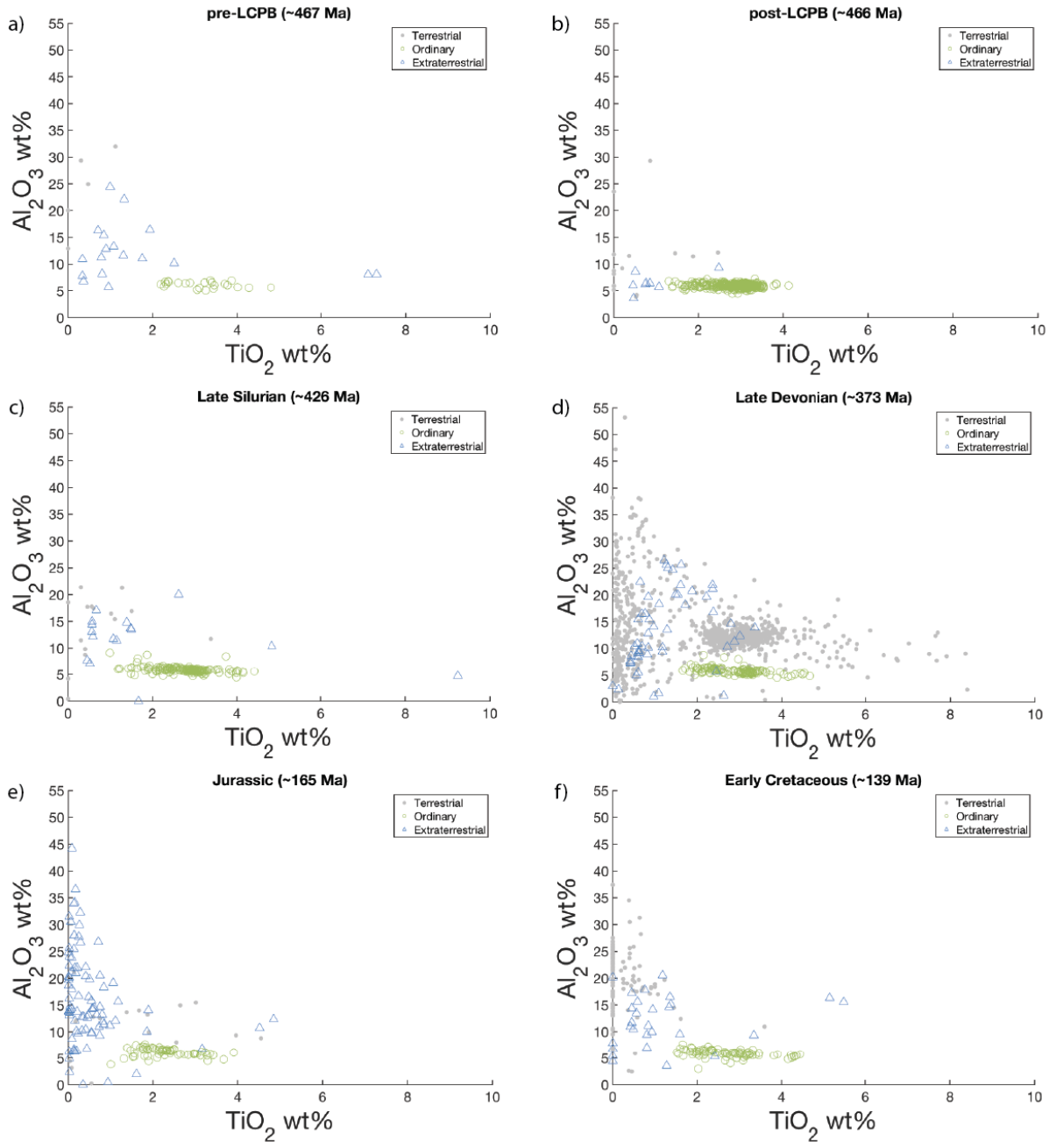

Figure 2.23. Sediment-dispersed chrome-spinel Al_2O_3 and TiO_2 abundances from different time periods. Each period was classified as such: pre-LCPB - chemistry and oxygen isotopes compared manually with chrome-spinel compositions from modern meteorites (Heck et al., 2017); Jurassic - chemistry matched with modern meteorite chrome-spinels using hierarchical clustering then manually confirmed with oxygen isotopes; other periods - classifications based on defined chemical ranges (see Schmitz et al., 2019 for most recent methodology). Data: pre-LCPB 467 Ma - Heck et al., 2017; post-LCPB 466 Ma - Martin et al., 2018; Late Silurian ~426 Ma - Martin et al., 2018; Upper Devonian ~373 Ma - Schmitz et al., 2019; Jurassic ~165 Ma - this study; Early Cretaceous ~139 Ma - Schmitz et al., 2017; Late Cretaceous ~91 Ma - Martin et al., 2019.

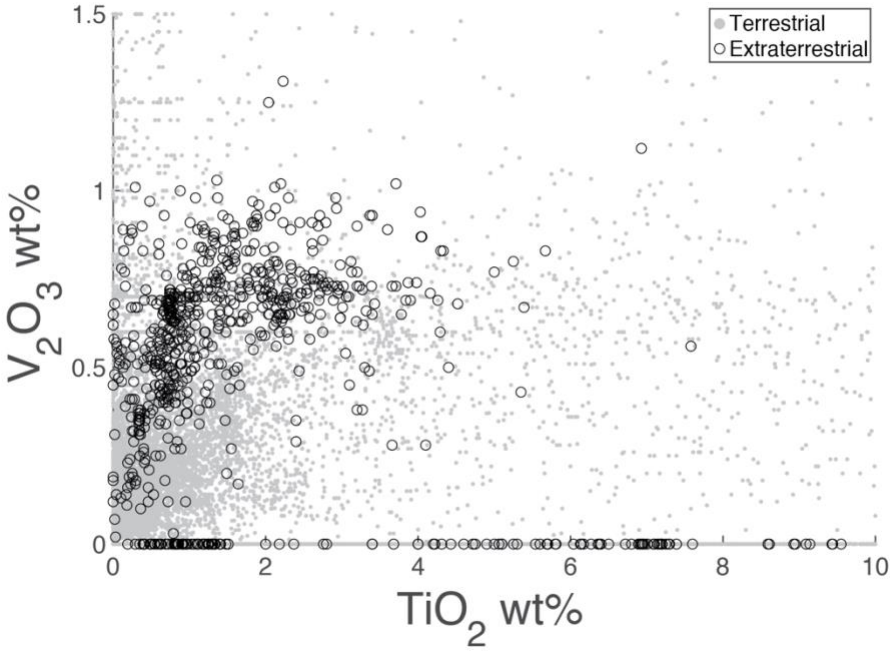

Figure 2.24. Abundances from extraterrestrial and terrestrial chrome-spinel databases (Chapter 4; Barnes and Roeder, 2001). The terrestrial grains have compositions all across the spectrum of V_2O_3 and TiO_2 (compositions continue to higher V_2O_3 and TiO_2 contents for terrestrial, the same scale is used for Figs. 2.22 and 2.23). The extraterrestrial chrome-spinels have a smaller range of V_2O_3 and TiO_2 contents, with most extraterrestrial grains containing < 1 V_2O_3 wt% and < 6 TiO_2 wt%.

Comparisons between Jurassic and modern-meteorite compositions

There are several obvious differences between the chemical populations of Jurassic chrome-spinels and those from modern meteorites. First, the High-Al group previously discussed may not have modern meteorite counterparts based on the current chrome-spinel database (Figs. 2.6 and 2.8). Second, there is a region with lower TiO_2 and Al_2O_3 that does not contain Jurassic grains (Fig. 2.25a; TiO_2 ~ 0-1.5 wt% and Al_2O_3 ~ 0-10 wt%). This region contains chrome-spinel database entries of acapulcoites, lodranites, and SNCs, which may suggest that these types were not falling during the Jurassic. Third, when comparing the entire database to the Jurassic grain distribution, there are some meteorite types that do not appear to overlap with the Jurassic distribution: angrite, eucrite, R chondrite, and the Moon (Fig. 2.25). All of the meteorite types noted were not definitively matched to Jurassic grains with the hierarchical method. More grain measurements from other locations need to be performed in order to confirm that these types of meteorites were not falling during the Jurassic.

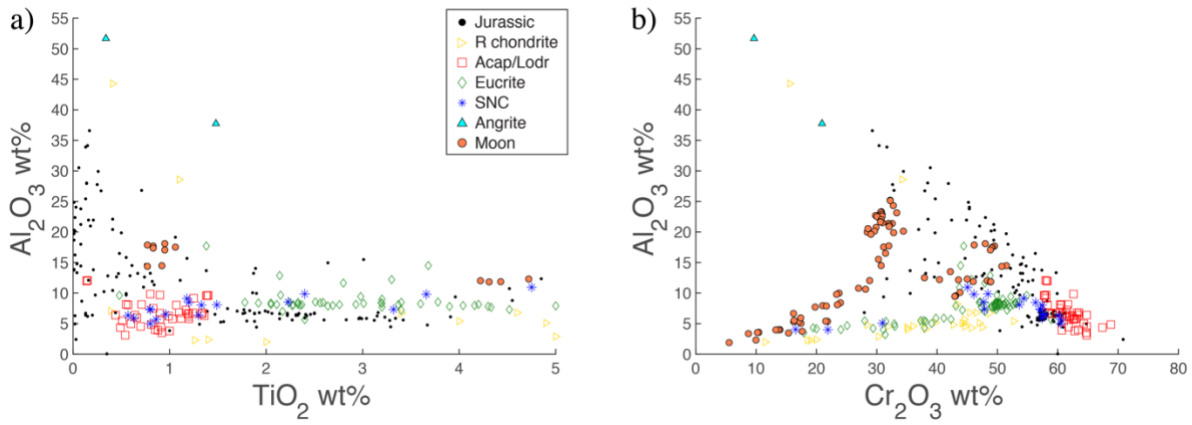

Figure 2.25. Chemical abundances of Jurassic grains and select modern day meteorite chrome-spinels. The meteorite types selected generally do not overlap with the compositions of the Jurassic grains.

2.5.4 Jurassic Relative Abundances

Jurassic grains to grams

The grains per gram correction discussed previously can be used to understand the relative mass of original material that fell for each parent meteorite type based on the number of chrome-spinel grains classified. For the Jurassic, ordinary-chondrite-like grains (n=67) are the most abundant type, with carbonaceous-chondrite-like (n=8), diogenite-like (n=2), and ureilite-like (n=6) types having lower abundances (Table 2.6). The remaining Extraterrestrial grains (including High-Al grains) from the Jurassic are likely from various achondrites, with the possibility of some carbonaceous-chondrite-like grains (n=75; Table 2.6 and Appendix A). These Jurassic grain abundances cannot be directly translated to relative meteorite abundances because the number of chrome-spinel grains per gram in different meteorites varies dramatically (Table 2.7). Also, not all of the extraterrestrial Jurassic grains have been definitively classified as originating from a specific meteorite type. In this case, a first order assumption can be made about the ordinary versus achondrite abundance of the Jurassic time period. If we assume that the majority of Jurassic Extraterrestrial grains are achondrite-like (not including possible carbonaceous origins), then the number of achondrite-like grains is higher or possibly similar to the number of ordinary chondrite-like grains (Table 2.6 and Appendix A). If we then compare the number of grains per gram for ordinary chondrites and achondrites, we see that their abundances are relatively equal or achondrites have a somewhat lower abundance of chrome-

spinels (Table 2.7). Taking the number of grains for the Jurassic and the grains per gram abundances, it is possible that achondrites had similar or higher meteorite abundances compared to ordinary chondrites during the Jurassic. This distribution is vastly different than the dominant abundance of ordinary chondrites of today. More definitive meteorite abundances may be possible in the future when the chrome-spinel database and the grain per gram correction is more robust, but the current conversion provides an initial indication of relative meteorite abundances.

Relation to asteroid families

The Jurassic time period was chosen as a focus for chrome-spinel parent body classifications in part to see if there was evidence of the break up of the Baptistina asteroid family. This parent body was believed to have spectroscopic characteristics similar to carbonaceous chondrites and to have broken up ~160 (+ 30, -20) Ma (Bottke et al., 2007). Refined spectral studies have shown that the Baptistina family members are LL chondrites (Reddy et al., 2014), and have a revised break up age of 190 ± 30 Ma based on *WISE*/NEOWISE data (Masiero et al., 2012). If there was evidence of the breakup of the Baptistina asteroid family during the Jurassic then there should be an increased abundance in LL-chondrite-like grains compared to other time periods, but this is not the case (Fig. 2.7). Chrome-spinel abundances of the Early Cretaceous constrained the breakup occurrence to be between 220 and 145 Ma (Schmitz et al., 2017). The addition of chrome-spinel abundances from the Jurassic puts a further constraint on the event to have likely occurred no later than 165 Ma. Studies of sediment-dispersed grains before 165 Ma may reveal evidence of the Baptistina asteroid family breakup.

The Jurassic chrome-spinels may also represent a multitude of different asteroid families that have breakup ages close to this time period. Contributions from these families likely originate from the inner or central main belt in order to arrive on the Earth within millions of years (Gladman et al., 1997; Zappalà et al., 1998). Such families include: Massalia (~150 ± 50 Ma), Agnia (~100 ± 100 Ma), Merxia (~250 ± 100 Ma), Astrid (~250 ± 100 Ma), and Nemesis (~200 ± 100 Ma) (Nesvorný et al., 2005 and 2015). These families vary amongst S- and C-types, which encompass stony (silicate) and carbonaceous compositions. The age uncertainties and connections to specific meteorite types make it difficult to pinpoint an asteroid family contribution for the Jurassic. Also, there is not an overly dominant meteorite type within the classified Jurassic grains that would pinpoint a possible asteroid family contribution. The lack of

dominant meteorite type may suggest that the grains measured for this study represent a background flux of material to the Earth during this time interval. Sampling chrome-spinels from other locations with the same time interval are needed to confirm that the abundances of this study are due to a general infall of material.

2.6 Conclusions

Extracted chrome-spinel grains from Jurassic limestone were classified as originating from parent meteorite types using elemental compositions and oxygen isotope abundances. Hierarchical clustering was implemented to match Jurassic grain compositions to chrome-spinel compositions from modern day meteorites. The use of hierarchical clustering improved the classification process by 1) not requiring the use of defined chemical ranges to reduce numbers of candidates and 2) removing unlikely database matches for a more manageable manual classification. Oxygen isotope abundances were used subsequently to confirm or refute a chemical match. Most of the grains were classified as having an extraterrestrial origin (88%). The classified grains include ordinary chondrite, carbonaceous chondrite, diogenite, and ureilite origins. Other possible sources for the grains include pallasites, acapulcoites, lodranites, brachinites, howardites, chassignites, eucrites, and irons. A cluster of grains, called the High-Al group, was determined to be distinct from other grains but did not have a database match to enable a classification as a known meteorite type. This may be due to gaps in the database or they could be from a meteorite type that is not falling today. Overall, the Jurassic grain abundances and grains per gram values of Heck et al. (2017) suggest that achondrites had similar or higher meteorite abundances compared to ordinary chondrites. This first order estimate of Jurassic meteorite abundances differs from the dominant abundance of ordinary chondrites today.

Comparing the chrome-spinel compositions of different time periods can show how the populations of meteorites changed throughout history. There is a concentration of ordinary-chondrite-like grains in all time periods suggesting that ordinary chondrites are a main source of material to the Earth's surface throughout history. Various compositions of chrome-spinels are shown throughout the other time periods as well. Differences in relative abundances amongst the time periods show a gradual change in material falling to Earth. The peak in ordinary chondrites during the Ordovician represents the breakup of the L-chondrite parent body. The effects of this breakup on the relative abundances decreased over time until our observed drop for the Jurassic.

This dramatic change was shown to be due to different classification methodologies. Our comparison of methodologies demonstrated the importance of collecting oxygen isotope data on grains before dismissing them as terrestrial based on element compositions alone. While the classification of chrome-spinels into their parent meteorite types is vital to understanding precise changes in meteorite type abundances, it is also important to look at the chemical and oxygen isotope data themselves to gain a clear understanding of the time periods without the issues of different classification methods.

Overall, this work shows that remnant chrome-spinels can be classified into parent meteorite types. The compilation of a modern day meteorite chrome-spinel database is an ongoing process and the addition of new chemical and oxygen isotope abundances will improve the classification process. Work on other time periods will also help with the understanding of how Solar System dynamics have changed throughout Earth's history.

Acknowledgments— Supported by NASA grant NNX16AQ08G to GRH and the ERC-Advanced Grant 213000 to BS.

CHAPTER 3

THE CLASSIFICATION OF RELICT EXTRATERRESTRIAL CHROME-SPINELS USING STEM TECHNIQUES ON SILICATE INCLUSIONS

3.1 Abstract

Remnant extraterrestrial chrome-spinels from terrestrial sediments provide information on how the mixture of meteoritic materials falling to Earth has changed over Earth's history. The parent meteorite type of each grain can be identified by characteristic elemental and oxygen-isotope abundances. Some meteorite types can be difficult to classify because their chrome-spinel compositional ranges overlap. Silicate inclusions within chrome-spinels of modern ordinary chondrites have been shown to have discriminating power amongst meteorite subclasses. We employed energy-dispersive X-ray spectroscopy in a scanning electron microscope and in a (scanning) transmission electron microscope to investigate inclusions in chrome-spinel grains from Ordovician and Jurassic sediments. Unaltered Ordovician inclusions allowed us to establish the size limits for reliable SEM analysis of inclusions. The Jurassic grains were more altered, but using S/TEM techniques on the small inclusions (< 3μm surface diameter) allowed us to determine chemical compositions and mineral structures of inclusions in three chrome-spinel grains. The parent meteorite type was determined for one grain based on its inclusion compositions. Our study confirms that silicate inclusions can be used to classify parent meteorite types of chrome-spinel grains, but the size of the inclusions and the complex effects of terrestrial alteration must be taken into account. During our study, we also found some interesting exsolution phenomena in the host chrome-spinel grains.

3.2 Introduction

Meteorites have been falling throughout Earth's history, but those in meteorite collections only provide us with physical samples of the solar system from the past few thousand years. Recent studies have shown that meteorites and their remnants can be preserved in limestone throughout the sedimentary record. Preserved whole samples are referred to as "fossil" meteorites because they retain their original texture, but most of the minerals that made up the meteorite have altered over time into calcite and clays (Schmitz, 2013). The retained texture of a whole fossil meteorite can be used for a preliminary classification. For example, the type of

ordinary chondrite (H, L, LL) can be identified based on the size of the chondrules within the sample (Bridges et al., 2007). However, the loss of original chemical information due to fossilization severely limits what we can learn about a sample. Fortunately, extraterrestrial chrome-spinels resist terrestrial weathering and retain their original characteristics. The major- and minor-element and oxygen-isotope compositions of relict chrome-spinels can be measured and can be used to classify the parent meteorite type. These spinels originate from meteorites or micrometeorites and are either found in whole fossil meteorites or as single grains distributed throughout the limestone (as "sediment dispersed" grains). The overall objective of classifying extraterrestrial chrome-spinel grains is to determine how the abundance and types of meteorite populations have changed over Earth's history. Studying different time periods may reveal shifts in the dominant meteorite types. Ordinary chondrites dominate today, but other types may have dominated in the past or had different relative abundances (e.g., ordinary chondrites were slightly less abundant during the Cretaceous Period (Schmitz et al., 2017)). Analyzing chrome-spinels may also lead to the discovery of a new meteorite type (e.g., Öst 65 from the Ordovician Period (Schmitz et al., 2016)). We are studying samples from the Jurassic Period, specifically the Callovian age (~165 Ma) in Southern Spain, near Carcabuey. Preliminary work on the Jurassic samples has been reported in several abstracts (e.g. Caplan et al., 2018 and 2019) and a complete report is in preparation.

Although chrome-spinels provide considerable information that allows many grains to be assigned to their parent meteorite type, there are often ambiguities because of the limited variability of chrome-spinel. For example, whole-rock oxygen-isotope compositions of ordinary chondrites cluster separately from most meteorite types, but the compositions of L- and LL-type subclasses partially overlap, making it difficult to distinguish between the two (Fig. 3.1a). Chrome-spinels can contain inclusions of olivine, pyroxene, merrillite, and plagioclase, which can be analyzed to help determine the parent meteorite type of the host spinel grain (e.g., Fig. 3.1b). This method assumes that silicate inclusions are in equilibrium with the bulk-rock silicates, as should be the case for type 4-6 chondrites (Alwmark and Schmitz, 2009a; Alwmark et al., 2011). Alwmark and Schmitz (2009a) showed that, in modern chondrites, the compositions of silicate inclusions within chrome-spinels parallel the compositions of silicates from the host meteorite (Fig. 3.2). However, they also showed that inclusions tend to have lower Fa contents compared to matrix contents. Alwmark and Schmitz (2009a) modified the Fa content range to

accommodate the lower Fa inclusion compositions. Overall, they determined that the fayalite (Fa) content of olivine inclusions and the ferrosilite (Fs) content of Ca-poor pyroxene inclusions within chrome-spinel grains can distinguish between L- and LL-type ordinary chondrites (Fa or Fs = (100 × Fe/(Mg + Fe)); Fig. 3.1b). With this technique, they studied a collection of chrome-spinel grains (fossil meteorites and sediment-dispersed grains) from the Ordovician Period and confirmed that all the analyzed grains originated from L-chondrites (Alwmark and Schmitz, 2009a).

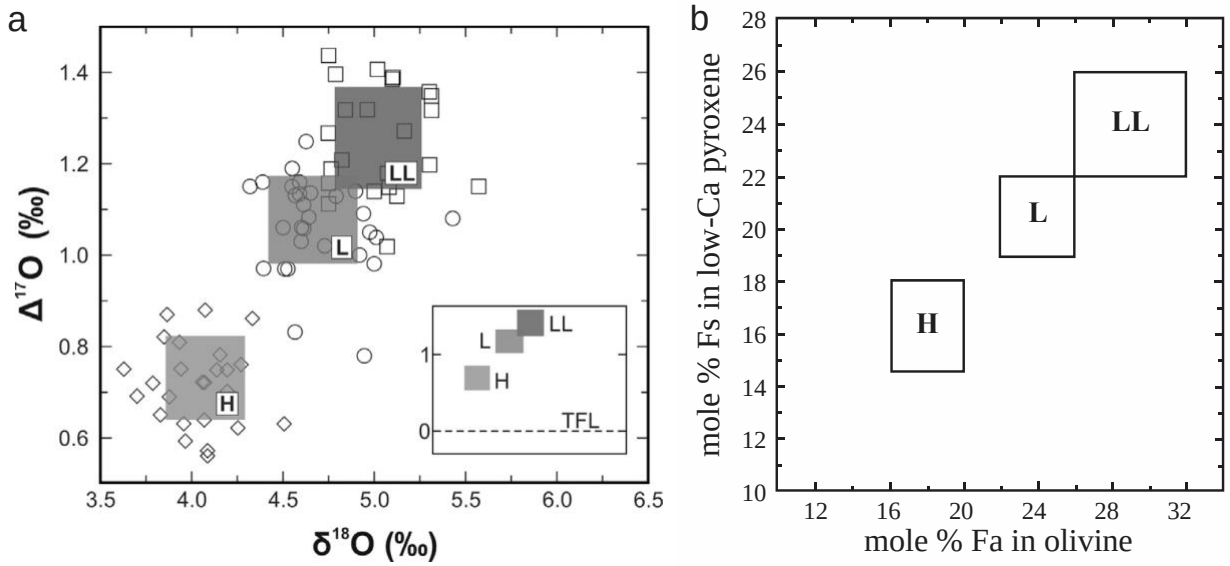

Figure 3.1. H, L and LL-type ordinary chondrites can be distinguished by oxygen isotope and silicate chemistry. a) Whole-rock $\Delta^{17}O$ versus $\delta^{18}O$ for equilibrated ordinary chondrites (from Schmitz, 2013, individual data points from Clayton et al., 1991) shows overlap between L- and LL-type ordinary chondrites. The grey boxes represent the 1σ error on the whole-rock mean values. b) Fs vs. Fa plot (modified from Brearley and Jones, 1998) for ordinary-chondrite silicates, shows how silicate compositions can distinguish between L- and LL-type ordinary chondrites.

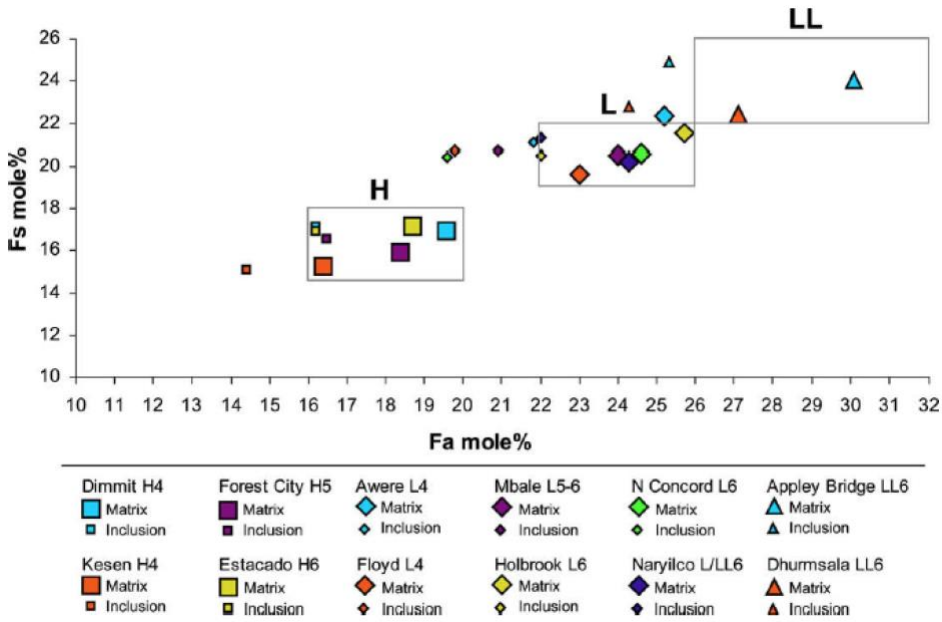

Figure 3.2. The Fa content of olivine and Fs content of Ca-poor pyroxene in the matrix and inclusions of chrome-spinels in H-, L-, and LL-chondrites (from Alwmark and Schmitz, 2009a). The grey lined boxes show the established Fa and Fs ranges for equilibrated H-, L-, and LL-chondrites (Brearley and Jones, 1998, and references therein). The inclusions tend to have lower Fa contents than the matrix contents, but the Fs contents are within the established Fs ranges.

Alwmark and Schmitz (2009a) also discussed the limitations of using inclusions in chrome-spinels to classify the parent meteorite type. For example, surrounding chrome-spinel can be incorporated into an electron probe or SEM-EDS measurement if the measured inclusion is smaller than the interaction volume created by the electron beam. Alwmark and Schmitz (2009a) concluded that inclusions larger than ~3 µm in diameter could be measured by SEM-EDS without fluorescing surrounding chrome-spinel, but that smaller inclusions would include host material in a measurement.

Alteration of the inclusions can also cause issues with identifying the parent meteorite type of the grain. Chrome-spinels are quite resistant to terrestrial weathering (Schmitz, 2013), but the inclusions within them are more susceptible to alteration, much like the minerals that made up the original host meteorite. As we will show in this paper, terrestrial alteration can compromise the inclusions, but altered inclusions can still provide information, depending on the nature and degree of alteration.

In this paper, we present chemistry data for inclusions from three extraterrestrial chrome-spinel grains found in Jurassic pelagic sediments. The inclusions were imaged by secondary

electron (SE) and backscattered-electron (BSE) imaging. They were analyzed in spot mode, and line scans were acquired across some inclusions by SEM-EDS. Portions of the inclusions were extracted using a dual beam focused ion beam-scanning electron microscope (FIB-SEM), thinned to electron transparency, and analyzed for elemental compositions using a (scanning) transmission electron microscope (S/TEM) equipped with a spectrometer for energy dispersive x-ray spectroscopy (EDS). The extracted section allows the inclusion to be measured without the possibility of fluorescing the surrounding chrome-spinel. S/TEM measurements showed that all of the inclusions from the Jurassic grains had at least some level of terrestrial alteration. In order to validate our analytical approach, we also analyzed inclusions in an extraterrestrial chrome-spinel grain from the Ordovician age Brunflo fossil meteorite that does not exhibit significant alteration (Thorslund et al., 1984; Schmitz et al., 2001; Alwmark and Schmitz, 2009a and 2009b). We show that despite the challenges of working with inclusions in chrome-spinels that have been on Earth for hundreds of millions of years, we can still obtain important information about the parent meteorite types of the grains.

3.3 Material and Methods

For this study, we investigated inclusions from Jurassic and Brunflo chrome-spinels. The Jurassic grains were extracted from limestone at Lund University using acid dissolution (Schmitz, 2013), embedded in epoxy, polished, and carbon-coated. The grains originate from a highly condensed sediment bed of the Ammonitico Rosso type sampled at Carcabuey, province of Córdoba, in southern Spain. The bed formed during the Callovian Age ca. 165 Ma ago. The Brunflo chrome-spinel was processed and mounted at Lund University (Alwmark and Schmitz, 2009a and 2009b). Alwmark and Schmitz (2009a and 2009b) did measurements of the Brunflo grain and inclusions previously. The Jurassic grains were analyzed at the University of Hawai‘i (UH) by electron microprobe for elemental compositions and by ion microprobe for their oxygen isotope compositions. Chrome-spinel compositions were measured using the JEOL JXA-8500F field emission electron microprobe with an accelerating voltage of 20 kV, a beam current of 20 nA, and beam diameters of 1-10 microns (based on surface area available). The elements Cr, Fe, Mg, Al, Ti, V, Mn, and Zn were measured. The values of Fe_2O_3 were calculated from the measurements based on the structural formula of spinel (Droop, 1987). Stillwater chromite grains mounted in the Jurassic-grain mounts and the UH electron probe lab standard (chromite USNM 117075) were used as standards for the measurements. Additional details for the measurements

can be found in Chapter 2. Several chrome-spinel grains were found to contain silicate inclusions during secondary and backscattered-electron imaging with a scanning electron microscope (SEM). The inclusions were avoided during chemistry and isotope measurements of the surrounding chrome-spinel, and several inclusions were chosen for further detailed investigation.

Initial major- and minor-element abundances of several of the inclusions were measured by EDS using an FEI Helios 660 dual beam Focused Ion Beam instrument (FIB-SEM) at the University of Hawai‘i. The EDS spectra were collected at 15 kV using an EDS (X-max N80 SDD-EDS, Oxford Instruments) with a large area silicon-drift detector. The spectra were quantified using commercial “remote standards” standardless quantitative-analysis software (AZtec Energy Advanced Microanalysis System, Oxford Instruments) calibrated using a Cu standard. Resulting elemental composition data are normalized to 100% and are considered semi-quantitative. We note that silicate mineral standards are readily identified by their stoichiometry using this approach. We assume uncertainties of ±1 in Fa and Fs numbers determined from SEM-EDS analyses, like those reported by Alwmark and Schmitz (2009a). Compositional data gathered using SEM-EDS were used to select inclusions for the preparation of FIB sections. The FIB extracted inclusions were analyzed using a (scanning) transmission electron microscope (S/TEM). Spectral line scans (0.1 μm steps) were also taken across inclusions in the Brunflo chrome-spinel grain to see if line scans can help determine the relation between interaction volume of a SEM-EDS measurement and an inclusion with unknown depth. Prior to extracting FIB cross sections, a protective Pt strap was deposited over the to-be-sectioned inclusion, as well as any nearby inclusions, in order to protect them from ion milling (Fig. 3.3a). Sections were removed by ion-milling trenches adjacent to, and an undercut beneath, each specific inclusion using the 30 kV Ga^+ ion beam (Fig. 3.3b). Once the section was lifted out and attached to a copper “half-grid” mount, the section was thinned to electron transparency (~100 nm) (Figs. 3.3c and 3.3d). A final FIB-polishing step at 5 kV removed most of the amorphous surface layer produced by the higher-energy milling (Ishii et al., 2010; Graham et al., 2008). The University of Hawai‘i Helios FIB is equipped with a sample holder that allows a FIB section to be mounted perpendicular to the electron beam (for scanning transmission imaging), and the FIB section prepared from one of the chrome-spinel grains was mapped with EDS spectra at each pixel to generate qualitative maps showing the distribution of elements in the thin section.

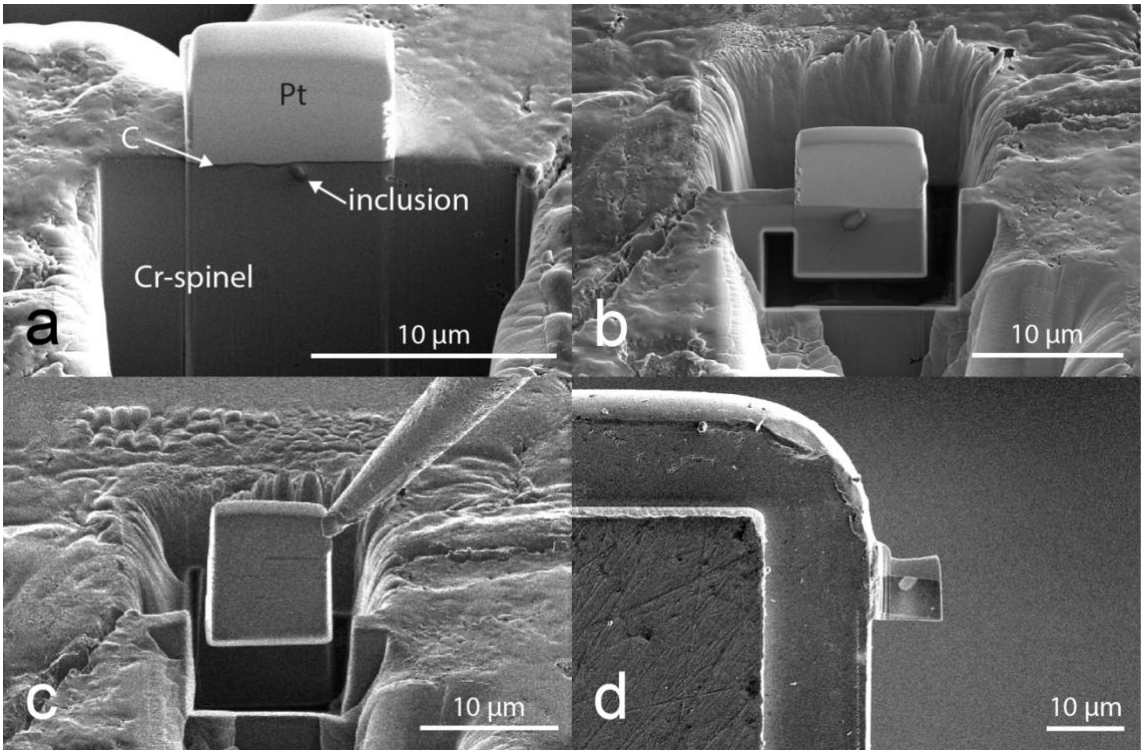

Figure 3.3. FIB section preparation for representative inclusion (Grain 1 Inclusion 1). a) Ion-milled trench revealed inclusion in cross-section, protected by Pt strap, b) trenches on both sides of the inclusion and undercut, c) lift out of section after cutting free from the host grain, and d) FIB section attached to copper grid and thinned for S/TEM analyses.

TEM imaging of the inclusions in the FIB sections was carried out at 300 kV using a high-base FEI 80-300 kV Titan dual C_s-corrected and monochromated (scanning) transmission electron microscope (S/TEM) (Bradley and Dai, 2009). Bright field (BF) and dark field (DF) TEM and high angle annular dark field (HAADF) and bright field STEM imaging modes were used. Bright field images are generated from the transmitted beam of electrons, and dark field images are generated from scattered/diffracted beam(s) of electrons. HAADF images are generated from electrons scattered at high angles, and the images have intensities proportional to the local average atomic number of the sample. For reference, in subsequent figures the Pt strap in FIB sections appears dark in BF images (e.g. Fig. 3.5 left side) and bright in HAADF images (e.g. Fig. 3.6a), where contrast is related to average atomic number. Elemental composition analyses with the TEM were performed using a solid state Si(Li) energy dispersive x-ray spectrometer (Genesis 4000, EDAX) at the University of Hawai‘i (UH). The sub-nanometer-scale spatial resolution of the Titan S/TEM allows for compositional and structural (crystallographic) analyses of fine structures within the inclusions and surrounding chrome-

spinel. The compositions of the inclusions were measured by rastering the beam in STEM mode over rectangular regions, positioned to exclude contributions from surrounding material. The beam was rastered for inclusion compositions to minimize sample damage and to minimize the buildup of contamination on the sample surface. The compositions of other structures were measured by positioning a stationary probe on the specimen (i.e. point-count analyses). Spectra were quantified using TIA (TEM Imaging & Analysis) ES Vision commercial software (Thermo Fisher, formerly FEI Co.), which applies a Cliff-Lorimer correction (Longo et al., 1999) to produce element abundances normalized to 100%. Because oxygen Kα X-rays are more readily attenuated within the sample due to their low energy, oxygen is not quantified from the characteristic X-ray peak and, instead, oxygen stoichiometry is assumed in order to calculate weight percent oxides. For reported STEM-EDS compositions, relative uncertainties are conservatively estimated at 3-5% for major elements, 10-15% for minor elements and 20-70% for trace elements (depending on abundance). These uncertainties result in higher uncertainties on calculated Fs and Fa numbers from STEM-EDS than from SEM-EDS. Element maps of some inclusions were collected at 200 kV using an 80-200 kV Titan STEM with ChemiSTEM technology consisting of four EDS detectors providing ~0.7 sr solid angle at Oregon State University. Pixel sizes of 9 and 17 nm and total acquisitions of 30-45 minutes were sufficient to produce element maps with good signal-to-noise. A full X-ray fluorescence spectrum is saved at each pixel of each map. Spectra were extracted from selected regions of the maps to determine the compositions of features of interest. Electron-diffraction patterns of inclusion rims and lamellae in surrounding chrome-spinel were obtained using selected-area electron diffraction (SAED) to determine crystal structures, and the nanocrystalline Pt strap in the FIB sections provided *in-situ* diffraction camera length calibration. Electron energy loss spectroscopy (EELS) was carried out at 300 kV on the UH S/TEM with its monochromator and electron energy imaging spectrometer (Tridium 866 GIF, Gatan Inc) in order to assess the oxidation state of Fe in oxide phases identified in one inclusion. Spectra were acquired in scanning transmission mode using a stationary probe, a zero-loss peak energy resolution (FWHM) of 0.3 eV, and a dispersion of 0.05 eV/channel.

3.4 Results

3.4.1 Jurassic Grain 1

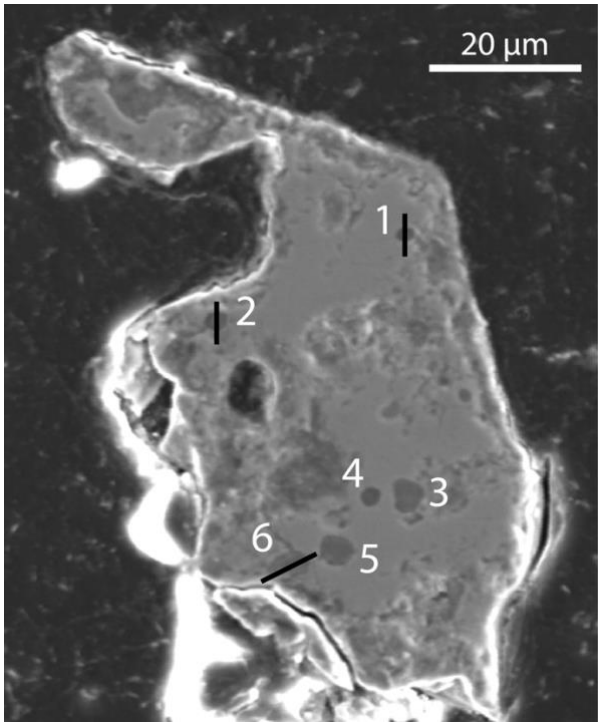

Figure 3.4. Secondary-electron (SE) image of Grain 1. Six dark-gray inclusions are identified with adjacent number labels. Locations of three FIB sections extracted from this grain are marked with black lines.

Grain 1 was characterized, based on element chemistry and oxygen isotopes, as originating from an ordinary chondrite. The chemistry of Grain 1 indicates that the host meteorite was an L or LL chondrite, but oxygen-isotope measurements indicate the parent meteorite was an L chondrite (Caplan et al., in prep). The initial polished surface did not show any inclusions in SEM imaging, but after re-polishing, six inclusions were identified (Fig. 3.4). The surface of the re-polished grain has a rough texture with small cracks and divots. Three FIB sections (Inclusion 1, 2 and 6 in Fig. 3.3) were extracted from this grain for TEM analysis and are described in more detail below.

Inclusion 6

Inclusion 6 contains a variety of textures and compositions. This inclusion had an oblong shape of ~3.4 x 5.4 µm on the grain surface (Fig. 3.4) and a maximum depth of ~3.0 µm in FIB cross section (Fig. 3.5, left). The central area of this inclusion is amorphous and has a pyroxene-like composition of $Mg_{10.9}$ $Fe_{5.4}$ $Mn_{0.4}$ $Ti_{0.5}$ $V_{0.1}$ $Al_{2.8}$ $Si_{19.3}$ $O_{60.6}$ with ferrosilite content of 33.0 ± 4.4, as determined by STEM-EDS. This composition is more iron-rich than ordinary-chondrite pyroxenes. There is also a small crystal in the center of the inclusion with a pyroxene-like composition $Mg_{9.5}$ $Fe_{6.2}$ $Mn_{0.3}$ $Ti_{0.6}$ $Al_{2.8}$ $Si_{19.7}$ $O_{60.8}$ with ferrosilite content of 39.6 ± 4.8. The rim of the inclusion contains iron oxide (FeO_x) within amorphous silica. The iron oxide is present as finger-like structures (laths) that protrude towards the interior of the inclusion.

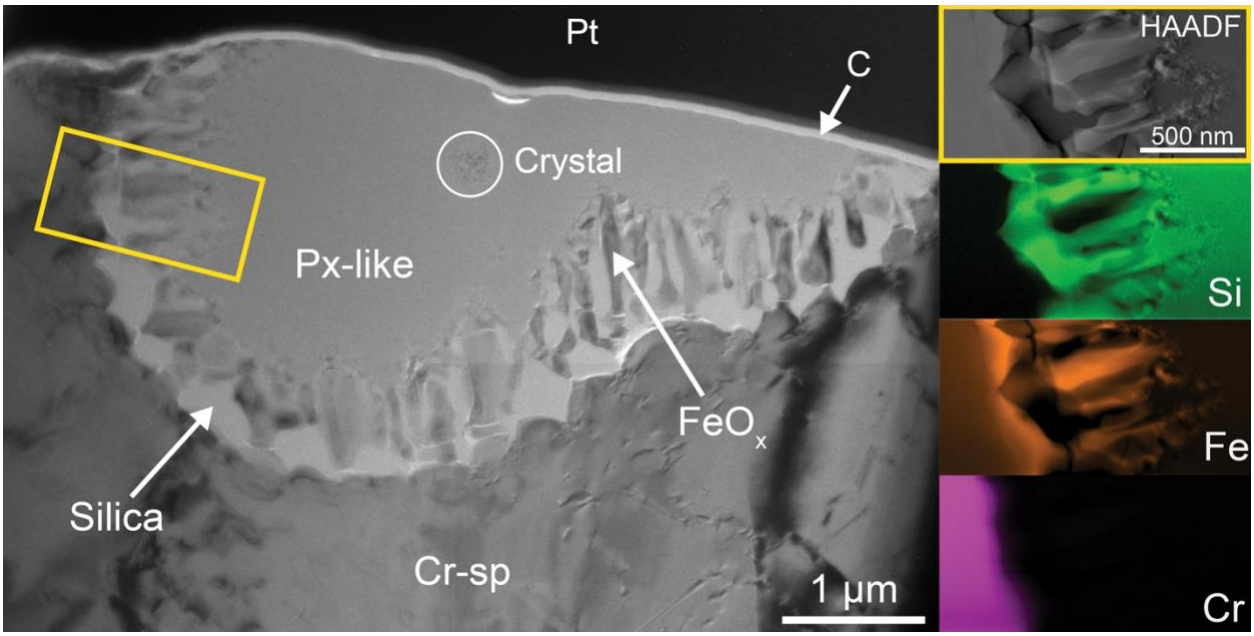

Figure 3.5. Complex rim on Inclusion 6 from Grain 1. (Left) Bright-field (BF) TEM image of the FIB section. The inclusion has an amorphous center with pyroxene-like composition and contains a small pyroxene crystal. The rim of the inclusion is amorphous silica with iron oxide laths. (Right) STEM-EDS element maps of a rim section (top to bottom: HAADF, Si, Fe, and Cr). Note that dark and light contrast is reversed between the BF and HAADF images.

STEM-EDS element maps of Si, Fe, and Cr and corresponding HAADF image (Fig. 3.5, right) were collected in order to study the structure of the rim. The suite of four images shows that there is a boundary to the left of the silica that corresponds with changing Fe and Cr contents. The Si map shows a sharp boundary at the base of the laths, whereas the Fe and Cr

maps show more gradual composition gradients. The Cr composition is constant in the host chrome-spinel region, but decreases close to the Si border. As the Cr content decreases, the Fe content increases up to the boundary where silica begins. The changing concentrations of Cr and Fe suggest that they were mobile during lath/rim formation. The Fe and Si maps show growth of the FeO_x laths and the silica filling in the remaining area. Diffraction patterns of the chrome-spinel and the FeO_x laths show that both have the same crystal orientation (Fig. 3.6a and b). Chrome-spinel has an fcc crystal lattice with a lattice parameter, a = 8.38 Å, and magnetite is also fcc with a = 8.32 Å. The iron oxide composition and lattice parameter of the laths are consistent with magnetite. However, EELS performed on the laths yielded spectra dominated by Fe^{3+} (Fig. 3.6c), inconsistent with magnetite. Together, the diffraction patterns and EELS data thus indicate that the iron oxide laths are maghemite, isostructural with magnetite but with more highly oxidized iron.

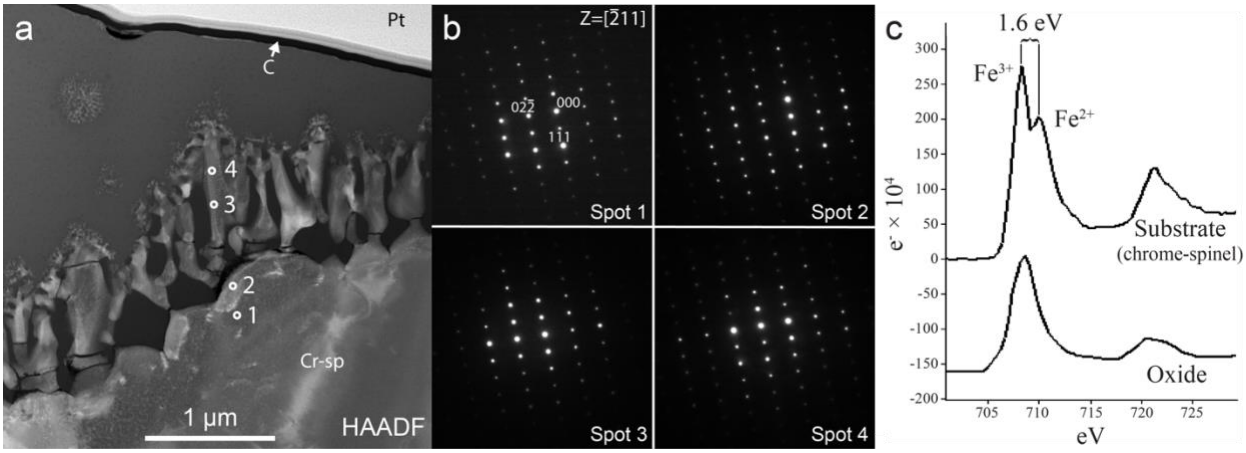

Figure 3.6. Characterization of iron oxide laths in rim on Inclusion 6 from Grain 1. a) HAADF STEM image of rim with locations indicated from which diffraction patterns were collected. b) Diffraction patterns of the surrounding chrome-spinel (spots 1 and 2) and one of the FeO_x laths (spots 3 and 4). c) EEL spectra from the oxide (FeO_x lath) and the chrome-spinel substrate adjacent to the oxide.

Inclusions 2a and 2b

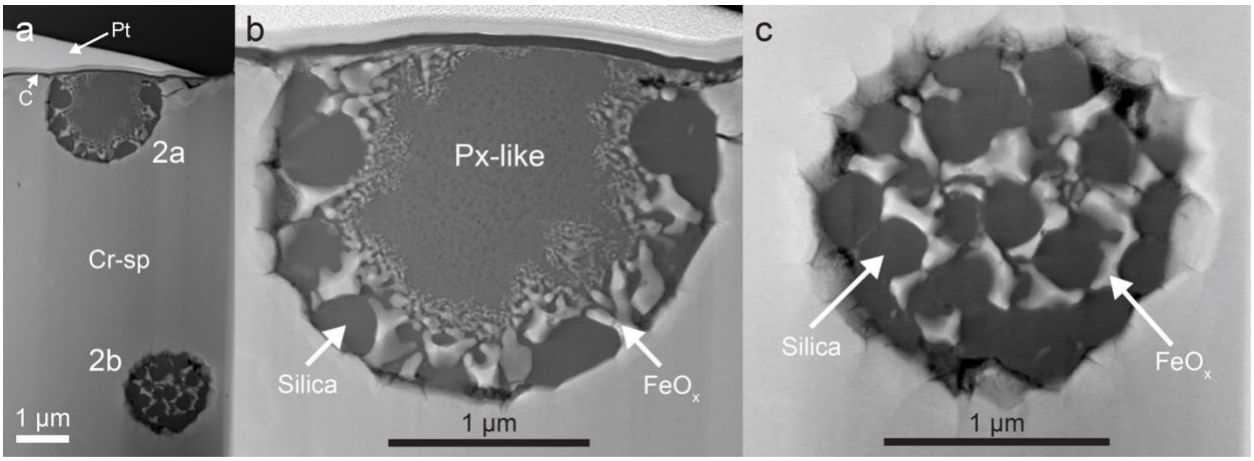

Figure 3.7. HAADF STEM images of a) the FIB section through Inclusions 2a and 2b in Grain 1, b) higher magnification image of Inclusion 2a, and c) higher magnification image of Inclusion 2b. The inclusions are surrounded by host chrome-spinel. Inclusion 2a was thinned to approximately its center, resulting in thinning of Inclusion 2b until only the edge remained.

The second FIB section of Grain 1 contained two inclusions, one below the original polished surface of the grain. Inclusion 2a was circular on the grain surface with an approximate diameter of 2.5 µm (Fig. 3.4) and a depth of ~1.7 µm in FIB cross section (Fig. 3.7). Inclusion 2a has a central amorphous area with a pyroxene-like composition $Ca_{0.8}$ $Mg_{6.2}$ $Fe_{4.2}$ $Mn_{0.5}$ $Ti_{1.3}$ $V_{0.4}$ $Al_{5.8}$ $Si_{19.2}$ $O_{61.7}$ and a ferrosilite content of 40.3 ± 6.0, which is more iron rich than ordinary-chondrite pyroxenes, and contains an iron oxide and silica rim. Inclusion 2b was discovered below the surface of Grain 1 during FIB milling, and a section was preserved throughout sample thinning. The cross-section through Inclusion 2b consists entirely of rim-like material because it was thinned until only the edge remained in order to preserve the center of Inclusion 2a within the same section. A series of images taken during FIB sectioning showed that Inclusion 2b had approximately the same maximum diameter as Inclusion 2a and contained a central area with similar texture to the amorphous central area of Inclusion 2a.

Inclusion 1

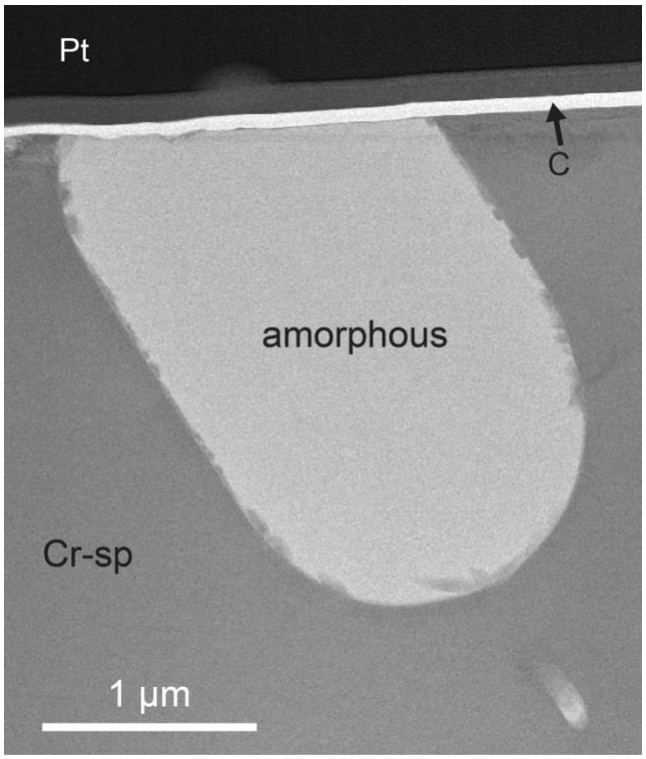

Figure 3.8. Bright field STEM image of the FIB section through Inclusion 1 from Grain 1.

Inclusion 1 from Grain 1 is amorphous with a composition of $Ca_{5.3}\,Fe_{1.4}\,Ti_{3.9}\,Al_{7.5}\,Si_{18.7}\,O_{63.2}$. This inclusion had a circular cross section on the polished surface of the grain and has an elongated area in FIB cross section extending below the original surface (Fig. 3.8). The full dimensions of the sectioned inclusion are estimated as ~1.7 × 3.1 µm. This inclusion contains crystallites of undetermined composition along its edges and lacks the prominent textured rims that Inclusions 6, 2a, and 2b exhibit.

3.4.2 Jurassic Grain 2

Grain 2 has elemental and oxygen-isotope compositions consistent with originating from an ordinary chondrite. The elemental composition indicates an L chondrite origin and the oxygen isotopes suggest an L or LL chondrite origin (Caplan et al., in prep). The majority of the grain surface is well-polished and solid. There are three inclusions exposed on the polished surface of this grain. A rim of alteration, which is cracked and porous on the outside of the grain, appears darker in backscattered-electron (BSE) imaging, and there are some incursions of alteration towards the center of the grain (Fig. 3.9b). Some of these altered regions appear to have

encompassed the three inclusions. A single FIB section (location shown as black line, Fig. 3.9a) that passes through Inclusion 1 and 2 was extracted for TEM analysis.

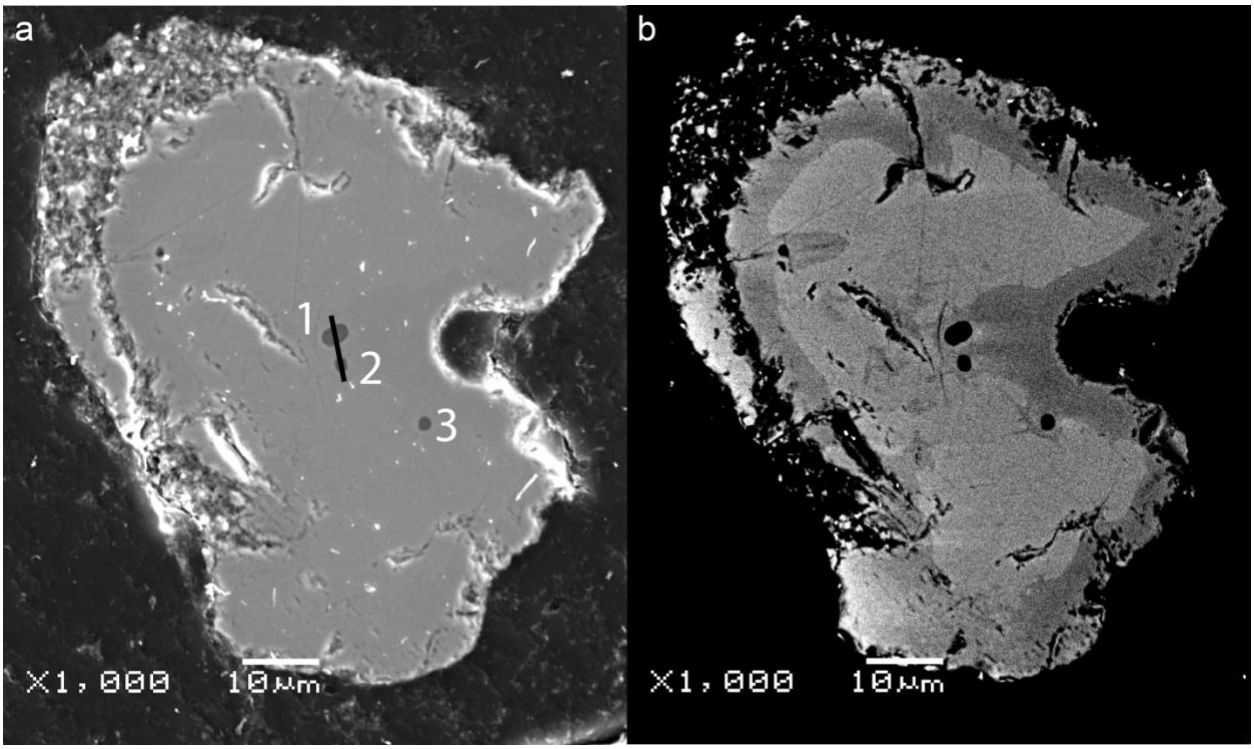

Figure 3.9. Imaging of Grain 2 by a) SE and b) backscattered-electron (BSE) imaging. Contrast was adjusted in the BSE image to reveal dark areas of alteration at the rim and small dark patches throughout the grain. Three inclusions can be seen in this polished surface. The dark alteration rims encompass the inclusions. The location of the FIB section extracted from this grain is indicated by a black line in a).

Inclusions 1 and 2

The two inclusions from Grain 2 are crystalline and have pyroxene compositions of $Ca_{0.1}$ $Mg_{15.8}$ $Fe_{3.8}$ $Mn_{0.1}$ Ti_{d} $Cr_{0.1}$ $Si_{20.0}$ $O_{60.0}$ (d=detected; uncertainty is too high to quantify) for Inclusion 1 and $Ca_{0.1}$ $Mg_{15.9}$ $Fe_{3.5}$ $Mn_{0.1}$ $Cr_{0.1}$ $Si_{20.2}$ $O_{60.1}$ for Inclusion 2. The ferrosilite contents are 19.2 ± 2.0 and 18.1 ± 1.9, respectively. Both compositions are within the ranges of ordinary chondrite pyroxenes. Inclusion 1 had an ovoid cross section of ~2.3 x 3.8 µm on the polished grain surface (Fig. 3.9) and an elongated shape in FIB section with a depth of ~1.8 µm that was truncated by the polished surface (Fig. 3.10). Inclusion 2 had a smaller ovoid shape of ~1.5 x 1.9 µm on the polished surface and a similar depth in FIB cross-section to Inclusion 1.

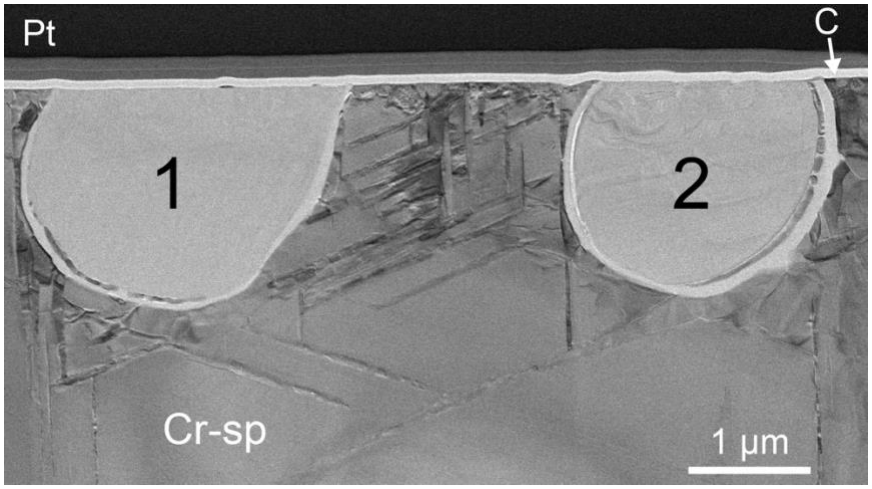

Figure 3.10. Bright-field STEM image of the FIB section through Inclusions 1 and 2 in Grain 2. The apparent texture in Inclusion 2 is due to slight bending of the crystal in the thin FIB section. Each inclusion contains rims of FeO_x (darker grey) and silica (lighter grey).

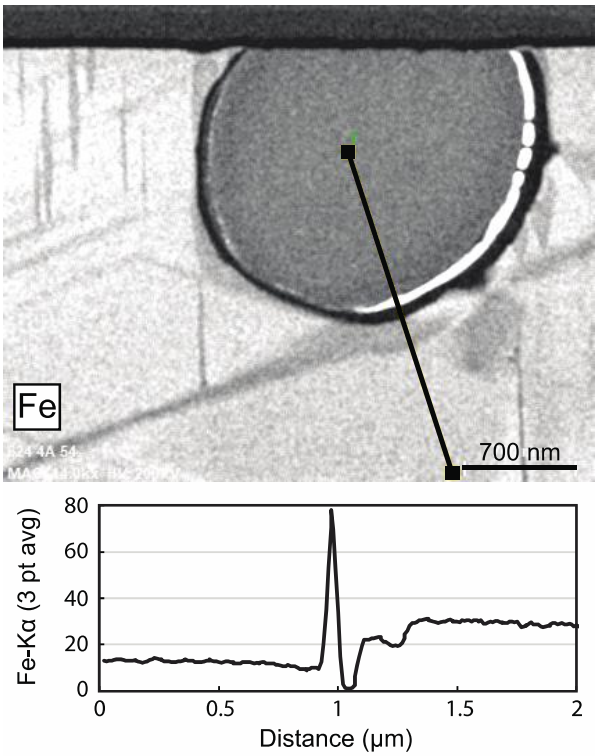

Figure 3.11. SEM-EDS map of Fe-Kα (top) and Fe-Kα line scan (bottom) extracted from the map and crossing from the interior of Inclusion 2 into the surrounding chrome-spinel of Grain 2. Pixel intensity correlates with Fe content, so the silica rim appears black, and the iron oxide rim appears white in the STEM-EDS map.

The inclusions from Grain 2 have rims of iron oxide (dark grey in BF images) and silica (light grey) (Fig. 3.10). The silica rims surround each inclusion, whereas the iron oxide rims are discontinuous. The rim of Inclusion 2 is thicker than that of Inclusion 1. An SEM-EDS map of Fe-Kα was collected using the UH FIB-SEM to examine the relationship of the rim to the inclusion. An Fe-Kα line scan was extracted from the map. The line scan begins at the center of the inclusion and ends in the surrounding chrome-spinel (Fig. 3.11). The scan shows a slight depletion of Fe within the inclusion approaching the iron oxide rim (at a distance of ~0.75-0.9 µm from the start). The Fe peaks in the FeO_x rim and drops to nearly zero in the silica rim. The decrease in Fe at around 1.25 µm coincides with one of the TiO_2-rich lamellae in the chrome-spinel (see below).

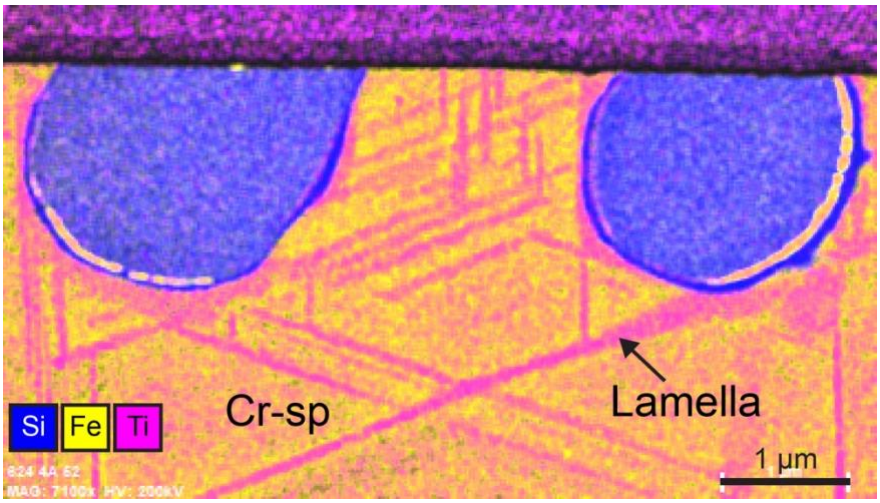

Figure 3.12. Overlaid STEM-EDS element maps of Si (blue), Fe (yellow), and Ti (magenta) in Inclusions 1 and 2 in Grain 2 with surrounding chrome-spinel. The inclusions are Si-rich with two-layer rims that are Fe-rich (discontinuous) and Si-dominant, respectively. The chrome-spinel contains lamellae of Ti-rich chrome-spinel.

Table 3.1. Element compositions (wt%) of the lamella and surrounding chrome-spinel (Cr-sp) in Grain 2 obtained by STEM-EDS.

Location	MgO	Al_2O_3	TiO_2	V_2O_3	Cr_2O_3	MnO	FeO	Total
Lamella	0.3	4.6	8.0	n.d.	70.8	n.d.	16.3	100.0
Cr-sp	1.6	5.3	2.4	n.d.	67.0	n.d.	23.7	100.0

Assumes oxygen is present in stoichiometric abundances for each oxide.
Some elements were not detected or below detection limits (n.d.).

The chrome-spinel exhibits a distinct exsolution texture in the vicinity of the silicate inclusions in the Grain 2 FIB section. The STEM-EDS map of the FIB section (Fig. 3.12) shows lamellae that are Ti-enriched and surrounding Fe-enriched chrome-spinel (Table 3.1). These lamellae are concentrated around the inclusions and do not extend throughout the host chrome-spinel grain. Diffraction patterns of the chrome-spinel and two almost-orthogonal lamellae were collected in order to explore the relationship between the lamellae and host spinel. The three patterns show that all three locations have spinel structure, but the surrounding chrome-spinel (spot 1) and the lamellae (spots 2 and 3) have different crystal orientations (Fig. 3.13). The two lamellae observed also have different crystal orientations relative to one another.

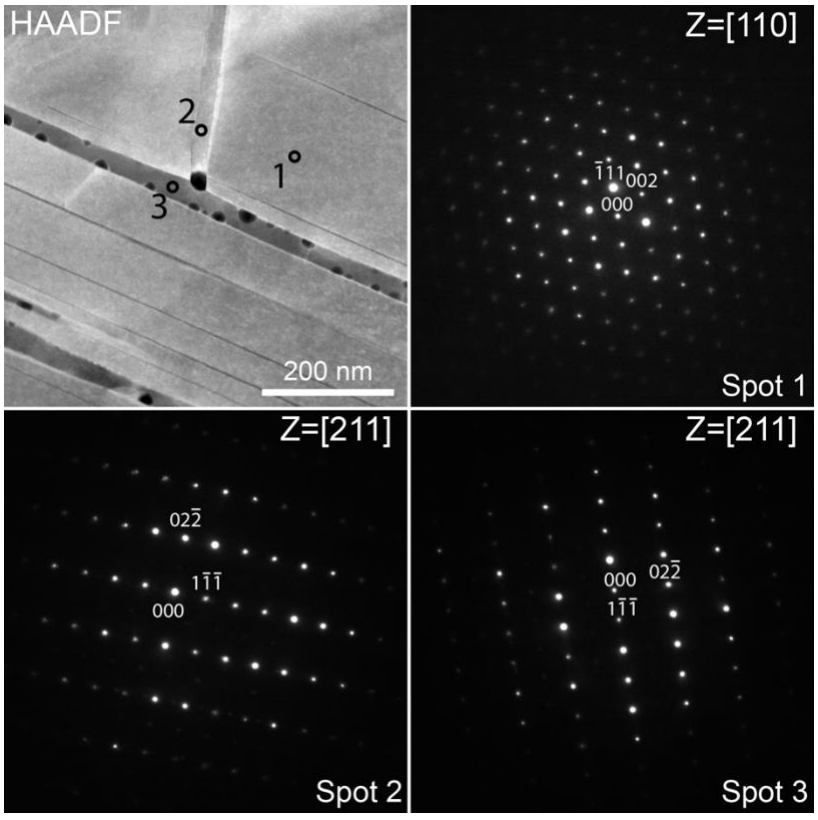

Figure 3.13. Diffraction patterns from two lamellae (spots 2 and 3) and surrounding chrome-spinel (spot 1). The lamellae analyzed are located below the lower right edge of Inclusion 1 in Fig. 3.10. The dark regions in the lamella containing spot 3 are most likely voids.

3.4.3 Jurassic Grain 3

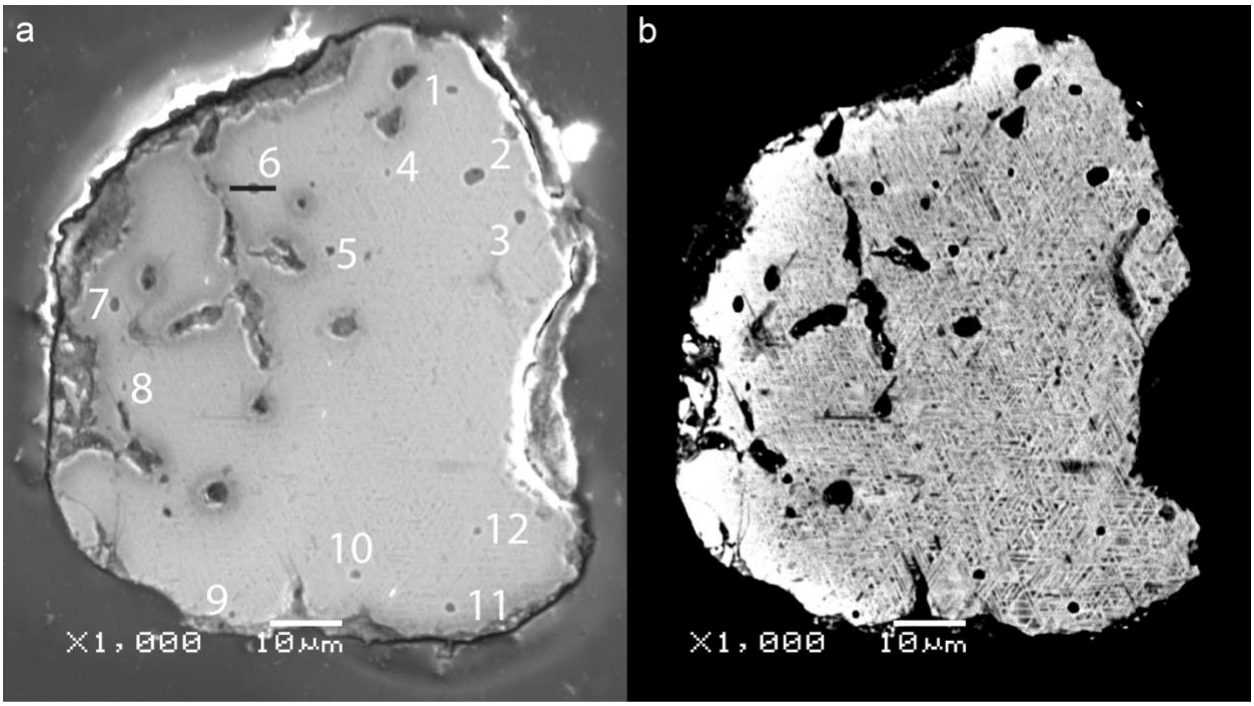

Figure 3.14. Imaging of Grain 3 by a) SE and b) BSE. Twelve inclusions can be seen in this polished surface. The unlabeled features on the grain surface are cracks and holes. A black line indicates the location of the extracted FIB section. The high contrast BSE image shows that this grain has exsolution lamellae throughout.

Grain 3 is very Fe-rich, and has an oxygen-isotope composition consistent with an H-chondrite or terrestrial origin (Caplan et al., in prep). The composition of Grain 3 is unlike most of the grains in this study. Electron microprobe analyses show that Grains 1 and 2 have lower Fe content and no Fe_2O_3, whereas Grain 3 has much higher Fe content with a large portion assignable as Fe_2O_3, or Fe^{3+} (Table 3.2). The Fe content of this grain may be related to the geometric exsolution pattern observed on the polished surface (Fig. 3.14b). The grain is generally coherent with some holes and cracks throughout. This surface reveals 12 inclusions. A single FIB section was extracted from this grain through Inclusion 6 for TEM analysis.

Table 3.2. The average element compositions (wt%) of the Jurassic chrome-spinel grains obtained by electron microprobe.

Grain	MgO	Al_2O_3	TiO_2	V_2O_3	Cr_2O_3	MnO	FeO	Fe_2O_3	ZnO	Total
1	3.1	6.1	3.2	0.7	55.2	0.5	29.1	0.0	0.2	98.2
2	2.5	5.7	2.7	0.7	57.0	0.7	28.3	0.0	0.8	98.4
3	2.9	6.8	3.2	0.8	27.9	0.2	31.2	22.0	0.1	95.2

Absolute errors (2SD) are ± 1 wt% for MgO, Al_2O_3, Cr_2O_3, FeO, and Fe_2O_3, ± 0.1 wt% for TiO_2, and ± 0.04 wt% for V_2O_3, MnO, and ZnO.

Inclusion 6

Inclusion 6 has a subhedral shape and an amorphous texture. It had a circular shape on the grain surface with a diameter of ~1.5 μm (Fig. 3.14) and a depth of ~1 μm in FIB section (Fig. 3.15). This inclusion contains regions with two different compositions. Area 1 has a composition of $F_{9.8}$ $Mg_{13.1}$ $Na_{2.3}$ $K_{1.9}$ $Al_{4.6}$ $Si_{15.4}$ $O_{52.9}$. Area 2 has a composition of $Al_{1.4}$ $Si_{32.2}$ $O_{66.4}$ consistent with silica. The interior structure of this inclusion is unique compared to the inclusions from Grains 1 and 2 because it does not exhibit distinct FeO_x rims.

The shapes of the inclusions in Grain 3 are also different than those from Grains 1 and 2. Inclusions from Grain 3 have flat faces that are defined by the chrome-spinel lamellae (Fig. 3.16), unlike the rounded (anhedral) shapes of the inclusions in the other grains. Linear edges of the inclusions in this grain are often aligned with the lamellae in the chrome-spinel (Fig. 3.16). Inclusion 11 shows the most prominent alignment of euhedral edges with many neighboring lamellae. Inclusion 6 has subhedral edges that also align with some surrounding lamellae. The image of the FIB cross section of Inclusion 6 (Fig. 3.15) also shows the same subhedral edges and lamellae alignments as those in the FIB-SEM image taken from the polished top surface (Fig. 3.16).

Unlike Grain 2 (Figs. 3.10-3.12), the lamellae in Grain 3 are a feature of the entire chrome-spinel grain, not just the region around the inclusion. These lamellae are Fe-rich, and the remaining chrome-spinel has higher concentrations of Cr, Al, and Mg compared to the lamellae (Figs. 3.17-3.18, Table 3.3).

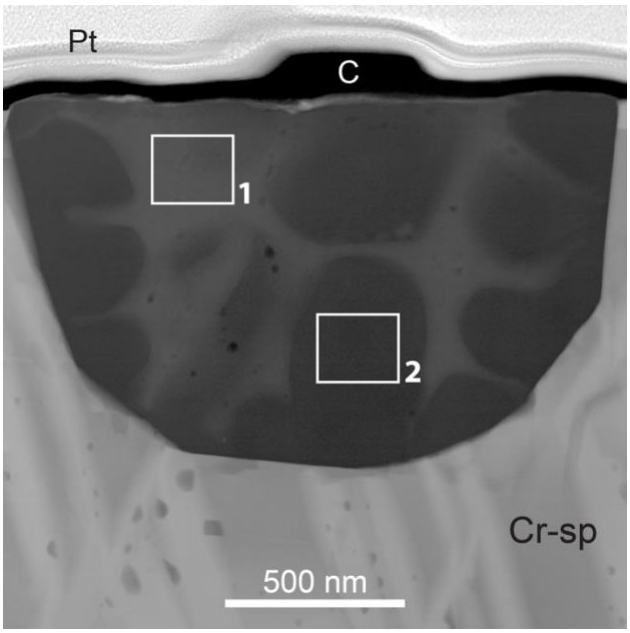

Figure 3.15. HAADF STEM image of the FIB section through Inclusion 6 in Grain 3. The inclusion contains areas of two different compositions. Representative areas of each are indicated. Area 1 appears is lighter grey and Area 2 appears is darker grey.

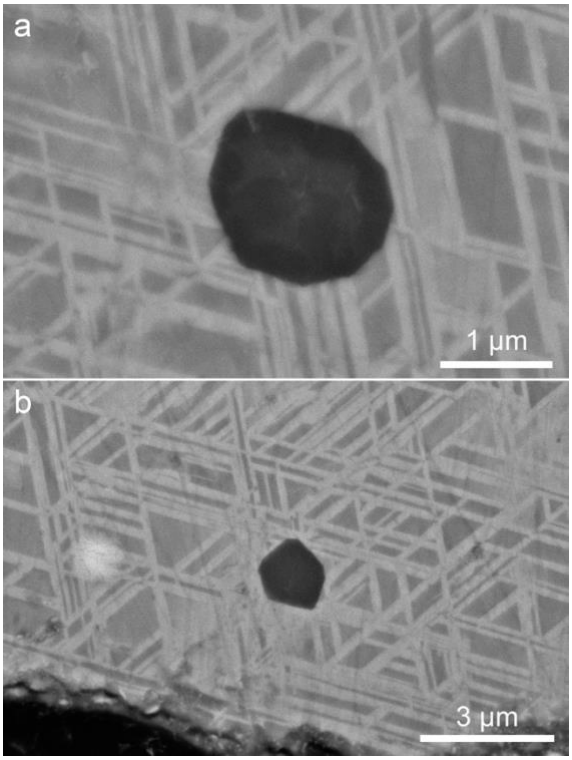

Figure 3.16. BSE images of the polished surface of Jurassic Grain 3 showing a) Inclusion 6 and b) Inclusion 11. Note that the orientations of the inclusions' edges often align with the lamellae directions in the chrome-spinel.

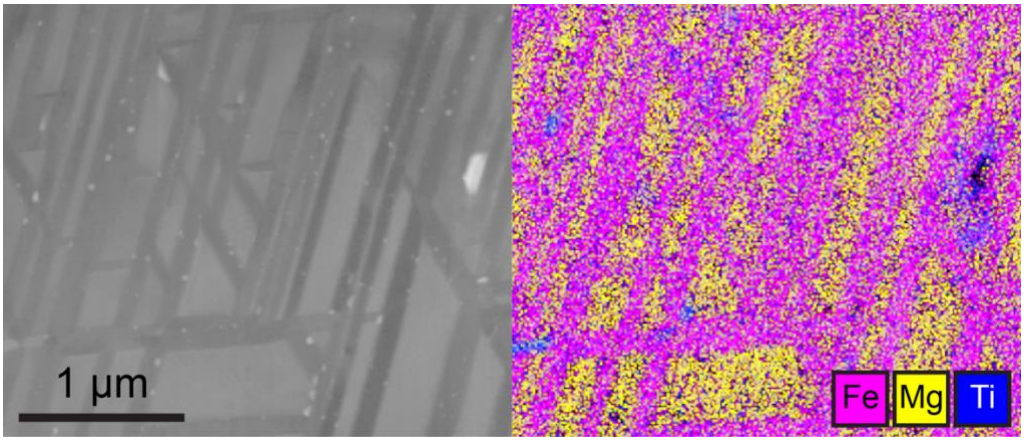

Figure 3.17. Lamellae in Jurassic Grain 3. (Left) Bright field image and (Right) corresponding overlaid element maps of Fe (magenta), Mg (yellow), and Ti (blue), collected by SEM-EDS on the FIB section containing Inclusions 6.

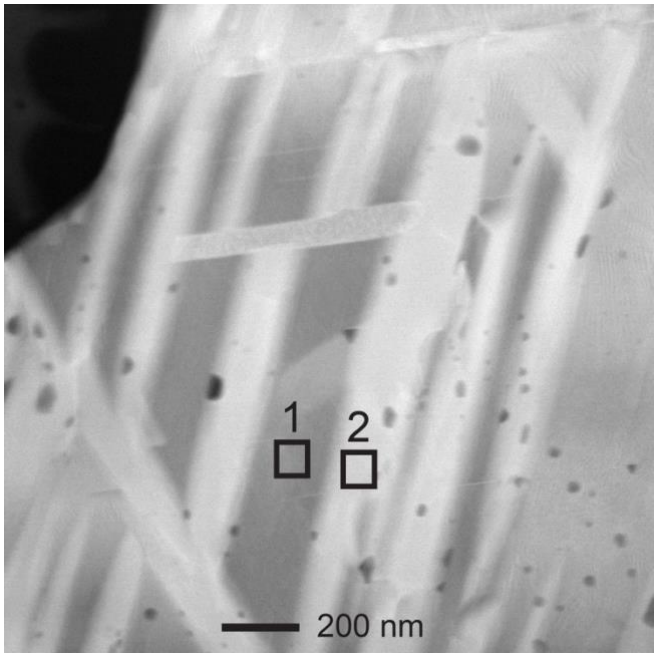

Figure 3.18. HAADF STEM image of Jurassic Grain 3 chrome-spinel lamellae (2) and surrounding chrome-spinel (1) near Inclusion 6. Compositions in Table 3.3 show that the lamellae are Fe-enriched compared to the host chrome-spinel.

Table 3.3. Element compositions (wt%) for Jurassic Grain 3 chrome-spinel lamellae (Area 2) and surrounding chrome-spinel (Area 1) obtained by STEM-EDS.

Area	MgO	Al_2O_3	TiO_2	V_2O_3	Cr_2O_3	MnO	FeO	Total
1	9.5	20.9	2.1	n.d.	42.5	4.5	20.5	100.0
2	n.d.	2.8	2.9	1.5	26.9	n.d.	66.0	100.0

Assumes oxygen is present in stoichiometric abundances for each oxide.
Some elements were not detected or below detection limits (n.d.).

3.4.3 Brunflo Grain

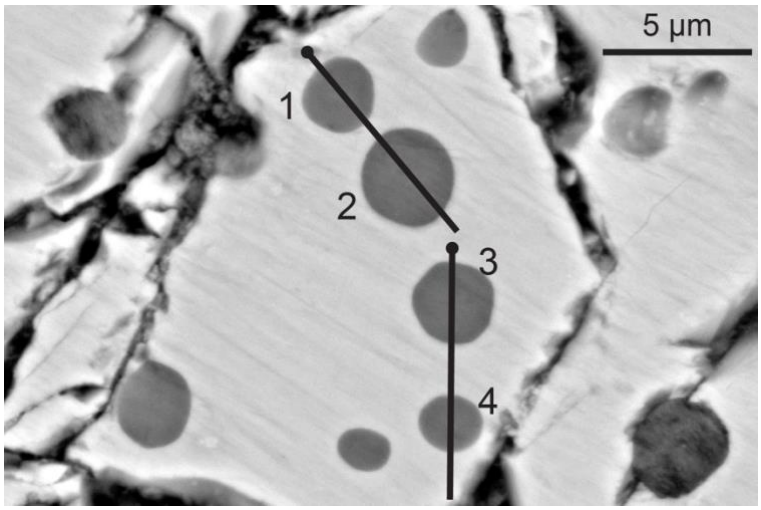

Figure 3.19. Backscatter electron image of olivine inclusions in a chrome-spinel grain from the Brunflo meteorite. The black lines represent locations of spectral line scans of inclusion pairs and surrounding chrome-spinel. The dots indicate the beginning of each line scan for data shown in Fig. 3.20.

A chrome-spinel grain from the Brunflo meteorite enables analysis of larger inclusions and inclusions that are not aqueously altered. The Brunflo meteorite was originally thought be an H-chondrite (Thorslund et al., 1984), but a study by Alwmark and Schmitz (2009b) shows that the fossil meteorite is an L-chondrite, based on chondrule sizes and the TiO_2 content of the chrome-spinels. Heck et al. (2010) showed that the oxygen isotopic composition is L-chondritic. The chrome-spinel used in our study contained many olivine and high-Ca-pyroxene inclusions. Four olivine inclusions with varying diameters were chosen for further analysis (Fig. 3.19). The olivine inclusions are roughly circular on the grain surface, with approximate diameters of 2.4 µm, 3.2 µm, 2.8 µm, and 1.9 µm (Fig. 3.19).

SEM-EDS point spectra were taken for the olivine inclusions before FIB-sectioning (Table 3.4). All of the inclusions contain Cr_2O_3, with the smallest inclusions having the largest Cr_2O_3 values. Similarly, the smallest inclusions are the only ones with Al_2O_3 and TiO_2. The fayalite contents of the four olivines were 26.0, 20.6, 20.7 and 24.4 (± 1), respectively. The fayalite contents of the largest inclusions (2 and 3) agree with the published fayalite value for the olivine inclusions in the Brunflo chrome-spinel (21.3 ± 1; Alwmark and Schmitz, 2009a). Inclusions 2 and 3 also have very similar oxide compositions to the published Brunflo olivine compositions. The two smaller inclusions of these measurements have higher Fa contents than the published contents of Brunflo olivine inclusions.

Table 3.4. Element compositions (wt %) of olivine inclusions from Brunflo grain measured by SEM-EDS.

Inclusion	MgO	Al_2O_3	TiO_2	V_2O_3	Cr_2O_3	MnO	FeO	SiO_2	Total	% Fa
1	31.9	1.6	0.8	0.2	17.8	0.5	20.0	27.0	100.0	26.0 ± 1.0
2	40.1	n.d.	n.d.	n.d.	2.3	0.5	18.6	38.5	100.0	20.6 ± 1.0
3	40.0	n.d.	n.d.	n.d.	2.5	0.5	18.6	38.5	100.0	20.7 ± 1.0
4	34.2	1.5	0.6	n.d.	13.7	0.5	19.6	29.8	100.0	24.4 ± 1.0

Assumes oxygen is present in stoichiometric abundances for each oxide.
Some elements were not detected or below detection limits (n.d.).

Line scans were also collected on the olivine inclusions using SEM-EDS before FIB-sectioning. The first scan crossed Inclusions 1 and 2 and the second scan crossed Inclusions 3 and 4 (Fig. 3.19 and 3.20). The line scans show a decrease in Cr and increase in Si content at the inclusion boundaries (Fig. 3.20). The centers of Inclusions 2 and 3 show a plateau ("bottoming out") with low Cr K-α X-ray counts. The Cr signal in the centers of these inclusions are likely due to a small amount of Cr present in the inclusions. The other two inclusions (1 and 4) show higher counts of Cr at their center compared to Inclusions 2 and 3, and the Cr signals do not "bottom out".

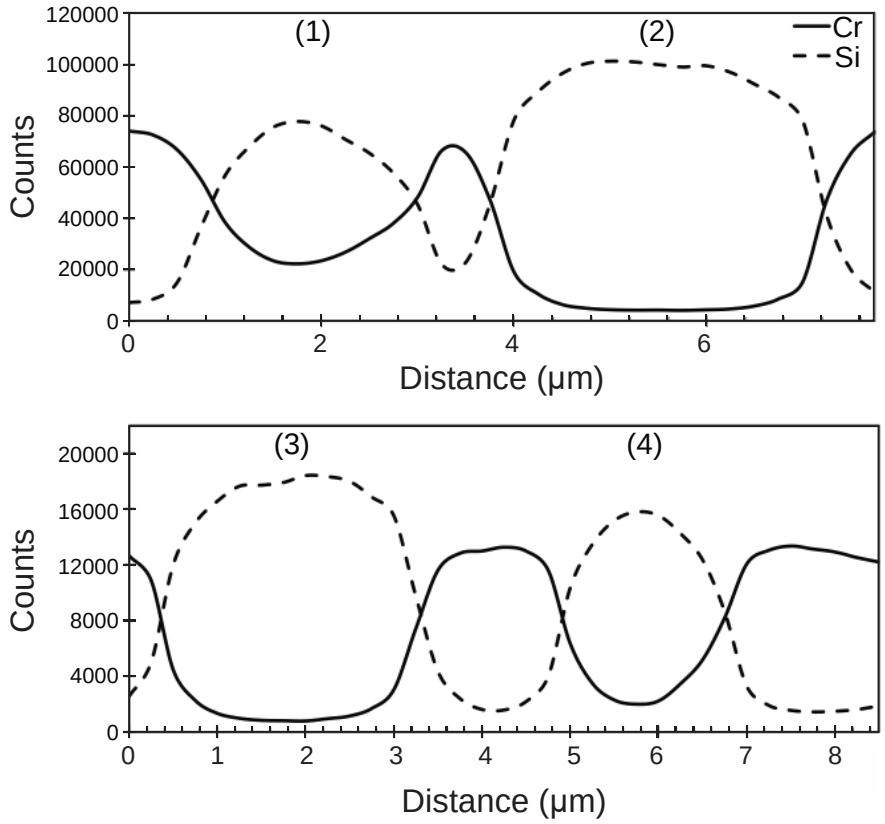

Figure 3.20. Cr and Si K-α X-ray signal from SEM-EDS line scans as a proxy for Cr and Si content in olivines 1 and 2 (top) and olivines 3 and 4 (bottom). The zero point of the distance axis corresponds to the black dot on the end of each line in Fig. 3.19.

The FIB section extracted from the Brunflo chrome-spinel grain contains olivine Inclusions 1 and 2 (Fig. 3.21). These inclusions were chosen because they are above and below the 3μm limitation and they are in close proximity to one another. Inclusion 1 is shallow with a depth of ~0.6 μm at the center of the inclusion's polished surface. Inclusion 2 is deeper with a rounded conical shape and has a maximum depth of ~4.0 μm in FIB cross section. Inclusions 3 and 4 were destroyed during the FIB section creation of Inclusions 1 and 2, but Inclusion 3 was observed during the process. The thick FIB section shows the cross section of Inclusion 3 where the SEM-EDS measurement was taken (center at the surface) (Fig. 3.22). The depth of Inclusion 3 at that location was 2.9 μm, which is greater than the minimum depth assumed for the interaction volume (2 μm; Alwmark and Schmitz, 2009a). Comparing Inclusions 1 and 2 at the intermediate step of the section preparation in Fig. 3.22 to the final section in Fig. 3.21 also illustrates how the shapes of the inclusions change in cross-section.

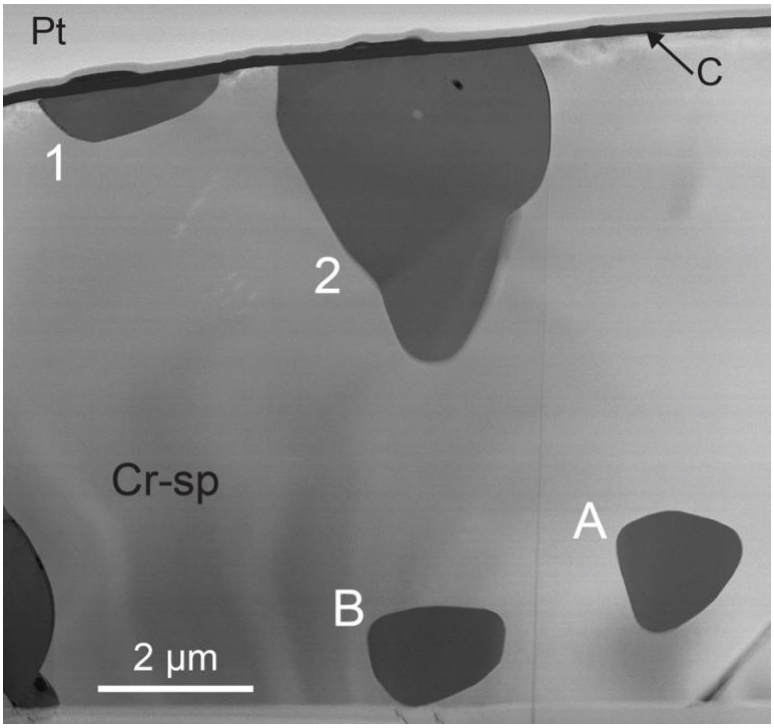

Figure 3.21. HAADF image of the Brunflo chrome-spinel FIB section with olivine Inclusions 1 and 2. Two additional inclusions were found below the olivine inclusions (Inclusions A and B).

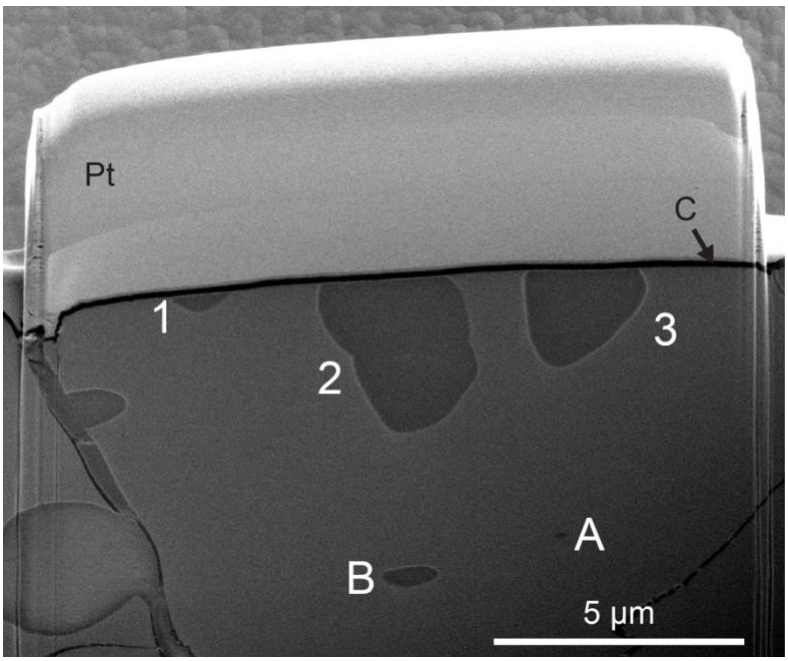

Figure 3.22. SE image of Brunflo FIB section before lift out (approximately 2 microns thick). Section shows three of the main olivine inclusions from Fig. 3.19 and two additional small inclusions (A and B) below. This section shows an intermediate stage of the FIB section preparation. Note that the scale bar is only accurate in the horizontal dimension because the image was acquired with the sample tilted ~53°.

STEM-EDS measurements give compositions for Inclusions 1 and 2 that are similar to each other with fayalite contents of 18.7 ± 2.0 and 20.7 ± 2.1, respectively. There are two subhedral inclusions that were discovered below the targeted olivine inclusions while the FIB section was being made. These additional inclusions (A and B) have high-Ca pyroxene compositions based on STEM-EDS measurements (Table 3.5). The maximum dimension of each inclusion is ~1.6 μm and ~1.7 μm, respectively. The inclusions in this FIB section do not show rims, unlike the inclusions found in the Jurassic chrome-spinel grains.

Table 3.5. Element compositions (wt %) of olivine (1 and 2) and high-Ca pyroxene (A and B) inclusions in Brunflo grain determined by STEM-EDS.

Inclusion	MgO	Cr_2O_3	MnO	FeO	SiO_2	CaO	Total	% Fa	
1	42.6	0.3	0.5	17.5	39.1	n.d.	100.0	18.7	± 2.0
2	41.4	0.2	0.5	19.3	38.7	n.d.	100.0	20.7	± 2.1
A	17.3	1.4	n.d.	3.4	57.4	20.5	100.0	10.0	± 5.0
B	18.2	1.0	n.d.	3.3	57.1	20.4	100.0	9.3	± 4.6

Assumes oxygen is present in stoichiometric abundances for each oxide.
Some elements were not detected or below detection limits (n.d.).

3.5 Discussion

The goal of using FIB/STEM techniques is to collect reliable compositions of small inclusions to help determine the parent meteorite type of the host grain. This study also shows the limits of SEM-EDS with small inclusions by comparing to STEM-EDS measurements. FIB techniques made it possible to collect compositions for smaller inclusions, but it also uncovered inclusion rims and evidence of alteration, and chrome-spinel lamellae, that we would not have observed otherwise.

3.5.1 SEM-EDS versus STEM-EDS

SEM-EDS measurements on an inclusion may include some signal from the surrounding chrome-spinel if the inclusion is smaller than the interaction volume of the electron beam. STEM-EDS analysis circumvents this issue because the FIB section used for STEM is so thin that the interaction volume is greatly reduced. FIB/STEM techniques can give reliable compositions for small inclusions because it eliminates fluorescence of host material.

We can test the reliability and limits of SEM-EDS measurements based on inclusion surface diameter by comparing SEM-EDS spectra and STEM-EDS spectra. Inclusions from the Brunflo fossil meteorite were chosen to evaluate the reliability of SEM-EDS data. Previous work using 15 kV accelerating voltage has shown that sufficiently large inclusions (>3 μm) of olivine from Brunflo chrome-spinel grains can be measured by SEM-EDS without fluorescing surrounding chrome-spinel and that smaller inclusions (1.5 – 3 μm) would need to be corrected for fluorescence of the surrounding chrome-spinel (Alwmark and Schmitz, 2009a). These authors also assumed that the approximate penetration depth of the measurement is 2 μm. Because accelerating voltage affects the interaction volume of a measurement, we used the same accelerating voltage (15 kV) as Alwmark and Schmitz (2009a) to ensure the same approximate penetration depth and enable comparison with their results. We selected four Brunflo olivine inclusions for SEM-EDS line scans and point analyses with surface diameters larger and smaller than the minimum size inferred to be necessary for a reliable analysis (Fig. 3.19-3.20). The initial SEM-EDS measurements for Inclusions 2 and 3, with diameters of 3.2 μm and 2.8 μm, respectively, gave fayalite values that agreed with the published composition for Brunflo olivine inclusions from Alwmark and Schmitz (2009a). Inclusions 1 and 4, with diameters of 2.4 μm and 1.9 μm, had much higher fayalite values. The higher fayalite values from SEM-EDS measurements for Inclusions 1 and 4 are most likely due to the inclusions being smaller than the interaction volume of the measurement, and subsequent STEM-EDS measurements show this to be the case. Two olivine inclusions, one large (Inclusion 2) and one small (Inclusion 1), were chosen for FIB sectioning.

The compositions obtained for Inclusions 1 and 2 using SEM-EDS and STEM-EDS are compared in Table 3.6. The measurements of the two inclusions by STEM-EDS gave compositions and fayalite values within errors of one another. The compositions obtained by SEM-EDS and STEM-EDS for the larger inclusion, Brunflo Inclusion 2, are very similar, indicating that Inclusion 2 is sufficiently large to give data that can be used to classify the host meteorite. SEM-EDS and STEM-EDS measurements give significantly different compositions for Brunflo Inclusion 1. The high Cr content and lower abundances of Mg and Si in the SEM-EDS measurement indicate significant fluorescence of surrounding chrome-spinel. Inclusion 1 is clearly smaller than the interaction volume of the SEM electron beam, as confirmed by the FIB cross-section in Fig. 3.21. The difference between the SEM-EDS and STEM-EDS measurements

of Inclusion 1 also suggest that Al, Ti, and V abundances arise from the fluorescence of surrounding chrome-spinel and are not naturally occurring elements in the olivine inclusions.

Our results generally confirm the results of Alwmark and Schmitz (2009a) and indicate that inclusions >3 μm in diameter should be large enough to give reliable SEM analyses when using a 15 kV accelerating voltage. However, non-spherical inclusion shapes, such as we observed in Figures 3.19, 3.21 and 3.22, and the arbitrary thickness at which an inclusion is terminated by the polished surface indicate that this may not always be the case. Inclusion 1 has a larger size of 2.4 μm diameter at the polished surface than Inclusion 4 at 1.9 μm diameter. If we assume all four inclusions have very similar compositions, as expected based on their proximity and consistent with the similarities in Inclusions 2 and 3 by SEM-EDS and in Inclusions 1 and 2 by STEM-EDS, then Cr content can be used as an indicator of the degree of contamination by surrounding chrome-spinel in the SEM-EDS measurement. The Cr content measured by SEM-EDS in Inclusion 1 is higher than in Inclusion 4 and thus corresponds to more contribution from surrounding chrome-spinel, which indicates that Inclusion 1 likely extends to a shallower depth below the polished surface than Inclusion 4 despite the larger diameter of Inclusion 1 at the surface.

To address the complications of non-spherical inclusion shapes and unknown inclusion depths, SEM-EDS line scans of the Brunflo olivine inclusions were collected before FIB sectioning to see if line scans can be used to evaluate whether an inclusion is large enough, and deep enough, for reliable SEM-EDS measurements. An inclusion with dimensions larger than the electron-beam interaction volume would "bottom out", reaching a plateau (even if non-zero), of an element that should be in low abundance in the inclusion but in high abundance in the host material, e.g. Cr in the host chrome-spinel grains (Fig. 3.23a). At the other extreme, if there is significant Cr in the inclusion line scan and the Cr level in the line scan does not plateau, then the inclusion is most likely smaller than the interaction volume and surrounding chrome-spinel has contributed to the measurement (Fig. 3.23c).

Table 3.6. Element composition (wt%) comparisons of SEM-EDS and STEM-EDS measurements for olivine inclusions (1 and 2) in Brunflo grain.

Measurement	MgO	Al_2O_3	TiO_2	V_2O_3	Cr_2O_3	MnO	FeO	SiO_2	Total	% Fa	
Inclusion 1											
SEM	31.9	1.6	0.8	0.2	17.8	0.5	20.0	27.0	100.0	26.0	± 1.0
STEM	42.6	n.d.	n.d.	n.d.	0.3	0.5	17.5	39.1	100.0	18.7	± 2.0
Inclusion 2											
SEM	40.1	n.d.	n.d.	n.d.	2.3	0.5	18.6	38.5	100.0	20.6	± 1.0
STEM	41.4	n.d.	n.d.	n.d.	0.2	0.5	19.3	38.7	100.0	20.7	± 2.1

Assumes oxygen is present in stoichiometric abundances for each oxide.
Some elements were not detected or below detection limits (n.d.).

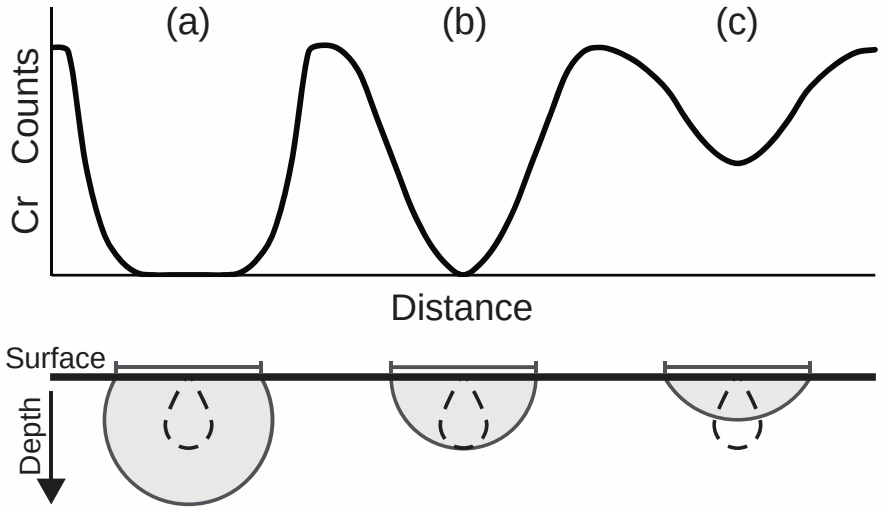

Figure 3.23. Hypothetical line scans of inclusions (grey shaded objects in bottom panel) with the same diameter at the surface but with varying depths in the chrome-spinel host grain. The electron-beam interaction volume is shown by the black dashes. The resulting line scans of Cr content in the top panel assume the inclusions are Cr-free. Inclusions (a), (b), and (c) have depths greater than, approximately equal to, and less than the interaction volume, respectively.

3.5.2 Compositions of Jurassic Inclusions

Inclusions from three Jurassic grains were studied by SEM-EDS and STEM-EDS. These Jurassic grains have ordinary chondrite chrome-spinel compositions, but the subtypes (H, L, or LL) could not be determined based on chemistry and oxygen isotopes alone. The inclusions from

Grain 1 have amorphous textures with either pyroxene-like compositions (Inclusions 6 and 2a) or a plagioclase-like composition (Inclusion 1). The inclusion from Grain 3 (Inclusion 1) contains two silicate compositions that are unlike the discriminatory minerals used to help classify a parent meteorite type. Grain 2 inclusions have crystalline textures and pyroxene compositions. Ferrosilite contents were higher in the SEM-EDS measurements for all pyroxene-like inclusions due to the fluorescence of surrounding chrome-spinel (Table 3.7). STEM techniques were necessary for the inclusions in the Jurassic grains because the inclusions were too small for reliable SEM measurements.

Table 3.7. Element composition (wt%) comparisons of SEM-EDS and STEM-EDS measurements for inclusions in the Jurassic grains.

Measurement	MgO	Al_2O_3	TiO_2	V_2O_3	Cr_2O_3	MnO	FeO	SiO_2	CaO	Total	%Fs	
Grain 1 - Incl 6												
SEM	16.9	5.5	2.4	n.d.	2.1	1.8	20.1	51.1	n.d.	100.0	40.0	± 1.0
STEM	20.0	6.4	1.8	0.5	n.d.	1.3	17.6	52.5	n.d.	100.0	33.0	± 4.4
Grain 1 - Incl 2a												
SEM	7.3	11.3	5.6	n.d.	3.5	1.3	19.1	50.8	1.1	100.0	56.9	± 1.0
STEM	11.4	13.3	4.6	1.2	n.d.	1.5	13.7	52.3	2.1	100.0	40.3	± 6.0
Grain 2 - Incl 1												
SEM	27.9	n.d.	n.d.	n.d.	2.7	n.d.	14.2	54.7	0.5	100.0	22.0	± 1.0
STEM	29.8	n.d.	0.1	n.d.	0.3	0.5	12.7	56.4	0.4	100.0	19.2	± 2.0
Grain 2 - Incl 2												
SEM	24.6	0.9	0.8	n.d.	7.7	0.5	15.2	49.7	0.5	100.0	25.4	± 1.0
STEM	30.0	n.d.	n.d.	n.d.	0.2	0.5	11.8	57.1	0.3	100.0	18.1	± 1.9

Assumes oxygen is present in stoichiometric abundances for each oxide.
Some elements were not detected or below detection limits (n.d.).

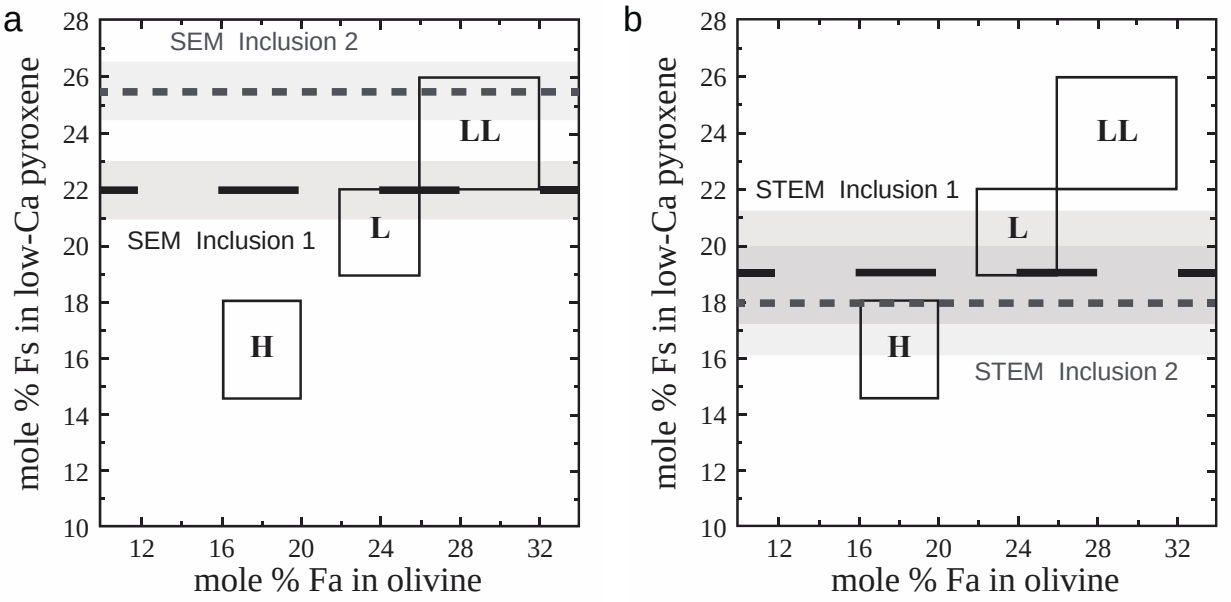

Figure 3.24. Ferrosilite compositions of Inclusions 1 and 2 from Jurassic Grain 2, determined by a) SEM-EDS before FIB sectioning and b) STEM-EDS after FIB thinning. The inclusion compositions are compared to fayalite and ferrosilite compositions for ordinary chondrite silicates. The Fs contents of the SEM-EDS and STEM-EDS measurements suggest different parent meteorite types for the inclusions in Grain 2. The higher Fs content of the SEM-EDS data likely includes the fluorescence of surrounding chrome-spinel.

The two inclusions from Grain 2 have ferrosilite compositions that are within the range of classification for pyroxenes from type 4-6 ordinary chondrites (Fig. 3.24). The SEM-EDS technique gives Fs contents of the inclusions that are not within errors of one another and give a classification of L or LL chondrite (Fig. 3.24a). The STEM-EDS measurement of Grain 2 Inclusion 1 falls just within the bottom of the L-chondrite range (Fs_{19}), and the Inclusion 2 measurement falls at the very top of the H-chondrite range (Fs_{18}) (Fig. 3.24b). The two STEM-EDS measurements are within errors of each other and there is no evidence of fluorescence. The two techniques suggest different parent meteorite classifications. The high Cr_2O_3 contents and higher Fs contents of the SEM-EDS measurements are due to the fluorescence of the surrounding chrome-spinel, which is eliminated by using STEM-EDS.

The Jurassic Grain 2 inclusions show evidence of alteration in the form of rims of iron oxide and silica (Figs. 3.10-3.12). The Fe line scan of Inclusion 2 shows a small depletion of Fe within the inclusion next to the iron oxide rim (Fig. 3.11). This depletion suggests that the Fs content may have been lowered from the L-chondrite range to the H-chondrite range during terrestrial alteration to form the iron oxide rim. The larger inclusion size and smaller iron oxide rim of

Inclusion 1 suggest less Fe loss, on average. Its Fs content is currently just within the L-chondrite range (Fig. 3.24) and its original Fs content may have been slightly higher. The Fs content of Inclusion 1 plus the chemistry and oxygen isotopes of the host chrome-spinel grain indicate that Grain 2 most likely came from an L chondrite.

The inclusions in Jurassic Grains 1 and 3 were too altered to help classify their parent meteorite types. Pyroxene-like inclusions from Grain 1 gave ferrosilite values higher than the range for ordinary chondrite pyroxenes (Inclusion 6 - Fs_{33}; Inclusion 2a – Fs_{40}). The third inclusion (Inclusion 1) from Grain 1 had a plagioclase-like composition, which is not diagnostic for identifying the parent meteorite type. The inclusion from Grain 3 contained two compositions (Fig. 3.15), neither of which were consistent with the diagnostic minerals used for an ordinary chondrite sub-classification. This inclusion showed immiscibility between the two amorphous silicates, demonstrating that inclusions can more complex than indicated by the initial imaging in an SEM.

The discovery of altered inclusions in the Jurassic chrome-spinels was an unexpected find. Most of the inclusions that were uncovered in the Jurassic grains were small (< 3 μm) so FIB/STEM techniques were necessary to obtain reliable compositional information. The small and partially altered inclusions from the Jurassic chrome-spinel grains are unlike the well-preserved large inclusions that are common in Ordovician L-chondrite grains (Alwmark and Schmitz, 2009a). Smaller inclusions were chosen for this work to investigate the limitations of SEM-EDS in characterizing inclusions. The alteration of inclusions in the Jurassic grains is likely due to the extremely condensed limestone in which they were found. This circumstance increases the number of chrome-spinel grains recovered, but it also means the grains have been on the sea floor for a very long time leading to cracks and water penetrating to the inclusions. While the Jurassic inclusions were altered, FIB/STEM techniques are still a valuable tool to uncover artifacts and to provide reliable compositions for small inclusions in grains.

3.5.3 Rims

Rims are observed in most of the silicate inclusions that were sectioned by FIB. It is unlikely that these rims formed while the host chrome-spinels were on the parent bodies. Each of the grains likely originated from a type of ordinary chondrite, most of which are metamorphic rocks with minerals in equilibrium. The rims of these inclusions are unexpected because the iron oxide and silica are not part of an equilibrium assemblage of chondritic minerals. Additionally, we

have not observed these types of inclusion rims in chrome-spinel grains from witnessed ordinary-chondrite falls. Nor do we know of any literature reports of such rimmed inclusions. Alwmark and Schmitz (2009a) reported inclusion rims of this nature in chrome-spinel grains from the Ordovician, but they did not analyze the inclusions in detail. It is likely that rims formed via terrestrial aqueous alteration while the chrome-spinel grains were on the sea floor for millions of years. Rims were less commonly observed in the Ordovician samples. This may be due to the grains chosen, or the Ordovician batch of grains may have been less altered in general compared to Jurassic grains.

We were initially unsure if the rims observed by SEM imaging were inherent to the inclusions or generated by polishing damage, but further analyses with STEM proved that the rims observed in the SEM were chemically distinct and made of iron oxide and silica. Inclusion 6 from Grain 1 has a rim that contains laths of maghemite, which is usually formed under hydrous conditions (Lindsley, 2018). The STEM-EDS Fe map of this rim shows an increase in Fe content from the host chrome-spinel towards the laths (Fig. 3.5). Grain 2 pyroxene inclusions show depletions of Fe next to the iron oxide rims, indicating that the Fe from the inclusions contributed to the rim formation. These observations suggest that Fe was mobile in the host grains and that aqueous fluids likely transported Fe both into and out of the inclusions. This is also supported by the abundance of Fe^{3+} in the host chrome-spinel near the inclusion (Fig. 3.6c). The host chrome-spinel nominally has no Fe^{3+} (Table 3.2), but the occurrence of both Fe^{2+} and Fe^{3+} near the inclusion may be the result of alteration. The confirmation of distinct rims using STEM techniques suggests that is it possible to screen inclusions for alteration rims using high-resolution backscatter-electron imaging (Fig. 3.25).

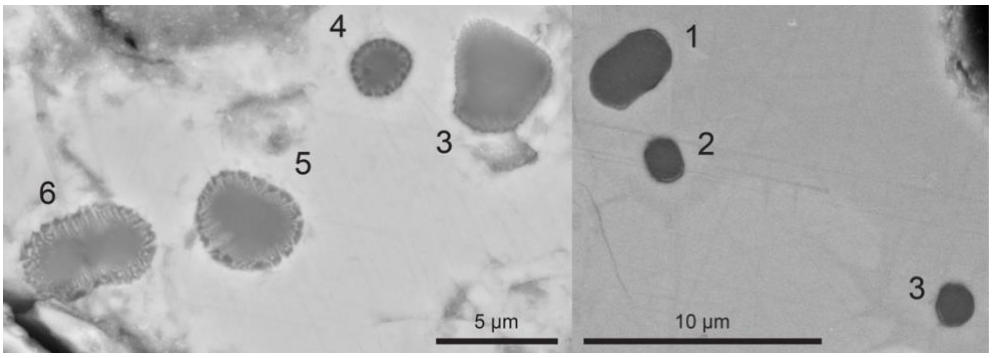

Figure 3.25. FIB-SEM BSE images of inclusions within a) Grain 1 and b) Grain 2. Grain 1 shows sharp structures protruding from the rim towards the center of the inclusions. Grain 2 inclusions have faint, light grey, thin structures that are only seen on part of the inclusions rims.

3.5.4 Lamellae

Exsolution lamellae in the Jurassic chrome-spinel grains were an unexpected find. Lamellae were only observed on the polished surface of two out of 170+ chrome-spinels from the Jurassic study, Grain 3 (Fig. 3.14) and another grain not studied here (Caplan et al., in prep). Additionally, chrome-spinel lamellae have not been reported in sediment-dispersed grains for other time periods. Two of the three FIB-sectioned grains contain lamellae. The FIB section from Grain 2 shows lamellae between the two inclusions and they do not occur far beyond the inclusions (Fig. 3.10 and 3.12). These lamellae are Ti-rich and Fe-poor in composition compared to the surrounding chrome-spinel. Lamellae in Grain 3 were observed throughout the entire grain (Fig. 3.14b) and are Fe-rich compared to the host chrome-spinel (Table 3.3).

Exsolution lamellae form when a host phase unmixes into two phases. Lamellae in chrome-spinels rarely form on Earth, but have been observed in the Giant Nickel mine, British Columbia (Muir and Naldrett, 1973), the Fiskenaesse Complex, Greenland (Ghisler, 1977; Steele et al., 1977), and the Red Lodge district, Montana (Loferski and Lipin, 1983). The grains from the Red Lodge district were either Al-rich with Fe-rich lamellae or Fe-rich with Al-rich lamellae. It was suggested that unmixing occurred around 600°C for the Red Lodge district chrome-spinels (Loferski and Lipin, 1983). Chrome-spinel unmixing has also been observed experimentally. Kapure et al. (2010) formed chrome-spinel lamellae while oxidizing a host grain in air and heating the sample to 900°C for 2 hours. The lamellae were Fe-rich compared to the host chrome-spinel and formed a pattern similar to Jurassic Grain 3.

The lamellae found in terrestrial chrome-spinels and experiments can help us to interpret the conditions for formation of the lamellae observed in Grains 2 and 3. The chemical and oxygen isotope data suggest that these grains originated from ordinary chondrites. Ordinary chondrites are equilibrated meteorites that reached inferred temperatures of ~750° – 950°C (Huss et al., 2006). These temperatures are similar to those in the experiments of Kapure et al. (2010), although the duration of the experiments was many orders of magnitude shorter than the natural metamorphism. The similar temperature ranges of the ordinary chondrites and the experiments suggest that the lamellae from Grains 2 and 3 needed these same temperatures for formation. We note that the grains were partially aqueously altered while on the ancient terrestrial sea floor, but it is unlikely that the alteration environment was hot enough (> 700°C) to create the lamellae in Grains 2 and 3 on Earth. While higher temperatures are needed to form lamellae, the rarity of

observed lamellae in extraterrestrial and terrestrial chrome-spinel grains suggests that additional conditions beyond temperature must be met in order to form lamellae, such as cooling rates. We conclude that the lamellae formed on an extraterrestrial body based on the temperatures needed for lamellae formation. Furthermore, the rarity of chrome-spinel lamellae observed on Earth and the lack of their presence in local rock of Southern Spain (where the Jurassic chrome-spinels were extracted) supports an extraterrestrial origin of Grains 2 and 3.

3.6 Conclusions

Silicate inclusions in three chrome-spinel grains from Jurassic sediments were characterized by SEM-EDS, FIB sectioned, and analyzed using STEM. All chrome-spinel grains appeared to be from ordinary chondrites, but their sub classifications using elemental compositions and oxygen isotopes were ambiguous. Many of the inclusions that were FIB sectioned were heavily altered by terrestrial aqueous activity, as indicated by their chemical compositions and amorphous textures, and could not be used to help classify the parent meteorite type. The crystalline inclusions from Grain 2 were slightly altered, but we were still able to show that the host grain most likely originated from an L-chondrite.

Analyses of Brunflo inclusions with the use of FIB/STEM techniques and SEM-EDS line scans helped determine SEM-EDS limitations. Our results confirm the conclusion of Alwmark and Schmitz (2009a) that inclusions >3 μm in diameter at the polished surface typically are sufficiently large for reliable SEM-EDS analyses when using a 15 kV accelerating voltage. STEM measurements are necessary to determine compositions for smaller inclusions and those with shallow depths, sometimes as the result of non-spherical shapes, so as not to include the fluorescence of host material. SEM-EDS line scans are able to show if an inclusion is deep enough for reliable SEM-EDS point analyses by showing a “bottoming out” feature.

We have observed that chrome-spinel grains and their inclusions can be more complicated than expected. The lamellae analyzed in two of the grains likely formed on a parent body due to the high temperatures needed for the host spinel to separate into different phases. Rims of iron oxide and/or silica were common throughout the inclusions and most likely formed while the host grains were on the Jurassic sea floor for millions of years. Some rims were observed in high resolution SEM imaging before FIB sectioning, suggesting that altered inclusions could be detected before measuring their compositions.

Overall, this work shows that analyzing small silicate inclusions with FIB/STEM can help determine the parent meteorite types of relict chrome-spinel grains. The FIB sectioned samples showed that the inclusions can be complex and undergo terrestrial alteration while confined within a host chrome-spinel. With this knowledge we can improve the selection of inclusions to be studied for grain sub-classification.

Acknowledgments—The authors thank Peter Eschbach at the Oregon State University's Electron Microprobe Facility for his assistance with STEM-EDS map data collection. Supported by NASA grant NNX16AQ08G to GRH and the ERC-Advanced Grant 213000 to BS.

CHAPTER 4

EXTRATERRESTRIAL CHROME-SPINEL DATABASE FOR THE CLASSIFICATION OF REMNANT GRAINS FROM THE SEDIMENTARY RECORD

4.1 Abstract

The classification of remnant chrome-spinels is important for understanding how meteorite populations have changed throughout Earth's history. Remnant chrome-spinel grains resist weathering and retain their original chemical and oxygen isotope abundances. The compositions of these grains can be compared to modern meteorite chrome-spinels in order to determine their parent meteorite type. This study describes how the database of chrome-spinel compositions was constructed and how it has been implemented for the classification of remnant grains to determine the changes in meteorite populations over time.

4.2 Introduction

The study and classification of meteorites are necessary for understanding the formation and evolution of the solar system. Meteorites can be composed of dozens of minerals with unique compositions that can determine the meteorite's class and how it formed. Pristine meteorite samples can provide reliable information, but samples that have been on Earth for thousands of years can lose their original characteristics due to the effects of Earth's environment (e.g., weathering, including aqueous alteration). Fortunately, there are robust minerals that can retain their original characteristics for millions of years. One of the most common of these resistant minerals is chrome-spinel. These remnant extraterrestrial grains are preserved in ancient limestone, and are contained within fossil meteorites or dispersed throughout the sediment. The chrome-spinels retain their original chemistry and oxygen isotope abundances, which are used to classify the grain into a parent meteorite type.

The goal of classifying remnant chrome-spinel grains is to determine meteorite abundance and population changes throughout Earth's history. For example, ordinary chondrites are the most abundant meteorite type today, but achondrites and ordinary chondrites had similar abundances during the mid Ordovician (~ 466 Ma; Heck et al., 2017). The study of various time

periods also showed evidence of the L-chondrite parent body break up (~465 Ma; Schmitz et al., 2001, 2003, 2008; Heck et al., 2010) and the discovery of a new meteorite type, Österplana 065 (Schmitz et al., 2016). Observing these changes in meteorite abundances is possible because we can determine the origin of the remnant chrome-spinels by comparing their compositions to modern meteorite chrome-spinel compositions.

A detailed understanding of chrome-spinel compositions for the different meteorite groups is necessary to classify meteorite populations throughout Earth's history. While the classification of modern meteorites is based on physical characteristics and chemical properties of a multitude of diverse minerals, the classification of ancient meteorites from different time periods is based on a single mineral, chrome-spinel. Chrome-spinels can be classified as originating from distinct meteorite types based on their characteristics, but there can be ambiguous classifications due to the limited chemical variability of chrome-spinel. Here we present a database of modern meteorite chrome-spinel compositions collected from the literature, as well as new measurements, to provide a framework for reliably classifying the host meteorites of remnant chrome-spinels. The creation of a chrome-spinel database presents challenges because not all meteorite types have abundant chrome-spinels and chrome-spinel is not a widely studied mineral. The addition of new measurements fills gaps in the database for specific meteorite types, adds to the previously minimal data for some meteorite types, and supports older literature compositions for chrome-spinels. A thorough database will lead to a better understanding of chrome-spinel compositions for each meteorite type, which will improve our ability to classify remnant chrome-spinels throughout the stratigraphic record.

4.3 Methods

The samples used to determine the range of chemical compositions for chrome-spinels were extracted grains from modern meteorites and grains exposed on modern meteorite sections. Meteorite types were chosen based on what was missing in our compiled literature database and samples that would support the current literature. Extracted grains were obtained via acid dissolution of various meteorite samples (NWA 8365, NWA 10403, NWA 3151, NWA 8287, NWA 10265, NWA 766, NWA 7317; grains provided by B. Schmitz at Lund University). These grains were obtained using a similar method to the collection of chrome-spinel grains from ancient limestone (Heck et al. 2017). Chips of large chrome-spinel grains were also extracted from iron and pallasite samples (Bear Creek, Brenham, and Seymchan; grains provided by J.

Davidson at Arizona State University). Extracted grains were mounted in ¼ inch stainless steal mounts ("bullets"), ground flat using diamond lapping paper, and carbon coated using the University of Hawai'i (UH) Cressington 208 carbon coater (see Section 2.3.1 for details). The modern meteorite sections were from the UH Hawai'i Institute of Geophysics and Planetology (HIGP) collection. All samples were mounted (epoxy or bakelite) and polished flat by various researchers and curators. Some samples were previously carbon coated. Uncoated HIGP sections were coated using the UH carbon coater.

In order to locate chrome-spinel grains for electron-microprobe analysis, energy dispersive X-ray spectroscopy (EDS) maps were collected from the meteorite sections using the Map Analysis function on the JEOL JXA-8500F field emission electron microprobe. Maps for Cr, Mg, Al, Fe, and Ti were collected because they are the most abundant elements in chrome-spinel. Each spectrometer was scanned over the corresponding standard to find the wavelength peak position of each element (Cr, Mg, Al, Fe peaked on Chromite USNM 117075; Ti peaked on Sphene Glass). The maps were collected with a beam current of 300 nA, a beam diameter of 10 μm, dwell time of 10 ms, and a step size of 10-15. A map could be made square/rectangle or "special", that is, defined as a unique shape (e.g. triangle or greater than four sides) to avoid degassing of epoxy via the intense e-beam.

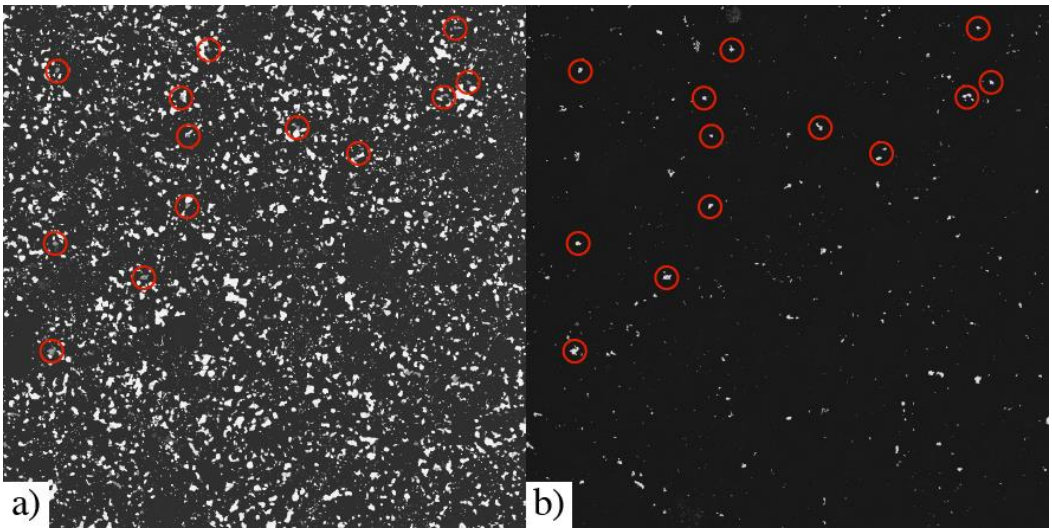

Figure 4.1. Representative a) Back-scattered electron (BSE) and b) Cr Kα X-ray map of a modern meteorite section (Guarena-H6). The brighter areas in b) show higher concentrations of Cr, which suggest a chrome-spinel. Those circled by red are confirmed as chrome-spinel.

The X-ray maps were used to pinpoint locations of chrome-spinels in sample sections for electron probe composition measurement. Locations of potential chrome-spinel grains were determined based on hot spots of the Cr chemistry maps (Fig. 4.1). Only the Cr chemistry map was referenced for potential chrome-spinels because the other elements measured did not help distinguish grains of interest. The mineral type of potential grains was confirmed by measuring their compositions with SEM-EDS. Grains with confirmed chrome-spinel compositions were imaged using secondary electron (SE) and back-scattered electron (BSE) imaging modes. Approximately 10 grains from each section were chosen, based on size and surface textures (cracks), for electron microprobe analysis using wavelength-dispersive X-ray spectroscopy (WDS).

Compositions of confirmed grains in modern meteorite sections and extracted chrome-spinels were collected using the UH electron microprobe. WDS measurements were collected using the same methods as described in Chapter 2 (Section 2.3.2 – *Elemental Abundances*). The Fe^{2+} and Fe^{3+} abundances of these chrome-spinel grains were also calculated using the Droop equation (Droop, 1987). The Droop equation was also used on the literature entries that did not provide Fe^{2+} and Fe^{3+} abundances separately (Appendix C). In the event a literature entry only has Fe^{2+} and Fe^{3+} oxide abundances, then all Fe was recalculated assuming it is present as FeO to ensure all entries have the same oxide abundances. All Fe as FeO (4.4) was calculated using a conversion (4.3) based on the mass percentages of FeO (4.1) and Fe_2O_3 (4.2), as follows:

$$\% \, FeO = \frac{(55.845+15.999)}{55.845} = 1.2865 \tag{4.1}$$

$$\% \, Fe_2O_3 = \frac{(2\times55.845+3\times15.999)}{(2\times55.845)} = 1.4297 \tag{4.2}$$

$$Conversion = \frac{1.2865}{1.4297} = 0.8998 \tag{4.3}$$

$$All \; Fe \; as \; FeO = (Fe_2O_3 \times 0.8998) + \; FeO \tag{4.4}$$

Oxygen isotopes were measured for the extracted grains from dissolved meteorites using the same methods described in Chapter 2 (Section 2.3.2 – *Oxygen Isotopes)*. These grains were measured over three ion probe sessions. The brachinite, lodranite, and ureilite grains were measured in the first and third ion probe sessions. The eucrite, diogenite, acapulcoite, and CR6 grains were measured in the second and third ion probe sessions. Measurements for the first session do not align with the third session and some measurements from the first session are not consistent with literature values, therefore measurements from the first session were not used. These measurements can be found in Appendix B.

4.4 Results

In order to create a database of compositions to use in the classification of remnant chrome-spinel grains from the sedimentary record, I undertook an intensive literature search focused on chrome-spinel (or chromite) and for data on mineral compositions of individual meteorites (Appendix C). While I found considerable data on chrome-spinels, there were still gaps in the resulting compilation (types without parentheses in Fig. 4.2). Chrome-spinels from meteorite samples were analyzed to help fill these gaps, to increase the entries for meteorites with few literature entries, and to compare our measurement techniques to the literature (indicated by yellow-highlights in Fig. 4.2). The samples consisted of polished sections, chrome-spinels extracted from dissolved meteorites, and loose grains extracted from meteorite samples. Extracted grains were identified as chrome-spinel by B. Schmitz (dissolved samples) and J. Davidson (loose grains). Grains from the dissolved meteorites were measured with the electron and ion probes. Chrome-spinels in the sections were located and identified before being measured with the electron probe.

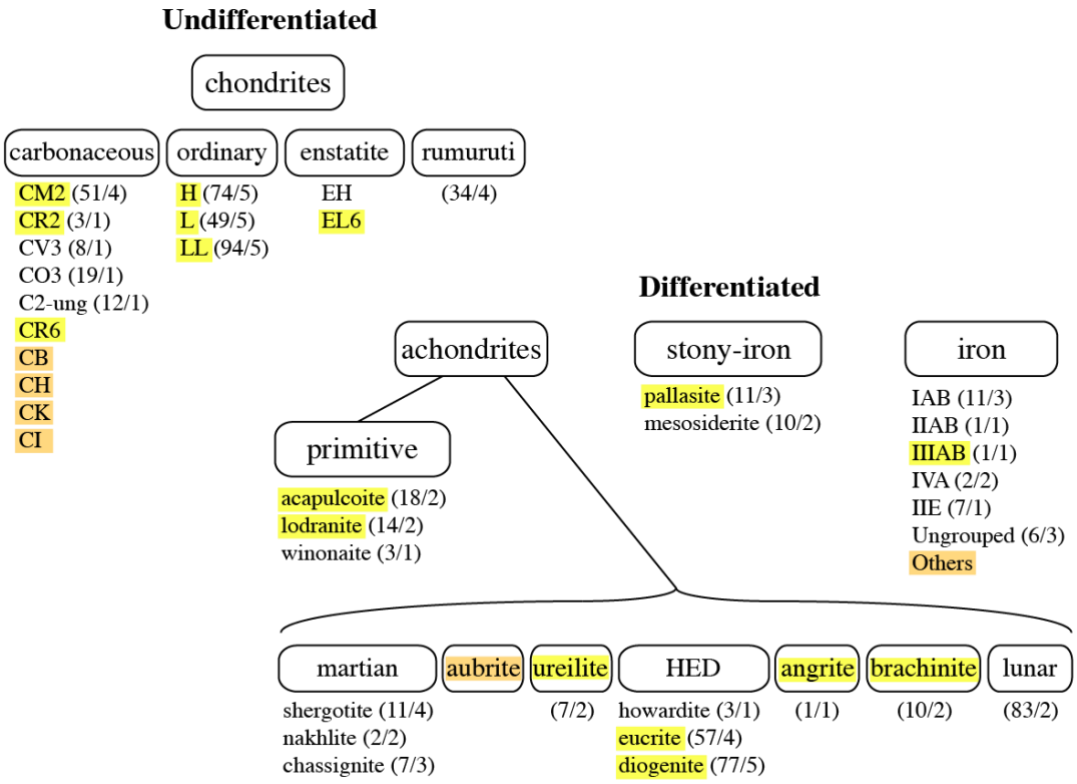

Figure 4.2. Different types, classes, and groups of modern meteorites. The parentheses show the number of entries and references for that meteorite in the database (entries/references). The yellow-highlighted types include new measurements from the current work (Table 4.1). The compiled database does not currently contain entries for the orange highlighted meteorites.

4.4.1 Search for chrome-spinels in modern meteorites

Polished sections of twenty-two modern meteorites were mapped by EDS to search for chrome-spinel grains. Areas with high concentrations of Cr in the Kα X-ray maps were further analyzed by SEM-EDS (Fig. 4.3) and those with characteristics of chrome-spinel were measured by WDS in the electron microprobe. For the Eagle (EL6) chondrite, the high concentrations of Cr in the Kα X-ray map were not from chrome-spinel, but were from sulfides (e.g., Fig. 4.4). This does not come as a surprise because oxides are extremely rare in the highly reduced enstatite meteorites (Rubin, 1997). The remaining mapped sections contained chrome-spinels (Table 4.1).

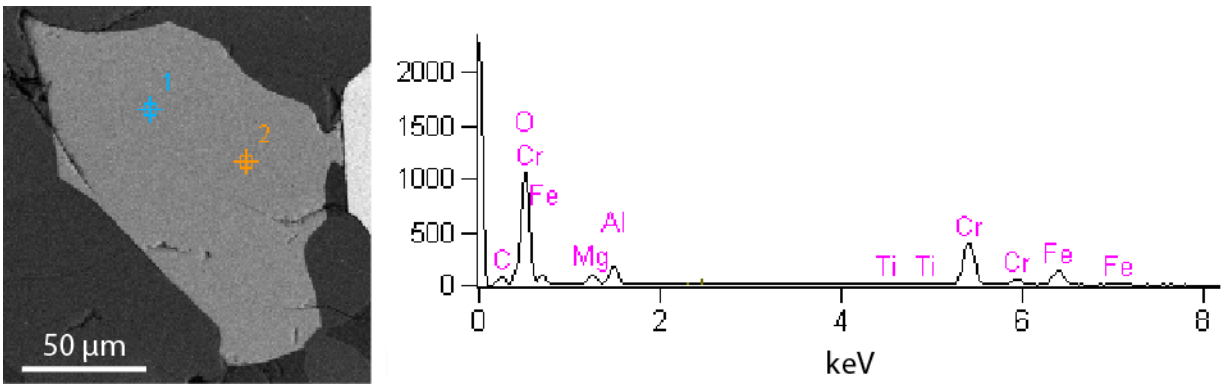

Figure 4.3. Representative chrome-spinel grain (Guarena, H6) and corresponding EDS spectrum (point 2). This spectra confirms a chrome-spinel composition.

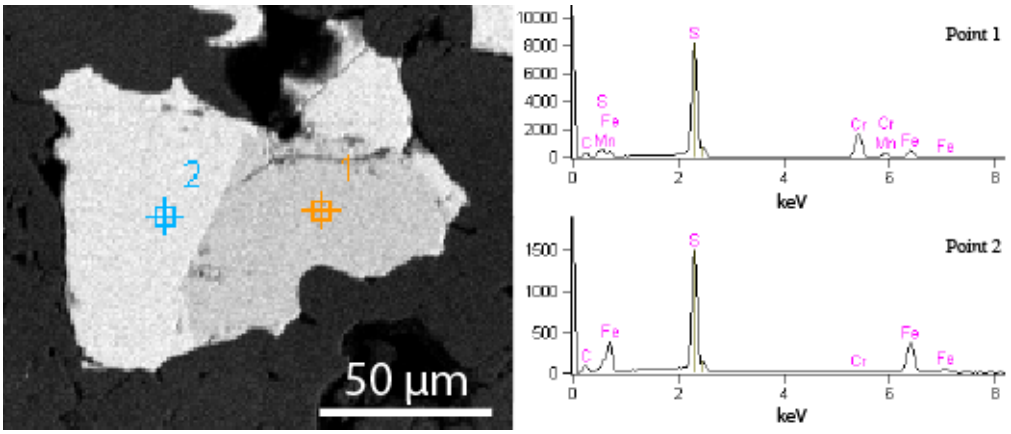

Figure 4.4. Representative grain from the Eagle (EL6) chondrite sample consisting of two phases, an Fe-Cr-sulfide, likely Daubréelite ($FeCr_2S_4$, point 1), and troilite (FeS, point 2). No chrome-spinel was identified in this sample.

4.4.2 Chemical compositions of modern meteorite chrome-spinels

Consistency between new measurements and the literature entries

Chrome-spinel measurements from each sample typically showed good reproducibility and showed compositions consistent with the literature (Table 4.1; Appendix B). This can be seen in Figure 4.5 with the equilibrated ordinary chondrite samples (LL4-6), which have consistent compositions within a single sample, and are consistent with the literature entries. Equilibrated meteorites have consistent compositions within a sample because they have come to chemical equilibrium via thermal metamorphism. The measurements of these samples can be averaged to reliably represent a given sample. However, some meteorite types are unequilibrated and have variable compositions within a single sample. For example, the chrome-spinels from each of the

CM2 samples exhibit a wide range of compositions (Fig. 4.6). The chrome-spinels from the Cold Bokkeveld and Murray samples encompass the continuous range of compositions from the literature entries. Samples with multiple chrome-spinel compositions should be presented separately because an averge of diverse compositions would misrepresent the true range of compositions of the meteorite sample. For these samples, data are shown as maximum and minimum values in Table 4.1, instead of average and standard deviation values. While many of the new measurements are consistent with their literature counterparts, some meteorite types do not have enough literature entries to determine the consistency of the new measurements (e.g., CR2, angrite, and ureilite chrome-spinel measurements).

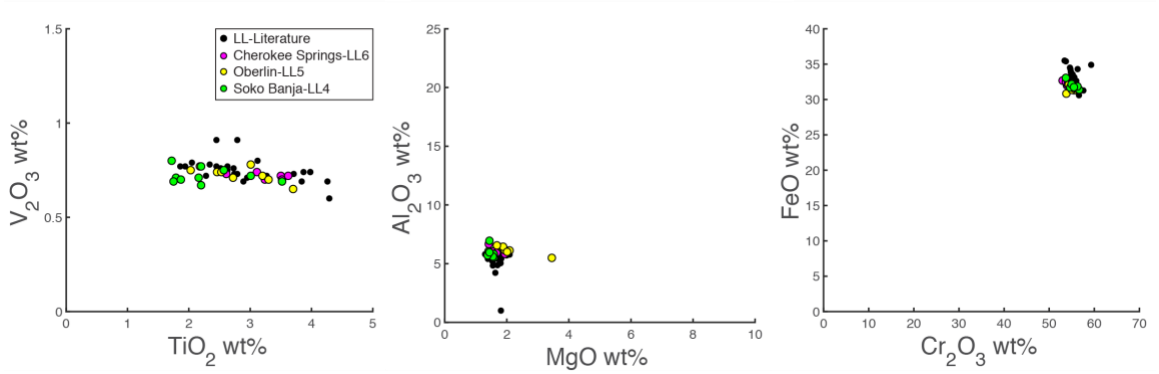

Figure 4.5. Comparisons between literature (Appendix C) and new measurement (Cherokee Springs-LL6, Oberlin-LL5, Soko Banja-LL4; Appendix B) compositions of chrome-spinels from LL-chondrites. All Fe assigned as FeO.

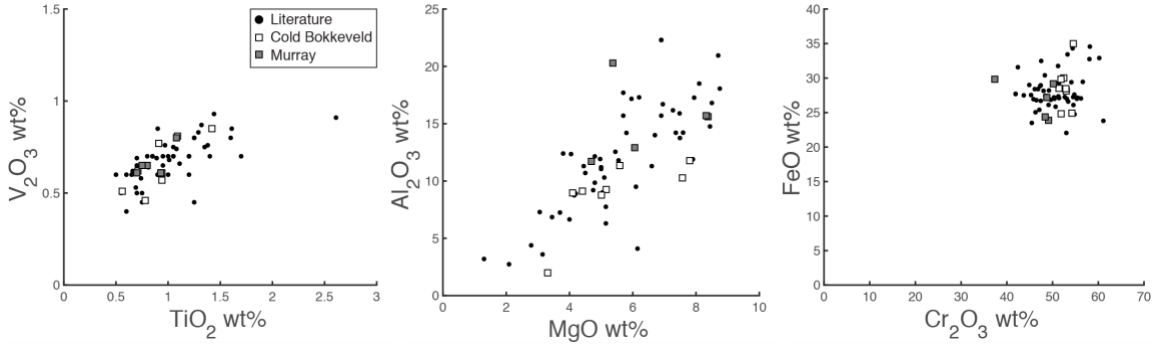

Figure 4.6. Comparisons between literature (Appendix C) and new measurement (Cold Bokkeveld and Murray; Appendix B) compositions of CM2 chrome-spinels. All Fe assigned as FeO.

Table 4.1. Chemical compositions (wt %) of chrome-spinel grains from modern meteorites.

Type	Name	MgO	*2SD*	Al_2O_3	*2SD*	TiO_2	*2SD*	V_2O_3	*2SD*	Cr_2O_3	*2SD*	MnO	*2SD*	All FeO	*2SD*	FeO	*2SD*	Fe_2O_3	*2SD*	ZnO	*2SD*	SiO_2	*2SD*	Total
Eucrite	NWA 8365*	0.31	*0.15*	7.81	*0.28*	4.22	*0.32*	0.84	*0.04*	49.24	*0.57*	0.55	*0.03*	35.71	*0.22*	35.67	*0.22*	0.05	*0.02*	0.01	*0.01*	0.00	*0.00*	98.69
Eucrite	Haraiya	0.07	*0.09*	8.16	*0.36*	2.53	*0.64*	0.72	*0.04*	49.48	*1.07*	0.55	*0.02*	33.35	*0.42*	33.30	*0.43*	0.06	*0.11*	0.01	*0.01*	0.10	*0.36*	94.98
		0.83	*1.10*	7.57	*6.13*	7.94	*12.85*	0.65	*0.48*	43.48	*20.21*	0.58	*0.17*	38.42	*11.60*	38.14	*11.27*	0.32	*0.88*	0.02	*0.05*			99.52
Diogenite	NWA 10403*	2.11	*0.38*	9.82	*3.81*	0.96	*0.80*	0.62	*0.54*	54.80	*5.06*	0.52	*0.02*	30.22	*1.14*	30.22	*1.14*	0.00	*0.00*	0.01	*0.00*	0.00	*0.00*	99.07
		3.56	*2.36*	11.15	*7.86*	0.79	*0.76*	0.51	*0.31*	54.41	*9.20*	0.59	*0.19*	28.45	*3.66*	28.07	*3.30*	0.42	*1.45*	0.06	*0.10*			99.55
Brachinite	NWA 3151*	4.49	*0.02*	12.65	*0.05*	0.89	*0.02*	0.66	*0.02*	52.32	*1.04*	0.30	*0.01*	27.19	*0.41*	27.00	*0.49*	0.22	*0.15*	0.41	*0.01*	0.00	*0.00*	98.94
		4.34	*1.12*	10.84	*5.79*	1.22	*1.12*	0.61	*0.32*	54.34	*5.81*	0.36	*0.10*	28.41	*1.10*	27.85	*1.11*	0.62	*1.59*	0.15	*0.46*			100.34
Acapulcoite	NWA 8287*	8.05	*0.17*	9.60	*0.06*	1.39	*0.02*	0.64	*0.05*	57.77	*0.14*	1.21	*0.03*	19.66	*0.23*	19.66	*0.23*	0.00	*0.00*	0.89	*0.04*	0.00	*0.00*	99.21
		7.57	*2.56*	6.32	*2.59*	1.04	*0.63*	0.58	*0.38*	61.88	*4.21*	1.79	*1.32*	19.54	*5.23*	19.32	*5.01*	0.25	*0.98*	1.04	*0.31*			99.78
Lodranite	NWA 10265*	9.97	*0.05*	12.01	*0.09*	0.14	*0.00*	0.81	*0.06*	58.15	*0.31*	0.50	*0.01*	18.01	*0.08*	18.01	*0.07*	0.01	*0.02*	0.07	*0.01*	0.00	*0.00*	99.65
		7.62	*8.17*	6.39	*3.98*	0.71	*0.34*	0.59	*0.20*	62.12	*6.33*	1.26	*0.81*	20.13	*12.49*	19.85	*12.73*	0.31	*1.06*	0.63	*0.48*			99.49
Ureilite	NWA 766*	17.54	*2.64*	19.27	*1.91*	0.81	*0.28*	0.40	*0.03*	53.71	*3.00*	0.64	*0.07*	6.72	*4.26*	6.72	*4.26*	0.00	*0.00*	0.12	*0.11*	0.05	*0.01*	99.27
		11.06	*9.08*	15.20	*3.60*	0.75	*0.51*	0.45	*0.12*	53.73	*6.24*	0.54	*0.41*	17.19	*14.62*	16.94	*14.42*	0.28	*0.75*	0.38	*0.14*			99.33
CR6	NWA 7317*	3.05	*0.08*	12.70	*0.07*	1.53	*0.04*	0.64	*0.04*	50.43	*0.26*	0.27	*0.01*	30.11	*0.21*	30.09	*0.20*	0.03	*0.02*	0.01	*0.01*	0.00	*0.00*	98.75
CR2	GRA95227 (min)	3.77		0.14		0.40		0.14		38.50		0.29		9.70		9.70		0.00		0.00		0.12		94.68
	GRA95227 (max)	16.67		26.48		4.03		1.02		59.93		2.07		29.69		27.95		2.96		0.02		3.54		98.32
		2.99	*4.46*	4.10	*11.55*	1.76	*0.51*	0.94	*0.57*	57.04	*12.89*	0.45	*0.30*	32.34	*4.93*	29.27	*4.37*	3.41	*3.17*	0.01	*0.05*			99.98
CM2	Cold Bokkeveld (min)	3.27		1.90		0.56		0.44		51.20		0.20		24.64		21.99		2.28		0.00		0.10		96.90
	Cold Bokkeveld (max)	7.83		11.96		1.53		0.86		54.94		0.39		35.03		28.64		7.21		0.03		1.15		99.13
CM2	Murray17b (min)	4.44		11.66		0.62		0.58		37.13		0.15		23.64		21.51		0.82		0.00		0.13		95.02
	Murray17b (max)	8.48		20.42		1.17		0.90		50.56		0.25		30.91		28.01		3.97		0.03		1.57		98.75
		5.64	*3.56*	12.16	*9.72*	1.02	*0.74*	0.67	*0.23*	50.56	*9.32*	0.23	*0.11*	28.06	*5.28*	25.68	*4.41*	2.65	*3.54*	0.02	*0.06*			98.63
Pallasite	Brenham_ASU10	8.26	*0.06*	0.44	*0.01*	0.04	*0.00*	0.56	*0.02*	70.16	*0.29*	0.30	*0.01*	19.88	*0.09*	19.17	*0.11*	0.78	*0.05*	0.02	*0.01*	0.02	*0.01*	99.76
Pallasite	Seymchan_ASU1626	9.93	*0.03*	0.92	*0.02*	0.09	*0.00*	0.52	*0.01*	71.37	*0.06*	0.40	*0.02*	16.63	*0.02*	16.63	*0.02*	0.00	*0.00*	0.02	*0.02*	0.00	*0.00*	99.88
		5.85	*1.86*	5.95	*7.76*	0.19	*0.19*	0.55	*0.12*	63.17	*9.40*	0.61	*0.37*	23.30	*2.45*	23.17	*2.45*	0.14	*0.51*	0.02	*N/A*			99.66
Iron (IIIAB)	BearCreek_ASU352-1	0.07	*0.01*	0.01	*0.01*	0.00	*0.00*	0.62	*0.04*	66.37	*0.21*	0.62	*0.01*	31.37	*0.01*	31.06	*0.06*	0.34	*0.05*	0.03	*0.02*	0.00	*0.00*	99.12
	IIIAB	0.02		0.11		0.02		0.07		67.30		0.29		32.60		31.87		0.81		0.15				100.64
		6.98	*7.93*	4.83	*9.80*	1.15	*2.71*	0.40	*0.47*	64.09	*15.26*	1.81	*2.35*	21.58	*19.02*	20.92	*18.48*	0.73	*1.68*	0.93	*1.77*			101.83
Angrite	Dorbigny	12.12	*0.18*	51.68	*0.21*	0.34	*0.01*	0.36	*0.02*	9.66	*0.22*	0.14	*0.01*	24.00	*0.32*	21.44	*0.26*	2.84	*0.19*	0.01	*0.01*	0.05	*0.01*	98.63
		6.98		37.75		1.48		0.60		20.93		0.26		31.42		28.32		3.44						99.77
H6	Kernouve	2.94	*0.35*	6.48	*0.21*	2.22	*0.18*	0.68	*0.06*	57.01	*0.43*	0.78	*0.10*	28.71	*0.63*	28.71	*0.63*	0.00	*0.00*	0.32	*0.04*	0.03	*0.04*	99.17
H6	Guarena	3.09	*0.30*	6.43	*0.33*	2.19	*0.20*	0.69	*0.09*	56.48	*0.65*	0.73	*0.07*	29.15	*0.62*	29.01	*0.48*	0.15	*0.30*	0.32	*0.06*	0.00	*0.01*	99.09
		4.52	*6.98*	11.08	*25.54*	2.05	*1.44*	0.61	*0.38*	52.43	*23.09*	0.77	*0.28*	28.45	*7.43*	27.79	*7.88*	0.74	*1.18*	0.34	*0.20*			100.33
H5	Richardten	2.99	*0.95*	5.72	*2.57*	2.02	*0.50*	0.74	*0.24*	57.15	*2.01*	0.84	*0.12*	28.66	*1.39*	28.44	*1.35*	0.24	*0.31*	0.59	*0.04*	0.04	*0.28*	98.78
H5	Forest City	2.84	*0.21*	6.37	*0.14*	2.03	*0.11*	0.68	*0.04*	56.67	*0.44*	0.85	*0.05*	29.05	*0.24*	29.00	*0.23*	0.06	*0.08*	0.29	*0.02*	0.01	*0.04*	98.81
		4.29	*6.08*	10.59	*19.43*	1.90	*1.55*	0.61	*0.31*	52.81	*16.94*	0.89	*0.32*	28.45	*7.28*	27.73	*7.46*	0.79	*1.52*	0.38	*0.32*			99.99
H4	Monroe	2.51	*0.31*	5.23	*1.16*	1.40	*0.22*	0.74	*0.05*	58.08	*1.03*	0.82	*0.07*	29.19	*0.46*	28.68	*0.37*	0.56	*0.41*	0.51	*0.05*	0.08	*0.27*	98.62
H4	Bushnell	2.94	*0.52*	6.65	*0.15*	1.95	*0.14*	0.70	*0.03*	55.98	*0.43*	0.86	*0.07*	29.23	*0.64*	28.87	*0.65*	0.40	*0.24*	0.31	*0.02*	0.03	*0.04*	98.68
		4.94	*8.46*	12.38	*31.85*	1.73	*1.38*	0.60	*0.35*	51.84	*30.35*	0.76	*0.50*	27.36	*9.41*	26.97	*9.25*	0.44	*0.98*	0.34	*0.34*			99.99
H3	Prairie Dog	1.96	*0.17*	1.95	*0.96*	1.11	*0.33*	0.72	*0.14*	61.34	*2.52*	0.83	*0.06*	29.94	*2.32*	28.87	*0.66*	1.19	*2.00*	0.44	*0.05*	0.14	*0.30*	98.57
		5.16	*12.36*	14.60	*45.27*	1.19	*1.45*	0.44	*0.76*	49.07	*42.68*	0.71	*0.82*	28.38	*14.35*	26.43	*12.97*	2.16	*3.29*	0.33	*0.34*			100.09
L6	Bruderheim	2.23	*0.15*	5.96	*0.35*	2.63	*0.71*	0.71	*0.05*	55.82	*0.52*	0.65	*0.04*	30.42	*0.50*	30.42	*0.54*	0.01	*0.05*	0.33	*0.05*	0.05	*0.04*	98.81
		3.12	*4.30*	7.86	*14.24*	2.67	*1.18*	0.65	*0.35*	54.05	*12.79*	0.65	*0.32*	30.51	*5.73*	29.90	*5.65*	0.68	*1.56*	0.26	*0.28*			99.83
L5	Bluff(a)	4.98	*0.34*	6.00	*0.16*	2.94	*0.19*	0.73	*0.03*	56.91	*0.29*	0.52	*0.03*	27.04	*0.50*	27.03	*0.50*	0.02	*0.04*	0.12	*0.01*	0.00	*0.01*	99.23
L5	Farmington	5.44	*0.41*	6.14	*0.50*	2.54	*0.76*	0.72	*0.06*	57.16	*0.74*	0.48	*0.05*	26.75	*0.80*	26.27	*0.83*	0.53	*1.02*	0.10	*0.04*	0.01	*0.06*	99.40
		4.17	*5.87*	10.11	*26.53*	2.45	*2.21*	0.66	*0.37*	52.29	*24.67*	0.67	*0.43*	29.64	*7.05*	28.68	*7.15*	1.07	*1.81*	0.46	*1.01*			100.54
L4	Bjurbole	1.81	*0.22*	5.61	*0.93*	2.08	*0.20*	0.68	*0.04*	56.87	*0.78*	0.61	*0.02*	30.79	*0.31*	30.73	*0.28*	0.07	*0.07*	0.36	*0.02*	0.00	*0.01*	98.83
L4	McKinney	2.38	*0.52*	4.73	*0.15*	2.24	*0.12*	0.69	*0.05*	57.43	*0.84*	0.60	*0.08*	30.61	*0.69*	29.99	*0.53*	0.69	*0.73*	0.37	*0.10*	0.01	*0.01*	99.13
		3.92	*7.01*	11.77	*31.57*	1.62	*1.34*	0.65	*0.36*	51.94	*29.29*	0.69	*0.42*	29.34	*8.26*	28.33	*8.08*	1.12	*2.13*	0.46	*0.60*			100.51
LL6	Cherokee Springs	1.67	*0.37*	6.15	*0.61*	3.27	*0.75*	0.72	*0.03*	53.94	*1.15*	0.54	*0.04*	32.11	*0.81*	32.10	*0.79*	0.01	*0.03*	0.24	*0.03*	0.05	*0.07*	98.70
		1.64	*0.38*	5.54	*0.62*	3.57	*1.26*	0.74	*0.18*	54.49	*1.40*	0.57	*0.19*	33.49	*2.32*	32.84	*1.86*	0.72	*1.52*	0.31	*0.13*			100.43
LL5	Oberlin	2.06	*0.52*	6.20	*0.31*	2.79	*0.55*	0.73	*0.04*	54.86	*0.60*	0.56	*0.03*	31.55	*0.40*	31.37	*0.53*	0.20	*0.30*	0.26	*0.04*	0.05	*0.05*	99.08
		1.84	*0.30*	5.80	*1.19*	2.52	*0.80*	0.76	*0.04*	55.53	*1.61*	0.64	*0.19*	32.57	*2.87*	31.43	*1.18*	1.26	*2.49*	0.32	*0.13*			100.11
LL4	Soko Banja	1.50	*0.08*	5.85	*0.43*	2.28	*0.60*	0.72	*0.04*	55.51	*0.95*	0.55	*0.02*	31.93	*0.49*	31.53	*0.53*	0.45	*0.26*	0.34	*0.03*	0.02	*0.02*	98.76
LL4	Hamlet	1.63	*0.11*	4.22	*1.40*	2.95	*0.70*	0.71	*0.05*	55.81	*1.55*	0.54	*0.04*	32.65	*0.75*	31.74	*0.50*	1.02	*0.64*	0.36	*0.06*	0.02	*0.04*	98.99
		1.66	*0.26*	4.62	*3.80*	2.48	*0.65*	0.75	*0.06*	56.85	*2.80*	0.56	*0.13*	32.73	*3.09*	31.67	*0.80*	1.18	*2.74*	0.39	*0.11*			100.15

Highlighted (light grey) rows are literature averages and other rows are from this study.
Individual measurements from this study are in Appendix B.
Individual literature entries and references are in Appendix C.
All FeO: all Fe assigned as FeO.
Totals do not include "All FeO".
2 SD: 2 standard deviations.
*Dissolved grains.

Distinguishing chrome-spinel compositions amongst meteorite types

Chrome-spinel grains within each meteorite type have characteristic chemical compositions. Some meteorite types can be resolved from one another using two-dimensional plots, but this is often not the case and more dimensions are needed. Oxide abundances of MgO, Al_2O_3, TiO_2, V_2O_3, Cr_2O_3, MnO, FeO (all Fe as FeO), FeO (2+), Fe_2O_3, and ZnO are used to discriminate amongst the chrome-spinel parent meteorite types. Examples of chrome-spinel compositions from different meteorite types are shown in Figures 4.7-4.10; these are two-dimensional plots that show partial overlaps.

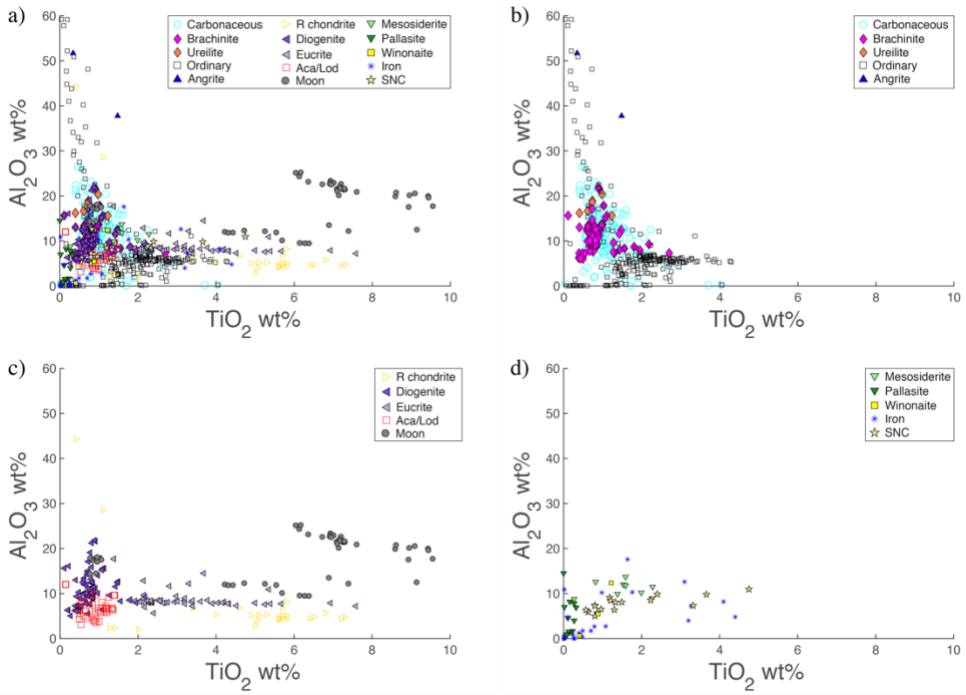

Figure 4.7. Compositions (Al_2O_3 and TiO_2 wt%) of chrome-spinel grains from modern meteorites. A) Contains all meteorite types, b-d) separate the types to show overlaps (data in Appendix C).

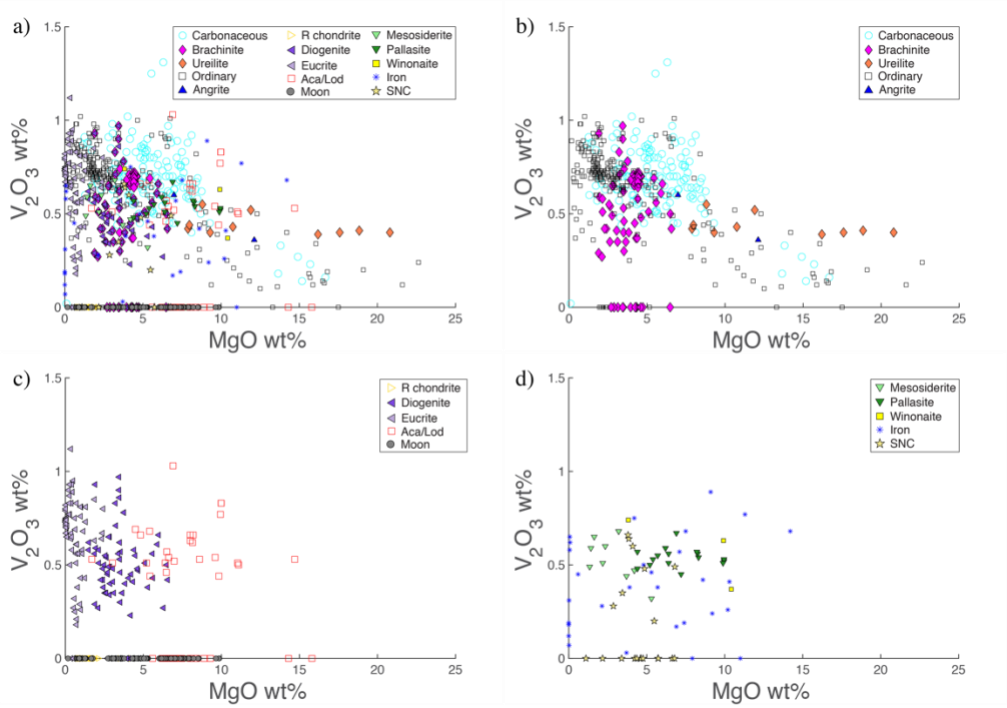

Figure 4.8. Compositions (V_2O_3 and MgO wt%) of chrome-spinel grains from modern meteorites. A) Contains all meteorite types, b-d) separate the types to show overlaps (data in Appendix C).

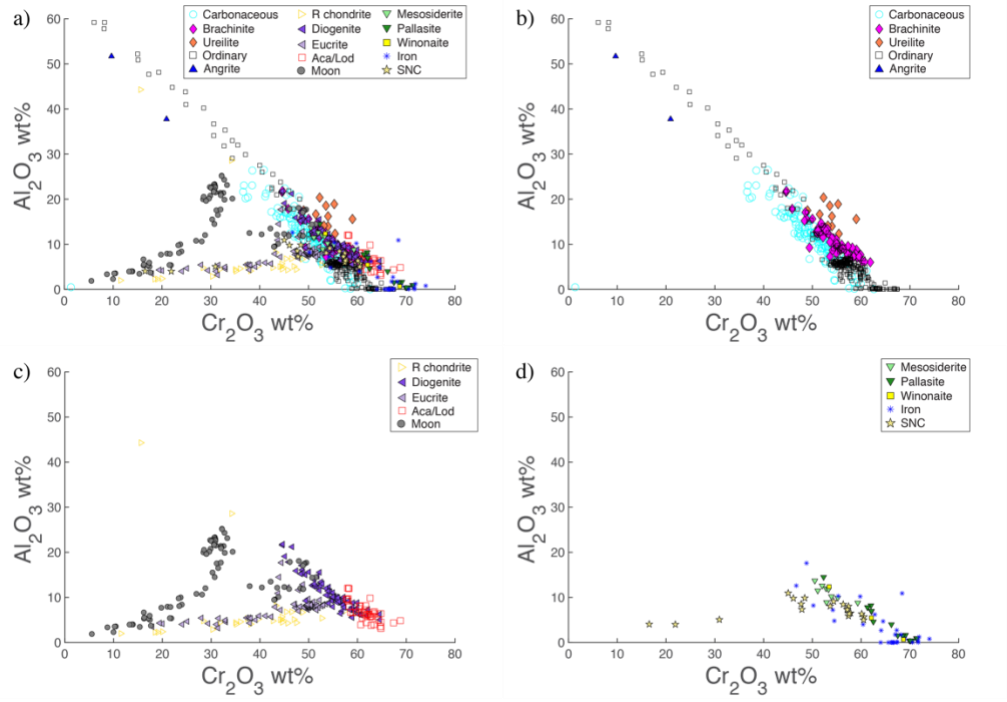

Figure 4.9. Compositions (Al_2O_3 and Cr_2O_3 wt%) of chrome-spinel grains from modern meteorites. A) Contains all meteorite types, b-d) separate the types to show overlaps (data in Appendix C).

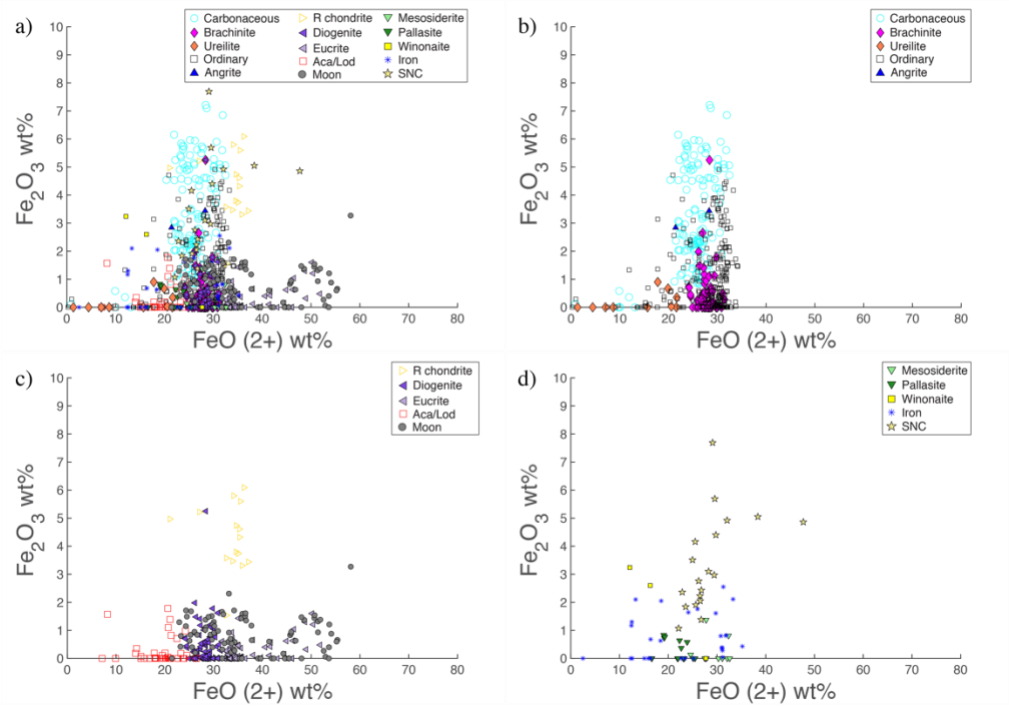

Figure 4.10. Compositions (Fe_2O_3 and FeO (2+) wt%) of chrome-spinel grains from modern meteorites. A) Contains all meteorite types, b-d) separate the types to show overlaps (data in Appendix C).

Chrome-spinels are found in ordinary chondrites of varying subgroups and petrologic types, which have varying compositions. Most equilibrated ordinary chondrites (types 4-6) are found within a well-defined chemical cluster that has distinct Al_2O_3 and V_2O_3 contents (grey filled markers; Fig. 4.11). The equilibrated ordinary chondrites also show a trend where the TiO_2 contents increase from H- to LL-chondrites (Fig. 4.11). The unequilibrated ordinary chondrites (type 3) have larger ranges of Al_2O_3, V_2O_3, TiO_2, and MgO contents (white markers). While there are differences among the subgroups, the overlap and outlier compositions make it difficult to distinguish amongst different petrologic types and groups based on chrome-spinel compositions alone.

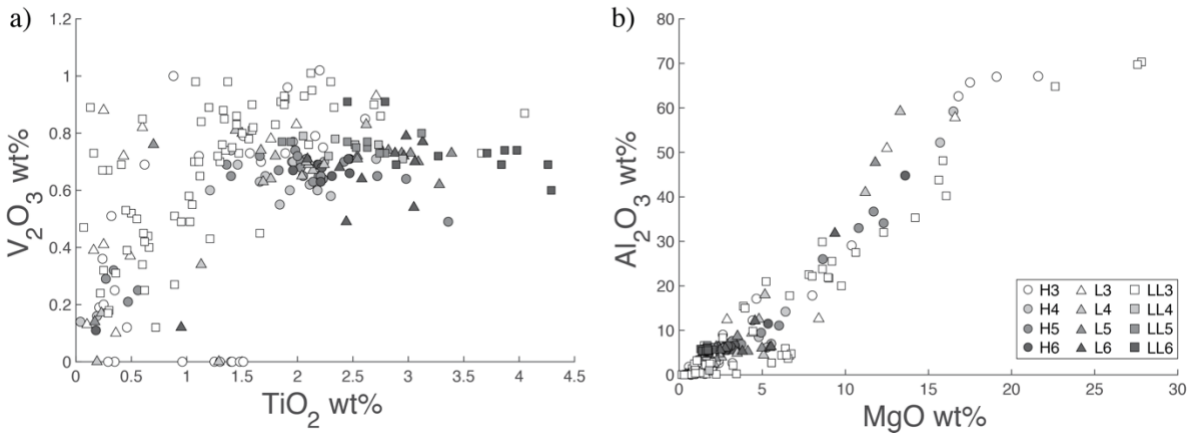

Figure 4.11. Compositions of H, L, and LL ordinary chondrites (types 3-6) (Bunch, 1967; Johnson and Prinz, 1991; Kimura et al., 2006; Snetsinger, 1967; Wlotzka et al., 2005; Appendix C).

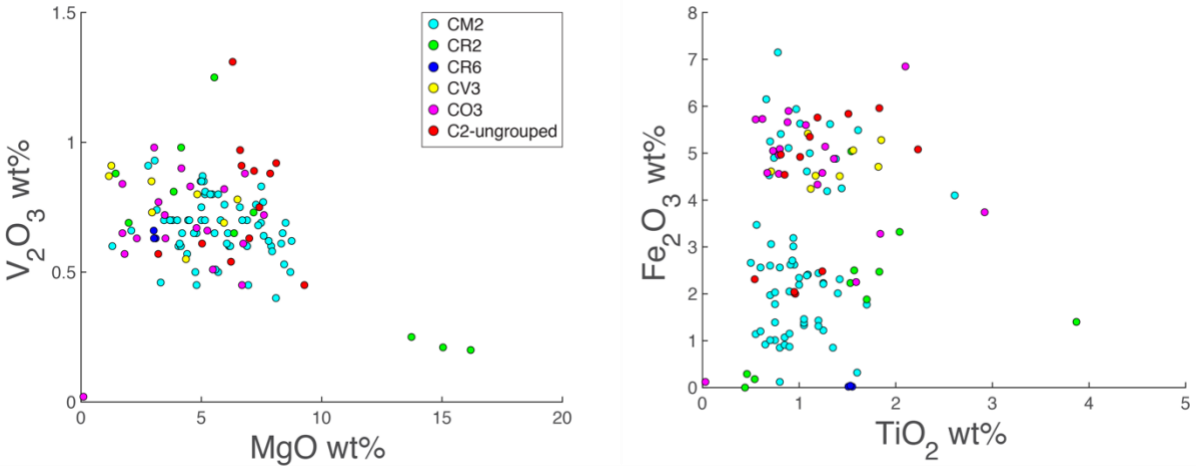

Figure 4.12. Compositions of chrome-spinels from carbonaceous chondrites (Appendix C).

Carbonaceous chondrites also contain subgroups, but these groups can be difficult to classify with chrome-spinel because their chemical compositions overlap. Carbonaceous chondrite chrome-spinels have well-defined values of V_2O_3, MgO, TiO_2, and other elements (Fig. 4.12; Appendix C). The CR2 grains with high MgO contents are from the new measurements of GRA95227 (Table 4.1 and Appendix B). There is limited CR2 literature data to compare the new measurements with in order to determine the extent of CR2 chrome-spinel chemical ranges. The most noticeable difference among the carbonaceous chondrite subtypes is the Fe_2O_3 content; the CR2 and most CM2 grains have lower Fe_2O_3 contents compared to CV3 and CO3 grains. The Fe_2O_3 content of a carbonaceous-like grain may be discriminatory, but the overlap in other

elements make it difficult to subtype a carbonaceous-chondrite-like chrome-spinel based on chemistry alone.

Many of the other meteorite types overlap to the extent that they are difficult to discriminate, but some types have characteristic features that may facilitate classifications. Chrome-spinels from the Moon, R chondrites, and eucrites fall within a unique chemical region that has the highest TiO_2 contents (Fig. 4.7c). These three types also form a triangle of compositions with lower Cr_2O_3 and Al_2O_3 contents that do not fall within the same Al/Cr trend as the remaining meteorite types (Fig. 4.9). Diogenites and eucrites have the same V_2O_3 ranges, but they can be differentiated because diogenites have slightly higher MgO contents (Fig. 4.8c). Ureilites are unique because they have some of the highest MgO contents, aside from unequilibrated ordinary-chondrite chrome-spinels. Finally, many of the extraterrestrial chrome-spinels in the database have Fe_2O_3 contents corresponding to iron present as Fe^{3+} (Fig. 4.10). Many of the grains have contents less than 3 wt% Fe_2O_3. However, there are some types with much higher Fe_2O_3 contents, including carbonaceous chondrites, ordinary chondrites, angrites, and SNCs. The grains with the highest Fe_2O_3 contents are R chondrite chrome-spinels with values up to 40 wt% (not shown in Fig 4.10; values in Appendix C). The extensive overlap amongst these types can make it difficult to classify remnant chrome-spinels based on chemistry alone. The introduction of oxygen isotope abundances, along with an understanding of these chemical trends, will allow us to better discriminate amongst the parent meteorite types for the reliable classification of remnant extraterrestrial chrome-spinels from the sedimentary record.

4.4.3 Oxygen Isotopes of modern meteorites

Oxygen isotope abundances of meteorites can also be used to help differentiate them from other meteorite types and from terrestrial sources (Fig. 4.13). Ordinary chondrite, R chondrite, and SNC meteorites plot above the TFL within distinct oxygen ranges making them easier to differentiate. Meteorite types below the TFL also have distinctive ranges, but some types have partial overlaps, such as ureilites, CM, and CR. This overlap can make it difficult to distinguish amongst types, which is why the combination of isotopes and chemistry is vital for the classification of remnant chrome-spinels.

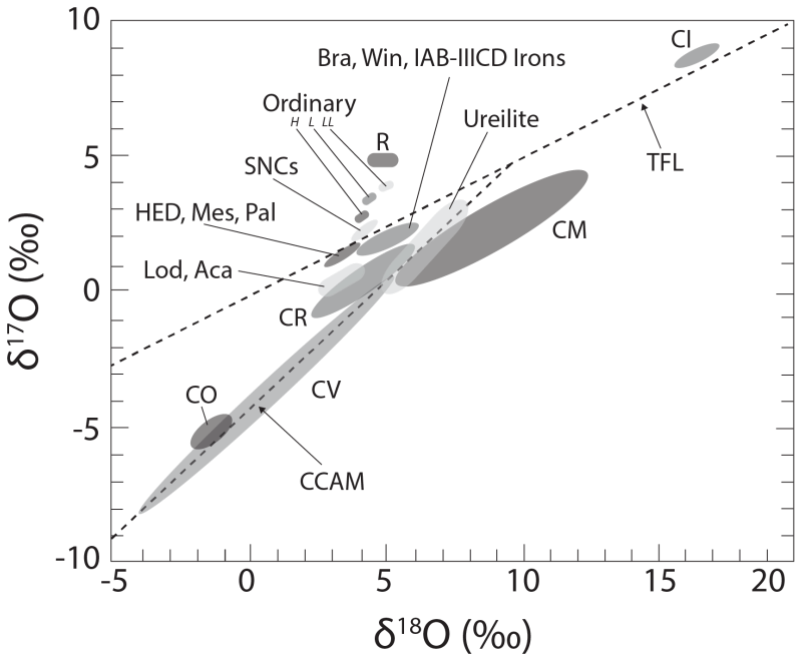

Figure 4.13. Bulk three-oxygen-isotope fields show partial overlaps of various meteorite types (after Clayton, 2004).

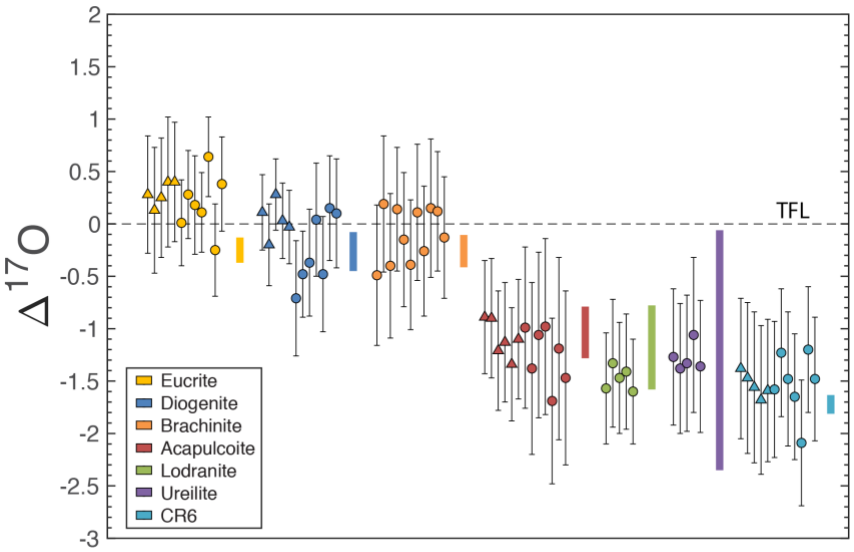

Figure 4.14. Oxygen isotope abundances of dissolved chrome-spinel grains from modern meteorites. Markers represent the second (triangles) and third (circles) ion probe sessions (See Section 4.2). Vertical colored bars represent the ranges in bulk $\Delta^{17}O$ values (average ± 2 st. dev.) for respective meteorite types (Clayton and Mayeda, 1996; CR6 (NWA7317, NWA2994, NWA3250, NWA6901, NWA6921) – Meteoritical Bulletin (MB 102, 93, 97, 100, 102)). TFL - Terrestrial Fractionation Line.

I also measured the oxygen isotope abundances of the chrome-spinels from dissolved modern meteorites to determine if there is agreement between bulk and chrome-spinel oxygen isotope abundances (Fig. 4.14 and Table 4.2). If the bulk measurements are consistent with chrome-spinels then the oxygen isotope database is complete. If they are not consistent, then the differences need to be understood and the oxygen isotope values need to be updated to create a reliable isotope database for chrome-spinel classifications. Figure 4.14 and Table 4.2 show that the measured chrome-spinel grains have $\Delta^{17}O$ values that are consistent with bulk values of the same meteorite type (color coordinated vertical bars), except for the slightly higher measured values of the eucrite sample.

4.5 Discussion

4.5.1 Database Limitations

Chemical compositions

The database compiled for the study of extraterrestrial chrome-spinels from the Jurassic contains 700+ entries, but it is currently not comprehensive. The current database does not have entries for aubrites, some carbonaceous chondrites (CB, CH, CK, CI), and some irons (Fig. 4.2). Aubrites, like enstatite chondrites, are highly reduced and likely do not contain chrome-spinels (Rubin, 1997). It is possible that the undocumented carbonaceous chondrite subtypes fall within the same compositional region as the carbonaceous chrome-spinels in the database (Fig. 4.12), but measurements from the undocumented types are required to test this assumption. Some meteorite types within the database contain few entries, which limits our knowledge of the range of their chemistries. For example, the angrites have one literature and one new measurement entry with high Al_2O_3 contents. More measurements are needed to establish the range of angrite chrome-spinels, but the high Al_2O_3 content of the current samples provide discriminatory power for possible classifications. There are similar database gaps for irons, SNC, and howardite meteorites (Fig. 4.2), but the current database allows for possible classifications of these types. The database is also limited for particular elements that are not reported in the literature. Many of the literature entries only contain FeO (assuming all Fe as FeO) and not the Fe^{2+} and Fe^{3+} constituents, FeO and Fe_2O_3, respectively. Fortunately, FeO and Fe_2O_3 can be calculated using the Droop equation (Section 4.3). Also, some literature sources did not provide abundances of

certain elements, especially V_2O_3 and ZnO. The abundances of V_2O_3 can been used as a possible discriminator of terrestrial versus extraterrestrial origins (Schmitz et al., 2017). Database values of ZnO can provide baseline abundances of meteorite types to determine the degree of terrestrial alteration for a remnant chrome-spinel. Classifications are possible with these gaps, but new measurements and literature additions are needed for robust chemical matches.

Oxygen isotopes

Oxygen isotope measurements of the chrome-spinel grains from dissolved meteorite samples suggest that chrome-spinels may have different $\delta^{18}O$ values compared to bulk literature values (Fig. 4.15). The measured chrome-spinels show a $\delta^{18}O$ shift to the left compared to bulk values, except for the ureilite chrome-spinel sample. This shift can be due to the partitioning of isotopes among co-existing phases at equilibrium. Some shift in $\delta^{18}O$ is expected between forsterite and chromite (end member), ~ 2.97-0.41‰ at 600-1200 °C (Chiba et al., 1989; Zheng, 1991), but the shifts observed between the chrome-spinel ion probe measurements and bulk data are larger than the expected values (Table 4.2 and Fig. 4.15). These shifts are not fully understood, but matrix-effects in the ion probe are a likely cause. The connection to matrix-effects can be seen in Figure 4.16, where higher FeO contents correlate with larger differences between the chrome-spinel and bulk $\delta^{18}O$ values. Matrix-effects may be related to the FeO content or a combination of the other elements in each chrome-spinel.

A matrix-effect for oxygen-isotope measurements is due to using a standard chrome-spinel with composition that is unlike the compositions of the measured chrome- spinels. Using a standard with a similar composition to the unknown gives the most reliable results. The ion probe at UH uses Stillwater chromite as the chrome-spinel standard, which does not closely match the various chemical compositions of extraterrestrial chrome-spinels. Similar shifts using Stillwater chromite as the standard were discussed in Chapter 2, Section 2.5.1 (*Compositions and Clustering*). These shifts ranged from ~3.8‰ (Milton pallasite - McCoy et al., 2019) to ~7.7‰ (Hessle H5 - our measurements) in $\delta^{18}O$. The differences in $\delta^{18}O$ values mean that bulk-meteorite $\delta^{18}O$ values do not reliably represent chrome-spinel oxygen isotope compositions. Fortunately, $\Delta^{17}O$ is not dependent on shifts in mass fractionation and can be used for the classification of remnant chrome-spinels (e.g., Fig. 4.14). The combination of $\delta^{18}O$ and $\Delta^{17}O$ values could be used to discriminate between overlapping meteorite types, but more chrome-

spinel oxygen isotope measurements are needed for classifications or a shift correction must be developed to reliably use $\delta^{18}O$ values.

Table 4.2. Oxygen isotope abundances of chrome-spinels from dissolved meteorites and bulk samples of meteorites.

Type	Measurement	$\delta^{18}O$	*2 SD*	$\delta^{17}O$	*2 SD*	$\Delta^{17}O$	*2 SD*
Eucrite							
	Cr-spinel°	-7.15	*2.16*	-3.48	*1.28*	0.23	*0.45*
	Bulk*	3.61	*0.38*	1.63	*0.28*	-0.24	*0.13*
	Difference	10.76		5.11		-0.47	
Diogenite							
	Cr-spinel°	-2.38	*2.21*	-1.37	*1.51*	-0.13	*0.62*
	Bulk*	3.32	*0.33*	1.46	*0.26*	-0.27	*0.18*
	Difference	5.70		2.83		-0.14	
Brachinite							
	Cr-spinel°	-0.97	*2.17*	-0.61	*0.90*	-0.10	*0.51*
	Bulk*	3.97	*1.19*	1.81	*0.6*	-0.26	*0.15*
	Difference	4.94		2.42		-0.16	
Acapulcoite							
	Cr-spinel°	-1.17	*1.15*	-1.79	*0.54*	-1.18	*0.47*
	Bulk*	3.45	*0.96*	0.77	*0.58*	-1.04	*0.24*
	Difference	4.62		2.56		0.14	
Lodranite							
	Cr-spinel°	-0.85	*0.65*	-1.92	*0.32*	-1.48	*0.22*
	Bulk*	3.38	*0.77*	0.57	*0.41*	-1.18	*0.41*
	Difference	4.23		2.49		0.30	
Ureilite							
	Cr-spinel°	10.16	*1.33*	4.00	*0.68*	-1.28	*0.26*
	Bulk*	6.93	*1.98*	2.41	*2.07*	-1.20	*1.14*
	Difference	-3.23		-1.59		0.08	
CR6							
	Cr-spinel°	-3.47	*3.09*	-3.34	*1.66*	-1.53	*0.46*
	Bulk^	3.22	*0.61*	-0.05	*0.28*	-1.73	*0.11*
	Difference	6.69		3.29		-0.20	

2 SD: two standard deviations.
Cr-spinel: chrome-spinel.
° This study, ion microprobe for oxygen isotopes.
* Clayton and Mayeda (1996), bromine pentaflouride (BrF_5) oxygen extraction on ground whole-rock.
^ Meteoritical Bulletin database (www.lpi.usra.edu/meteor/) for NWA7317 (MB 102), NWA2994 (MB 93), NWA3250 (MB 97), NWA6901 (MB 100), and NWA6921 (MB 102) via laser fluorination.

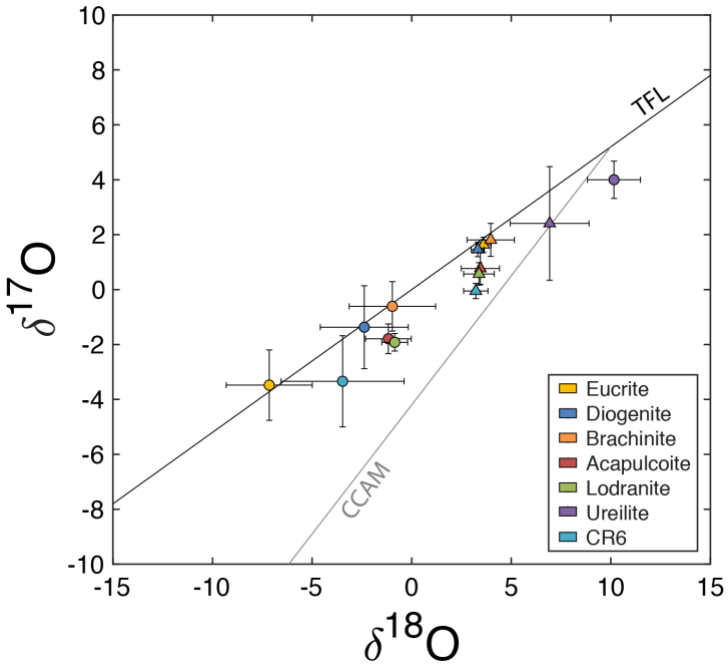

Figure 4.15. Oxygen isotope values of modern meteorites. The circle markers show oxygen isotope values for the chrome-spinels from dissolved meteorites in this study (Table 4.2). The triangle markers show bulk oxygen isotope abundances from Clayton and Mayeda (1996) and the Meteoritical Bulletin for the CR6 values (NWA7317, NWA2994, NWA3250, NWA6901, NWA6921) (Table 4.2). Horizontal and vertical bars show the 2 st. dev. of the chrome-spinel measurements (circles) and bulk oxygen isotopes (diamonds) of each meteorite type. TFL - Terrestrial Fractionation Line. CCAM - Carbonaceous Chondrite Anhydrous Mineral.

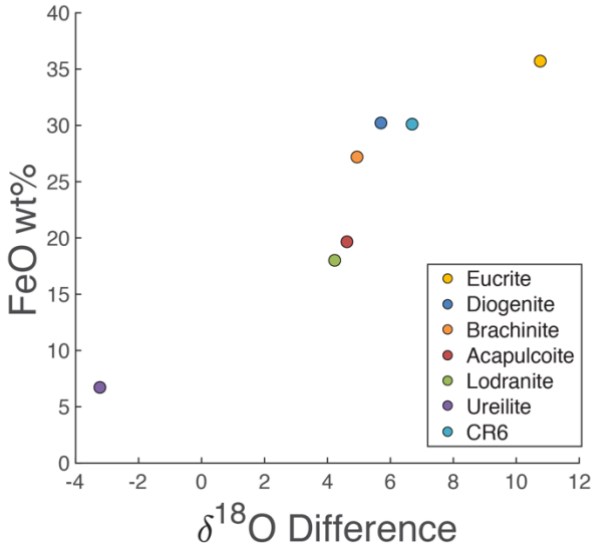

Figure 4.16. The FeO wt% (all Fe assigned as FeO) versus the difference (shift) in $\delta^{18}O$ values of the chrome-spinels from dissolved meteorite samples and their respective bulk meteorite values. Data are found in Tables 4.1 and 4.2.

4.5.2 Extraterrestrial versus Terrestrial chrome-spinel abundances

An important step in the classification of remnant chrome-spinels is to determine if the grains have terrestrial or extraterrestrial origins. We attempt to limit the number of terrestrial grains by choosing ancient limestone samples that originally formed far from shore, effectively reducing terrestrial contamination. If terrestrial grains still appear in the sample, then the grains can possibly be removed from the sample set based on chemical compositions and oxygen isotope abundances (Figs. 4.13 and 4.17). The extraterrestrial chrome-spinel compositions show limited chemical ranges, such as lower Fe^{3+}# (=Fe^{3+}/(Fe^{3+}+Al+Cr)) contents and higher Cr# (= Cr/(Cr+Al)) and Fe^{2+}# (= Fe^{2+}/(Fe^{2+}+Mg)) contents (Figs. 4.17b and d). The clustering of extraterrestrial chrome-spinel compositions may help to distinguish terrestrial grains that are outside of the extraterrestrial compositional ranges. However, the extensive overlap between the two sources suggests that there is no definitive way to distinguish between extraterrestrial and terrestrial grains based on chemistry alone. Oxygen isotopes can help determine terrestrial sources because terrestrial grains have consistent $\Delta^{17}O$ values of zero. Most extraterrestrial grains have non-zero $\Delta^{17}O$ values, but there are some types that overlap with the terrestrial value. In this event, oxygen isotopes can be inconclusive when $\Delta^{17}O$ is within error of zero. Overall, the use of chemistry, oxygen isotopes, and sample selection are needed to limit and identify terrestrial sources in a grain collection.

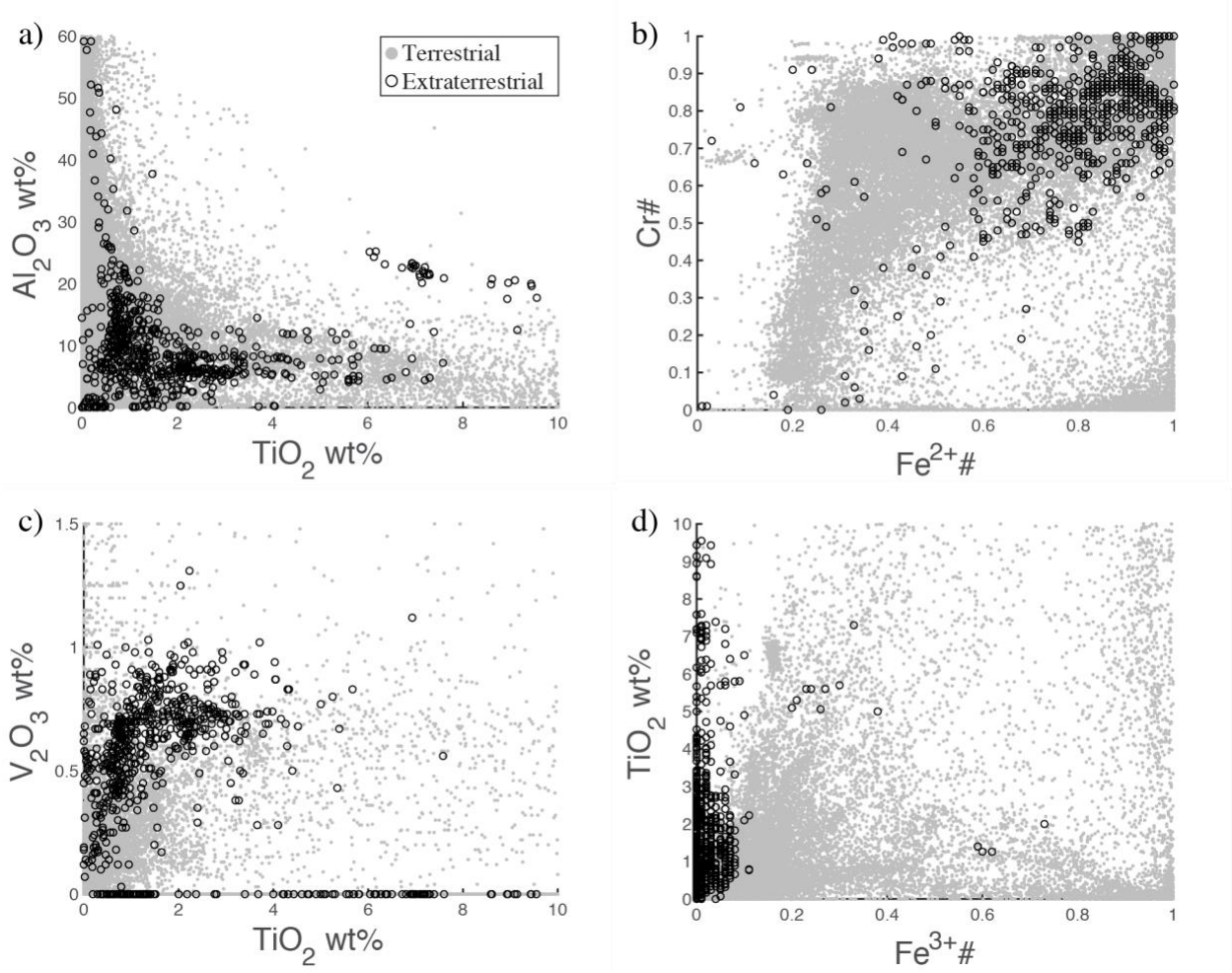

Figure 4.17. Chrome-spinel compositions from terrestrial (Barnes and Roeder, 2001) and extraterrestrial (Appendix C) sources. Cr# = Cr/(Cr+Al); Fe^{2+}# = Fe^{2+}/(Fe^{2+}+Mg); Fe^{3+}# = Fe^{3+}/(Fe^{3+}+Al+Cr).

4.5.3 Database Uses

Classifications

Compiling a modern meteorite chrome-spinel database with over 700 entries provides the abundances necessary for classifications, but the large amount of data and compositional overlaps makes it difficult to manually classify each remnant grain. Clustering techniques were implemented to constrain matches between Jurassic chrome-spinels and database entries to provide a manageable number of matches for manual classifications (Chapter 2). Hierarchical clustering compares all eight elements between all remnant grains and database entries simultaneously to find the closest matches. The closest matches are manually compared and a

final classification is determined using oxygen isotope values. Many of the Jurassic chrome-spinels had clearly defined chemical matches that were supported by oxygen isotopes (e.g., ordinary-chondrite-like grains). Some Jurassic grains were chemically matched with more than one meteorite type, but oxygen isotopes were used to determine the closest match. For a number of grains, termed Extraterrestrial, a parent meteorite type was not determined because the possible matches had overlapping oxygen isotope abundances. However, the isotope values of these grains showed that they had extraterrestrial origins. Implementing reliable $\delta^{18}O$ values and expanding upon the database will help to determine the parent meteorite types of the remaining extraterrestrial Jurassic grains, as well as to reliably classify grains from other time periods throughout the sedimentary record.

Grain Abundances

The Cr Kα X-ray maps were initially collected to determine the locations of possible chrome-spinel grains, but these maps may also help us to understand the diverse sizes and distributions of chrome-spinel grains among meteorite types (Fig. 4.18). Of the samples mapped, ordinary chondrites contain the most chrome-spinels with the largest surface areas. Within the equilibrated ordinary chondrites, the type 4 samples appear to have fewer grains and the surface areas are smaller compared to types 5 and 6. The eucrite and angrite samples appear to have similar sizes and abundances of grains to the type 4 ordinary chondrites. The CM2 map has the smallest number and size of chrome-spinels. These relative abundances align with the grains per gram values of dissolved modern meteorites from Heck et al. (2017) (See *Section 2.5.1 – Grains to Meteorites*). However, it is important to note that each map shows a limited region and may not entirely represent the chrome-spinel distribution of the bulk meteorite or of the meteorite type. While grain size and distribution is not within the scope of this study, mapping meteorite samples with greater resolution may ultimately improve our understanding of grain distributions to determine meteorite fluxes throughout history.

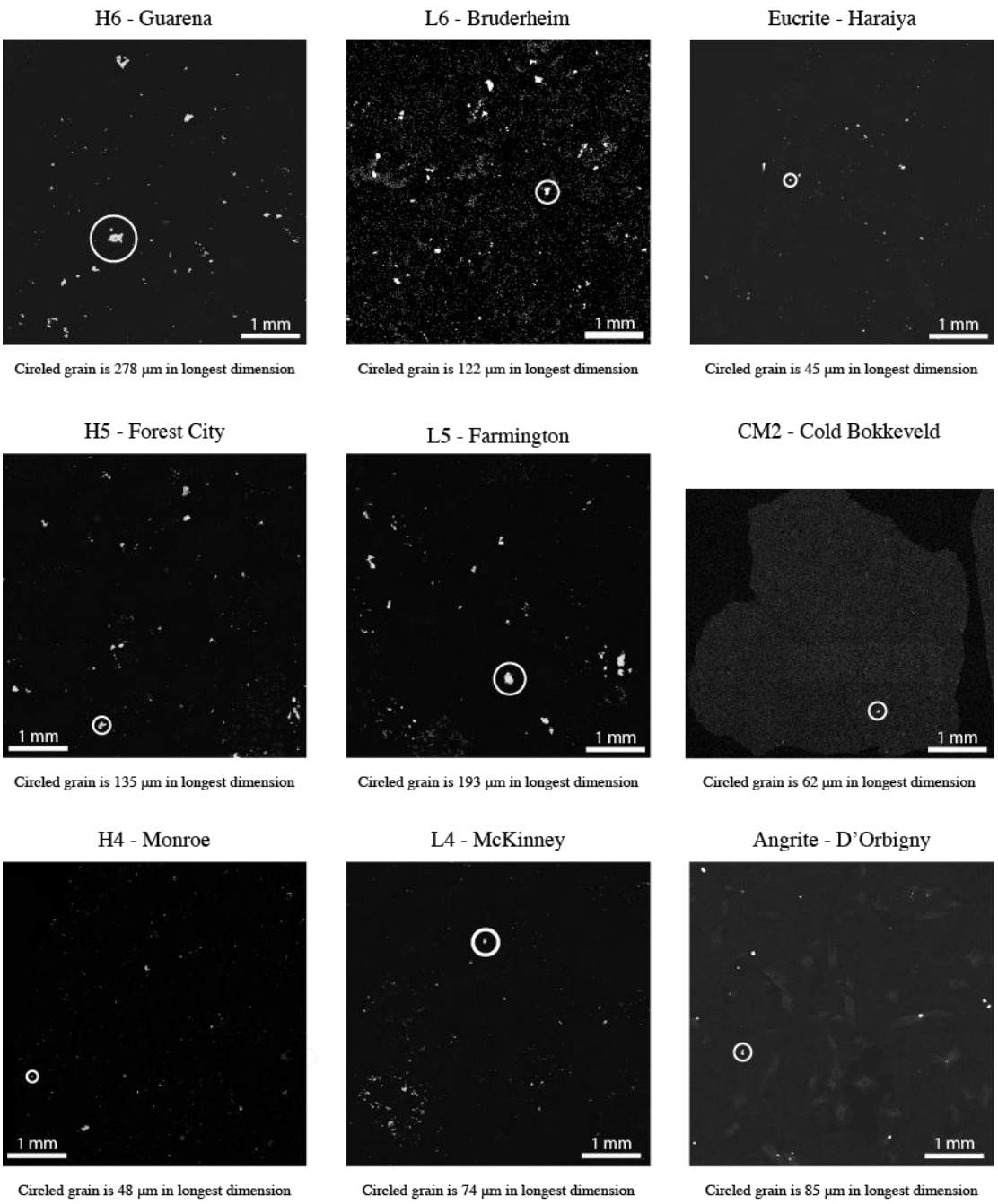

Figure 4.18. Cr Kα X-ray maps of modern meteorite sections. The brightest areas show higher concentrations of Cr, which suggest chrome-spinels. Each map was cropped to show the same area with the same 1 mm scale bar for direct comparison of grain size and distribution. The circle in each map identifies a representative grain and its longest dimension is noted below each map.

4.6 Conclusions

The chrome-spinel database was created to help classify remnant chrome-spinels in the sedimentary record to understand how meteorite populations have changed throughout Earth's history. The database was compiled from literature entries and new measurements of grains from modern meteorites. The new measurements were collected to fill gaps in the literature, increase the number of entries for specific meteorites types, and to compare the literature values to our new measurements. The new measurements showed good reproducibility and aligned with literature values. Compositional comparisons showed that meteorite types overlap, making it challenging to classify remnant chrome-spinels based on chemistry alone. This issue can be overcome by incorporating oxygen isotope abundances into the classification process, and has been shown to help with chrome-spinel grains from the Jurassic (Chapter 2).

While the database has been shown to be effective, there are still some limitations to address in order to create a more robust database. For example, a few meteorite types do not have compositional data or there are types that do not contain chrome-spinels. There are also meteorite types that need more entries in order to fully understand their compositional range. Additionally, the $\delta^{18}O$ shift between chrome-spinels and silicates showed that bulk $\delta^{18}O$ values are not reliable to help with the classification of chrome-spinels at this time. Fortunately, $\Delta^{17}O$ abundances can be used for classifications because it is consistent for chrome-spinel and bulk values. These limitations do not prevent reliable grain classifications, but additional measurements would create a more robust database.

Even with the current limitations, our database contains sufficient information to classify the parent meteorite types of the chrome-spinels from Jurassic sediment (Chapter 2). The compilation of a chrome-spinel database from modern meteorites is an ongoing process to which we have made a significant contribution, and the addition of chemical and isotopic abundances will continue to improve the classification and understanding of remnant grains throughout Earth's history.

Acknowledgments— The authors thank Jemma Davidson (Arizona State University) for the chrome-spinel grains from Bear Creek, Brenham, and Seymchan. Supported by NASA grant NNX16AQ08G to GRH and the ERC-Advanced Grant 213000 to BS.

CHAPTER 5

CRYSTAL ORIENTATION EFFECTS FOR OXYGEN-ISOTOPE MEASUREMENTS OF CHROME-SPINEL AND MAGNETITE

5.1 Abstract

Chrome-spinel from meteorite remnants in the terrestrial sediment record can be used to understand how the meteorite populations have changed throughout history. These grains can be classified into parent meteorites using their original chemical compositions and oxygen isotope abundances. Before parent meteorite types can be determined, we need to fully understand instrumental artifacts that could affect oxygen isotope abundances during ion probe measurements. Huberty et al. (2010) report a crystal-orientation fractionation effect for magnetite, which could also occur in chrome-spinel due to similarities in their crystal structures. To investigate this potential fractionation effect, we carried out a set of measurements to examine whether crystal orientation influences the oxygen isotopic ratios in chrome-spinel and compared these results with our own magnetite measurements. Crystal orientations of the grains were determined with electron backscatter diffraction (EBSD). We did not observe isotopic variations for chrome-spinels based on crystal orientation. A large range of oxygen isotope values was observed for the magnetite sample (3.2‰), but we were unable to attribute the variation to crystal orientation.

5.2 Introduction

Chrome-spinel ($FeCr_2O_4$), also known as chromite, is a refractory, alteration-resistant mineral in meteorites that can be used to determine meteorite populations throughout Earth's history. Extraterrestrial chrome-spinel grains are preserved in terrestrial sediment for millions of years and retain their original characteristics. The parent meteorite type can be determined based on the grain's chemical compositions and oxygen isotope abundances (Schmitz, 2013). However, it is necessary to understand potential instrumental artifacts that could affect $\delta^{18}O$ measurements before parent meteorites are assigned.

Huberty et al. (2010) considered four possible causes for variations in instrumental mass fractionation due to the properties of magnetite (Fig. 5.1). Two phenomena have been proposed

based on the structure of the sample: channeling of incident ions by the structure, and focusing of secondary ions by the structure (Benninghoven 1987). Channeling and focusing effects for face-centered cubic crystals are greatest when the ion beam is parallel to the [110]-type direction (Gnaser 2007) (Fig. 5.2). The [110] direction is crystallographically equivalent to the [101] and [011] directions because magnetite and chrome-spinel are cubic crystals. Huberty et al. (2010) report high measured $\delta^{18}O$ values when the incident beam is parallel to the preferred channeling and focusing directions for magnetite. Lyon et al. (1998) and Valley and Kita (2009) have also observed large variation in $\delta^{18}O$ due to varying crystal orientations for magnetite.

The crystal structures of chrome-spinel and magnetite are both hexoctahedral, face-centered cubic, with very similar unit cell lengths (a = 8.344Å and a = 8.397Å, respectively) (Fig. 5.3); therefore, the same $\delta^{18}O$ variation in magnetite may also occur in chrome-spinel. Thus far, chrome-spinel has not been shown to have variation in $\delta^{18}O$ (e.g., Valley and Kita, 2009). To investigate orientation effects on oxygen isotopes in magnetite and chrome-spinel by secondary ion mass spectrometry (SIMS), we measured randomly oriented grains in multi-grain terrestrial magnetite and chrome-spinel samples.

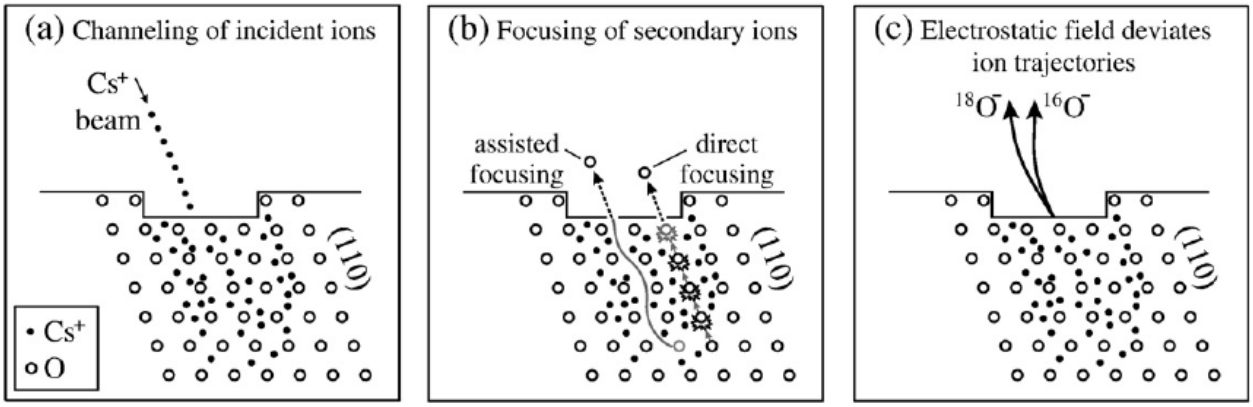

Figure 5.1. Possible crystal orientation effects that may occur during SIMS analysis (figure from Huberty et al., 2010).

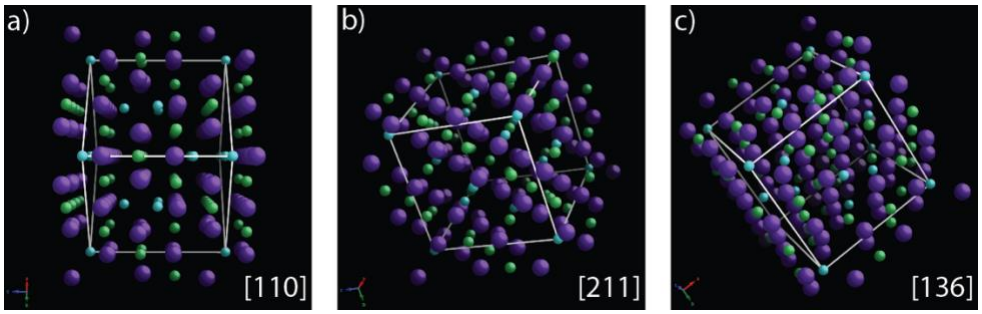

Figure 5.2. Chrome-spinel crystal orientations favorable (a,b) and unfavorable (c) for focusing and channeling. Purple = oxygen, blue = iron, and green = chromium.

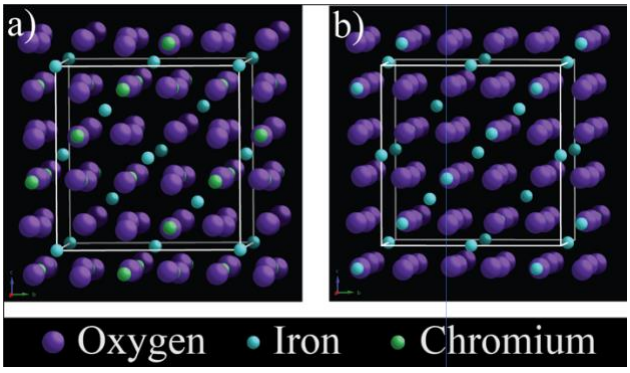

Figure 5.3. Crystal structures (slightly offset from [100]) of a) chrome-spinel and b) magnetite.

5.3 Methods

5.3.1 Samples and Preparation

To investigate the effects of crystal orientation in magnetite and chrome-spinel, we obtained natural samples consisting of many randomly oriented individual crystals. The magnetite sample is from a magnetite lava flow of the El Laco volcano in the Andean Cordillera of northern Chile (provided by J. Hammer). The chrome-spinel sample is from a lower cumulate chrome-spinel layer of the Stillwater complex on the northeastern margin of the Beartooth Mountains, Montana (Fig. 5.4). Each sample was cut into a one-inch round thick section, ground flat, and polished to 0.3 μm with alumina slurry. The void spaces of the magnetite sample were filled with epoxy prior to polishing. In preparation for electron backscatter diffraction (EBSD) analysis, the surface of sample needs to be polished flat so that each grain surface lies within the same plane and the only difference between grains is their orientation. The sample rounds were subjected to a final

polish with colloidal silica on a vibrating polisher to prepare the grain surfaces for electron backscatter diffraction (EBSD) analysis.

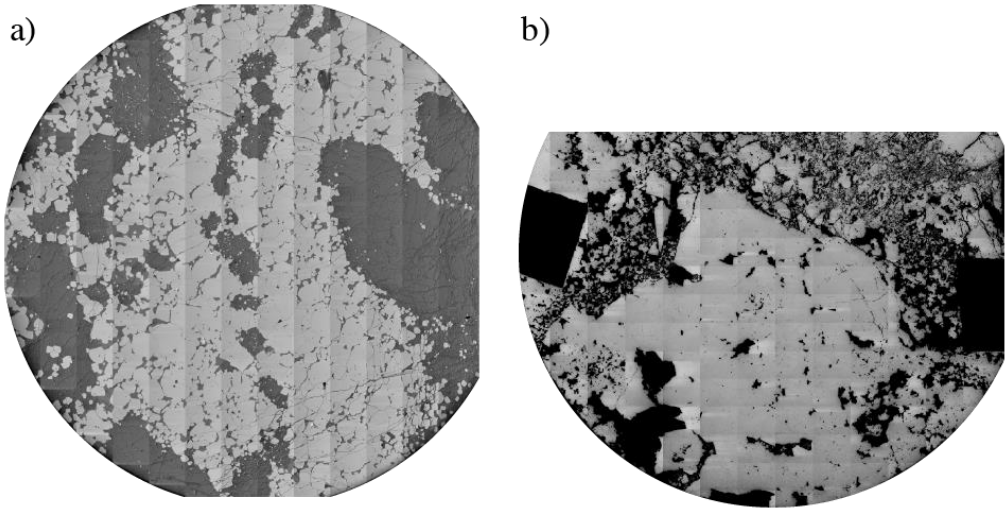

Figure 5.4. SEM backscatter electron montage images of the a) chrome-spinel and b) magnetite one-inch round sections. The lighter regions of a) are chrome-spinel and the darker regions are olivine. The lighter regions of b) are magnetite and the darker regions are epoxy.

5.3.2 Analysis

Crystal orientations were determined by EBSD using an Oxford Instruments Nordlys detector in the JEOL JSM-5900LV scanning electron microscope (SEM) at the University of Hawai‘i. The sample was analyzed using 20 kV accelerating voltage, sample tilt of 70°, and a working distance of 12-15 mm. The electron backscatter diffraction patterns (Fig. 5.5a) were processed using the Channel 5 software package. The straight bands in Figure 5.5b are Kikuchi bands, which are related to the lattice planes of the crystal. The geometry of these bands is used to determine the crystal orientation (Maitland and Sitzman, 2007).

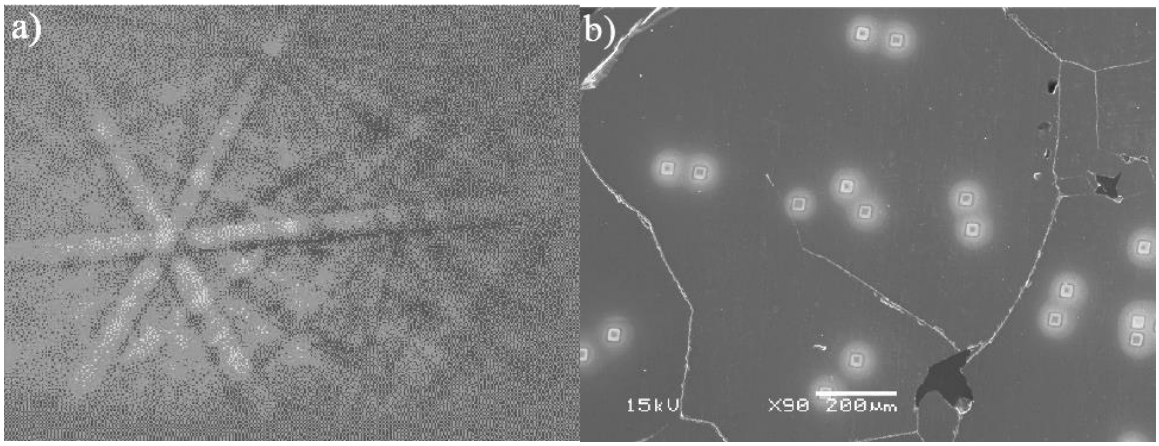

Figure 5.5. Representative chrome-spinel grain with a) an electron backscatter diffraction pattern, and b) secondary electron image with small square SIMS pits of the same grain.

Oxygen isotopes (^{16}O and ^{18}O) were measured in the magnetite and chrome-spinel grains using the Cameca ims 1280 ion microprobe at the University of Hawai'i. We used a ~2 nA Cs^+ primary beam focused to ~10 µm, and a 15x15 μm^2 raster. The sample was pre-sputtered for 120 seconds using a 2 nA beam and 25 μm^2 raster. Secondary $^{16}O^-$ and $^{18}O^-$ ions were counted in multi-collection mode using Faraday cups. The mass resolving power was set to ~2000. Each run consisted of 30 cycles of ~8 seconds each. Each SIMS spot was checked after isotope analyses with SEM imaging to ensure that measurement spots were free from cracks (Fig. 5.5b).

Measuring isotopic compositions with SIMS can be challenging. Small changes in instrument conditions can result in mass-fractionation effects that are larger than our measurement errors. Initial measurements of chrome-spinel were made without ensuring constant distance between the sample surface and the immersion lens. We corrected the beam position using the X deflector, but we found a systematic shift in $\delta^{18}O$ with position on the sample (and with X deflector setting). The procedure was modified to correct the beam position by adjusting sample height (with the stage Z control). Under the new conditions, the total range of $\delta^{18}O$ values exhibited by the chrome-spinel decreased from 2‰ to 0.5‰. Only data collected with a constant distance between the immersion lens and sample are shown in Section 5.4.

Each grain was analyzed in an original position and then with a 90° rotation for ion probe measurements. A 90° rotation provides a different orientation for SIMS measurements for a single grain. Measurements at two rotations permit observation of how different orientations affect $\delta^{18}O$ values within the same grain.

Crystal orientation is based on the surface that is detected by the EBSD detector, therefore if a crystal is tilted or rotated, the orientation changes relative to the detector. For the SIMS analyses, the Cs^+ primary beam is incident on the sample at ~20° to the normal; therefore, the orientation of a crystal relative to the incident ion beam is different from the orientation determined by EBSD. To interpret the SIMS results for the correct crystal orientation, the EBSD orientations must be tilted to the reference frame of the primary ion beam. We perform a coordinate transformation to account for this (e.g., Fig. 5.6). Orientations are reported in the reference frame of a plane perpendicular to the incident primary ion beam, except as noted.

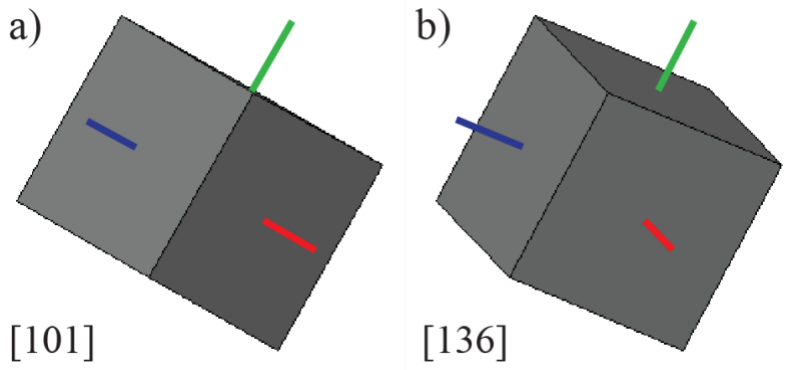

Figure 5.6. Three dimensional crystal structure of a sample chrome-spinel a) before and b) after a 20° tilt to account for the SIMS reference frame.

5.4 Results

Eighteen magnetite crystals and sixteen chrome-spinel crystals with a wide range of orientations were selected for SIMS analysis. Three to six individual measurements were made on each grain. EBSD analyses confirmed that individual grains were randomly oriented in both samples. After eliminating analysis spots that hit cracks, most measurements showed good reproducibility within individual grains. Magnetite exhibited a total range of $\delta^{18}O$ values of ~3‰ and chrome-spinel showed a range of ~0.5‰ (Fig. 5.7).

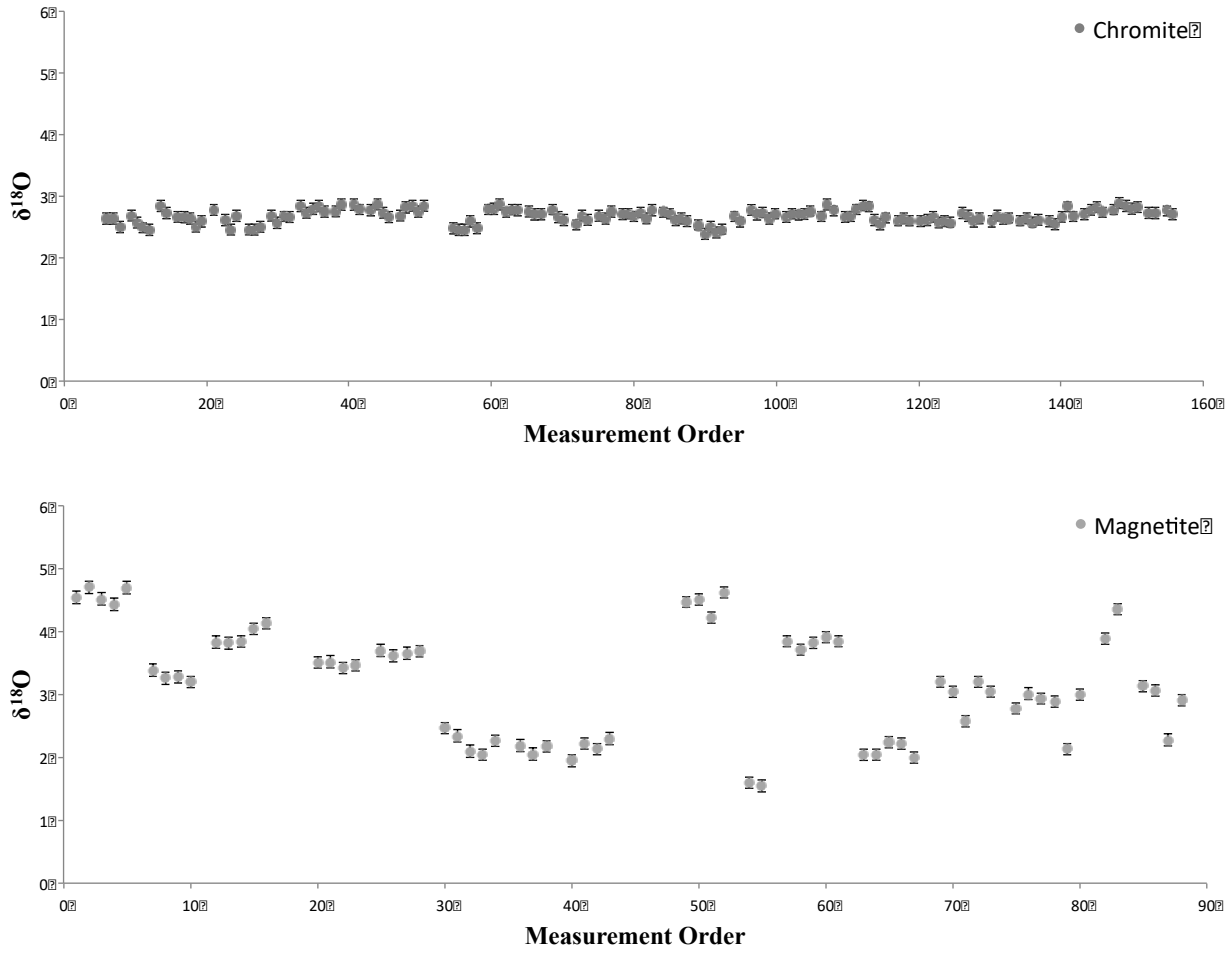

Figure 5.7. $\delta^{18}O$ values of chrome-spinel (top) and magnetite (bottom) grains based on measurement order. The chrome-spinel grains show a total $\delta^{18}O$ range of ~0.5‰ and the magnetite grains show a total $\delta^{18}O$ range of ~3‰. Error bars are 0.09‰ for magnetite and chrome-spinel measurements.

5.4.1 Inverse Pole Figures

Comparisons between oxygen isotope abundances and orientations for chrome-spinel and magnetite grains can be shown using inverse pole figures (Figs. 5.8 and 5.9). Inverse pole figures show the orientation of a grain relative to the standard triangle for cubic crystal structures, with directions [001], [101], and [111]. Oxygen isotopic compositions are shown within the inverse pole figures using a color gradient. An orientation effect would be indicated by a grouping of one color near a specific direction. Figures 5.8 and 5.9 show two inverse pole figures each; the first contains measurements made at the original sample position in the SIMS, and the second, at 90° rotation from the original position. We measured two SIMS sample orientations to see how the

change in orientation for a single grain changes $\delta^{18}O$ values. Based on Huberty et al. (2010) observations, the [101] direction should have higher $\delta^{18}O$ values; therefore if a grain were originally near the [101] direction then rotated away from that direction then one would expect a decrease in the $\delta^{18}O$ value of that grain.

The chrome-spinel sample does not show an orientation effect in either SIMS sample orientation because there are no defined clusters of $\delta^{18}O$ values (Fig. 5.8). Also, a difference between $\delta^{18}O$ values based on sample rotation was not observed for single chrome-spinel grains. It is difficult to observe orientation affects for this chrome-spinel sample because the range in $\delta^{18}O$ values across the entire sample is small relative to the magnetite range, 0.5‰ versus 3‰, respectively (Figs. 5.8 and 5.9).

Similar to the chrome-spinel sample, there is no clearly defined clustering of $\delta^{18}O$ values based on grain orientation in the magnetite sample (Fig. 5.9). There is a small cluster $\delta^{18}O$ values near the [101] orientation for the grains measured in the 90° rotation, but is it not clearly defined group because there are measurements with similar orientations but higher $\delta^{18}O$ values. Also, we would expect higher values in this region based on Huberty et al. (2010) observations, not lower values. While no clear orientation affects are observed for the magnetite sample, individual grains did show different $\delta^{18}O$ values between the original and 90° rotation (Fig. 5.10). The first example (Grain 1) had nearly the same orientation on the pole figure and the $\delta^{18}O$ value changed by more than 1‰. If there were an orientation affect, then the similar directions would be expected to have similar $\delta^{18}O$ values. The second example (Grain 2) changed orientations on the pole figure from near the [101] orientation to near the [111] orientation and showed an increase in $\delta^{18}O$ greater than 1‰. The change in $\delta^{18}O$ is expected, but the higher value is expected to be near [101] and not near [111]. The remaining magnetite grains in our measurements showed varied $\delta^{18}O$ differences based on SIMS sample orientation.

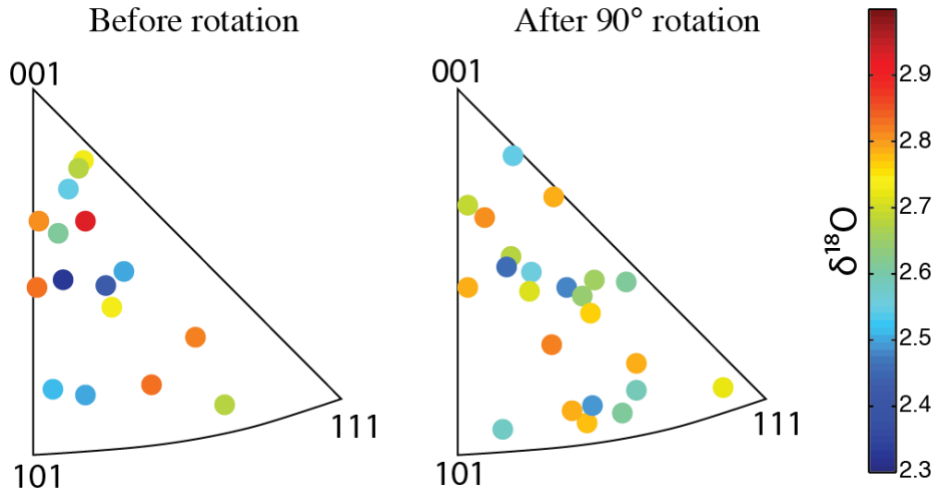

Figure 5.8. Chrome-spinel inverse pole figures a) before rotation and b) after a 90° rotation. The vertical color bar represents $\delta^{18}O$ values. The directions [001], [101], and [111] define the standard triangle for cubic crystal structures.

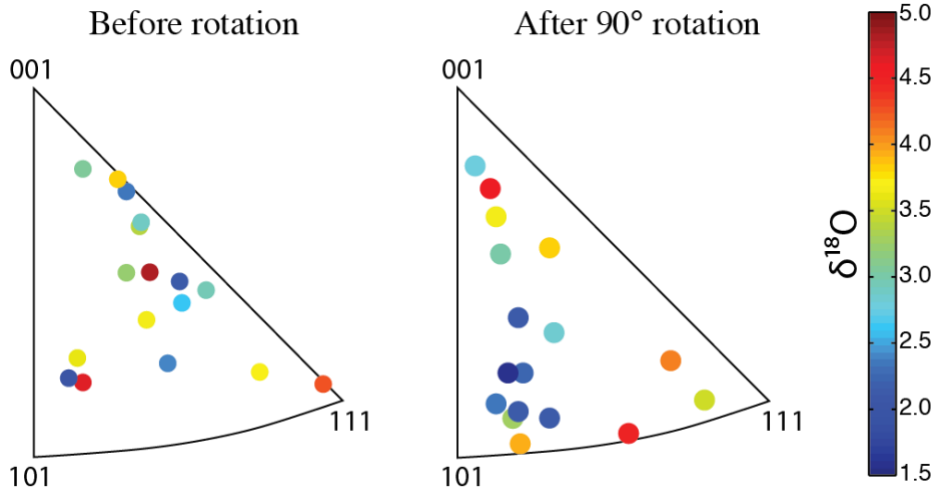

Figure 5.9. Magnetite inverse pole figures a) before rotation and b) after a 90° rotation. The vertical color bar represents $\delta^{18}O$ values. The directions [001], [101], and [111] define the standard triangle for cubic crystal structures.

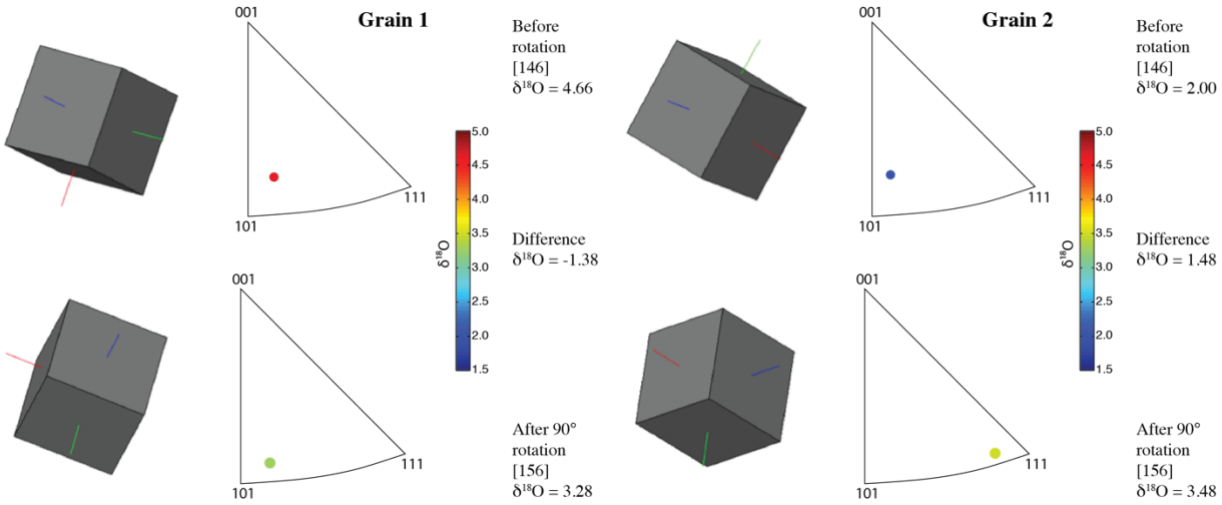

Figure 5.10. Inverse-pole figures and orientations for representative magnetite a) grain 1 and b) grain 2. Both grains show $\delta^{18}O$ values and orientations before and after the 90° rotation sample rotation. The directions [001], [101], and [111] define the standard triangle for cubic crystal structures.

5.4.2 SIMS pit textures

SIMS pits were imaged after each session to ensure that the measurements did not hit cracks. We also observed differing pit textures between the chrome-spinel and magnetite samples. Measurement pits of the chrome-spinel grains showed smooth textures, while all pits in the magnetite grains showed various degrees of cratering (Figs. 5.11 and 5.12). For some magnetite grains, lower $\delta^{18}O$ values correspond with more abundantly cratered SIMS pits within the same grain (e.g., Fig. 5.12). Comparisons between cracked and non-cracked SIMS pits show that cracks correlate with lower $\delta^{18}O$ values within the same grain (e.g., Fig. 5.13). The crack in grain 1 is also shown to have widened throughout the SIMS measurement, which may have also affected the change in $\delta^{18}O$ compared to the non-cracked pit.

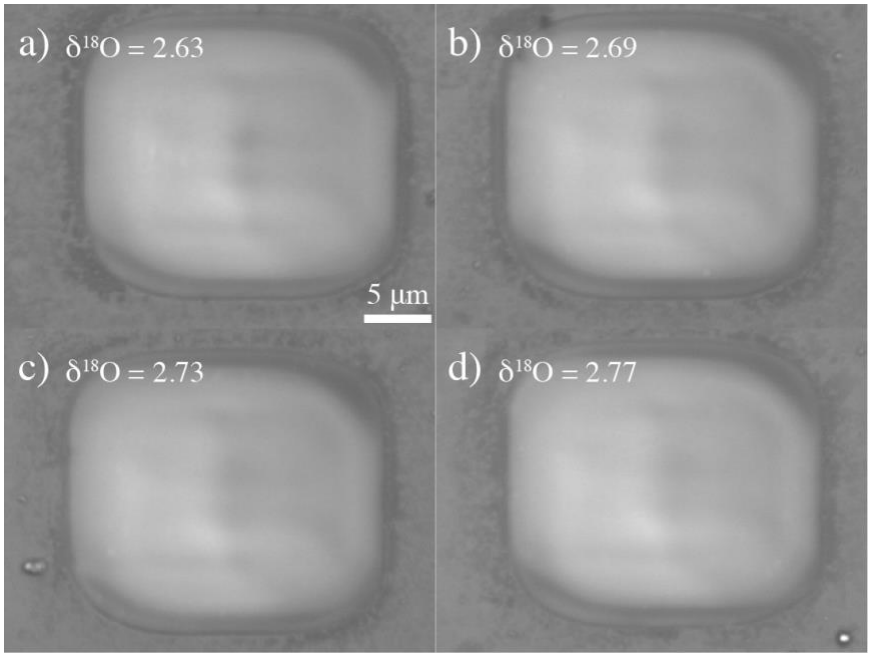

Figure 5.11. SIMS pits of chrome-spinel grains are smooth and show little variation in $\delta^{18}O$ values.

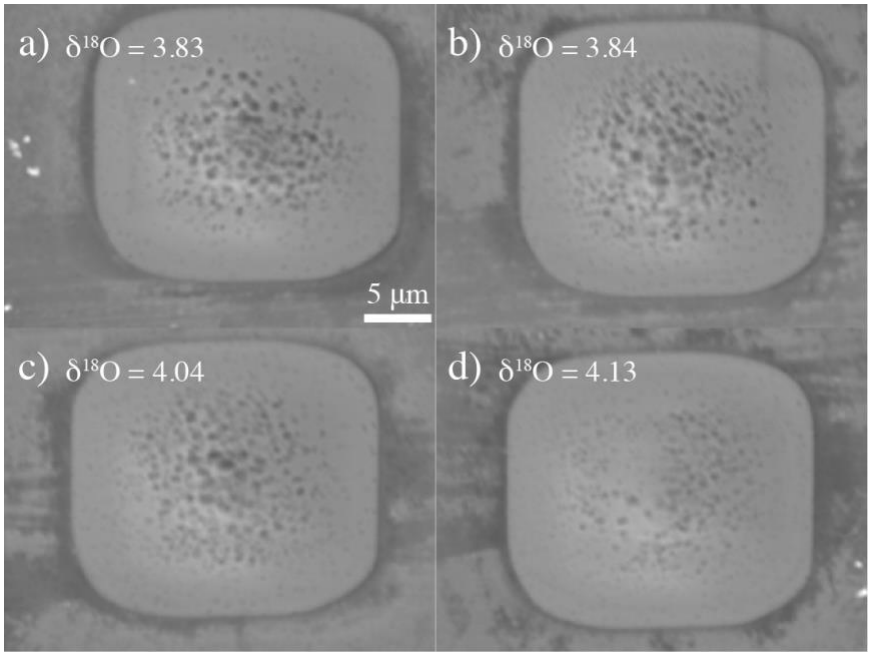

Figure 5.12. SIMS pits of magnetite grains contain small craters of varying intensities. These four SIMS pits are from the same magnetite grain and show different degrees of cratering that may be connected to $\delta^{18}O$ variations.

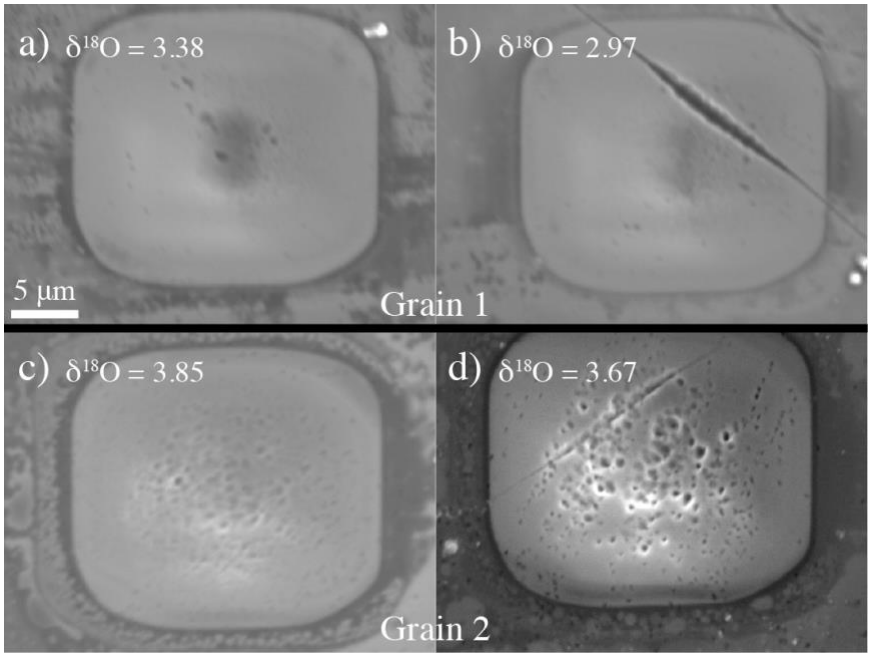

Figure 5.13. SIMS pits in two magnetite grains with (b, d) and without cracks (a, c). Cracks give different $\delta^{18}O$ values, especially if they are larger. Cracks widen during SIMS measurements.

5.5 Discussion

The goal of comparing grain orientations and SIMS measurements was to determine if there are instrumental artifacts for chrome-spinel grains that could affect oxygen isotope values, which are needed for classifying parent meteorite types. SIMS measurements of chrome-spinel show little variability, ~0.5‰, and there is no evidence that crystal orientation affects $\delta^{18}O$ values in chrome-spinel. Thus, oxygen isotopes measurements of remnant chrome-spinels can be reliably used for the classification of grains into parent meteorite types without concern for crystal orientation based instrumental artifacts.

Magnetite grains were measured to reproduce what has been observed in previous studies by Huberty et al. (2010) and Lyon et al. (1998) who observed high $\delta^{18}O$ values near the [101] direction for magnetite. Huberty et al. (2010) hypothesized that the electrostatic field between sample surface and extraction plate may deviate secondary ion trajectories based on crystal orientations (Fig. 5.1c). The trajectories of secondary ions ($^{16}O^-$ and $^{18}O^-$) are affected differently depending on emission angles. In the case of $^{16}O^-$ and $^{18}O^-$, $^{16}O^-$ is easier to deflect because it is lighter. When the grain is oriented in the preferred direction with respect to the mass spectrometer, [101], then both $^{16}O^-$ and $^{18}O^-$ go straight into the mass spectrometer and are not

fractioned. However, when the grain is orientated away from the preferred direction (i.e., change in emission angle), then $^{16}O^-$ is more accepted by the mass spectrometer than $^{18}O^-$ as $^{16}O^-$ is more easily deflected. As a result, the measured $\delta^{18}O$ becomes lower in varying degrees depending on emission angles. Huberty et al. (2010) observed this effect for magnetite, but we did not see clear evidence that the orientation of magnetite grains directly influences the $\delta^{18}O$ values. However, we did observe small craters in the magnetite SIMS pits, which may be due to the grain structure and possibly correlate with $\delta^{18}O$ variations, but this requires further investigation (Fig. 5.12). Overall, we observed a $\delta^{18}O$ variation in magnetite, but did not see the same correlation between orientation and $\delta^{18}O$ as Huberty et al. (2010) and Lyon et al. (1998).

The final possibility for the $\delta^{18}O$ variation is the magnetic field of magnetite shifting ion trajectories. This is a significant difference between magnetite and chrome-spinel. Huberty et al. (2010) carried out experiments to test this possibility and discounted the magnetic field as the cause of the observed fractionations.

5.6 Conclusions

We prepared and carefully documented samples of magnetite and chrome-spinel and measured $\delta^{18}O$ in crystals with a wide range of orientations. We found no isotopic variations for chrome-spinel that can be attributed to crystallographic orientation. While we found larger variation in $\delta^{18}O$ in magnetite compared to those in chrome-spinel (range of 3.2‰ versus 0.5‰, respectively), we are so far unable to attribute this variation to crystal orientation in the ion probe. A possible explanation for some of the variation in $\delta^{18}O$ for magnetite might be due to the small craters that developed in the SIMS pits. Our observations also showed that cracks crossing through the ion probe pit were excavated and widened by the ion beam, resulting in lower $\delta^{18}O$ values. Overall, there is no observable orientation effect or significant $\delta^{18}O$ variation in chrome-spinel that would impede the classification of chrome-spinels into parent meteorite types.

Acknowledgments— The authors thank John Sinton for the chrome-spinel sample, and Scott Sitzman for help with the EBSD software. Supported by NASA grant NNX14AI19G to GRH.

CHAPTER 6

CONCLUSIONS

This dissertation presents the process of classifying remnant extraterrestrial chrome-spinel grains to determine meteorite abundances of the Jurassic.

Chapter 2 classified remnant chrome-spinel grains from Jurassic sediments using chemical compositions and oxygen isotope abundances. Hierarchical clustering was implemented to provide likely matches for remnant grains on a manageable scale. The classifications and knowledge of grains/gram abundances suggest that achondrites had similar or higher meteorite abundances compared to ordinary chondrites, unlike today. The Jurassic sample also contained High-Al grains with distinct compositions that are unlike those in the compiled database (Chapter 4). Comparisons between the Jurassic classifications and those of other time periods showed that meteorite abundances have gradually changed from the Ordovician to today. However, the abundances of time periods can be affected by classification methodologies. The comparison of methodologies showed that relying on chemistry alone can create classification bias for certain meteorite types. The classification process of the Jurassic grains showed that the addition of oxygen isotopes is helpful for classifying grains and distinguishing between terrestrial and extraterrestrial sources.

Chapter 3 evaluated the use of FIB and S/TEM techniques on small inclusions within chrome-spinels for the classification of parent meteorite types. Analyses of sections showed that many of the inclusions were heavily altered by terrestrial aqueous activity and could not be used to help classify their parent meteorite types. However, inclusions from one grain were only slightly altered and their compositions suggested an L-chondrite origin. Analyses of inclusions from an Ordovician remnant grain, Brunflo, confirmed that inclusions >3 μm in diameter at the polished surface are typically large enough for reliable SEM-EDS analyses, whereas smaller inclusions must be measured using S/TEM techniques. We also observed that chrome-spinel grains and their inclusions can be more complicated than expected, including alteration rims of inclusions and chrome-spinel lamellae.

Chapter 4 compiled a database of chemical compositions and oxygen isotope abundances for the classification of extraterrestrial chrome-spinels into parent meteorite types. Compositional

comparisons showed that meteorite types overlap, but types can be differentiated with the use of oxygen isotope abundances. The combination of chemistry and isotopes was shown to help with the classification of chrome-spinels from the Jurassic (Chapter 2). New oxygen isotope measurements of chrome-spinels grains show that there is a $\delta^{18}O$ shift between chrome-spinels and silicates, suggesting that bulk $\delta^{18}O$ values are not reliable for chrome-spinel classifications at this time. Fortunately, $\Delta^{17}O$ abundances were shown to be consistent between chrome-spinel and bulk values; therefore, these values can be used for reliable parent meteorite classifications. The formulation of a chrome-spinel database is an ongoing process and will become more robust as more entries and new measurements are added.

Chapter 5 demonstrated that there are no orientation effects within chrome-spinel for ion microprobe measurements of oxygen isotopes. Large variations of $\delta^{18}O$ in magnetite were observed, but we were unable to connect this variation to crystal orientation in the ion probe. Overall, chrome-spinel measurements in the ion microprobe are reliable and can be used the help with the classification of remnant grains into parent meteorite types.

APPENDIX A. COMPOSITIONS AND CLASSIFICATIONS OF JURASSIC CHROME-SPINELS

Table A.1. Chemical compositions, oxygen isotopes, and classifications (first and second order) for Jurassic chrome-spinels.

Grain	MgO	Al_2O_3	TiO_2	V_2O_3	Cr_2O_3	MnO	All FeO	FeO	Fe_2O_3	ZnO	SiO_2	Total	$\delta^{18}O$	2 SD	$\delta^{17}O$	2 SD	$\Delta^{17}O$	2 SD	1st Order	2nd Order
m3_G12	2.20	6.65	1.76	0.76	57.36	0.64	27.77	27.77	0.00	0.87	0.00	98.01	-2.78	0.73	-0.56	0.54	0.88	0.53	H	
m3_G13	2.71	6.41	2.41	0.70	58.19	0.69	26.57	26.57	0.00	0.37	0.00	98.03	-2.30	0.49	-0.46	0.52	0.74	0.48	H	
m4_G12	3.12	6.91	2.02	0.68	57.90	0.87	25.72	25.72	0.00	1.64	0.00	98.86	-4.46	0.82	-1.46	0.56	0.86	0.52	H	
m4_G13	2.80	6.48	2.33	0.68	57.50	0.71	25.39	25.39	0.00	2.52	0.00	98.41	-2.85	1.19	-0.52	1.09	0.97	0.65	H	
m5_G13	3.32	6.55	2.22	0.70	57.92	0.95	27.06	27.06	0.00	0.23	0.00	98.95	-4.62	0.85	-1.77	0.54	0.63	0.47	H	
m6_G06	2.63	6.62	1.88	0.72	58.29	0.73	25.96	25.96	0.00	0.97	0.01	97.80	-6.43	1.13	-1.94	0.64	1.40	0.54	H	
m8_G02	3.37	6.39	2.33	0.67	57.89	0.66	23.28	23.28	0.00	3.38	0.00	97.97	-2.22	1.02	-0.34	0.64	0.82	0.50	H	
sm1_G06	2.87	6.76	1.78	0.76	57.67	0.83	27.35	27.35	0.00	0.60	0.00	98.62	-5.30	1.09	-1.68	0.73	1.07	0.63	H	
sm1_G09	2.45	6.67	2.34	0.70	58.99	0.61	18.75	18.75	0.00	6.74	0.00	97.25	-2.81	1.46	-1.01	0.88	0.45	0.74	H	
sm1_G13	2.68	7.05	1.70	0.76	57.77	0.87	24.38	24.38	0.00	3.78	0.00	98.99	-3.30	1.68	-1.21	0.83	0.51	0.68	H	
sm1_G16	2.65	6.79	1.93	0.71	57.29	0.74	28.18	28.18	0.00	0.37	0.00	98.67	-4.73	1.34	-1.70	0.76	0.76	0.65	H	
sm3_G03	3.66	6.68	2.22	0.69	61.26	0.80	17.72	17.72	0.00	6.22	0.00	99.25	-2.05	1.34	-0.86	0.86	0.20	0.73	H	
sm3_G04	2.20	5.59	2.27	0.63	57.51	0.79	19.49	19.49	0.00	9.99	0.00	98.46	-2.53	1.55	-0.69	0.96	0.62	0.65	H	
sm3_G12	2.69	5.91	1.56	0.72	55.49	0.81	23.30	23.30	0.00	3.02	0.00	93.50	-4.40	2.78	-1.45	0.76	0.84	0.86	H	
sm3_G17	3.30	6.33	2.22	0.69	57.74	0.77	24.32	24.32	0.00	3.32	0.00	98.69	-2.80	3.06	-0.64	2.18	0.82	0.59	H	
sm3_G27	3.24	6.62	2.14	0.71	57.72	0.75	27.39	27.39	0.00	0.39	0.00	98.98	-3.39	2.08	-1.03	0.89	0.74	0.74	H	
sm3_G30	2.63	6.51	2.41	0.69	57.31	0.88	27.53	27.53	0.00	0.92	0.00	98.88	-5.23	1.29	-2.02	0.65	0.70	0.45	H	
sm3_G31	2.68	6.46	2.31	0.66	57.23	0.70	22.75	22.75	0.00	6.08	0.00	98.87	-3.52	1.13	-1.16	0.86	0.67	0.55	H	
sm4_G02	2.35	6.67	2.06	0.67	57.64	0.69	26.34	26.24	0.11	0.16	0.00	96.58	-5.74	2.26	-2.33	1.17	0.66	0.60	H	
sm4_G28	2.35	5.80	2.14	0.64	57.66	0.68	13.52	13.52	0.00	15.93	0.00	98.72	-0.45	3.35	0.33	1.80	0.56	0.59	H	
sm4_G31	2.32	7.46	1.60	0.75	57.10	0.77	24.76	24.76	0.00	3.80	0.00	98.55	-4.55	1.27	-1.63	0.68	0.74	0.39	H	
sm4_G32	2.72	7.12	1.83	0.74	57.04	0.55	22.99	22.99	0.00	5.53	0.00	98.53	-3.24	1.40	-0.93	0.94	0.76	0.70	H	

sm4_G35	2.92	7.01	1.39	0.76	57.76	0.82	22.79	22.79	0.00	4.87	0.00	98.31	-4.46	1.62	-0.94	0.96	1.38	0.64	H
m2_G04	2.41	6.45	2.27	0.66	57.33	0.59	19.99	19.99	0.00	7.67	0.00	97.36							H
m3_G03	1.93	5.12	2.10	0.74	54.61	0.59	22.92	22.92	0.00	5.07	0.01	93.11							H
m8_G06	3.61	7.12	2.15	0.66	57.13	0.50	21.03	21.03	0.00	1.10	0.04	93.35							H
sm3_G22	2.67	6.69	1.88	0.73	57.05	0.83	27.17	27.17	0.00	0.89	0.00	97.92							H
sm4_G19	5.19	6.16	2.19	0.67	57.54	0.39	19.49	19.49	0.00	6.33	0.00	97.95							H
sm4_G33	2.26	6.52	1.47	0.75	57.54	0.75	18.27	18.27	0.00	11.17	0.00	98.73							H
m1_G02	2.71	5.54	3.12	0.65	57.04	0.60	28.50	28.50	0.00	0.36	0.00	98.52	-1.82	0.51	0.01	0.48	0.96	0.51	L
m1_G04	2.50	5.73	2.74	0.72	56.97	0.65	28.29	28.29	0.00	0.78	0.00	98.38	-1.60	0.48	0.44	0.49	1.27	0.48	L
m2_G03	4.13	6.27	2.42	0.66	58.18	0.93	24.68	24.68	0.00	0.70	0.01	97.97	-2.51	0.42	-0.28	0.57	1.02	0.58	L
m4_G01	3.07	6.06	3.23	0.75	55.22	0.46	29.13	29.13	0.00	0.24	0.00	98.16	-3.27	0.57	-0.74	0.45	0.96	0.49	L
m6_G15	2.46	5.52	3.28	0.65	56.90	0.54	28.08	28.08	0.00	0.33	0.01	97.78	-4.92	1.90	-0.98	1.35	1.58	0.50	L
m7_G14	2.54	5.85	3.04	0.69	56.80	0.68	25.21	25.21	0.00	2.30	0.00	97.13	-5.22	2.65	-0.88	1.34	1.84	0.41	L
m8_G08	4.64	6.52	2.46	0.62	58.31	0.83	22.88	22.88	0.00	1.18	0.01	97.45	-5.83	3.28	-1.67	1.95	1.36	0.52	L
sm1_G07	2.06	5.95	2.97	0.66	57.27	0.55	28.90	28.90	0.00	0.22	0.00	98.57	-5.01	1.28	-0.99	0.90	1.61	0.69	L
sm1_G14	4.10	5.25	1.53	0.57	55.62	0.54	23.06	23.06	0.00	0.59	0.00	91.27	-2.74	1.37	-0.61	0.78	0.82	0.68	L
sm1_G15	2.41	5.62	2.83	0.68	57.59	0.66	28.22	28.22	0.00	0.45	0.00	98.47	-4.66	1.28	-1.20	0.78	1.22	0.68	L
sm1_G23	4.56	5.37	1.88	0.66	60.61	1.26	21.55	21.55	0.00	3.20	0.00	99.10	0.79	1.12	1.37	0.70	0.97	0.67	L
sm3_G01	3.10	4.77	3.67	0.70	56.60	0.56	28.61	28.61	0.00	0.30	0.00	98.31	-4.66	1.33	-0.81	0.78	1.61	0.57	L
sm3_G05	2.98	5.32	1.56	0.74	59.36	1.05	14.48	14.48	0.00	13.20	0.00	98.69	-0.24	1.58	0.56	0.85	0.68	0.60	L
sm3_G16	6.81	6.32	2.31	0.61	59.32	0.58	21.27	21.27	0.00	1.84	0.00	99.06	-1.25	1.40	0.39	0.76	1.05	0.46	L
sm3_G24	3.25	4.90	1.31	0.77	60.17	0.75	19.45	19.45	0.00	8.17	0.00	98.76	0.50	1.36	1.72	0.75	1.46	0.44	L
sm4_G06	2.15	5.81	2.96	0.66	57.13	0.56	28.24	28.24	0.00	0.24	0.00	97.74	-5.72	2.09	-1.84	1.05	1.14	0.51	L
sm4_G09	3.04	5.43	1.80	0.67	59.19	1.12	21.16	21.16	0.00	6.30	0.00	98.70	-2.39	2.81	-0.07	1.16	1.17	0.52	L
sm4_G27	4.91	5.87	3.34	0.72	56.95	0.52	26.07	26.07	0.00	0.35	0.00	98.74	-3.51	1.31	-0.39	0.79	1.44	0.54	L
m3_G02	1.34	6.11	3.91	0.79	57.02	0.45	24.44	24.44	0.00	0.43	0.01	94.50	-1.59	0.56	0.78	0.46	1.61	0.56	LL
m5_G10	1.48	5.59	3.42	0.77	56.60	0.47	29.17	29.17	0.00	0.30	0.00	97.80	-2.34	1.84	0.07	0.95	1.28	0.46	LL
m7_G13	1.66	5.93	2.40	0.77	56.62	0.57	29.61	29.61	0.00	0.45	0.00	98.00	-3.30	0.66	0.05	0.47	1.77	0.44	LL
sm1_G01	1.41	4.47	3.29	0.64	54.08	0.43	27.76	27.76	0.00	0.27	0.00	92.35	-4.10	0.98	-0.30	0.71	1.83	0.61	LL
sm1_G12	1.64	5.85	2.65	0.71	56.66	0.48	30.08	30.08	0.00	0.43	0.00	98.52	-5.12	1.39	-1.23	0.91	1.43	0.68	LL
sm1_G08	2.09	6.25	3.15	0.74	55.00	0.43	29.95	29.95	0.00	0.25	0.00	97.87							LL

sm1_G11	8.45	7.27	1.77	0.73	57.99	0.52	20.08	20.07	0.02	0.46	0.00	97.28	0.25	1.26	0.87	0.64	0.73	0.95	Ord	H
sm4_G08	2.80	7.07	1.99	0.73	59.36	0.53	22.40	22.40	0.00	0.44	0.00	95.32	-4.00	2.21	-1.28	1.20	0.81	0.52	Ord	H
m4_G10	1.41	3.84	1.00	0.56	50.41	0.72	20.64	20.64	0.00	2.75	0.00	81.32	-3.83	0.79	-1.39	0.49	0.60	0.46	Ord	H/L
m7_G03	2.52	6.73	2.50	0.71	61.20	0.76	19.27	19.27	0.00	0.68	0.01	94.37	-3.92	0.52	-0.96	0.41	1.08	0.39	Ord	H/L
sm4_G03	3.88	5.60	2.60	0.63	59.24	0.36	22.18	22.18	0.00	0.24	0.08	94.81	-4.18	2.33	-1.54	1.20	0.63	0.53	Ord	H/L
sm4_G18	2.83	4.42	1.90	0.70	60.86	1.01	23.60	23.60	0.00	2.19	0.00	97.51	-4.15	2.21	-0.77	0.93	1.38	1.26	Ord	H/L
sm4_G24	4.92	7.62	1.81	0.73	57.80	0.80	24.73	24.73	0.00	0.36	0.00	98.77	-2.85	1.35	-0.75	0.78	0.73	0.47	Ord	H/L
sm4_G25	2.46	5.75	2.97	0.64	56.41	0.51	23.30	23.30	0.00	5.71	0.00	97.74							Ord	H/L
sm4_G39													-4.30	1.64	-1.25	1.00	0.98	0.64	Ord	H/L
sm1_G25													-5.71	1.51	-2.28	0.91	0.70	0.66	Ord	H/L
m8_G13	2.08	5.81	2.99	0.66	57.98	0.60	26.42	26.42	0.00	0.29	0.01	96.85	-3.56	1.21	-0.19	0.79	1.66	0.55	Ord	H/LL
sm4_G20	1.76	6.64	2.50	0.70	60.99	0.49	22.24	22.24	0.00	0.27	0.00	95.59	-4.18	1.36	-1.04	0.74	1.14	0.52	Ord	L
sm1_G24													-3.03	1.66	-0.23	0.80	1.34	0.39	Ord	L/LL
sm4_G40													-1.76	1.38	0.39	0.87	1.30	0.63	Ord	L/LL
sm3_G29	7.78	14.51	0.61	0.46	50.94	0.19	24.39	22.71	1.86	0.01	0.14	99.22	-1.81	1.21	-3.62	0.74	-2.68	0.53	CM2	
sm4_G10	4.61	19.14	1.06	0.57	46.33	0.25	26.54	26.54	0.00	0.02	0.00	98.52	0.43	1.99	-1.77	1.05	-2.00	0.55	CM2	
m5_G04	12.85	22.37	0.02	0.13	48.01	0.17	14.93	14.93	0.00	0.13	0.01	98.61	4.09	0.57	2.43	0.48	0.30	0.55	CR2	
m6_G14	12.71	23.79	0.08	0.19	45.34	0.19	15.07	15.07	0.00	0.15	0.00	97.53	8.51	3.81	3.41	1.46	-1.02	0.58	CR2	
m8_G03	12.53	20.98	0.18	0.11	47.04	0.25	15.88	14.81	1.20	0.15	0.10	97.34	6.84	0.89	3.01	0.63	-0.55	0.52	CR2	
m8_G09	13.46	24.86	0.01	0.14	45.19	0.17	14.06	14.06	0.00	0.15	0.00	98.06	8.03	2.50	3.46	1.16	-0.72	0.61	CR2	
sm3_G15	12.76	24.06	0.03	0.24	45.35	0.21	15.83	15.58	0.27	0.16	0.00	98.65	6.84	1.36	2.91	0.68	-0.64	0.63	CR2	
sm3_G25	11.08	21.95	0.16	0.18	44.87	0.16	17.90	17.15	0.83	0.06	0.04	96.50	6.44	1.15	2.72	0.71	-0.63	0.47	CR2	
sm4_G11	3.22	6.79	0.44	0.92	60.26	0.54	25.94	25.94	0.00	0.03	0.00	98.14	-5.26	3.44	-3.00	1.49	-0.26	0.53	Di	
sm4_G22	2.80	6.69	0.13	0.91	59.16	0.66	15.30	15.30	0.00	12.27	0.00	97.92	0.67	2.63	-0.08	1.56	-0.43	0.61	Di	
m3_G17	18.32	16.49	0.48	0.47	56.28	0.14	6.53	6.50	0.03	0.03	0.00	98.75	0.86	0.80	-2.05	0.58	-2.50	0.49	Ur	
m4_G04	10.31	18.67	0.01	0.26	49.38	0.25	19.31	18.25	1.17	0.32	0.00	98.63	4.64	0.54	1.75	0.51	-0.66	0.53	Ur	
m4_G05	11.19	16.24	0.02	0.24	52.52	0.25	18.00	16.59	1.57	0.39	0.00	99.01	4.31	0.56	1.80	0.51	-0.44	0.50	Ur	
m5_G06	11.38	20.30	0.01	0.18	49.51	0.24	17.03	17.03	0.00	0.20	0.01	98.85	5.37	1.79	2.69	1.11	-0.10	0.50	Ur	
m6_G01	11.41	17.99	0.08	0.21	51.76	0.22	16.71	16.60	0.12	0.24	0.01	98.64	6.95	2.57	3.13	1.37	-0.49	0.59	Ur	
sm1_G05	10.66	20.16	0.02	0.24	48.96	0.23	18.25	18.07	0.20	0.31	0.00	98.86	7.99	0.73	3.09	0.69	-1.07	0.67	Ur	
m4_G03	13.68	28.03	0.14	0.16	38.44	0.17	17.15	14.95	2.44	0.07	0.08	98.17	7.13	0.47	2.26	0.49	-1.45	0.58	High-Al	

m5_G15	13.02	44.18	0.09	0.15	21.94	0.15	16.69	16.69	0.00	0.19	0.00	96.42	7.15	2.98	2.72	0.83	-1.00	0.98	High-Al	
m7_G04	9.63	32.29	0.28	0.20	31.71	0.21	21.72	21.01	0.79	0.20	0.01	96.33	8.16	0.56	2.94	1.03	-1.30	1.04	High-Al	
m7_G08	12.14	26.81	0.71	0.13	32.86	0.20	16.93	15.10	2.04	0.07	0.12	90.18	6.69	0.79	3.00	0.52	-0.48	0.50	High-Al	
m7_G09	13.82	30.52	0.06	0.14	38.87	0.16	13.83	13.83	0.00	0.15	0.00	97.55	8.94	0.64	3.76	0.53	-0.88	0.54	High-Al	
m7_G11	8.02	27.77	0.25	0.23	32.62	0.23	26.27	22.69	3.98	0.22	0.00	96.02	3.56	1.02	1.67	1.17	-0.18	0.64	High-Al	
m7_G12	16.39	34.14	0.15	0.13	30.38	0.22	14.91	11.33	3.98	0.10	0.11	96.94	9.26	1.07	3.97	0.50	-0.84	0.51	High-Al	
m8_G04	11.22	36.59	0.17	0.15	29.27	0.16	18.63	18.63	0.00	0.10	0.09	96.37	9.47	2.86	4.22	1.14	-0.70	0.55	High-Al	
m8_G10	13.31	27.94	0.14	0.13	41.87	0.15	13.64	13.64	0.00	0.13	0.00	97.32	10.32	0.61	4.47	0.66	-0.90	0.51	High-Al	
sm1_G10	8.37	26.74	0.29	0.33	37.96	0.23	24.05	22.86	1.33	0.13	0.02	98.25	6.53	0.97	2.40	0.61	-0.99	0.66	High-Al	
sm1_G18	13.47	33.91	0.13	0.12	31.68	0.16	17.28	15.88	1.56	0.06	0.09	97.07	7.70	3.12	3.02	0.87	-0.98	0.75	High-Al	
sm1_G20	13.02	25.66	0.02	0.24	40.33	0.21	18.80	15.42	3.76	0.21	0.00	98.86	7.09	4.36	3.04	1.11	-0.64	1.15	High-Al	
sm3_G28	9.95	25.43	0.13	0.15	39.70	0.22	21.70	19.87	2.03	0.11	0.00	97.59	3.46	1.97	1.43	1.39	-0.37	0.45	High-Al	
sm4_G17	9.97	29.92	0.26	0.17	34.42	0.21	20.28	20.00	0.31	0.13	0.03	95.41	7.17	1.21	3.05	0.68	-0.68	0.62	High-Al	
sm4_G34	11.42	31.52	0.02	0.15	35.76	0.25	19.72	18.83	0.99	0.26	0.00	99.20	6.68	1.20	3.22	0.76	-0.25	0.91	High-Al	
m1_G01	6.87	15.68	1.18	0.20	44.64	0.21	27.45	23.80	4.06	0.10	0.04	96.77	2.47	0.44	1.15	0.45	-0.14	0.49	Ext	Iron/Carb
m1_G03	10.18	1.97	1.61	0.55	67.61	1.10	5.58	5.58	0.00	10.89	0.00	99.49	1.51	0.64	0.41	0.44	-0.37	0.47	Ext	Iron
m1_G05	4.99	11.91	0.82	0.57	55.10	0.51	24.58	24.58	0.00	0.25	0.00	98.73	-1.69	1.17	-1.15	0.52	-0.27	0.55	Ext	Carb
m2_G01	6.81	13.24	0.80	0.80	53.82	0.48	22.32	22.32	0.00	0.00	0.01	98.28	-0.82	0.57	-0.86	0.81	-0.43	0.93	Ext	Ur/Pall/CM2
m2_G02	8.11	14.04	1.89	0.43	52.17	0.49	21.32	21.32	0.00	0.00	0.01	98.46	-0.23	0.53	-0.49	0.77	-0.37	0.55	Ext	Ur
m2_G05	4.11	12.65	0.45	0.40	46.46	0.49	30.54	26.01	5.03	0.51	0.00	96.12	0.72	0.43	0.81	0.61	0.44	0.63	Ext	Carb/Di
m3_G04	7.57	13.11	0.02	0.36	51.15	0.38	25.28	21.50	4.20	0.24	0.00	98.52	1.55	0.58	0.25	0.61	-0.56	0.54	Ext	CM2
m3_G06	6.11	12.83	0.33	0.12	53.38	0.23	21.89	21.89	0.00	0.13	0.00	95.00	1.51	0.40	0.93	0.43	0.15	0.50	Ext	Pall/Ur
m3_G09	2.50	9.34	0.74	0.90	56.37	0.57	27.75	27.75	0.00	0.03	0.04	98.23	-3.43	0.67	-1.60	0.57	0.18	0.46	Ext	Di
m3_G15	7.59	21.23	0.08	0.18	49.39	0.16	16.17	16.17	0.00	0.17	0.01	94.97	3.51	0.41	2.11	0.49	0.28	0.56	Ext	Ur
m3_G18	6.03	20.41	0.41	0.27	36.94	0.31	30.86	24.71	6.84	0.25	0.00	96.18	1.76	1.11	0.92	1.08	0.01	0.66	Ext	Carb
m4_G08	4.36	12.09	1.11	0.48	54.12	0.60	25.48	25.48	0.00	0.02	0.02	98.28	-1.74	0.62	-1.58	0.51	-0.68	0.50	Ext	Br/Di
m5_G02	13.13	19.72	0.01	0.17	51.46	0.17	14.26	14.26	0.00	0.23	0.01	99.15	5.27	3.76	2.48	1.87	-0.26	0.50	Ext	CR2/Ur
m5_G05	9.40	14.11	0.04	0.13	53.28	0.22	12.93	11.97	1.06	7.74	0.02	97.96							Ext	Lo/Ur
m5_G07	7.87	14.78	0.04	0.30	54.01	0.25	15.91	15.91	0.00	3.30	0.01	96.47	2.20	0.56	1.21	0.44	0.07	0.54	Ext	Lo/Ur
m5_G08	4.69	13.81	0.21	0.20	49.07	0.24	27.08	25.45	1.81	0.17	0.00	95.66	0.33	0.59	0.62	0.45	0.45	0.53	Ext	Carb/Di
m5_G12	8.84	6.29	0.02	0.06	59.92	0.79	21.20	17.07	4.59	1.54	0.00	99.13	0.11	3.50	0.25	1.68	0.20	0.45	Ext	Chass

m5_G14	9.89	9.68	0.23	0.06	55.82	0.29	21.70	17.84	4.29	0.15	0.10	98.35	2.53	0.59	0.94	0.37	-0.37	0.44	Ext	Ac
m6_G03	7.93	12.34	4.85	0.37	31.66	0.27	39.18	25.84	14.82	0.09	0.03	98.20	-2.52	2.81	-0.59	1.44	0.72	0.48	Ext	
m6_G04	9.58	13.87	0.01	0.21	56.06	0.23	17.36	17.36	0.00	1.51	0.00	98.84	5.84	0.93	2.56	0.53	-0.48	0.50	Ext	Lo
m6_G05	9.13	8.67	0.09	0.22	58.24	0.23	19.09	16.21	3.20	3.09	0.02	99.11	5.12	1.03	2.06	0.64	-0.60	0.54	Ext	Ac
m6_G07	8.75	6.38	0.13	0.11	59.61	0.25	23.16	19.17	4.43	0.12	0.03	98.98	0.38	1.02	0.23	0.55	0.03	0.43	Ext	Chass
m7_G01	2.89	6.80	3.16	0.78	27.93	0.24	51.06	31.23	22.04	0.10	0.00	95.18	-2.62	1.45	-0.77	1.05	0.59	0.67	Ext	R
m7_G02													3.15	0.87	1.31	0.56	-0.33	0.49	Ext	
m7_G07	10.56	14.43	0.08	0.19	54.75	0.21	17.41	16.81	0.67	0.23	0.02	97.95	7.36	0.81	3.11	0.52	-0.72	0.48	Ext	Lo
m8_G01	5.11	10.04	1.86	0.60	52.88	0.31	26.70	26.32	0.42	0.28	0.03	97.84	-1.43	0.87	-0.75	0.58	-0.01	0.54	Ext	Iron
m8_G07	6.35	10.43	0.41	0.08	53.15	0.29	24.46	22.45	2.23	0.25	0.00	95.62	-1.00	2.28	-0.35	1.13	0.17	0.52	Ext	Carb/Br/Di
m8_G12	3.63	11.35	0.84	0.77	53.50	0.26	25.59	25.59	0.00	0.68	0.17	96.79	-2.08	2.54	-0.94	1.13	0.14	0.56	Ext	Br/Di
sm1_G04	9.23	6.19	0.15	0.05	59.43	4.15	17.91	14.10	4.23	0.27	0.12	97.92	4.28	1.02	1.70	0.78	-0.52	0.63	Ext	Ac/Pall
sm1_G19	6.83	13.22	0.67	0.67	54.19	0.25	23.09	23.09	0.00	0.18	0.05	99.14	-4.69	2.17	-7.71	1.18	-5.27	0.70	Ext	Ur/Pall/CM2
sm1_G21	11.31	6.38	0.20	0.05	60.64	0.18	16.51	12.60	4.34	3.13	0.05	98.89	2.32	1.66	1.07	1.02	-0.13	0.55	Ext	Iron/Win
sm1_G22	10.43	16.72	0.24	0.19	48.12	0.27	22.80	18.37	4.93	0.15	0.00	99.41	4.43	2.73	1.90	1.60	-0.41	0.63	Ext	Carb
sm3_G02	5.73	10.14	0.19	0.12	52.48	0.22	26.13	23.29	3.16	0.10	0.00	95.44	-0.65	1.58	-0.59	0.93	-0.25	0.64	Ext	Carb/Br/Di
sm3_G06	11.51	13.75	0.01	0.28	57.36	0.34	15.58	15.58	0.00	0.31	0.00	99.14	5.03	1.35	2.15	0.80	-0.47	0.68	Ext	Lo
sm3_G07	4.65	10.23	0.32	0.37	50.17	0.21	25.14	23.92	1.36	0.01	0.06	91.30	1.86	1.64	3.23	0.86	2.26	0.60	Ext	CM2
sm3_G08	2.16	10.73	4.52	0.58	47.39	0.52	31.67	31.67	0.00	0.00	0.00	97.56	-3.63	1.14	-2.22	0.66	-0.33	0.47	Ext	HED/SNC
sm3_G09	5.82	11.19	0.98	0.58	55.75	0.44	23.50	23.50	0.00	0.82	0.04	99.12	1.51	1.30	0.21	1.05	-0.58	0.70	Ext	Carb
sm3_G10	8.31	18.32	0.84	0.47	42.22	0.25	25.52	21.54	4.43	0.12	0.01	96.52							Ext	CM2
sm3_G11	6.78	2.41	0.03	0.14	70.84	0.44	8.91	8.91	0.00	8.53	0.17	98.24	1.61	1.49	2.57	0.77	1.73	0.70	Ext	Iron/Pall
sm3_G13	6.76	22.10	0.41	0.15	38.50	0.34	28.15	24.12	4.48	0.19	0.00	97.07	2.80	1.06	0.90	0.63	-0.55	0.60	Ext	Carb
sm3_G14	4.39	9.68	0.55	0.49	53.70	0.32	29.27	26.83	2.71	0.00	0.13	98.79	0.70	1.33	2.31	0.70	1.95	0.55	Ext	CM2
sm3_G19	9.25	12.81	0.36	0.15	50.60	0.28	25.02	19.71	5.89	0.09	0.03	99.17	3.45	1.35	1.68	0.78	-0.11	0.57	Ext	CM2
sm3_G20	0.00	0.45	0.94	0.01	28.76	0.56	16.97	8.63	9.26	13.72	0.33	62.66	-8.35	1.80	-5.43	1.04	-1.09	0.74	Ext	
sm3_G23	7.99	13.59	0.03	0.20	57.42	0.44	18.11	18.11	0.00	0.17	0.00	97.96	4.35	1.22	1.93	0.81	-0.33	0.73	Ext	Lo
sm3_G32	1.34	20.50	0.75	0.32	41.07	0.18	29.45	29.45	0.00	0.81	0.00	94.41							Ext	Di
sm3_G33													2.20	1.34	0.65	0.91	-0.49	0.66	Ext	
sm4_G05	5.04	19.86	0.50	0.17	39.66	0.35	30.49	26.38	4.57	0.18	0.00	96.70	-0.13	2.19	-0.69	1.15	-0.62	0.63	Ext	Carb
sm4_G07	9.66	9.92	0.55	0.38	59.90	3.79	7.46	7.46	0.00	7.43	0.00	99.10	3.87	2.25	1.05	1.18	-0.96	0.53	Ext	Iron/Ac/Lo

sm4_G12	4.11	10.97	0.73	0.53	52.61	0.34	28.75	27.56	1.32	0.01	0.20	98.38	-3.02	1.45	-0.62	0.79	0.95	0.51	Ext	
sm4_G13	11.66	12.10	0.16	0.10	55.87	0.24	17.69	15.31	2.64	0.17	0.00	98.26	0.63	1.73	0.06	0.98	-0.26	0.60	Ext	Lo
sm4_G14	11.72	21.95	0.21	0.18	42.41	0.23	21.50	17.04	4.95	0.16	0.00	98.85	5.19	1.76	2.29	0.98	-0.41	0.60	Ext	CR2
sm4_G15	9.98	14.34	0.58	0.13	47.35	0.21	24.19	18.52	6.30	0.08	0.00	97.50	0.70	3.36	0.31	2.39	-0.05	0.66	Ext	Carb
sm4_G16	1.17	0.05	0.35	0.61	59.99	0.23	15.47	13.96	1.67	15.94	0.11	94.08	-6.77	1.50	-5.66	0.87	-2.14	0.46	Ext	
sm4_G21	4.60	14.65	0.75	0.55	53.80	0.26	22.35	22.35	0.00	0.00	0.07	97.05	-2.37	1.29	-1.89	0.91	-0.65	0.62	Ext	Ur
sm4_G23	5.47	4.95	0.02	0.20	64.74	3.52	8.96	8.96	0.00	9.65	0.00	97.49	0.85	1.28	0.53	0.86	0.09	0.56	Ext	Pall
sm4_G26	6.64	13.19	0.47	0.17	47.80	0.32	29.63	23.68	6.61	0.17	0.00	99.06	-0.03	1.49	-0.04	0.84	-0.03	0.58	Ext	Carb/Di
sm4_G29	10.71	14.23	0.56	0.12	46.33	0.24	24.38	17.36	7.79	0.07	0.00	97.41							Ext	Carb
sm4_G30	3.49	15.83	0.55	0.57	54.27	0.17	19.25	19.25	0.00	0.40	0.11	94.64	2.52	1.66	2.51	1.00	1.20	0.69	Ext	
sm4_G37													-4.76	2.34	-2.08	1.14	0.40	0.67	Ext	
sm4_G38													7.66	1.98	3.48	1.12	-0.51	0.66	Ext	
m3_G01	6.76	11.91	0.17	0.07	61.38	0.29	13.11	13.11	0.00	0.14	0.00	93.84	1.97	0.56	1.07	0.44	0.05	0.50	Uncl	
m3_G10	4.22	9.37	3.96	0.61	31.13	0.40	46.50	30.35	17.94	0.20	0.00	98.18	-1.24	1.18	-0.63	0.58	0.01	0.56	Uncl	
m5_G01	3.36	12.62	0.74	0.17	39.55	0.35	37.45	27.85	10.66	0.17	0.00	95.49	-0.91	0.74	-0.28	0.40	0.19	0.46	Uncl	
m6_G02	8.94	15.49	3.01	0.34	37.96	0.19	29.04	22.06	7.76	0.12	0.05	95.91	-0.69	2.14	0.03	1.12	0.39	0.78	Uncl	
m6_G08	4.86	9.95	1.90	0.47	35.54	0.29	42.74	27.50	16.93	0.11	0.02	97.56	-4.73	1.07	-2.25	1.15	0.21	0.99	Uncl	
m6_G12	4.71	13.23	1.87	0.69	38.11	0.29	36.27	27.27	10.00	0.12	0.03	96.31	-1.42	1.10	-1.22	0.75	-0.48	0.50	Uncl	
m7_G05	4.30	12.21	0.19	0.10	36.63	0.28	36.80	24.83	13.30	0.50	0.01	92.34	-5.53	0.79	-2.38	0.46	0.49	0.40	Uncl	
m7_G06													2.65	1.14	1.52	0.67	0.14	0.43	Uncl	
m7_G10	3.79	13.67	1.38	0.44	35.53	0.59	36.34	26.96	10.43	0.17	0.04	93.01	-1.59	1.55	-0.48	0.84	0.35	0.41	Uncl	
m8_G05	0.92	8.79	4.55	0.69	50.02	0.47	30.53	30.53	0.00	0.02	0.00	96.02	-6.43	4.84	-3.30	2.14	0.05	0.45	Uncl	
m8_G11	4.94	13.98	1.67	0.71	42.11	0.28	30.65	26.22	4.92	0.16	0.00	94.99	-1.69	4.64	-0.71	2.95	0.17	1.22	Uncl	
sm1_G02	0.05	3.16	0.08	0.21	47.31	0.22	36.07	27.11	9.96	2.87	0.03	91.02							Uncl	
sm1_G03	0.15	12.83	0.59	0.24	47.51	1.64	30.89	29.16	1.92	2.83	0.00	96.89	1.48	0.71	0.71	0.66	-0.06	0.59	Uncl	
sm1_G17	6.84	14.95	2.64	0.32	40.23	0.21	28.49	24.25	4.71	0.08	0.02	94.25	0.43	1.37	-0.06	0.89	-0.28	0.73	Uncl	
sm3_G21	1.49	4.45	0.04	0.30	45.81	0.56	41.10	28.71	13.76	0.34	0.00	95.47							Uncl	
sm3_G26	0.14	8.03	2.55	0.28	47.76	0.31	33.73	31.53	2.44	2.27	0.00	95.32							Uncl	
sm4_G01	0.37	21.29	0.13	0.56	34.40	0.14	38.64	33.31	5.92	0.53	0.00	96.66	0.23	2.02	0.04	1.08	-0.08	0.64	Uncl	
sm4_G04	8.06	13.33	0.04	0.23	59.73	0.26	15.40	15.40	0.00	0.20	0.00	97.26							Uncl	
sm4_G36	0.10	0.21	0.55	0.09	37.37	3.32	43.29	23.03	22.51	6.32	0.00	93.49							Uncl	

sm4_G41													6.26	1.33	3.40	0.81	0.14	0.74	Uncl	
sm3_G18	0.00	0.05	59.57	0.20	0.45	0.05	11.58	11.58	0.00	0.00	0.28	72.19	-9.12	1.87	-5.26	0.72	-0.51	1.38	Uncl	not Cr-sp

All FeO: all Fe assigned as FeO
Total does not include All FeO
2SD: 2 standard deviations
Uncl: unclassified, possibly terrestrial, oxygen not discriminative, not database matches, not chrome-spinel (Cr-sp)
Ext: extraterrestrial
Ac: acapulcoite; Br: brachinite; Carb: carbonaceous; Chass: chassignite; Di: diogenite; H: H chondrite; L: L chondrite; LL: LL chondrite; Lo: lodranite; Ord: ordinary; Pall: pallasite; R: R chondrite; Ur: ureilite; Win: winonaite

APPENDIX B. NEW MEASUREMENTS OF MODERN METEORITE CHROME-SPINELS

Table B.1. Chemical compositions of chrome-spinel grains from modern meteorites.

Type	Sample	Grain #	MgO	Al_2O_3	TiO_2	V_2O_3	Cr_2O_3	MnO	All FeO	FeO	Fe_2O_3	ZnO	SiO_2	Total
Eucrite	NWA 8365	1	0.27	7.95	4.04	0.87	49.55	0.56	35.68	35.63	0.06	0.01	0.00	98.94
		3	0.39	7.67	4.33	0.83	49.18	0.53	35.61	35.58	0.04	0.01	0.00	98.56
		6	0.25	7.81	4.30	0.83	49.00	0.55	35.83	35.79	0.04	0.00	0.00	98.57
		Average	**0.31**	**7.81**	**4.22**	**0.84**	**49.24**	**0.55**	**35.71**	**35.67**	**0.05**	**0.01**	**0.00**	**98.69**
		2SD	**0.15**	**0.28**	**0.32**	**0.04**	**0.57**	**0.03**	**0.22**	**0.22**	**0.02**	**0.01**	**0.00**	**0.43**
	Haraiya	1	0.08	7.94	2.27	0.70	50.21	0.56	33.01	33.01	0.00	0.03	0.04	94.83
		2	0.07	8.03	2.32	0.73	49.77	0.55	33.15	33.05	0.10	0.01	0.01	94.64
		4	0.03	7.91	2.66	0.74	49.86	0.54	33.46	33.46	0.00	0.00	0.05	95.25
		5	0.06	8.08	3.25	0.73	48.89	0.57	33.43	33.30	0.15	0.03	0.00	95.05
		6	0.02	8.46	2.33	0.79	50.26	0.53	33.16	33.16	0.00	0.02	0.01	95.57
		7	0.03	8.42	2.14	0.72	50.10	0.53	33.27	33.25	0.02	0.00	0.04	95.26
		9	0.02	8.13	2.08	0.77	50.38	0.54	33.02	33.02	0.00	0.01	0.01	94.96
		10	0.05	8.34	2.78	0.67	49.67	0.56	33.37	33.37	0.00	0.01	0.01	95.46
		11	0.06	8.42	1.85	0.73	50.12	0.54	32.96	32.77	0.21	0.02	0.01	94.73
		12	0.10	8.50	3.59	0.65	47.08	0.54	34.42	34.32	0.12	0.02	0.02	94.92
		Average	**0.05**	**8.22**	**2.53**	**0.72**	**49.63**	**0.55**	**33.32**	**33.27**	**0.06**	**0.01**	**0.02**	**95.07**
		2SD	**0.06**	**0.46**	**1.09**	**0.08**	**1.99**	**0.03**	**0.85**	**0.84**	**0.16**	**0.02**	**0.03**	**0.62**
Diogenite	NWA 10403	2	2.283	10.123	0.809	0.424	54.956	0.517	29.881	29.881	0.000	0.005	0.000	99.00
		4	2.154	11.552	1.420	0.506	52.194	0.515	30.881	30.881	0.000	0.007	0.000	99.23
		7	1.906	7.778	0.666	0.928	57.245	0.534	29.905	29.905	0.000	0.007	0.000	98.97
		Average	**2.11**	**9.82**	**0.96**	**0.62**	**54.80**	**0.52**	**30.22**	**30.22**	**0.00**	**0.01**	**0.00**	**99.07**
		2SD	**0.38**	**3.81**	**0.80**	**0.54**	**5.06**	**0.02**	**1.14**	**1.14**	**0.00**	**0.00**	**0.00**	**0.29**

Brachinite	NWA 3151	2	4.48	12.62	0.89	0.66	52.74	0.30	27.29	27.16	0.14	0.41	0.00	99.41
		3	4.49	12.67	0.89	0.66	52.49	0.30	27.34	27.11	0.25	0.40	0.00	99.26
		6	4.50	12.66	0.88	0.67	51.74	0.30	26.96	26.71	0.28	0.41	0.00	98.15
		Average	**4.49**	**12.65**	**0.89**	**0.66**	**52.32**	**0.30**	**27.19**	**27.00**	**0.22**	**0.41**	**0.00**	**98.94**
		2SD	**0.02**	**0.05**	**0.02**	**0.02**	**1.04**	**0.01**	**0.41**	**0.49**	**0.15**	**0.01**	**0.00**	**1.37**
Acapulcoite	NWA 8287	2	8.15	9.57	1.39	0.62	57.74	1.21	19.53	19.53	0.00	0.87	0.00	99.08
		4	8.00	9.63	1.40	0.66	57.73	1.20	19.74	19.74	0.00	0.88	0.00	99.26
		7	8.01	9.60	1.38	0.63	57.86	1.23	19.70	19.70	0.00	0.91	0.00	99.31
		Average	**8.05**	**9.60**	**1.39**	**0.64**	**57.77**	**1.21**	**19.66**	**19.66**	**0.00**	**0.89**	**0.00**	**99.21**
		2SD	**0.17**	**0.06**	**0.02**	**0.05**	**0.14**	**0.03**	**0.23**	**0.23**	**0.00**	**0.04**	**0.00**	**0.25**
Lodranite	NWA 10265	1	9.99	12.00	0.14	0.83	58.19	0.49	17.97	17.97	0.00	0.06	0.00	99.66
		2	9.94	12.06	0.15	0.77	57.98	0.50	18.03	18.03	0.00	0.07	0.00	99.49
		6	9.98	11.97	0.14	0.83	58.27	0.50	18.04	18.03	0.02	0.06	0.00	99.81
		Average	**9.97**	**12.01**	**0.14**	**0.81**	**58.15**	**0.50**	**18.01**	**18.01**	**0.01**	**0.07**	**0.00**	**99.65**
		2SD	**0.05**	**0.09**	**0.00**	**0.06**	**0.31**	**0.01**	**0.08**	**0.07**	**0.02**	**0.01**	**0.00**	**0.32**
Ureilite	NWA 766	2	18.84	18.91	0.73	0.41	55.27	0.64	4.45	4.45	0.00	0.10	0.05	99.40
		3	16.20	18.55	0.73	0.39	53.57	0.68	8.66	8.66	0.00	0.18	0.06	99.02
		6	17.59	20.36	0.98	0.40	52.28	0.61	7.06	7.06	0.00	0.07	0.05	99.39
		Average	**17.54**	**19.27**	**0.81**	**0.40**	**53.71**	**0.64**	**6.72**	**6.72**	**0.00**	**0.12**	**0.05**	**99.27**
		2SD	**2.64**	**1.91**	**0.28**	**0.03**	**3.00**	**0.07**	**4.26**	**4.26**	**0.00**	**0.11**	**0.01**	**0.44**
CR6	NWA 7317	2	3.02	12.74	1.51	0.66	50.56	0.28	30.13	30.12	0.02	0.01	0.00	98.92
		5	3.10	12.69	1.55	0.63	50.30	0.27	30.00	29.98	0.02	0.01	0.00	98.55
		7	3.03	12.67	1.53	0.63	50.43	0.27	30.21	30.17	0.04	0.01	0.00	98.78
		Average	**3.05**	**12.70**	**1.53**	**0.64**	**50.43**	**0.27**	**30.11**	**30.09**	**0.03**	**0.01**	**0.00**	**98.75**
		2SD	**0.08**	**0.07**	**0.04**	**0.04**	**0.26**	**0.01**	**0.21**	**0.20**	**0.02**	**0.01**	**0.00**	**0.37**
CR2	GRA95227	1	13.73	20.91	0.54	0.25	44.67	2.06	12.67	12.51	0.18	0.01	1.85	96.71

		3	7.17	7.36	1.57	0.73	54.52	0.31	25.08	22.84	2.50	0.00	0.26	97.26
		4	16.19	24.43	0.44	0.20	42.99	1.78	9.73	9.73	0.00	0.02	1.11	96.88
		5	15.04	23.84	0.46	0.21	42.40	1.73	10.24	9.98	0.29	0.01	1.22	95.17
		6	3.85	1.48	1.83	0.81	59.63	0.74	29.08	26.87	2.47	0.00	0.18	97.85
		7	4.16	0.20	3.87	0.98	58.07	0.81	29.13	27.88	1.40	0.00	0.19	97.55
		8	6.36	8.01	1.53	0.65	54.11	0.38	26.17	24.16	2.23	0.01	0.24	97.68
		Average	**9.50**	**12.32**	**1.46**	**0.55**	**50.91**	**1.11**	**20.30**	**19.14**	**1.30**	**0.01**	**0.72**	**97.01**
		2SD	**10.62**	**20.99**	**2.43**	**0.64**	**14.71**	**1.45**	**17.96**	**16.15**	**2.26**	**0.01**	**1.34**	**1.82**
CM2	Cold Bokkeveld	1	5.59	11.35	0.56	0.51	51.39	0.20	28.51	25.38	3.47	0.00	0.17	98.63
		2	5.16	9.26	1.09	0.81	52.98	0.28	28.14	25.97	2.41	0.00	0.18	98.15
		3	5.01	8.78	1.42	0.85	52.89	0.34	28.46	26.38	2.31	0.00	0.19	98.17
		4	7.57	10.27	0.91	0.77	54.21	0.27	24.91	22.55	2.62	0.01	0.10	99.29
		5	4.10	8.96	0.94	0.61	52.43	0.38	30.02	27.30	3.01	0.00	0.22	97.95
		6	7.80	11.78	0.71	0.62	51.86	0.23	24.83	22.08	3.06	0.03	0.18	98.34
		7	3.31	1.99	0.78	0.46	54.53	0.25	34.98	28.54	7.15	0.02	1.02	98.05
		8	4.41	9.12	0.94	0.57	51.84	0.22	29.84	26.97	3.19	0.01	0.28	97.55
		Average	**5.37**	**8.94**	**0.92**	**0.65**	**52.77**	**0.27**	**28.71**	**25.65**	**3.40**	**0.01**	**0.29**	**98.27**
		2SD	**3.18**	**6.05**	**0.52**	**0.29**	**2.26**	**0.13**	**6.42**	**4.53**	**3.13**	**0.02**	**0.60**	**1.03**
	Murray17b	2	5.37	20.29	1.08	0.80	37.36	0.21	29.83	27.67	2.39	0.01	0.87	96.06
		3	6.06	12.91	0.93	0.61	48.73	0.24	27.19	24.75	2.71	0.02	0.19	97.14
		4	4.69	11.71	0.80	0.65	50.16	0.22	29.17	26.87	2.56	0.02	0.24	97.92
		5	8.38	15.61	0.75	0.65	49.12	0.17	23.87	22.05	2.03	0.01	0.15	98.93
		6	8.32	15.70	0.70	0.61	48.37	0.16	24.37	22.02	2.60	0.01	0.14	98.63
		Average	**6.56**	**15.25**	**0.85**	**0.67**	**46.75**	**0.20**	**26.89**	**24.67**	**2.46**	**0.01**	**0.32**	**97.74**
		2SD	**3.40**	**6.61**	**0.31**	**0.16**	**10.58**	**0.07**	**5.43**	**5.27**	**0.53**	**0.01**	**0.62**	**2.32**
Pallasite	Brenham*	1	8.32	0.43	0.05	0.54	70.48	0.29	19.83	19.17	0.73	0.01	0.01	100.04
		2	8.26	0.44	0.05	0.56	69.90	0.32	19.82	19.07	0.83	0.02	0.02	99.48
		3	8.21	0.45	0.04	0.57	70.09	0.30	19.98	19.28	0.77	0.01	0.03	99.75

		Average	**8.26**	**0.44**	**0.04**	**0.56**	**70.16**	**0.30**	**19.88**	**19.17**	**0.78**	**0.02**	**0.02**	**99.76**
		2SD	**0.12**	**0.02**	**0.00**	**0.03**	**0.59**	**0.02**	**0.18**	**0.21**	**0.10**	**0.01**	**0.02**	**0.56**
	Seymchan*	1	9.95	0.93	0.09	0.52	71.33	0.38	16.61	16.61	0.00	0.04	0.00	99.84
		2	9.95	0.94	0.08	0.53	71.35	0.40	16.65	16.64	0.00	0.00	0.00	99.90
		3	9.89	0.90	0.08	0.51	71.44	0.43	16.63	16.63	0.00	0.03	0.00	99.92
		Average	**9.93**	**0.92**	**0.09**	**0.52**	**71.37**	**0.40**	**16.63**	**16.63**	**0.00**	**0.02**	**0.00**	**99.88**
		2SD	**0.07**	**0.04**	**0.00**	**0.01**	**0.12**	**0.05**	**0.04**	**0.04**	**0.00**	**0.04**	**0.00**	**0.08**
Iron	Bear Creek*	1	0.09	0.01	0.00	0.62	66.59	0.62	31.38	31.12	0.28	0.00	0.00	99.34
		2	0.06	0.03	0.01	0.58	66.17	0.61	31.35	31.01	0.39	0.03	0.00	98.87
		3	0.07	0.01	0.00	0.65	66.35	0.62	31.37	31.05	0.36	0.05	0.00	99.16
		Average	**0.07**	**0.01**	**0.00**	**0.62**	**66.37**	**0.62**	**31.37**	**31.06**	**0.34**	**0.03**	**0.00**	**99.12**
		2SD	**0.03**	**0.02**	**0.01**	**0.07**	**0.42**	**0.02**	**0.03**	**0.12**	**0.11**	**0.05**	**0.00**	**0.48**
Angrite	Dorbigny	1	12.23	51.65	0.33	0.33	9.93	0.15	23.71	21.27	2.71	0.01	0.06	98.66
		2	11.95	51.55	0.34	0.37	9.74	0.14	24.06	21.60	2.73	0.01	0.04	98.47
		3	12.32	51.67	0.34	0.33	9.94	0.15	23.84	21.23	2.90	0.01	0.05	98.96
		4	12.06	51.83	0.35	0.37	9.48	0.14	24.20	21.59	2.91	0.01	0.04	98.78
		5	11.98	51.38	0.34	0.37	9.63	0.14	24.32	21.55	3.08	0.00	0.03	98.51
		6	12.04	51.73	0.34	0.35	9.42	0.14	24.26	21.57	2.99	0.01	0.05	98.63
		8	12.27	51.86	0.35	0.38	9.59	0.15	23.84	21.28	2.85	0.00	0.05	98.78
		9	12.08	51.74	0.34	0.36	9.59	0.13	23.73	21.44	2.54	0.00	0.07	98.29
		Average	**12.12**	**51.68**	**0.34**	**0.36**	**9.66**	**0.14**	**24.00**	**21.44**	**2.84**	**0.01**	**0.05**	**98.63**
		2SD	**0.28**	**0.31**	**0.01**	**0.04**	**0.39**	**0.02**	**0.49**	**0.32**	**0.34**	**0.01**	**0.03**	**0.42**
H6	Kernouve	1	3.09	6.45	2.29	0.65	57.20	0.78	28.52	28.52	0.00	0.30	0.02	99.30
		2	2.57	6.50	2.23	0.66	56.91	0.68	29.32	29.32	0.00	0.29	0.01	99.17
		3	3.10	6.39	2.26	0.66	57.09	0.78	28.57	28.57	0.00	0.33	0.03	99.21
		4	2.96	6.43	2.27	0.66	57.03	0.74	28.66	28.66	0.00	0.33	0.03	99.10
		5	3.01	6.61	2.11	0.72	57.00	0.82	28.49	28.49	0.00	0.34	0.04	99.14

		6	2.98	6.48	2.23	0.68	56.79	0.79	28.62	28.62	0.00	0.31	0.06	98.93
		7	2.92	6.47	2.20	0.69	56.77	0.85	28.64	28.64	0.00	0.34	0.01	98.90
		8	2.89	6.53	2.22	0.65	56.82	0.78	28.60	28.60	0.00	0.33	0.03	98.85
		9	3.07	6.30	2.32	0.69	57.17	0.80	28.44	28.44	0.00	0.33	0.01	99.13
		10	2.96	6.53	2.22	0.67	56.73	0.81	28.67	28.67	0.00	0.33	0.07	98.99
		11	2.83	6.35	2.25	0.71	57.22	0.83	28.74	28.74	0.00	0.34	0.01	99.29
		12	3.26	6.35	2.32	0.67	57.22	0.78	28.27	28.27	0.00	0.34	0.04	99.26
		13	2.98	6.64	1.99	0.76	57.28	0.88	28.34	28.34	0.00	0.35	0.01	99.23
		14	2.95	6.40	2.28	0.65	57.03	0.72	28.91	28.91	0.00	0.30	0.06	99.29
		15	2.55	6.66	2.06	0.70	56.64	0.73	29.47	29.47	0.00	0.31	0.05	99.16
		16	2.97	6.50	2.23	0.68	57.35	0.76	28.95	28.95	0.00	0.31	0.05	99.80
		17	2.90	6.60	2.18	0.67	56.91	0.77	28.84	28.84	0.00	0.33	0.03	99.22
		Average	**2.94**	**6.48**	**2.22**	**0.68**	**57.01**	**0.78**	**28.71**	**28.71**	**0.00**	**0.32**	**0.03**	**99.17**
		2SD	**0.35**	**0.21**	**0.18**	**0.06**	**0.43**	**0.10**	**0.63**	**0.63**	**0.00**	**0.04**	**0.04**	**0.43**
	Guarena	2	3.17	6.22	2.28	0.62	56.89	0.70	28.95	28.95	0.00	0.28	0.00	99.12
		3	3.17	6.40	2.20	0.67	56.72	0.68	29.10	29.02	0.08	0.28	0.00	99.20
		4	3.04	6.39	2.26	0.65	56.72	0.69	29.17	29.17	0.00	0.28	0.00	99.20
		6	2.83	6.62	2.07	0.75	56.07	0.78	29.45	29.22	0.25	0.33	0.00	98.92
		7	3.25	6.69	1.98	0.73	56.51	0.76	28.72	28.56	0.17	0.33	0.00	98.98
		8	3.20	6.36	2.23	0.68	56.62	0.75	28.88	28.83	0.05	0.34	0.00	99.06
		9	3.15	6.25	2.26	0.69	56.64	0.76	29.09	28.96	0.15	0.35	0.01	99.20
		10	2.92	6.64	2.18	0.70	56.02	0.72	29.54	29.31	0.26	0.34	0.00	99.09
		11	2.92	6.37	2.17	0.68	56.17	0.71	29.62	29.25	0.41	0.34	0.00	99.03
		14	3.22	6.37	2.25	0.69	56.46	0.74	28.97	28.84	0.15	0.34	0.00	99.06
		Average	**3.09**	**6.43**	**2.19**	**0.69**	**56.48**	**0.73**	**29.15**	**29.01**	**0.15**	**0.32**	**0.00**	**99.09**
		2SD	**0.30**	**0.32**	**0.19**	**0.07**	**0.60**	**0.07**	**0.60**	**0.46**	**0.26**	**0.06**	**0.00**	**0.19**
H5	Richardten	1	2.69	4.99	1.94	0.75	58.32	0.84	28.91	28.80	0.12	0.61	0.00	99.06
		2	2.56	4.88	2.06	0.81	57.29	0.93	29.13	28.78	0.39	0.59	0.01	98.30
		4	3.02	5.59	1.76	0.69	57.54	0.79	28.39	28.08	0.34	0.59	0.00	98.41

		5	4.13	9.01	1.60	0.46	54.95	0.73	26.96	26.85	0.12	0.56	0.29	98.70
		6	3.20	5.07	2.21	0.82	57.65	0.85	28.71	28.33	0.43	0.57	0.00	99.13
		7	2.70	5.25	2.27	0.81	57.40	0.88	29.20	29.09	0.11	0.60	0.00	99.10
		12	2.61	4.92	2.13	0.86	57.71	0.87	29.11	28.99	0.13	0.59	0.00	98.81
		13	2.89	5.81	2.13	0.77	56.93	0.86	28.88	28.73	0.17	0.60	0.00	98.90
		14	2.96	5.60	2.16	0.76	56.87	0.82	28.84	28.58	0.29	0.60	0.00	98.62
		Average	**2.97**	**5.68**	**2.03**	**0.75**	**57.18**	**0.84**	**28.68**	**28.47**	**0.23**	**0.59**	**0.03**	**98.78**
		2SD	**0.96**	**2.58**	**0.44**	**0.24**	**1.89**	**0.11**	**1.38**	**1.37**	**0.26**	**0.03**	**0.19**	**0.60**
	Forest City	1	3.05	6.17	2.03	0.72	56.84	0.88	28.94	28.72	0.24	0.30	0.00	98.94
		2	3.11	6.31	2.14	0.65	56.96	0.79	28.82	28.82	0.00	0.29	0.00	99.07
		4	2.54	6.54	1.85	0.76	56.48	0.87	29.36	29.29	0.07	0.32	0.03	98.73
		5	2.79	6.48	2.05	0.70	56.78	0.85	29.17	29.17	0.00	0.29	0.01	99.11
		6	2.89	6.20	2.15	0.69	56.87	0.92	28.86	28.86	0.00	0.30	0.00	98.88
		7	2.66	6.50	1.89	0.68	55.76	0.87	29.17	29.04	0.14	0.30	0.08	97.93
		8	2.73	6.45	2.03	0.70	56.76	0.88	29.17	29.17	0.00	0.30	0.00	99.02
		9	2.88	6.37	2.10	0.65	57.05	0.85	28.88	28.88	0.00	0.29	0.00	99.06
		10	2.61	6.44	1.97	0.67	56.31	0.87	29.39	29.29	0.11	0.28	0.01	98.57
		11	3.17	6.20	2.12	0.62	56.88	0.74	28.77	28.76	0.01	0.26	0.02	98.77
		Average	**2.84**	**6.37**	**2.03**	**0.68**	**56.67**	**0.85**	**29.05**	**29.00**	**0.06**	**0.29**	**0.01**	**98.81**
		2SD	**0.43**	**0.27**	**0.20**	**0.08**	**0.78**	**0.10**	**0.45**	**0.44**	**0.17**	**0.03**	**0.05**	**0.71**
H4	Monroe	1	2.52	4.90	1.46	0.72	58.70	0.83	29.20	28.65	0.61	0.52	0.00	98.92
		3	2.55	5.00	1.39	0.76	58.04	0.80	28.99	28.40	0.65	0.48	0.03	98.09
		5	2.53	4.99	1.30	0.77	58.03	0.84	29.15	28.75	0.45	0.53	0.30	98.49
		6	2.37	5.10	1.32	0.72	58.18	0.79	29.41	28.87	0.61	0.54	0.11	98.60
		8	2.75	6.77	1.32	0.75	56.97	0.86	28.93	28.48	0.49	0.55	0.03	98.98
		9	2.49	5.11	1.54	0.74	58.40	0.85	29.20	28.87	0.36	0.48	0.04	98.89
		11	2.58	5.12	1.41	0.73	58.12	0.79	29.09	28.68	0.45	0.52	0.15	98.57
		12	2.25	5.03	1.32	0.72	57.97	0.87	29.61	28.85	0.85	0.52	0.06	98.44
		13	2.58	5.05	1.50	0.72	58.29	0.79	29.13	28.59	0.60	0.50	0.00	98.61

		Average	**2.51**	**5.23**	**1.40**	**0.74**	**58.08**	**0.82**	**29.19**	**28.68**	**0.56**	**0.51**	**0.08**	**98.62**
		2SD	**0.28**	**1.17**	**0.17**	**0.04**	**0.95**	**0.06**	**0.42**	**0.34**	**0.29**	**0.05**	**0.20**	**0.56**
	Bushnell	1	2.97	6.74	2.07	0.69	56.22	0.84	29.00	28.97	0.03	0.29	0.01	98.83
		3	2.62	6.87	1.74	0.68	55.40	0.91	29.56	29.03	0.58	0.33	0.07	98.24
		4	2.68	6.62	1.87	0.71	55.98	0.92	29.55	29.26	0.31	0.32	0.12	98.80
		5	4.32	6.48	2.06	0.73	56.94	0.70	27.47	27.08	0.44	0.26	0.00	99.01
		6	2.64	6.82	1.94	0.69	56.00	0.90	29.43	29.31	0.12	0.31	0.02	98.77
		7	3.06	6.73	2.00	0.70	55.88	0.83	29.40	28.81	0.65	0.32	0.00	99.00
		8	2.54	6.46	1.90	0.72	55.71	0.93	29.60	29.16	0.49	0.31	0.01	98.22
		9	3.01	6.45	2.06	0.67	55.85	0.84	29.43	28.87	0.61	0.31	0.05	98.73
		10	2.49	6.67	1.82	0.71	55.93	0.93	29.68	29.36	0.36	0.30	0.04	98.60
		11	3.02	6.66	2.04	0.66	55.88	0.80	29.18	28.84	0.37	0.31	0.03	98.61
		Average	**2.94**	**6.65**	**1.95**	**0.70**	**55.98**	**0.86**	**29.23**	**28.87**	**0.40**	**0.31**	**0.03**	**98.68**
		2SD	**1.07**	**0.29**	**0.23**	**0.05**	**0.80**	**0.14**	**1.30**	**1.32**	**0.41**	**0.04**	**0.07**	**0.55**
H3	Prairie Dog	1	1.91	1.58	0.83	0.59	62.96	0.83	29.41	28.55	0.96	0.44	0.04	98.69
		5	1.89	1.57	1.12	0.69	60.10	0.78	31.99	29.28	3.01	0.41	0.22	99.07
		6	1.90	2.21	1.14	0.74	61.29	0.85	29.83	28.99	0.94	0.45	0.12	98.61
		7	2.00	1.59	1.04	0.70	61.99	0.83	29.34	28.48	0.96	0.45	0.09	98.13
		8	2.03	2.19	1.11	0.72	60.90	0.82	30.22	29.06	1.30	0.46	0.27	98.87
		9	1.95	2.36	1.17	0.80	60.46	0.83	29.90	28.81	1.22	0.46	0.11	98.16
		10	2.05	2.74	1.38	0.75	60.40	0.83	29.50	28.83	0.74	0.47	0.04	98.23
		11	1.98	1.36	1.08	0.77	62.64	0.85	29.35	28.98	0.41	0.41	0.28	98.77
		Average	**1.96**	**1.95**	**1.11**	**0.72**	**61.34**	**0.83**	**29.94**	**28.87**	**1.19**	**0.44**	**0.14**	**98.57**
		2SD	**0.12**	**0.98**	**0.31**	**0.12**	**2.16**	**0.04**	**1.77**	**0.53**	**1.57**	**0.05**	**0.20**	**0.71**
L6	Bruderheim	1	2.33	5.75	2.95	0.71	55.82	0.66	30.55	30.55	0.00	0.32	0.03	99.13
		2	2.15	5.88	2.84	0.67	55.57	0.62	30.79	30.79	0.00	0.32	0.02	98.87
		3	2.26	5.76	2.96	0.71	55.65	0.63	30.73	30.73	0.00	0.31	0.03	99.05
		4	2.30	6.03	2.69	0.70	55.89	0.66	30.31	30.31	0.00	0.33	0.03	98.93

		5	2.19	5.98	2.00	0.76	56.38	0.68	29.99	29.93	0.07	0.35	0.02	98.36
		7	2.12	6.24	2.19	0.74	56.01	0.68	30.33	30.33	0.00	0.37	0.07	98.75
		8	2.31	5.86	2.78	0.70	55.87	0.65	30.40	30.40	0.00	0.32	0.05	98.94
		9	2.30	5.87	2.89	0.69	55.44	0.62	30.53	30.53	0.00	0.31	0.07	98.72
		11	2.15	6.26	2.22	0.73	55.81	0.68	30.10	30.08	0.02	0.37	0.06	98.38
		12	2.23	5.97	2.77	0.73	55.74	0.65	30.51	30.51	0.00	0.32	0.08	98.99
		Average	**2.23**	**5.96**	**2.63**	**0.71**	**55.82**	**0.65**	**30.42**	**30.42**	**0.01**	**0.33**	**0.05**	**98.81**
		2SD	**0.15**	**0.35**	**0.71**	**0.05**	**0.52**	**0.04**	**0.50**	**0.54**	**0.05**	**0.05**	**0.04**	**0.52**
L5	Bluff(a)	2	5.12	6.03	3.00	0.73	56.93	0.49	26.77	26.77	0.00	0.10	0.00	99.18
		3	4.17	5.83	3.06	0.76	56.62	0.55	28.21	28.21	0.00	0.11	0.00	99.31
		4	5.00	6.09	2.82	0.71	56.76	0.54	27.03	26.99	0.05	0.13	0.00	99.08
		6	5.29	6.23	2.68	0.76	57.22	0.50	26.43	26.43	0.00	0.13	0.00	99.22
		7	5.19	6.22	2.71	0.76	57.22	0.52	26.70	26.68	0.02	0.13	0.00	99.45
		8	4.63	5.92	2.96	0.70	56.86	0.52	27.47	27.47	0.00	0.12	0.00	99.17
		9	5.24	5.90	3.04	0.68	56.91	0.55	26.79	26.77	0.02	0.12	0.01	99.25
		10	5.14	5.84	3.08	0.70	56.75	0.52	26.84	26.84	0.00	0.13	0.01	99.03
		11	4.97	5.89	3.12	0.74	57.06	0.49	27.16	27.16	0.00	0.12	0.00	99.55
		12	5.01	6.03	2.87	0.75	56.74	0.48	27.05	26.97	0.08	0.12	0.01	99.07
		Average	**4.98**	**6.00**	**2.94**	**0.73**	**56.91**	**0.52**	**27.04**	**27.03**	**0.02**	**0.12**	**0.00**	**99.23**
		2SD	**0.68**	**0.29**	**0.31**	**0.06**	**0.41**	**0.05**	**1.00**	**1.00**	**0.06**	**0.02**	**0.01**	**0.34**
	Farmington	1	5.58	5.62	3.09	0.67	57.08	0.49	27.03	26.55	0.54	0.09	0.00	99.71
		2	5.36	6.11	2.88	0.71	56.85	0.51	26.84	26.64	0.22	0.09	0.00	99.38
		3	5.20	6.19	2.37	0.72	56.82	0.49	27.38	26.47	1.01	0.09	0.01	99.38
		4	5.55	5.86	2.87	0.71	56.96	0.48	26.75	26.38	0.41	0.08	0.04	99.33
		6	5.57	6.19	2.43	0.73	56.80	0.51	26.46	25.75	0.79	0.13	0.01	98.91
		7	5.50	6.15	1.95	0.76	57.67	0.45	26.68	25.64	1.16	0.11	0.00	99.39
		8	5.53	6.38	2.47	0.74	57.61	0.45	26.31	26.21	0.11	0.08	0.01	99.58
		9	5.04	6.22	2.29	0.72	57.47	0.50	26.82	26.70	0.14	0.11	0.09	99.28
		10	5.51	6.16	2.94	0.74	57.15	0.47	26.53	26.53	0.00	0.10	0.00	99.60

		12	5.51	6.50	2.14	0.74	57.20	0.47	26.70	25.87	0.92	0.09	0.00	99.44
		Average	**5.44**	**6.14**	**2.54**	**0.72**	**57.16**	**0.48**	**26.75**	**26.27**	**0.53**	**0.10**	**0.01**	**99.40**
		2SD	**0.36**	**0.49**	**0.76**	**0.05**	**0.65**	**0.05**	**0.61**	**0.77**	**0.84**	**0.03**	**0.06**	**0.43**
L4	Bjurbole	1	1.75	5.28	2.20	0.71	57.44	0.64	30.90	30.90	0.00	0.35	0.00	99.26
		3	1.71	5.22	2.21	0.69	56.97	0.62	31.12	30.99	0.14	0.35	0.00	98.91
		5	1.67	5.38	2.14	0.66	56.84	0.63	31.03	30.95	0.09	0.37	0.01	98.73
		6	1.75	5.33	2.07	0.70	57.17	0.62	30.83	30.79	0.04	0.37	0.00	98.84
		7	1.78	5.47	1.80	0.72	57.65	0.60	30.59	30.59	0.00	0.36	0.01	98.99
		8	1.81	5.18	2.29	0.65	56.95	0.59	30.85	30.82	0.03	0.35	0.01	98.68
		10	1.74	5.25	2.02	0.70	57.07	0.63	30.77	30.65	0.13	0.36	0.00	98.55
		11	1.70	5.56	1.86	0.68	56.99	0.61	30.73	30.61	0.14	0.37	0.00	98.52
		12	1.76	5.13	2.30	0.69	56.86	0.60	31.07	30.96	0.12	0.37	0.01	98.80
		13	2.44	8.29	1.90	0.60	54.80	0.59	30.04	30.04	0.00	0.35	0.00	99.02
		Average	**1.81**	**5.61**	**2.08**	**0.68**	**56.87**	**0.61**	**30.79**	**30.73**	**0.07**	**0.36**	**0.00**	**98.83**
		2SD	**0.45**	**1.90**	**0.36**	**0.07**	**1.55**	**0.03**	**0.62**	**0.57**	**0.12**	**0.02**	**0.01**	**0.45**
	McKinney	1	2.62	4.73	2.33	0.70	57.99	0.56	30.13	29.87	0.29	0.35	0.00	99.44
		2	2.64	4.85	2.30	0.69	56.74	0.55	30.88	29.77	1.23	0.29	0.00	99.05
		3	1.89	4.74	2.15	0.66	57.11	0.65	30.92	30.40	0.58	0.46	0.01	98.64
		4	2.30	4.78	2.22	0.70	57.36	0.64	30.60	30.03	0.63	0.37	0.01	99.05
		5	2.09	4.70	2.20	0.71	57.66	0.62	30.70	30.37	0.37	0.37	0.01	99.09
		6	2.22	4.75	2.22	0.67	57.30	0.63	30.66	30.08	0.64	0.40	0.00	98.90
		7	2.65	4.58	2.29	0.69	57.53	0.56	30.43	29.65	0.86	0.37	0.00	99.18
		8	2.45	4.72	2.24	0.70	57.54	0.59	30.62	29.92	0.77	0.41	0.00	99.35
		9	2.57	4.80	2.19	0.71	57.39	0.60	30.31	29.65	0.73	0.36	0.02	99.03
		10	2.42	4.69	2.28	0.69	57.63	0.59	30.85	30.12	0.81	0.35	0.00	99.58
		Average	**2.38**	**4.73**	**2.24**	**0.69**	**57.43**	**0.60**	**30.61**	**29.99**	**0.69**	**0.37**	**0.01**	**99.13**
		2SD	**0.51**	**0.15**	**0.11**	**0.03**	**0.68**	**0.07**	**0.51**	**0.53**	**0.53**	**0.09**	**0.01**	**0.55**
LL6	Cherokee Springs	1	1.82	6.17	3.11	0.74	54.52	0.55	31.72	31.72	0.00	0.26	0.02	98.89

		2	1.94	5.83	3.50	0.72	54.47	0.55	31.65	31.65	0.00	0.26	0.00	98.92
		3	1.67	6.29	3.24	0.70	53.93	0.57	31.99	31.99	0.00	0.25	0.07	98.72
		4	1.54	6.03	3.52	0.70	52.96	0.55	32.68	32.65	0.04	0.23	0.10	98.31
		5	1.67	5.92	3.62	0.72	53.68	0.52	32.44	32.44	0.00	0.22	0.05	98.83
		6	1.42	6.67	2.61	0.73	54.11	0.52	32.16	32.14	0.02	0.24	0.08	98.53
		Average	**1.67**	**6.15**	**3.27**	**0.72**	**53.94**	**0.54**	**32.11**	**32.10**	**0.01**	**0.24**	**0.05**	**98.70**
		2SD	**0.37**	**0.61**	**0.75**	**0.03**	**1.15**	**0.04**	**0.81**	**0.79**	**0.03**	**0.03**	**0.07**	**0.48**
LL5	Oberlin	2	1.85	6.40	2.46	0.74	55.11	0.55	31.46	31.39	0.08	0.28	0.05	98.90
		3	1.81	6.40	2.18	0.77	55.51	0.55	31.31	31.15	0.18	0.30	0.04	98.90
		4	3.45	5.49	3.70	0.65	53.80	0.48	30.83	30.18	0.72	0.15	0.15	98.77
		5	1.88	6.25	3.01	0.78	54.63	0.57	31.88	31.88	0.00	0.25	0.06	99.30
		6	1.93	6.15	3.20	0.72	54.32	0.57	32.09	31.94	0.16	0.24	0.00	99.23
		7	2.09	6.12	2.72	0.71	55.03	0.56	31.36	31.21	0.17	0.27	0.04	98.92
		8	1.88	6.44	2.53	0.74	55.24	0.58	31.65	31.53	0.14	0.26	0.03	99.36
		9	1.68	6.55	2.03	0.75	55.40	0.57	31.60	31.27	0.37	0.29	0.05	98.95
		10	2.01	6.00	3.30	0.70	54.72	0.58	31.80	31.80	0.00	0.25	0.00	99.35
		Average	**2.06**	**6.20**	**2.79**	**0.73**	**54.86**	**0.56**	**31.55**	**31.37**	**0.20**	**0.26**	**0.05**	**99.08**
		2SD	**1.07**	**0.64**	**1.10**	**0.08**	**1.10**	**0.06**	**0.74**	**1.07**	**0.44**	**0.09**	**0.09**	**0.46**
LL4	Soko Banja	1	1.41	6.05	2.20	0.77	55.56	0.55	31.92	31.66	0.29	0.35	0.02	98.85
		3	1.57	5.48	2.20	0.67	56.31	0.57	31.67	31.32	0.39	0.35	0.02	98.88
		4	1.59	5.53	2.16	0.71	56.41	0.54	31.51	31.30	0.24	0.32	0.03	98.82
		5	1.46	5.65	1.79	0.71	56.65	0.54	31.39	31.09	0.33	0.33	0.03	98.59
		6	1.44	6.95	1.72	0.80	54.65	0.56	31.68	31.10	0.64	0.39	0.04	98.30
		7	1.58	5.76	3.01	0.72	55.10	0.56	32.28	32.23	0.06	0.30	0.01	99.33
		8	1.58	5.82	2.57	0.75	54.96	0.55	32.17	31.72	0.50	0.33	0.04	98.84
		9	1.55	5.60	3.52	0.69	53.69	0.56	33.06	32.61	0.51	0.33	0.01	99.07
		11	1.38	5.71	1.87	0.70	56.27	0.56	31.85	31.25	0.66	0.38	0.00	98.78
		13	1.44	5.96	1.75	0.69	55.48	0.53	31.75	30.99	0.84	0.34	0.05	98.09
		Average	**1.50**	**5.85**	**2.28**	**0.72**	**55.51**	**0.55**	**31.93**	**31.53**	**0.45**	**0.34**	**0.02**	**98.76**

	2SD	**0.16**	**0.85**	**1.19**	**0.08**	**1.86**	**0.02**	**0.97**	**1.07**	**0.46**	**0.05**	**0.03**	**0.71**
Hamlet	1	1.71	4.76	2.86	0.70	56.30	0.54	32.21	31.77	0.49	0.35	0.00	99.49
	3	1.61	3.28	3.23	0.71	56.79	0.52	32.82	32.01	0.90	0.34	0.00	99.39
	5	1.61	3.37	3.08	0.75	56.02	0.52	32.79	31.66	1.26	0.33	0.01	98.60
	6	1.59	3.52	3.01	0.70	56.36	0.55	32.68	31.78	1.00	0.33	0.05	98.89
	7	1.59	4.23	3.16	0.70	55.28	0.55	32.83	31.89	1.04	0.39	0.01	98.84
	8	1.64	4.41	3.12	0.71	54.93	0.52	32.96	31.85	1.23	0.38	0.03	98.82
	9	1.69	4.44	3.10	0.67	54.85	0.51	32.82	31.72	1.22	0.37	0.02	98.60
	11	1.61	5.46	2.06	0.75	56.42	0.55	31.94	31.20	0.82	0.41	0.01	99.30
	12	1.64	4.51	2.93	0.72	55.31	0.55	32.81	31.74	1.19	0.37	0.03	98.99
	Average	**1.63**	**4.22**	**2.95**	**0.71**	**55.81**	**0.54**	**32.65**	**31.74**	**1.02**	**0.36**	**0.02**	**98.99**
	2SD	**0.09**	**1.43**	**0.70**	**0.05**	**1.44**	**0.03**	**0.68**	**0.45**	**0.50**	**0.05**	**0.03**	**0.66**

All FeO: all Fe assigned as FeO
Total does not include All FeO
2SD: 2 standard deviations

Table B.2. Ion microprobe spot measurements (oxygen isotopes) of chrome-spinel grains from modern meteorites.

Type	Sample	Session	Spot #	$\delta^{18}O$	*2 SD*	$\delta^{17}O$	*2 SD*	$\Delta^{17}O$	*2 SD*
Eucrite	NWA 8365	2	Eu_G01@1	-7.42	*1.00*	-3.58	*0.62*	0.28	*0.56*
			Eu_G01@2	-7.63	*0.94*	-3.84	*0.66*	0.13	*0.60*
			Eu_G06@1	-5.11	*0.91*	-2.41	*0.63*	0.25	*0.57*
			Eu_G06@2	-5.36	*0.96*	-2.39	*0.71*	0.40	*0.62*
			Eu_G03@1	-6.95	*0.92*	-3.22	*0.66*	0.40	*0.57*
			Average	**-6.50**	***2.36***	**-3.09**	***1.33***	**0.29**	***0.23***
		3	Eu_G01@1	-7.31	*1.71*	-3.79	*0.87*	0.01	*0.41*
			Eu_G01@2	-7.82	*1.65*	-3.78	*0.90*	0.28	*0.42*
			Eu_G03@1	-8.92	*1.78*	-4.46	*0.95*	0.18	*0.47*
			Eu_G03@2	-8.31	*1.64*	-4.21	*0.86*	0.11	*0.38*
			Eu_G03@3	-7.14	*1.66*	-3.07	*0.89*	0.64	*0.38*
			Eu_G06@1	-6.73	*1.72*	-3.74	*0.87*	-0.25	*0.44*
			Eu_G06@2	-7.13	*1.70*	-3.33	*0.96*	0.38	*0.45*
			Average	**-7.62**	***1.54***	**-3.77**	***0.95***	**0.19**	***0.56***
			Sample Average	**-7.15**	***2.16***	**-3.49**	***1.28***	**0.23**	***0.45***
Diogenite	NWA 10403	2	Di_G02@1	-3.58	*1.24*	-1.75	*1.27*	0.11	*0.36*
			Di_G02@2	-3.74	*1.31*	-2.15	*1.36*	-0.20	*0.39*
			Di_G04@1	-1.34	*1.01*	-0.42	*1.21*	0.28	*0.34*
			Di_G04@2	-1.17	*0.99*	-0.57	*1.17*	0.03	*0.36*
			Di_G07@1	-3.48	*1.16*	-1.84	*1.21*	-0.03	*0.35*
			Average	**-2.66**	***2.58***	**-1.35**	***1.58***	**0.04**	***0.35***

		3	Di_G07@1	-3.78	*1.14*	-2.68	*0.70*	-0.71	*0.55*
			Di_G07@2	-3.36	*1.20*	-2.22	*0.74*	-0.48	*0.41*
			Di_G02@1	-2.01	*1.16*	-1.42	*0.73*	-0.37	*0.51*
			Di_G02@2	-2.12	*1.12*	-1.07	*0.73*	0.04	*0.54*
			Di_G04@1	-1.20	*1.00*	-1.11	*0.76*	-0.48	*0.55*
			Di_G04@2	-1.54	*1.08*	-0.66	*0.63*	0.15	*0.50*
			Di_G04@3	-1.29	*1.04*	-0.57	*0.66*	0.10	*0.52*
			Average	**-2.19**	***2.02***	**-1.39**	***1.58***	**-0.25**	***0.68***
			Sample Average	**-2.38**	***2.21***	**-1.37**	***1.51***	**-0.13**	***0.62***
Brachinite	NWA 3151	1	Br_G02@1	2.04	*0.96*	0.26	*0.64*	-0.80	*0.57*
			Br_G02@2	1.19	*0.95*	0.18	*0.56*	-0.43	*0.51*
			Br_G03@1	2.74	*0.89*	0.74	*0.64*	-0.69	*0.58*
			Br_G03@2	2.46	*0.92*	0.69	*0.64*	-0.60	*0.56*
			Br_G06@1	5.97	*0.86*	1.86	*0.67*	-1.25	*0.66*
			Br_G06@2	6.55	*0.94*	1.93	*0.67*	-1.47	*0.62*
			Average	**3.49**	***4.43***	**0.94**	***1.54***	**-0.87**	***0.81***
		3	Br_G02@1	0.17	*1.52*	-0.40	*0.93*	-0.49	*0.67*
			Br_G02@2	-0.31	*1.48*	0.02	*0.91*	0.19	*0.65*
			Br_G02@3	1.58	*1.55*	0.42	*1.01*	-0.40	*0.69*
			Br_G01@1	-1.88	*1.53*	-0.84	*0.94*	0.14	*0.59*
			Br_G01@2	-0.89	*1.57*	-0.62	*0.97*	-0.15	*0.64*
			Br_G01@3	-0.97	*1.52*	-0.90	*0.95*	-0.39	*0.62*
			Br_G03@1	-1.52	*1.57*	-0.68	*0.97*	0.11	*0.65*
			Br_G03@2	-1.36	*1.54*	-0.97	*0.98*	-0.26	*0.62*
			Br_G04@1	-1.89	*1.52*	-0.83	*0.94*	0.15	*0.66*
			Br_G04@2	-1.90	*1.56*	-0.87	*0.95*	0.12	*0.57*
			Br_G06@1	-1.69	*1.45*	-1.01	*0.91*	-0.13	*0.58*

			Average	**-0.97**	***2.17***	**-0.61**	***0.90***	**-0.10**	***0.51***
			Sample Average	**-0.97**	***2.17***	**-0.61**	***0.90***	**-0.10**	***0.51***
Acapulcoite	NWA 8287	2	Ac_G02@1	-1.37	*1.28*	-1.60	*0.74*	-0.89	*0.54*
			Ac_G02@2	-1.50	*1.37*	-1.68	*0.75*	-0.90	*0.57*
			Ac_G04@1	-1.57	*1.42*	-2.02	*0.79*	-1.21	*0.57*
			Ac_G04@2	-1.69	*1.37*	-2.01	*0.79*	-1.13	*0.57*
			Ac_G07@1	-0.09	*1.12*	-1.39	*0.56*	-1.34	*0.54*
			Ac_G07@2	-0.48	*1.07*	-1.35	*0.66*	-1.10	*0.57*
			Average	**-1.12**	***1.33***	**-1.67**	***0.59***	**-1.09**	***0.35***
		3	Ac_G02@1	-1.99	*1.32*	-2.02	*0.98*	-0.99	*0.77*
			Ac_G02@2	-1.58	*1.29*	-2.20	*1.07*	-1.38	*0.82*
			Ac_G02@3	-1.57	*1.28*	-1.88	*0.96*	-1.06	*0.79*
			Ac_G04@1	-1.37	*1.22*	-1.70	*0.97*	-0.98	*0.84*
			Ac_G06@1	-0.60	*1.23*	-2.01	*0.99*	-1.69	*0.79*
			Ac_G06@2	-0.65	*1.32*	-1.53	*1.00*	-1.19	*0.87*
			Ac_G06@3	-0.77	*1.24*	-1.87	*1.00*	-1.47	*0.83*
			Average	**-1.22**	***1.09***	**-1.89**	***0.45***	**-1.25**	***0.54***
			Sample Average	**-1.17**	***1.15***	**-1.79**	***0.54***	**-1.18**	***0.47***
Lodranite	NWA 10265	1	Lo_G01@1	2.08	*1.03*	-0.74	*0.54*	-1.82	*0.41*
			Lo_G01@2	1.53	*1.13*	-0.91	*0.62*	-1.71	*0.42*
			Lo_G02@1	1.92	*1.16*	-0.97	*0.63*	-1.97	*0.50*
			Lo_G02@2	2.04	*0.96*	-0.78	*0.56*	-1.84	*0.42*
			Lo_G06@1	2.74	*1.04*	-0.65	*0.59*	-2.08	*0.44*
			Average	**2.06**	***0.87***	**-0.81**	***0.26***	**-1.88**	***0.29***

		3	Lo_G01@1	-0.41	*2.03*	-1.78	*1.14*	-1.57	*0.53*
			Lo_G01@2	-0.73	*2.01*	-1.71	*1.14*	-1.33	*0.61*
			Lo_G02@1	-1.12	*2.07*	-2.06	*1.14*	-1.47	*0.53*
			Lo_G02@2	-1.21	*2.07*	-2.04	*1.17*	-1.41	*0.55*
			Lo_G06@1	-0.77	*2.09*	-2.01	*1.14*	-1.60	*0.50*
			Average	**-0.85**	***0.65***	**-1.92**	***0.32***	**-1.48**	***0.22***
			Sample Average	**-0.85**	***0.65***	**-1.92**	***0.32***	**-1.48**	***0.22***
Ureilite	NWA 766	1	Ur_G02@1	13.15	*0.89*	5.42	*0.59*	-1.41	*0.63*
			Ur_G02@2	12.99	*0.82*	5.58	*0.55*	-1.18	*0.57*
			Ur_G03@1	11.40	*0.89*	4.84	*0.52*	-1.09	*0.50*
			Ur_G03@2	11.72	*0.80*	4.84	*0.57*	-1.25	*0.55*
			Ur_G06@1	12.01	*0.90*	4.84	*0.50*	-1.41	*0.45*
			Average	**12.25**	***1.56***	**5.10**	***0.73***	**-1.27**	***0.29***
		3	Ur_G02@1	10.92	*1.05*	4.41	*0.76*	-1.27	*0.65*
			Ur_G02@2	10.85	*1.10*	4.26	*0.81*	-1.38	*0.62*
			Ur_G03@1	9.62	*1.17*	3.68	*0.86*	-1.33	*0.65*
			Ur_G03@2	9.76	*1.19*	4.01	*0.90*	-1.06	*0.74*
			Ur_G06@1	9.64	*1.04*	3.65	*0.78*	-1.36	*0.63*
			Average	**10.16**	***1.33***	**4.00**	***0.68***	**-1.28**	***0.26***
			Sample Average	**10.16**	***1.33***	**4.00**	***0.68***	**-1.28**	***0.26***
CR6	NWA 7317	2	CR_G02@1	-1.43	*0.96*	-2.13	*0.73*	-1.38	*0.67*
			CR_G02@2	-1.87	*0.93*	-2.44	*0.68*	-1.47	*0.72*
			CR_G05@1	-1.64	*1.11*	-2.41	*0.78*	-1.56	*0.72*

	CR_G05@2	-1.65	*1.04*	-2.54	*0.77*	-1.68	*0.71*
	CR_G07@1	-2.29	*1.16*	-2.78	*0.84*	-1.59	*0.68*
	Average	**-1.78**	***0.65***	**-2.46**	***0.47***	**-1.54**	***0.23***
3	CR_G05@1	-3.64	*1.45*	-3.48	*0.81*	-1.58	*0.65*
	CR_G04@1	-5.02	*1.46*	-3.84	*0.87*	-1.23	*0.61*
	CR_G04@2	-4.80	*1.47*	-3.97	*0.86*	-1.48	*0.64*
	CR_G07@1	-4.84	*1.48*	-4.17	*0.85*	-1.65	*0.60*
	CR_G01@1	-4.80	*1.49*	-4.58	*0.87*	-2.09	*0.60*
	CR_G01@2	-4.84	*1.48*	-3.72	*0.84*	-1.20	*0.60*
	CR_G01@3	-4.81	*1.49*	-3.98	*0.86*	-1.48	*0.59*
	Average	**-4.68**	***0.93***	**-3.96**	***0.70***	**-1.53**	***0.60***
	Sample Average	**-3.47**	***3.09***	**-3.34**	***1.66***	**-1.53**	***0.46***

2SD: 2 standard deviations.
Session 1 measurements are not included in sample averages because the values did not align with literature values.

APPENDIX C. EXTRATERRESTRIAL CHROME-SPINEL DATABASE

Table C.1. Chemical composition database for chrome-spinels from modern meteorites.

Reference	Type	Sample	MgO	Al_2O_3	TiO_2	V_2O_3	Cr_2O_3	MnO	All FeO	FeO	Fe_2O_3	ZnO	Total
Berkley and Boynton, 1992	howardite	EET87503*	3.77	10.70	0.63		55.90	0.58	27.97	27.80	0.19		99.57
Berkley and Boynton, 1992	howardite	LEW 85441	2.83	12.30	0.82		54.30	0.54	28.90	28.90	0.00		99.69
Berkley and Boynton, 1992	howardite	LEW 85313*	1.91	8.70	1.31		55.30	0.59	31.00	30.50	0.56		98.87
Mittlefehldt, 2015	eucrite	ALHA81001	0.36	9.66	2.15	0.64	49.90	0.57	33.90	33.53	0.41		97.22
Mittlefehldt, 2015	eucrite	Bouvante	0.52	8.15	4.20		51.70	0.57	34.50	34.50	0.00		99.64
Mittlefehldt, 2015	eucrite	BTN 00300	1.01	5.49	12.20	0.81	37.30	0.59	42.00	41.62	0.42		99.44
Mittlefehldt, 2015	eucrite	BTN 00300	0.94	5.65	2.40	0.29	58.92	0.41	31.33	31.33	0.00		99.93
Mittlefehldt, 2015	eucrite	BTN 00300	0.99	4.01	17.51	0.26	31.08	0.59	45.11	45.11	0.00		99.54
Mittlefehldt, 2015	eucrite	Caldera	0.98	4.55	15.30	0.81	33.00	0.55	44.60	44.47	0.15		99.80
Mittlefehldt, 2015	eucrite	Chervony Kut	1.08	5.49	12.10	0.58	37.80	0.47	41.50	41.41	0.10		99.03
Mittlefehldt, 2015	eucrite	EET 87520	1.08	5.36	12.10	0.56	38.10	0.52	41.50	41.41	0.10		99.23
Mittlefehldt, 2015	eucrite	EET 90020	0.43	5.44	16.70	0.58	28.00	0.61	47.40	46.46	1.04		99.26
Mittlefehldt, 2015	eucrite	EET 90020	0.79	5.90	10.35	0.38	41.11	0.56	40.94	40.58	0.40		100.07
Mittlefehldt, 2015	eucrite	EET 90020	0.54	4.96	15.00	0.27	32.90	0.55	45.47	44.91	0.62		99.74
Mittlefehldt, 2015	eucrite	EET 90020	0.71	4.02	19.89	0.18	24.05	0.64	49.90	48.73	1.30		99.53
Mittlefehldt, 2015	eucrite	EET 90029	0.72	7.73	5.67	0.83	47.30	0.47	36.50	36.50	0.00		99.22
Mittlefehldt, 2015	eucrite	EET 92004	0.46	8.24	3.60	0.89	49.50	0.52	35.40	34.97	0.48		98.66
Mittlefehldt, 2015	eucrite	EET 92023	1.25	10.91	5.35	0.43	43.70	0.53	35.90	35.57	0.37		98.11
Mittlefehldt, 2015	eucrite	GRA 98098	0.69	4.15	21.70	0.51	20.00	0.55	51.50	50.41	1.21		99.22
Mittlefehldt, 2015	eucrite	GRA 98098	0.58	5.37	16.07	0.32	31.51	0.50	46.02	46.02	0.00	0.00	100.37
Mittlefehldt, 2015	eucrite	GRA 98098	0.62	4.67	19.59	0.25	25.09	0.55	49.24	48.95	0.32	0.03	100.06
Mittlefehldt, 2015	eucrite	GRA 98098	0.73	4.31	22.89	0.21	19.46	0.59	52.25	51.82	0.48	0.00	100.49
Mittlefehldt, 2015	eucrite	GRO 95533	0.69	7.20	7.58	0.56	44.20	0.59	38.20	38.09	0.12		99.03
Mittlefehldt, 2015	eucrite	Juvinas	0.24	7.90	5.00	0.77	50.60	0.63	35.50	35.50	0.00		100.64
Mittlefehldt, 2015	eucrite	LEW 85305	0.71	4.21	17.00	0.61	29.40	0.50	46.80	46.24	0.63		99.29
Mittlefehldt, 2015	eucrite	LEW 85353	0.60	8.46	2.59	0.75	53.00	0.45	33.80	33.80	0.00		99.65
Mittlefehldt, 2015	eucrite	LEW 88009	0.45	4.32	13.00	0.89	37.90	0.60	43.10	43.10	0.00		100.26
Mittlefehldt, 2015	eucrite	LEW 88010	0.38	8.54	2.51	0.67	53.50	0.47	33.90	33.90	0.00		99.97

Mittlefehldt, 2015	eucrite	MAC 02522	0.99	3.51	22.60	0.43	17.90	0.58	51.60	50.16	1.60		97.77
Mittlefehldt, 2015	eucrite	MET 01081	0.35	7.89	6.93	1.12	43.10	0.59	38.60	38.01	0.66		98.65
Mittlefehldt, 2015	eucrite	Millbillillie	0.36	8.09	2.37		52.60	0.58	33.40	33.40	0.00		97.40
Mittlefehldt, 2015	eucrite	Pasamonte	0.74	17.70	1.38	0.61	44.40	0.46	34.50	34.46	0.04		99.79
Mittlefehldt, 2015	eucrite	PCA 91078	1.00	11.64	2.80	0.00	47.90	0.55	34.50	33.86	0.71		98.46
Mittlefehldt, 2015	eucrite	Petersburg	1.63	14.50	3.68		43.90	0.51	34.30	34.21	0.10		98.53
Mittlefehldt, 2015	eucrite	Pomozdino	1.15	7.30	4.52	0.68	49.80	0.67	34.20	34.20	0.00		98.32
Mittlefehldt, 2015	eucrite	QUE 97014	0.50	8.14	2.93	0.95	51.10	0.58	34.30	34.19	0.12		98.51
Mittlefehldt, 2015	eucrite	QUE 99658	0.83	12.87	2.14	0.56	48.80	0.50	34.20	34.20	0.00		99.90
Mittlefehldt, 2015	eucrite	RKPA80224	0.43	8.12	3.37	0.93	51.00	0.57	35.10	35.03	0.08		99.53
Mittlefehldt, 2015	eucrite	Sioux County	0.28	7.20	3.40	0.93	51.60	0.62	35.50	35.10	0.45		99.57
Mittlefehldt, 2015	eucrite	ALHA81313	2.34	9.43	2.98	0.64	52.20	0.56	32.10	32.10	0.00		100.25
Mittlefehldt, 2015	eucrite	Moama	2.38	7.72	5.39	0.67	50.10	0.81	32.70	32.70	0.00		99.77
Mittlefehldt, 2015	eucrite	Moama	2.42	7.59	5.25	0.80	49.50	0.63	33.10	33.10	0.00		99.29
Mittlefehldt, 2015	eucrite	Moore County	1.31	5.70	10.10	0.81	42.30	0.66	39.50	39.50	0.00		100.38
Mittlefehldt, 2015	eucrite	Moore County	1.87	5.89	11.10	0.85	39.80	0.53	39.00	39.00	0.00		99.04
Mittlefehldt, 2015	eucrite	Serra de Mage	1.87	8.43	3.19	0.63	51.40	0.58	32.30	32.30	0.00		98.40
Mittlefehldt, 2015	eucrite	Serra de Magé	1.30	8.30	3.20	0.73	53.00	0.58	33.10	33.10	0.00		100.21
Mittlefehldt, 2015	eucrite	Vissannapeta	0.83	9.62	0.48		54.85	0.65	32.26	31.71	0.61		98.75
Mittlefehldt, 2015	eucrite	Y-791195	0.98	5.02	11.90	0.76	39.10	0.60	42.20	41.69	0.57		100.62
Patzer et al., 2005	eucrite	DaG 983	0.52	8.10	2.76		51.70	0.83	34.60	33.76	0.93		98.60
Bunch and Keil, 1971	eucrite-cm	Serra de Mage	1.30	8.30	3.20	0.73	53.00	0.58	33.10	33.10	0.00	0.02	100.23
Bunch and Keil, 1971	eucrite-mmict	Cachari (normal)	0.29	7.70	3.20	0.77	52.00	0.56	34.80	34.80	0.00	0.02	99.34
Bunch and Keil, 1971	eucrite-mmict	Cachari (shocked)	0.03	3.20	17.60	0.82	31.40	0.88	46.10	46.10	0.00	0.02	100.05
Bunch and Keil, 1971	eucrite-mmict	Sioux Co.	0.28	7.20	3.40	0.93	51.60	0.62	35.50	35.09	0.46	0.02	99.60
Bunch and Keil, 1971	eucrite-mmict	Haraiya	0.20	9.00	3.20	0.90	50.90	0.63	34.70	34.70	0.00	0.02	99.55
Bunch and Keil, 1971	eucrite-mmict	Juvinas	0.24	7.90	5.00	0.77	50.60	0.63	35.50	35.50	0.00	0.02	100.66
Bunch and Keil, 1971	eucrite-pmict	Petersburg	0.64	7.80	3.90	0.69	49.60	0.59	36.40	35.11	1.43	0.10	99.86
Bunch and Keil, 1971	eucrite-pmict	Nobleborough	0.30	12.20	3.30	0.50	45.70	0.57	37.30	35.93	1.52	0.02	100.04
Bunch and Keil, 1971	eucrite-pmict	Pasamonte	0.74	17.70	1.38	0.61	44.40	0.46	34.50	34.45	0.05	0.02	99.82
Bunch and Keil, 1971	eucrite-cm	Moore Co.	1.31	5.70	10.10	0.81	42.30	0.66	39.50	39.50	0.00	0.02	100.40
This Study	eucrite	NWA 8365	0.31	7.81	4.22	0.84	49.24	0.55	35.71	35.67	0.05	0.01	98.69
This Study	eucrite	Haraiya	0.05	8.22	2.53	0.72	49.63	0.55	33.32	33.27	0.06	0.01	95.05

Mittlefehldt, 2015	diogenite	A-87147	2.83	9.96	0.69	0.34	55.80	0.61	29.50	29.25	0.27	99.76
Mittlefehldt, 2015	diogenite	A-880785	3.54	10.00	0.75	0.57	55.90	0.58	28.80	28.39	0.45	100.19
Mittlefehldt, 2015	diogenite	A-880936	3.40	10.10	0.61	0.56	55.70	0.61	28.80	28.35	0.50	99.83
Mittlefehldt, 2015	diogenite	A-881239	3.91	12.30	0.82		54.10	0.56	28.50	28.28	0.24	100.21
Mittlefehldt, 2015	diogenite	A-881377	1.88	6.97	0.50	0.56	56.80	0.70	30.50	29.41	1.21	98.03
Mittlefehldt, 2015	diogenite	A-881377	2.87	15.90	0.81	0.40	47.40	0.65	30.90	29.96	1.05	99.04
Mittlefehldt, 2015	diogenite	A-881548	4.08	14.30	0.69		51.10	0.65	28.30	27.79	0.57	99.18
Mittlefehldt, 2015	diogenite	A-881838	1.51	6.42	1.08	0.62	56.50	0.66	32.30	30.85	1.62	99.25
Mittlefehldt, 2015	diogenite	A-881838	2.40	15.00	0.70	0.48	49.30	0.64	31.00	30.62	0.42	99.56
Mittlefehldt, 2015	diogenite	A-881944	1.49	5.53	0.72	0.58	58.90	0.67	31.00	30.32	0.76	98.97
Mittlefehldt, 2015	diogenite	A-881944	2.86	19.10	0.77	0.49	45.10	0.59	30.70	30.70	0.00	99.61
Mittlefehldt, 2015	diogenite	Aioun el Atrouss	4.05	12.00	0.68	0.43	53.63	0.46	28.91	28.00	1.01	100.27
Mittlefehldt, 2015	diogenite	ALHA77256	6.28	21.21	0.81	0.27	46.58	0.41	26.02	26.02	0.00	101.57
Mittlefehldt, 2015	diogenite	Bilanga	3.55	10.31	0.48		55.26	0.81	27.54	27.24	0.33	97.98
Mittlefehldt, 2015	diogenite	Dhofar 700	4.66	14.00	0.97	0.47	51.00	0.58	27.50	27.19	0.34	99.21
Mittlefehldt, 2015	diogenite	EET 83246	3.52	17.10	0.72	0.30	48.56	0.51	28.57	28.57	0.00	99.28
Mittlefehldt, 2015	diogenite	EET 83247	2.71	8.72	0.62	0.45	56.61	0.48	29.95	29.26	0.77	99.60
Mittlefehldt, 2015	diogenite	EET 87530	3.49	11.40	0.86	0.62	54.00	0.59	28.32	28.32	0.00	99.28
Mittlefehldt, 2015	diogenite	EETA79002	5.61	10.06	0.97	0.43	57.12	0.53	25.46	25.46	0.00	100.17
Mittlefehldt, 2015	diogenite	Ellemeet	3.75	15.63	0.11	0.78	50.01	0.57	28.06	27.99	0.08	98.92
Mittlefehldt, 2015	diogenite	Garland	3.46	6.34	0.21	0.86	60.60	0.55	27.73	27.35	0.42	99.77
Mittlefehldt, 2015	diogenite	GRA 98108	5.29	15.56	1.13	0.38	52.22	0.53	26.49	26.49	0.00	101.60
Mittlefehldt, 2015	diogenite	GRO 95555	4.48	8.59	0.63	0.55	57.17	0.67	27.01	26.22	0.88	99.20
Mittlefehldt, 2015	diogenite	Ibbenburen	2.64	9.85	0.82	0.54	55.12	0.67	28.85	28.85	0.00	98.49
Mittlefehldt, 2015	diogenite	Johnstown	2.54	9.37	0.42	0.35	56.26	0.51	30.11	29.42	0.77	99.65
Mittlefehldt, 2015	diogenite	LAP 91900	2.57	6.11	0.42	0.55	60.70	0.65	27.97	27.97	0.00	98.97
Mittlefehldt, 2015	diogenite	LEW 88011	3.04	12.69	1.49	0.48	50.74	0.48	31.17	30.34	0.92	100.20
Mittlefehldt, 2015	diogenite	LEW 88679	3.49	15.22	1.07	0.53	48.39	0.62	29.11	28.98	0.14	98.44
Mittlefehldt, 2015	diogenite	Manegaon	4.33	16.09	0.22	0.41	48.67	0.49	27.82	27.07	0.83	98.11
Mittlefehldt, 2015	diogenite	MET 00422	2.44	8.84	0.52	0.38	59.96	0.49	29.17	29.17	0.00	101.80
Mittlefehldt, 2015	diogenite	MET 00424	2.72	5.05	0.27	0.46	64.58	0.59	27.98	27.98	0.00	101.65
Mittlefehldt, 2015	diogenite	MET 00425	4.18	6.31	0.19	0.23	64.55	0.51	25.80	25.80	0.00	101.77
Mittlefehldt, 2015	diogenite	MET 00436	2.48	7.34	0.42	0.50	62.12	0.56	28.72	28.72	0.00	102.14

Mittlefehldt, 2015	diogenite	NWA 1877	2.88	7.04	0.50		59.20	0.67	28.80	28.29	0.57	99.15
Mittlefehldt, 2015	diogenite	QUE 93009	1.90	8.81	0.84	0.29	59.04	0.51	30.00	30.00	0.00	101.38
Mittlefehldt, 2015	diogenite	Roda	3.64	12.43	1.47	0.35	51.04	0.58	28.41	28.41	0.00	97.92
Mittlefehldt, 2015	diogenite	Shalka	3.44	6.24	0.38	0.90	60.19	0.61	27.95	27.46	0.53	99.75
Mittlefehldt, 2015	diogenite	Tatahouine	5.58	9.26	0.77	0.56	58.19	0.43	24.91	24.91	0.00	99.69
Mittlefehldt, 2015	diogenite	TIL 82410	2.84	8.88	0.65	0.65	55.83	0.50	29.46	28.85	0.67	98.87
Mittlefehldt, 2015	diogenite	Y-74013	4.40	9.26	0.86	0.58	54.71	1.09	27.93	26.15	1.98	99.03
Mittlefehldt, 2015	diogenite	Y-74097	5.89	7.67	0.75	0.61	59.90	0.45	24.89	24.55	0.38	100.20
Mittlefehldt, 2015	diogenite	Y-74097	5.98	7.83	0.77	0.66	58.90	0.58	24.80	24.14	0.73	99.59
Mittlefehldt, 2015	diogenite	Y-74097	6.49	14.70	0.73	0.50	51.80	0.52	24.90	24.50	0.45	99.69
Mittlefehldt, 2015	diogenite	Y-75032	1.95	7.94	1.95	0.59	54.92	0.55	31.70	31.44	0.28	99.61
Mittlefehldt, 2015	diogenite	Y-791194	2.11	8.32	1.55	0.27	57.00	0.55	29.75	29.75	0.00	99.55
Mittlefehldt, 2015	diogenite	Y-791199	2.14	8.69	1.80	0.58	54.12	0.53	31.54	31.09	0.49	99.44
Mittlefehldt, 2015	diogenite	Y-791203	2.40	6.01	0.49	0.42	61.88	0.55	27.64	27.64	0.00	99.40
Berkley and Boynton, 1992	diogenite	ALHA 77256 cum.*	6.48	21.60	0.91		44.60	0.48	26.12	25.90	0.25	100.22
Berkley and Boynton, 1992	diogenite	ALHA 77256 int.*	4.73	15.60	1.10		48.80	0.58	28.36	27.30	1.18	99.29
Berkley and Boynton, 1992	diogenite	ALH 84001*	4.33	9.26	2.18		49.40	0.47	33.12	28.40	5.25	99.29
Berkley and Boynton, 1992	diogenite	EET 79002*	3.47	11.30	0.81		54.30	0.54	29.50	29.00	0.56	99.98
Berkley and Boynton, 1992	diogenite	EET 83247*	3.13	9.53	0.72		55.70	0.57	24.83	24.20	0.70	94.55
Berkley and Boynton, 1992	diogenite	TIL 82410*	2.88	9.92	0.60		56.00	0.56	29.29	28.30	1.10	99.36
Berkley and Boynton, 1992	diogenite	EET 83246*	2.70	12.30	0.84		51.70	0.58	30.42	29.40	1.13	98.65
Berkley and Boynton, 1992	diogenite	EET 87530	3.44	11.20	0.91		54.40	0.55	28.20	28.20	0.00	98.70
Bowman et al., 1999	diogenite	Aioun el Atrouss	4.21	13.20	0.79	0.45	52.56	0.52	27.44	27.44	0.00	99.17
Bowman et al., 1999	diogenite	Ellemeet	3.75	15.63	0.11	0.78	50.01	0.57	28.06	27.99	0.08	98.92
Bowman et al., 1999	diogenite	Garland	3.21	7.27	0.39	0.83	58.58	0.65	27.51	27.51	0.00	98.44
Bowman et al., 1999	diogenite	Ibbenburen	2.64	9.85	0.82	0.54	55.12	0.67	28.85	28.85	0.00	98.49
Bowman et al., 1999	diogenite	Johnstown	3.11	11.98	0.62	0.35	53.55	0.63	28.83	28.83	0.00	99.07
Bowman et al., 1999	diogenite	Manegaon	4.62	13.41	0.62	0.48	52.51	0.74	26.84	26.70	0.16	99.24
Bowman et al., 1999	diogenite	Peckelsheim	2.79	10.43	0.85	0.65	53.98	0.55	29.41	29.25	0.18	98.68
Bowman et al., 1999	diogenite	Roda	3.64	12.43	1.47	0.35	51.04	0.58	28.41	28.41	0.00	97.92
Bowman et al., 1999	diogenite	Shalka	3.44	7.25	0.48	0.97	58.45	0.61	27.35	27.32	0.03	98.55
Bowman et al., 1999	diogenite	ALHA 77256	6.56	21.81	0.88	0.42	44.67	0.49	25.67	25.67	0.00	100.50
Bowman et al., 1999	diogenite	EET 83246	3.52	17.10	0.72	0.30	48.56	0.51	28.57	28.57	0.00	99.28

Bowman et al., 1999	diogenite	EET 83247	3.52	11.07	0.73	0.46	54.93	0.62	27.93	27.93	0.00		99.26
Bowman et al., 1999	diogenite	EET 87530	3.49	11.40	0.86	0.62	54.00	0.59	28.32	28.32	0.00		99.28
Bowman et al., 1999	diogenite	EETA 79002	3.83	12.56	0.82	0.40	52.48	0.66	27.96	27.87	0.10		98.72
Bowman et al., 1999	diogenite	LAP 91900	2.57	6.11	0.42	0.55	60.70	0.65	27.97	27.97	0.00		98.97
Bowman et al., 1999	diogenite	LEW 88008	2.76	17.85	1.02	0.49	45.86	0.62	30.80	30.78	0.02		99.40
Bowman et al., 1999	diogenite	LEW 88679	3.49	15.22	1.07	0.53	48.39	0.62	29.11	28.98	0.14		98.44
Bowman et al., 1999	diogenite	PCA 91077	3.05	10.06	0.67	0.41	55.14	0.60	28.46	28.46	0.00		98.39
Bowman et al., 1999	diogenite	TIL 82410	3.24	9.09	0.81	0.71	56.21	0.59	28.49	28.43	0.07		99.15
Papike et al., 2000	diogenite	GRO 95555 (average)	4.30	7.26	0.55		59.60	0.68	26.20	26.01	0.21		98.61
Bunch and Keil, 1971	diogenite	Shalka	5.10	9.60	1.27	0.51	57.30	0.59	26.10	26.10	0.00	0.09	100.56
Bunch and Keil, 1971	diogenite	Johnstown	2.62	10.50	0.87	0.35	53.60	0.78	31.40	29.80	1.78	0.02	100.32
This Study	diogenite	Dho700	4.26	12.84	0.54		51.79	0.65	27.66	26.72	1.05		97.84
This Study	diogenite	NWA 10403	2.11	9.82	0.96	0.62	54.80	0.52	30.22	30.22	0.00	0.01	99.07
Gardner-Vandy et al., 2013	brachinite	Brachina*	5.44	7.28	2.70	0.69	53.60	0.38	29.38	27.00	2.65		99.74
Gardner-Vandy et al., 2013	brachinite	ALH 84025*	3.53	7.26	1.29	0.74	58.00	0.42	28.89	28.70	0.21		100.15
Gardner-Vandy et al., 2013	brachinite	Hughes 26*	4.63	12.50	0.95	0.70	52.40	0.37	28.15	27.40	0.83		99.78
Gardner-Vandy et al., 2013	brachinite	EET 99402*	4.12	13.60	1.00	0.71	51.20	0.36	29.24	28.60	0.71		100.30
Gardner-Vandy et al., 2013	brachinite	NWA 3151*	4.60	12.70	0.89	0.70	53.00	0.37	27.97	27.60	0.41		100.27
Gardner-Vandy et al., 2013	brachinite	NWA 4969*	4.48	12.40	0.74	0.71	52.40	0.38	28.30	27.40	1.00		99.51
Gardner-Vandy et al., 2013	brachinite	NWA 5400 *	4.47	8.03	1.43	0.71	57.40	0.45	27.88	27.50	0.42		100.41
Mittlefehldt et al., 2003	brachinite	ALH 84025	3.50	7.52	1.27	0.40	59.70	0.34	28.00	28.00	0.00	0.42	101.15
Mittlefehldt et al., 2003	brachinite	EET 99402	4.29	13.69	0.97	0.37	52.58	0.29	28.20	28.20	0.00	0.02	100.41
Mittlefehldt et al., 2003	brachinite	EET 99407	4.37	13.40	0.96	0.37	53.10	0.29	28.08	28.08	0.00	0.02	100.59
This Study	brachinite	NWA 4872	4.36	12.89	0.74	0.68	51.69	0.31	27.38	27.17	0.24		98.08
This Study	brachinite	NWA 3151	4.49	12.65	0.89	0.66	52.32	0.30	27.19	27.00	0.22	0.41	98.94
Keil and McCoy, 2018	acap/lodr	EET 84302 3	11.04	8.15	0.55	0.51	61.70	1.92	14.52	14.20	0.35	0.52	98.95
Keil and McCoy, 2018	acap/lodr	EET 84302 5*	11.10	8.04	1.07	0.50	60.60	1.12	15.16	15.10	0.07	0.51	98.11
Keil and McCoy, 2018	acap/lodr	FRO 90011 %6	8.42	7.51	0.83		60.40	1.54	18.10	18.10	0.00	0.44	97.24
Keil and McCoy, 2018	acap/lodr	FRO 93001 %2	6.97	4.53	0.70	0.52	64.80	1.92	20.10	20.10	0.00	0.47	100.01
Keil and McCoy, 2018	acap/lodr	FRO 03001 %6	7.42	5.79	1.03		62.90	1.44	20.70	20.66	0.04	0.37	99.65
Keil and McCoy, 2018	acap/lodr	GRA 95209 14,19	1.70	3.80	1.00	0.53	62.80	1.40	26.50	26.50	0.00		97.73
Keil and McCoy, 2018	acap/lodr	GRA 95209 17	3.02	3.91	0.88	0.51	60.67	1.37	25.09	24.20	0.98	3.09	98.64
Keil and McCoy, 2018	acap/lodr	NWA 4735 1	9.30	5.70	0.90		62.60	2.60	15.80	15.80	0.00		96.90

Keil and McCoy, 2018	acap/lodr	TIL 99002 4	8.89	5.84	1.12		63.10	0.32	16.90	16.90	0.00	0.82	96.99
Mittlefehldt et al., 1996	acap/lodr	EET 84302, 20*	11.10	8.04	1.07	0.50	60.60	1.12	15.16	15.10	0.07	0.51	98.11
Mittlefehldt et al., 1996	acapulcoite	ALHA 81187, 17*	9.84	6.40	0.44	0.44	63.40	3.05	14.16	14.00	0.18	0.93	98.68
Mittlefehldt et al., 1996	acapulcoite	ALHA 81261, 13	6.62	6.52	1.19	0.54	60.80	1.20	21.10	21.10	0.00	1.06	99.03
Keil and McCoy, 2018	acapulcoite	Acapulco 13	6.65	6.75	1.24		63.20	1.85	20.60	20.60	0.00	1.34	101.63
Keil and McCoy, 2018	acapulcoite	Acapulco 14,19	6.50	5.80	1.20	0.57	62.70	1.30	21.20	21.20	0.00		99.27
Keil and McCoy, 2018	acapulcoite	Acapulco 15	6.90	6.30	1.36	1.03	62.00	1.34	20.60	20.60	0.00	0.96	100.49
Keil and McCoy, 2018	acapulcoite	ALH A77081 +18	6.21	6.16	1.20		61.50	2.46	21.20	21.20	0.00	0.83	99.56
Keil and McCoy, 2018	acapulcoite	ALH A78230 +13	6.79	6.75	1.34		59.70	1.25	22.00	21.26	0.82	1.27	99.18
Keil and McCoy, 2018	acapulcoite	ALH A81187 %%5*	9.84	6.40	0.44	0.44	63.40	3.05	14.16	14.00	0.18	0.93	98.68
Keil and McCoy, 2018	acapulcoite	ALH A81187 %%14,19	9.60	6.40	0.64	0.54	64.80	2.90	15.10	15.10	0.00		99.98
Keil and McCoy, 2018	acapulcoite	ALH A81261 +5	6.62	6.52	1.19	0.54	60.80	1.20	21.10	21.10	0.00	1.06	99.03
Keil and McCoy, 2018	acapulcoite	Dho 290 4	7.46	7.22	1.17		61.50	1.48	20.20	20.20	0.00	1.02	100.05
Keil and McCoy, 2018	acapulcoite	FRO 95029 6 granoblastic	8.01	9.17	1.25		58.10	1.81	19.10	19.10	0.00		97.44
Keil and McCoy, 2018	acapulcoite	GRA 98028 4	6.50	3.51	0.92		64.70	2.23	20.20	20.03	0.19	1.03	99.11
Keil and McCoy, 2018	acapulcoite	GRA 98028 7 (2 sm gr)	6.70	3.10	0.54		64.80	1.60	21.70	20.71	1.10		98.55
Keil and McCoy, 2018	acapulcoite	GRA 98028 7 (1 course gr)	7.20	6.70	0.90		58.60	1.40	22.20	20.60	1.78		97.18
Keil and McCoy, 2018	acapulcoite	MET 1195 7	9.30	6.70	1.20		61.30	1.50	18.00	17.83	0.19		98.02
Keil and McCoy, 2018	acapulcoite	MET 01195 14,19	8.60	6.80	1.10	0.53	63.50	1.30	18.00	18.00	0.00		99.83
Keil and McCoy, 2018	acapulcoite	Y-740638	6.94	6.58	1.33		59.06	1.23	21.06	21.06	0.00		96.20
This Study	acapulcoite	NWA 8287	8.05	9.60	1.39	0.64	57.77	1.21	19.66	19.66	0.00	0.89	99.21
Mittlefehldt et al., 1996	lodranite	LEW 88280, 23*	4.49	5.45	0.51	0.69	61.00	0.93	24.60	24.50	0.11	0.54	98.22
Mittlefehldt et al., 1996	lodranite	MAC 88177, 37*	5.40	8.06	0.57	0.68	58.30	1.06	23.46	23.30	0.18	0.60	98.15
Keil and McCoy, 2018	lodranite	Gibson 13	14.30	9.83	0.80		62.60	2.31	9.89	9.89	0.00	0.23	99.96
Keil and McCoy, 2018	lodranite	LEW 88280 5*	4.49	5.45	0.51	0.69	61.00	0.93	24.60	24.50	0.11	0.54	98.22
Keil and McCoy, 2018	lodranite	Lodran 16	6.47	4.43	0.91	0.46	61.80	1.10	22.30	21.05	1.39	1.27	98.88
Keil and McCoy, 2018	lodranite	MAC 88177 3	6.40	9.69	0.90	0.51	58.10	1.03	22.70	22.70	0.00	0.61	99.94
Keil and McCoy, 2018	lodranite	MAC 88177 5*	5.40	8.06	0.57	0.68	58.30	1.06	23.46	23.30	0.18	0.60	98.15
Keil and McCoy, 2018	lodranite	Y-74357 3	8.19	6.23	0.99	0.66	62.40	1.40	19.59	19.49	0.11	0.59	100.06
Keil and McCoy, 2018	lodranite	Y-791491 @3 (Al-poor)	5.20	4.97	0.60	0.51	64.30	0.87	23.80	23.80	0.00		100.25
Keil and McCoy, 2018	lodranite	Y-791491 @3 (Al-rich)	5.42	8.13	0.71	0.44	60.40	0.93	23.70	23.70	0.00		99.73
Keil and McCoy, 2018	lodranite	Y-791491 @13	5.59	3.99	0.85		63.40	1.67	23.10	22.46	0.71	0.58	99.25
Keil and McCoy, 2018	lodranite	Y-791493 @9	4.82	5.98	0.66	0.66	61.90	1.36	23.90	23.90	0.00	0.80	100.08

Keil and McCoy, 2018	lodranite	Y-8002 10	14.70	4.36	0.49	0.53	67.40	1.72	9.64	8.22	1.57	0.68	99.68
Keil and McCoy, 2018	lodranite	Y-8002 13	15.80	4.84	0.81		68.80	1.33	7.12	7.12	0.00	0.51	99.21
This Study	lodranite	NWA 10265	9.97	12.01	0.14	0.81	58.15	0.50	18.01	18.01	0.01	0.07	99.65
Chikami et al., 1997	ureilite	Lewis Cliff 88774 *Fe-rich	7.88	14.00	0.71	0.42	54.00	0.50	21.60	21.60	0.00	0.44	99.55
Chikami et al., 1997	ureilite	Lewis Cliff 88774 *Fe-poor	20.80	15.60	1.23	0.40	59.00	0.99	1.34	1.34	0.00		99.36
Goodrich et al., 2014	ureilite	LEW 88774	7.97	14.13	0.74	0.44	53.17	0.51	22.00	21.68	0.35	0.43	99.43
Goodrich et al., 2014	ureilite	NWA 766	9.30	17.50	0.69	0.40	49.00	0.38	20.50	19.90	0.67	0.40	98.24
Goodrich et al., 2014	ureilite	NWA 3109	8.80	12.33	0.86	0.55	55.43	0.43	20.60	20.57	0.03		98.99
Goodrich et al., 2014	ureilite	EET 96328	11.90	16.20	0.40	0.52	54.00	0.49	15.70	15.70	0.00	0.27	99.48
Goodrich et al., 2014	ureilite	HaH 064	10.75	16.65	0.61	0.43	51.50	0.50	18.60	17.79	0.90	0.36	99.48
This Study	ureilite	NWA 766	17.54	19.27	0.81	0.40	53.71	0.64	6.72	6.72	0.00	0.12	99.22
Mikouchi et al., 1996	angrite	Asuka 881371	6.98	37.75	1.48	0.60	20.93	0.26	31.42	28.32	3.44		99.77
This Study	angrite	Dorbigny	12.12	51.68	0.34	0.36	9.66	0.14	24.00	21.44	2.84	0.01	98.59
Schmitz et al., 2014	winonaite	Winona	10.42	0.66	0.41	0.37	68.68	2.85	15.02	12.11	3.24	2.00	100.75
Schmitz et al., 2014	winonaite	NWA 725	9.92	5.45	0.88	0.63	62.08	2.24	18.64	16.30	2.60		100.09
Schmitz et al., 2014	winonaite	NWA 4024	3.82	12.38	1.22	0.74	53.44	1.25	27.71	27.71	0.00		100.56
Gardner-Vandy et al., 2012	achondrite-ungrp	Tafassasset	3.83	8.55	2.58	0.58	54.18	0.84	29.60	29.11	0.54		100.21
Bunch et al., 1972	Iron, IAB-MG	Landes A	9.10	0.79	0.24	0.89	69.00	3.85	15.20	13.31	2.10	1.76	101.04
Bunch et al., 1972	Iron, IAB-MG	Landes B	11.30	2.72	1.08	0.77	67.30	1.98	13.50	12.45	1.17	2.22	100.99
Bunch et al., 1970	Iron, IAB-MG	Odessa (6)	10.20	1.24	0.40	0.26	71.90	2.28	12.60	12.60	0.00	1.39	100.27
Bunch et al., 1970	Iron, IAB-MG	Campo del Cielo (8)	9.20	0.79	0.42	0.24	74.00	2.32	12.30	12.30	0.00	1.44	100.71
Bunch et al., 1970	Iron, IAB-MG	Linwood (4)	10.30	0.03	0.28	0.41	70.50	1.90	13.70	12.53	1.30	2.06	99.31
Bunch et al., 1970	Iron, IAB-sLL	Toluca (10)	7.40	0.03	0.26	0.19	71.70	3.40	15.90	15.90	0.00	1.12	100.00
Bunch et al., 1970	Iron, IAB-MG	Copiapo (5)	7.10	0.42	0.48	0.57	71.70	3.40	15.10	15.10	0.00	1.70	100.47
Bunch et al., 1970	Iron, IAB-ung	Udei Station (5)	7.50	1.73	0.70	0.68	68.20	2.66	16.40	16.40	0.00	1.88	99.75
Bunch et al., 1970	Iron, IIE-an	Weekeroo Station A (6)	4.80	4.80	4.40	0.50	54.50	1.47	27.60	26.01	1.76	2.31	100.56
Bunch et al., 1970	Iron, IIE-an	Weekeroo Station B (4)	3.70	2.68	0.79	0.03	64.10	1.91	25.60	24.13	1.64	1.94	100.91
Bunch et al., 1970	Iron, IIE	Colomera A (8)	5.70	4.00	3.20	0.38	60.40	1.21	25.20	25.20	0.00	0.47	100.56
Bunch et al., 1970	Iron, IIE	Colomera B (6)	6.90	17.60	1.64	0.17	48.80	1.31	23.40	23.40	0.00	0.41	100.23
Bunch et al., 1970	Iron, IIE	Kodaikanal A (5)	3.90	7.20	3.27	0.38	54.20	0.75	31.20	29.75	1.61	0.03	101.09
Bunch et al., 1970	Iron, IIE	Kodaikanal B (5)	2.13	8.20	4.10	0.28	50.20	0.84	35.20	33.30	2.11	0.03	101.19
Bunch et al., 1970	Iron, ungrouped	Enon (5)	8.60	6.20	0.63	0.42	62.80	1.86	19.00	18.43	0.63	0.02	99.59
Bunch et al., 1970	Iron, IAB-ung	Kendall County (5)	14.20	10.90	0.02	0.68	68.40	4.20	2.50	2.50	0.00	0.02	100.92

Bunch et al., 1970	Iron, IIE-an	Netschaevo (7)	4.20	10.30	1.76	0.75	55.30	0.82	27.80	27.80	0.00	0.02	100.95
Bunch and Keil, 1971	Iron-IIAB	Esterville	0.60	12.60	3.10	0.45	46.70	0.65	35.60	35.21	0.43		99.74
Bunch and Keil, 1971	Iron-IVA-an	Steinbach	5.30	4.70	0.11	0.46	64.50	1.57	22.70	22.70	0.00	0.02	99.36
Bunch and Keil, 1971	Iron-IVA	Putnam	0.02	0.02	0.02	0.31	67.40	0.51	32.60	31.86	0.82	0.02	100.98
Bunch and Keil, 1971	Iron-IIIAB	Bagdad	0.02	0.11	0.02	0.07	67.30	0.29	32.60	31.87	0.81	0.15	100.64
Desnoyers et al., 1985	Iron-ungrp	Bocaiuva A	7.92	1.74	0.49		67.00	2.01	20.40	18.56	2.05		99.77
Desnoyers et al., 1985	Iron-ungrp	Bocaiuva B	11.00	10.20	0.98		59.80	1.50	17.00	16.39	0.68		100.55
McCoy et al., 2019	Iron-ungrp	South Byron				0.12	66.70	0.44	31.20	31.16	0.04		98.46
McCoy et al., 2019	Iron-ungrp	Babb's Mill (Troost's Iron)				0.18	65.60	0.67	31.50	30.78	0.80		98.03
McCoy et al., 2019	Iron-ungrp	ILD 83500				0.19	64.00	0.22	33.60	31.30	2.55		98.27
This Study	Iron-IIIAB	BearCreek_ASU352-1	0.07	0.01	0.00	0.62	66.37	0.62	31.37	31.06	0.34	0.03	99.12
Bunch and Keil, 1971	pallasite-PMG	Brahin	5.40	1.66	0.23	0.53	69.10	0.67	23.30	23.30	0.00		100.89
Bunch and Keil, 1971	pallasite-PMG-an	Phillips County	4.40	1.45	0.16	0.57	68.50	0.75	25.10	25.10	0.00		100.93
Bunch and Keil, 1971	pallasite-PMG	Santa Rosalia	5.20	1.55	0.13	0.50	67.50	0.57	24.40	23.88	0.58		99.91
Bunch and Keil, 1971	pallasite-PMG	Marjalahti	6.40	4.00	0.27	0.56	66.20	0.79	21.90	21.90	0.00		100.12
Bunch and Keil, 1971	pallasite-PMG	Albin	5.70	4.60	0.11	0.55	62.50	0.57	23.00	22.67	0.37		97.07
Bunch and Keil, 1971	pallasite-PMG-an	Glorieta Mt.	6.90	6.90	0.32	0.67	62.10	0.77	22.00	22.00	0.00		99.66
Bunch and Keil, 1971	pallasite-PES	Eagle Station	4.40	7.00	0.02	0.48	62.10	0.29	25.50	25.50	0.00		99.79
Bunch and Keil, 1971	pallasite-PMG	Ollague (Imilac)	6.40	8.20	0.16	0.51	62.00	0.55	22.00	22.00	0.00		99.82
Bunch and Keil, 1971	pallasite-PMG	Mt. Vernon	6.20	7.80	0.27	0.59	61.30	0.75	23.10	23.10	0.00		100.01
McCoy et al., 2019	pallasite-ungrp	Milton	7.20	14.50		0.45	52.30	0.28	22.90	22.32	0.64		97.69
This Study	pallasite-PMG-an	Brenham_ASU10	8.26	0.44	0.04	0.56	70.16	0.30	19.88	19.17	0.78	0.02	99.74
This Study	pallasite-PMG	Seymchan_ASU1626	9.93	0.92	0.09	0.52	71.37	0.40	16.63	16.63	0.00	0.02	99.88
Bunch and Keil, 1971	mesosiderite-A1	Crab Orchard	2.18	9.90	1.38	0.51	55.20	0.78	30.30	30.30	0.00		100.25
Bunch and Keil, 1971	mesosiderite-B4	Mincy	1.42	10.20	1.99	0.59	53.90	0.57	32.10	32.10	0.00		100.77
Bunch and Keil, 1971	mesosiderite-A4	Hainholz	3.20	11.80	1.59	0.68	53.30	1.12	27.80	27.80	0.00		99.49
Bunch and Keil, 1971	mesosiderite-A2	Clover Springs	1.63	8.90	2.26	0.65	52.90	0.73	33.10	32.37	0.81		100.25
Bunch and Keil, 1971	mesosiderite-A4	Pinnaroo	3.70	12.00	1.53	0.44	52.80	1.63	27.50	27.50	0.00		99.60
Bunch and Keil, 1971	mesosiderite-B2	Veramin	4.20	12.60	0.82	0.47	52.00	0.52	29.00	27.77	1.37		99.75
Bunch and Keil, 1971	mesosiderite-A1	Patwar	2.34	11.50	2.28	0.60	51.10	0.88	31.10	31.10	0.00		99.80
Bunch and Keil, 1971	mesosiderite-B4	Budulan	1.34	13.70	1.59	0.49	50.50	0.63	32.60	32.60	0.00		100.85
Bunch and Keil, 1971	mesosiderite-B4	Bondoc	5.30	8.80	0.27	0.32	59.30	0.86	24.70	24.59	0.13	0.02	99.58
Ikeda, 1994	shergottite	ALH-77005 A	4.23	7.37	0.80		57.11	0.57	28.54	26.53	2.23		98.84

Ikeda, 1994	shergottite	ALH-77005 B	4.60	9.11	1.18		54.35	0.41	28.40	26.55	2.05		98.26
Ikeda, 1994	shergottite	ALH-77005 C	6.64	5.68	0.86		60.54	0.53	24.99	22.87	2.36		99.48
Ikeda, 1994	shergottite	ALH-77005 D	6.78	8.03	1.33		57.40	0.36	25.22	23.57	1.84		99.30
Ikeda, 1994	shergottite	ALH-77005 E	4.62	6.52	0.96		57.84	0.45	28.72	26.24	2.76		99.39
Ikeda, 1994	shergottite	ALH-77005 F	5.72	10.95	4.75		45.04	0.50	31.06	28.27	3.10		98.33
Ikeda, 1994	shergottite	ALH-77005 G	4.36	5.07	14.48		30.93	0.46	42.92	38.38	5.05		98.73
Mikouchi & Miyamoto, 1997	shergottite	Y-793605 (core)	4.10	5.00	0.80	0.60	60.50	0.40	28.00	26.76	1.38		99.54
Folco et al., 2000	shergottite	DaG 489*	4.76	8.46	1.20		56.32	0.59	28.98	26.79	2.43		100.55
Folco et al., 2000	shergottite	DaG 489 (high Ti)*	3.39	4.05	23.05		16.55	0.69	52.08	47.71	4.86		100.30
Barrat et al., 2002	shergottite	NWA 1068	2.17	5.89	0.63		57.39	0.48	32.10	29.43	2.97		98.96
Mittlefehldt, 1994	nakhlites	ALH 84001*	3.85	8.53	2.23	0.64	47.70	0.39	36.02	29.10	7.69		100.13
Treiman, 2005	nakhlites (Cr-Mt)	Nakhla	1.10	4.00	10.50		21.90	0.51	58.20	40.53	19.64		98.18
Baumgartner et al., 2017	chassignite	NWA 2737 (avg)	5.48	8.07	1.49	0.20	53.64	0.46	29.27	25.53	4.16		99.03
Baumgartner et al., 2017	chassignite	Chassigny (avg)	3.44	9.86	2.40	0.35	48.43	0.48	33.73	29.77	4.40		99.13
Baumgartner et al., 2017	chassignite	Y-980459 (avg)	6.80	6.35	0.57	0.49	60.11	0.38	23.09	22.12	1.07		97.90
Baumgartner et al., 2017	chassignite	Tissint (avg)	4.86	7.28	0.80	0.48	57.16	0.38	27.36	25.64	1.91		98.51
Baumgartner et al., 2017	chassignite	Dhofar 019 (avg)	3.80	7.32	3.32	0.66	47.85	0.44	34.67	29.55	5.69		98.63
Beck et al., 2006	chassignite	NWA 2737 ('spinel')	5.74	6.39	1.30		57.55	0.45	28.14	24.98	3.51		99.92
Bunch and Keil, 1971	chassignite	Chassigny	2.86	9.80	3.66	0.28	46.10	0.54	36.50	32.07	4.92	0.02	100.25
Haggerty and Meyer, 1970	moon	12052,6	7.43	12.02	4.22		48.30	0.75	26.02	25.26	0.84		98.82
Haggerty and Meyer, 1970	moon	12052,6	7.74	11.83	4.31		48.84	0.76	26.87	25.36	1.68		100.52
Haggerty and Meyer, 1970	moon	12052,6	7.43	11.86	4.43		48.90	0.76	25.95	25.59	0.40		99.37
Haggerty and Meyer, 1970	moon	12020,10	4.94	12.30	4.72		45.00	0.17	31.20	30.03	1.30		98.46
Haggerty and Meyer, 1970	moon	12052,6	6.46	11.88	5.54		45.99	0.64	29.41	28.41	1.11		100.03
Haggerty and Meyer, 1970	moon	12020,10	6.93	13.50	6.89		42.20	0.23	30.90	29.81	1.21		100.77
Haggerty and Meyer, 1970	moon	12040,4	4.59	12.20	7.39		40.40	0.72	35.20	33.13	2.31		100.73
Haggerty and Meyer, 1970	moon	12064,6	5.29	12.50	9.14		37.90	0.21	33.80	33.61	0.22		98.86
Haggerty, 1972	moon	Group 1 (Cr-rich Al Mg)	6.67	14.48	0.92		51.49	0.46	25.85	24.51	1.49		100.02
Haggerty, 1972	moon	Group 1 (Cr-rich Al Mg)	6.43	14.37	0.77		50.72	0.46	25.87	24.33	1.71		98.79
Haggerty, 1972	moon	Group 1 (Cr-rich Al Mg)	7.75	17.70	0.83		49.52	0.53	23.58	23.20	0.42		99.95
Haggerty, 1972	moon	Group 1 (Cr-rich Al Mg)	6.77	17.52	1.06		49.16	0.63	25.63	25.06	0.63		100.83
Haggerty, 1972	moon	Group 1 (Cr-rich Al Mg)	7.05	17.36	0.83		49.00	0.53	25.33	24.30	1.15		100.22
Haggerty, 1972	moon	Group 1 (Cr-rich Al Mg)	7.48	17.05	0.95		48.83	0.53	24.01	23.29	0.80		98.93

Haggerty, 1972	moon	Group 1 (Cr-rich Al Mg)	8.00	18.09	0.95	47.98	0.50	24.11	22.95	1.29	99.76
Haggerty, 1972	moon	Group 1 (Cr-rich Al Mg)	3.63	17.87	0.77	46.14	0.38	30.97	29.61	1.51	99.91
Haggerty, 1972	moon	Group 2 (Cr-rich Al)	1.32	10.11	5.69	43.80	0.52	37.33	35.90	1.59	98.93
Haggerty, 1972	moon	Group 2 (Cr-rich Al)	1.76	12.16	5.25	43.54	0.42	36.97	35.68	1.43	100.24
Haggerty, 1972	moon	Group 2 (Cr-rich Al)	1.01	9.55	6.14	43.07	0.55	37.81	36.46	1.50	98.28
Haggerty, 1972	moon	Group 2 (Cr-rich Al)	1.06	9.48	6.27	42.99	0.59	37.97	36.52	1.61	98.52
Haggerty, 1972	moon	Group 2 (Cr-rich Al)	1.09	9.46	6.38	42.93	0.46	37.85	36.64	1.35	98.31
Haggerty, 1972	moon	Group 3 (Chr-pleonastes)	9.86	24.32	6.13	32.74	0.39	26.94	26.08	0.95	100.48
Haggerty, 1972	moon	Group 3 (Chr-pleonastes)	9.84	25.21	6.17	32.22	0.39	26.41	26.23	0.20	100.26
Haggerty, 1972	moon	Group 3 (Chr-pleonastes)	9.65	25.14	6.04	32.23	0.32	27.41	26.65	0.84	100.87
Haggerty, 1972	moon	Group 3 (Chr-pleonastes)	8.56	21.39	7.25	32.56	0.40	29.21	28.29	1.02	99.47
Haggerty, 1972	moon	Group 3 (Chr-pleonastes)	8.51	20.13	7.14	34.41	0.40	29.58	28.33	1.38	100.31
Haggerty, 1972	moon	Group 3 (Chr-pleonastes)	8.22	21.41	7.30	31.96	0.38	30.28	28.95	1.48	99.70
Haggerty, 1972	moon	Group 3 (Chr-pleonastes)	7.90	23.33	6.93	30.76	0.38	30.11	29.35	0.85	99.49
Haggerty, 1972	moon	Group 3 (Chr-pleonastes)	7.62	22.91	6.97	30.88	0.34	30.24	29.64	0.67	99.03
Haggerty, 1972	moon	Group 3 (Chr-pleonastes)	7.59	23.14	6.36	33.31	0.37	30.11	29.75	0.40	100.92
Haggerty, 1972	moon	Group 3 (Chr-pleonastes)	7.45	23.26	6.94	30.65	0.38	30.92	30.10	0.91	99.69
Haggerty, 1972	moon	Group 3 (Chr-pleonastes)	7.43	22.93	7.01	30.72	0.40	31.18	30.15	1.15	99.79
Haggerty, 1972	moon	Group 3 (Chr-pleonastes)	7.35	19.98	9.43	28.42	0.39	33.22	31.72	1.66	98.96
Haggerty, 1972	moon	Group 3 (Chr-pleonastes)	7.12	20.55	9.09	28.54	0.35	33.39	31.98	1.57	99.20
Haggerty, 1972	moon	Group 3 (Chr-pleonastes)	7.02	22.65	7.20	30.59	0.37	21.42	21.42	0.00	89.25
Haggerty, 1972	moon	Group 4 (Mg-Al-Chr)	5.30	22.58	6.72	30.89	0.40	33.53	33.00	0.59	99.48
Haggerty, 1972	moon	Group 4 (Mg-Al-Chr)	5.25	22.70	6.91	29.80	0.41	33.97	33.14	0.92	99.13
Haggerty, 1972	moon	Group 4 (Mg-Al-Chr)	4.82	22.49	6.95	30.05	0.44	34.40	33.80	0.66	99.22
Haggerty, 1972	moon	Group 4 (Mg-Al-Chr)	4.60	21.51	7.09	30.96	0.36	34.42	34.12	0.33	98.97
Haggerty, 1972	moon	Group 4 (Mg-Al-Chr)	6.01	21.11	7.10	32.08	0.44	32.07	31.78	0.32	98.84
Haggerty, 1972	moon	Group 4 (Mg-Al-Chr)	6.77	22.03	7.16	30.74	0.40	31.77	30.89	0.98	98.97
Haggerty, 1972	moon	Group 4 (Mg-Al-Chr)	4.53	21.70	7.18	30.61	0.42	34.54	34.29	0.28	99.01
Haggerty, 1972	moon	Group 4 (Mg-Al-Chr)	4.67	21.65	7.29	30.61	0.41	34.87	34.35	0.58	99.56
Haggerty, 1972	moon	Group 4 (Mg-Al-Chr)	6.25	20.89	7.60	32.04	0.42	32.68	32.20	0.54	99.93
Haggerty, 1972	moon	Group 4 (Mg-Al-Chr)	6.31	19.89	8.59	32.79	0.39	31.75	31.75	0.00	99.72
Haggerty, 1972	moon	Group 4 (Mg-Al-Chr)	4.36	20.76	8.61	29.88	0.40	35.33	35.33	0.00	99.34
Haggerty, 1972	moon	Group 4 (Mg-Al-Chr)	5.21	17.54	8.93	31.14	0.43	35.73	34.19	1.71	99.15

Haggerty, 1972	moon	Group 4 (Mg-Al-Chr)	4.57	20.14	8.95	29.63	0.42	35.36	35.36	0.00	99.07
Haggerty, 1972	moon	Group 4 (Mg-Al-Chr)	4.30	19.62	9.44	29.03	0.44	35.80	35.80	0.00	98.63
Haggerty, 1972	moon	Group 4 (Mg-Al-Chr)	6.09	17.72	9.55	31.99	0.47	34.16	33.68	0.53	100.03
Haggerty, 1972	moon	Group 4 (Mg-Al-Chr)	6.17	16.51	10.06	31.45	0.45	34.07	33.44	0.70	98.78
Haggerty, 1972	moon	Group 4 (Mg-Al-Chr)	1.66	15.52	10.70	30.28	0.41	41.92	41.38	0.60	100.55
Haggerty, 1972	moon	Group 4 (Mg-Al-Chr)	2.94	14.50	11.47	30.73	0.47	39.11	39.11	0.00	99.22
Haggerty, 1972	moon	Group 4 (Mg-Al-Chr)	4.89	12.04	13.70	28.82	0.50	38.39	37.81	0.65	98.40
Haggerty, 1972	moon	Group 4 (Mg-Al-Chr)	5.19	10.63	14.57	28.14	0.52	38.79	37.74	1.17	97.96
Haggerty, 1972	moon	Group 4 (Mg-Al-Chr)	5.16	10.79	16.37	26.98	0.42	39.65	39.65	0.00	99.37
Haggerty, 1972	moon	Group 5 (Al-Ti-Chr)	3.66	9.99	18.36	23.75	0.53	44.45	44.29	0.17	100.76
Haggerty, 1972	moon	Group 5 (Al-Ti-Chr)	2.73	9.79	18.40	23.34	0.48	44.81	44.81	0.00	99.55
Haggerty, 1972	moon	Group 5 (Al-Ti-Chr)	0.95	7.94	19.23	21.04	0.45	49.83	48.59	1.37	99.58
Haggerty, 1972	moon	Group 5 (Al-Ti-Chr)	4.81	8.41	19.24	23.98	0.48	41.90	41.90	0.00	98.82
Haggerty, 1972	moon	Group 5 (Al-Ti-Chr)	4.89	8.08	20.02	23.47	0.47	42.34	42.34	0.00	99.27
Haggerty, 1972	moon	Group 5 (Al-Ti-Chr)	3.34	7.88	20.66	21.65	0.52	44.58	44.58	0.00	98.63
Haggerty, 1972	moon	Group 5 (Al-Ti-Chr)	3.77	5.36	21.41	21.84	0.55	46.44	45.69	0.83	99.45
Haggerty, 1972	moon	Group 5 (Al-Ti-Chr)	3.77	5.40	21.54	21.54	0.50	46.70	45.89	0.89	99.54
Haggerty, 1972	moon	Group 5 (Al-Ti-Chr)	3.42	7.71	21.65	19.79	0.46	45.48	45.48	0.00	98.51
Haggerty, 1972	moon	Group 5 (Al-Ti-Chr)	0.71	5.18	22.67	17.29	0.52	52.58	51.39	1.32	99.08
Haggerty, 1972	moon	Group 5 (Al-Ti-Chr)	1.26	5.04	22.78	17.44	0.52	51.94	50.64	1.44	99.12
Haggerty, 1972	moon	Group 5 (Al-Ti-Chr)	0.82	5.37	22.82	17.11	0.47	52.23	51.39	0.93	98.91
Haggerty, 1972	moon	Group 5 (Al-Ti-Chr)	3.13	6.66	22.84	16.20	0.49	49.34	48.01	1.47	98.81
Haggerty, 1972	moon	Group 5 (Al-Ti-Chr)	3.29	5.94	23.53	17.39	0.46	48.02	48.02	0.00	98.63
Haggerty, 1972	moon	Group 5 (Al-Ti-Chr)	1.28	3.73	23.95	17.65	0.51	53.11	51.87	1.38	100.37
Haggerty, 1972	moon	Group 5 (Al-Ti-Chr)	5.18	5.31	24.37	16.23	0.49	46.79	45.93	0.95	98.47
Haggerty, 1972	moon	Group 5 (Al-Ti-Chr)	5.04	5.51	24.71	16.29	0.50	47.37	46.80	0.63	99.48
Haggerty, 1972	moon	Group 5 (Al-Ti-Chr)	1.26	3.46	25.28	15.37	0.46	52.81	52.57	0.27	98.67
Haggerty, 1972	moon	Group 5 (Al-Ti-Chr)	0.77	4.00	25.38	13.96	0.52	54.80	53.71	1.21	99.55
Haggerty, 1972	moon	Group 5 (Al-Ti-Chr)	0.85	4.00	25.68	13.76	0.52	54.00	53.64	0.40	98.85
Haggerty, 1972	moon	Group 5 (Al-Ti-Chr)	0.90	3.98	25.88	13.73	0.50	54.91	54.12	0.88	99.99
Haggerty, 1972	moon	Group 5 (Al-Ti-Chr)	2.98	3.97	25.97	13.27	0.45	52.09	50.70	1.54	98.88
Haggerty, 1972	moon	Group 5 (Al-Ti-Chr)	0.89	3.36	28.14	8.73	0.43	55.97	55.37	0.66	97.59
Haggerty, 1972	moon	Group 5 (Al-Ti-Chr)	0.89	2.31	28.19	9.98	0.50	55.75	55.21	0.60	97.68

Haggerty, 1972	moon	Group 5 (Al-Ti-Chr)	3.14	3.57	28.67	10.45	0.51	52.97	52.92	0.06		99.32
Haggerty, 1972	moon	Group 5 (Al-Ti-Chr)	3.08	3.54	29.37	10.23	0.52	53.62	53.62	0.00		100.36
Haggerty, 1972	moon	Group 5 (Al-Ti-Chr)	0.17	1.89	29.70	5.54	0.46	61.05	58.11	3.27		99.14
Schulze et al., 1994	R chondrite	Rumuruti 1*	0.84	5.20	5.10	39.70	0.59	45.27	34.20	12.30	0.86	98.79
Schulze et al., 1994	R chondrite	Rumuruti 2*	1.69	5.40	4.00	52.70	0.42	33.99	32.60	1.54	0.63	98.98
Schulze et al., 1994	R chondrite	Rumuruti 3*	7.30	44.30	0.41	15.60	0.23	31.80	27.10	5.22	1.13	101.29
Bischoff et al., 1993	R chondrite	Acfer 217	0.89	4.10	5.60	38.10	0.63	48.50	36.00	13.90		99.21
Rubin and Kallemeyn, 1993	R chondrite	Pecora Escarpment 91002	1.40	6.70	3.40	48.70	0.45	35.80	32.58	3.58		96.81
Bischoff et al., 2011	R chondrite	Acfer 217 1	0.89	4.10	5.60	38.10	0.63	48.50	36.00	13.90		99.21
Bischoff et al., 2011	R chondrite	A- 881988 2	1.60	2.00	2.00	11.50		75.20	38.27	41.04		96.41
Bischoff et al., 2011	R chondrite	ALH 85151 3	1.80	6.80	5.70	45.40	0.48	38.00	34.58	3.80		98.56
Bischoff et al., 2011	R chondrite	ALH 85151 4	1.00	4.40	5.60	35.00	0.48	51.00	36.24	16.40		99.12
Bischoff et al., 2011	R chondrite	Bencubbin R6 clast 2	2.10	2.90	5.00	30.30		54.80	34.59	22.46		97.35
Bischoff et al., 2011	R chondrite	Carlisle Lakes 2	1.10	4.50	6.40	44.60	0.52	39.20	35.31	4.32		96.75
Bischoff et al., 2011	R chondrite	LAP 02238 2	1.20	5.30	5.30	37.40		47.10	35.48	12.92		97.59
Bischoff et al., 2011	R chondrite	LAP 02238 2	1.20	4.50	5.70	31.90		51.70	35.93	17.53		96.76
Bischoff et al., 2011	R chondrite	LAP 02238 2	1.10	6.80	4.60	46.50		39.40	35.25	4.61		98.86
Bischoff et al., 2011	R chondrite	LAP 03645 2	1.10	4.60	5.60	36.00		49.10	36.02	14.54		97.86
Bischoff et al., 2011	R chondrite	LAP 03645 2	1.30	4.80	7.30	28.40		54.00	37.61	18.21		97.62
Bischoff et al., 2011	R chondrite	LAP 04840 2	1.70	2.40	1.40	20.00		68.10	35.60	36.12		97.22
Bischoff et al., 2011	R chondrite	LAP 04840 4	1.62	2.28	1.26	19.07	0.25	70.19	36.26	37.71		98.45
Bischoff et al., 2011	R chondrite	LAP 04840 8;b	1.63	2.28	1.26	18.50	0.23	64.56	33.49	34.53		91.92
Bischoff et al., 2011	R chondrite	MET 01149 2	1.20	5.10	4.90	44.50		39.30	34.08	5.80		95.58
Bischoff et al., 2011	R chondrite	NWA 830 2	1.00	5.10	5.70	47.00		38.80	35.82	3.31		97.93
Bischoff et al., 2011	R chondrite	NWA 978 2	1.90	8.20	5.80	43.30		38.40	35.03	3.74		97.97
Bischoff et al., 2011	R chondrite	NWA 2198 2	1.00	5.70	6.80	44.50		40.20	37.10	3.44		98.55
Bischoff et al., 2011	R chondrite	NWA 2821 9	0.97	5.05	5.81	44.15	0.34	40.51	35.47	5.60		97.39
Bischoff et al., 2011	R chondrite	PCA 91002 5	1.40	6.70	3.40	48.70	0.45	35.80	32.58	3.58		96.81
Bischoff et al., 2011	R chondrite	PRE 95404 2	1.10	4.80	6.50	42.70		41.70	36.22	6.09		97.41
Bischoff et al., 2011	R chondrite	PRE 95411 2	4.20	28.60	1.10	34.20		29.40	29.40	0.00		97.50
Bischoff et al., 2011	R chondrite	PRE 95411 2	1.50	4.30	5.80	45.70		38.90	34.63	4.74		96.68
Bischoff et al., 2011	R chondrite	Y- 82002 7	7.83	7.07	0.39	57.48	0.20	25.50	21.03	4.97		98.97
Bischoff et al., 2011	R chondrite	Y- 82002 7	0.76	4.05	5.06	35.13	0.38	48.71	34.97	15.27		95.62

Bischoff et al., 2011	R chondrite	Y- 980702 2	3.50	4.40	7.20		47.50		37.00	33.88	3.47		99.95
Schmitz et al., 2014	Ost 065	Al-rich chrome	4.74	25.93	0.61	0.52	40.82	0.49	25.90	25.90	0.00	0.69	99.70
Schmitz et al., 2014	Ost 065	Al-poor chrome	1.70	0.26	0.29	1.01	69.50	0.89	22.20	22.20	0.00	1.14	96.98
Bjarnborg and Schmitz, 2013	CM2	Acfer 331-1	6.10	9.50	0.75	0.65	54.80		24.75	23.84	1.01		96.65
Bjarnborg and Schmitz, 2013	CM2	Acfer 331-2	3.45	6.85	1.05	0.70	56.60		29.45	28.26	1.33		98.23
Bjarnborg and Schmitz, 2013	CM2	Acfer 331-3	4.80	12.15	0.80	0.65	50.65		25.85	25.74	0.12		94.91
Bjarnborg and Schmitz, 2013	CM2	Acfer 331-4	6.60	11.30	1.05	0.75	54.55		26.10	24.85	1.38		100.49
Bjarnborg and Schmitz, 2013	CM2	Acfer 331-5	5.00	11.20	0.80	0.70	53.10		27.00	26.23	0.85		97.89
Bjarnborg and Schmitz, 2013	CM2	Acfer 331-6	3.80	12.40	0.95	0.70	48.30		30.40	28.04	2.62		96.81
Bjarnborg and Schmitz, 2013	CM2	Acfer 331-7	5.15	6.30	1.25	0.80	55.50		27.15	25.14	2.23		96.37
Bjarnborg and Schmitz, 2013	CM2	Acfer 331-8	5.45	12.55	1.25	0.80	49.60		26.85	25.75	1.22		96.62
Bjarnborg and Schmitz, 2013	CM2	Acfer 331-9	7.90	11.90	0.65	0.60	53.00		22.05	21.22	0.92		96.19
Bjarnborg and Schmitz, 2013	CM2	Acfer 331-10	5.55	11.80	0.95	0.65	50.40		27.00	25.18	2.02		96.55
Bjarnborg and Schmitz, 2013	CM2	Acfer 331-11	6.95	16.70	1.25	0.45	46.45		26.80	24.81	2.21		98.82
Bjarnborg and Schmitz, 2013	CM2	Acfer 331-12	4.00	6.65	0.85	0.70	55.30		27.00	26.04	1.07		94.61
Bjarnborg and Schmitz, 2013	CM2	Acfer 331-13	4.05	12.35	1.00	0.60	47.40		28.95	26.98	2.19		94.57
Bjarnborg and Schmitz, 2013	CM2	Acfer 331-14	4.20	8.90	0.70	0.65	54.75		27.60	26.69	1.01		96.90
Bjarnborg and Schmitz, 2013	CM2	Acfer 331-15	5.00	11.05	1.35	0.75	51.40		27.10	26.34	0.85		96.74
Bjarnborg and Schmitz, 2013	CM2	Acfer 331-16	6.90	15.70	1.20	0.70	46.25		25.05	23.76	1.43		95.94
Bjarnborg and Schmitz, 2013	CM2	Acfer 331-17	4.45	11.30	0.85	0.70	51.25		27.35	26.53	0.91		95.99
Bjarnborg and Schmitz, 2013	CM2	Acfer 331-18	8.70	20.95	0.55	0.50	45.45		23.50	22.47	1.14		99.76
Bjarnborg and Schmitz, 2013	CM2	Acfer 331-19	6.15	4.10	0.60	0.60	61.10		23.80	22.72	1.20		96.47
Bjarnborg and Schmitz, 2013	CM2	Acfer 331-20	4.75	9.20	0.75	0.50	54.50		27.25	26.00	1.39		97.09
Bjarnborg and Schmitz, 2013	CM2	Acfer 331-21	5.15	7.75	1.05	0.70	56.20		27.05	25.73	1.46		98.05
Bjarnborg and Schmitz, 2013	CM2	Acfer 331-22	4.15	8.75	1.20	0.60	53.25		28.15	26.97	1.31		96.23
Bjarnborg and Schmitz, 2013	CM2	Acfer 331-23	3.70	7.25	1.00	0.70	54.10		29.40	27.29	2.34		96.38
Bjarnborg and Schmitz, 2013	CM2	Acfer 331-24	4.80	9.85	0.75	0.45	52.65		27.25	25.65	1.78		95.93
Bjarnborg and Schmitz, 2013	CM2	Acfer 331-25	5.10	10.30	0.90	0.85	53.40		26.60	25.82	0.87		97.24
Fuchs et al., 1973	CM2	Murchison (C2)-1	6.20	17.30	0.90	0.60	47.40	0.30	26.70	25.66	1.15		99.52
Fuchs et al., 1973	CM2	Murchison (C2)-2	5.70	17.70	0.70	0.50	46.80	0.20	28.40	26.63	1.97		100.20
Fuchs et al., 1973	CM2	Murchison (C2)-3	8.10	18.50	0.60	0.40	47.10	0.20	25.40	23.10	2.56		100.56
Fuchs et al., 1973	CM2	Murchison (C2)-4	1.30	3.20	0.50	0.60	60.20	0.30	32.90	30.51	2.66		99.27
Fuchs et al., 1973	CM2	Murchison (C2)-5	5.70	15.70	1.60	0.80	48.90	0.30	27.40	27.11	0.32		100.43

Fuchs et al., 1973	CM2	Murchison (C2)-6	4.50	10.70	1.70	0.70	51.40	0.30	29.30	27.71	1.77		98.78
Fuchs et al., 1973	CM2	Murchison (C2)-7	6.90	22.30	0.90	0.60	41.90	0.20	27.70	25.85	2.05		100.71
Fuchs et al., 1973	CM2	Murchison (C2)-8	6.70	14.00	1.20	0.70	50.30	0.30	27.20	25.00	2.44		100.64
Fuchs et al., 1973	CM2	Murchison (C2)-9	5.80	14.20	1.40	0.70	49.20	0.30	28.20	26.39	2.01		100.00
Johnson and Prinz, 1991	CM2 -C	Erakot (C1)	8.50	16.81	0.70	0.69	45.81	0.18	26.94	22.22	5.25	0.00	100.15
Johnson and Prinz, 1991	CM2 -C	Erakot (C7)	7.94	17.27	0.74	0.58	45.28	0.18	27.54	23.13	4.90	0.00	100.03
Johnson and Prinz, 1991	CM2 -C	Boriskino (C6)	3.06	7.29	1.44	0.93	53.26	0.20	33.43	29.61	4.25	0.08	100.11
Johnson and Prinz, 1991	CM2 -C	Murchison, -2 (C14)	8.44	14.76	0.69	0.53	49.11	0.14	26.11	22.03	4.53	0.00	100.24
Johnson and Prinz, 1991	CM2 -C	Murchison, -2 (C14)	2.09	2.74	1.11	0.66	58.14	0.26	34.56	30.06	5.00	0.04	100.08
Johnson and Prinz, 1991	CM2 -C	Murchison, -2 (C19)	7.48	15.90	0.89	0.69	46.09	0.18	28.40	23.80	5.11	0.00	100.15
Johnson and Prinz, 1991	CM2 -C	Murchison, -2 (C22)	5.05	9.01	1.32	0.87	51.19	0.28	31.75	26.69	5.62	0.04	100.07
Johnson and Prinz, 1991	CM2 -C	Murchison, -4 (C7)	4.97	11.92	1.61	0.85	47.50	0.31	32.48	27.54	5.49	0.04	100.23
Johnson and Prinz, 1991	CM2 -C	Murchison, -4 (C8)	7.36	14.21	1.01	0.68	47.27	0.22	28.85	23.79	5.63	0.04	100.20
Johnson and Prinz, 1991	CM2 -C	ALH84054 (C6)	7.27	16.17	1.38	0.76	44.89	0.18	29.00	24.61	4.88	0.00	100.15
Johnson and Prinz, 1991	CM2 -C	ALH85013 (C2)	7.59	14.22	0.81	0.64	48.01	0.18	28.15	23.28	5.41	0.04	100.18
Johnson and Prinz, 1991	CM2 -C	ALH85013 (C6)	3.15	3.60	1.08	0.74	58.05	0.17	32.75	28.60	4.61	0.08	100.07
Johnson and Prinz, 1991	CM2 -C	ALH85013 (C8)	2.79	4.39	2.61	0.91	54.38	0.27	34.31	30.62	4.10	0.00	100.07
Johnson and Prinz, 1991	CM2 -C	ALH85013 (C7)	5.96	17.17	0.97	0.76	42.40	0.22	31.57	26.23	5.94	0.00	99.65
Johnson and Prinz, 1991	CM2 -C	ALH85013 (C9)	7.49	13.75	1.29	0.83	48.41	0.21	27.44	23.67	4.19	0.00	99.84
Johnson and Prinz, 1991	CM2 -C	LEW87022 (C1)	8.75	18.06	0.66	0.62	43.69	0.22	27.50	21.97	6.15	0.00	100.12
This Study	CM2	ColdBokkeveld_G01	5.59	11.35	0.56	0.51	51.39	0.20	28.51	25.38	3.47	0.00	98.46
This Study	CM2	ColdBokkeveld_G02	5.16	9.26	1.09	0.81	52.98	0.28	28.14	25.97	2.41	0.00	97.97
This Study	CM2	ColdBokkeveld_G03	5.01	8.78	1.42	0.85	52.89	0.34	28.46	26.38	2.31	0.00	97.98
This Study	CM2	ColdBokkeveld_G04	7.57	10.27	0.91	0.77	54.21	0.27	24.91	22.55	2.62	0.01	99.19
This Study	CM2	ColdBokkeveld_G05	4.10	8.96	0.94	0.61	52.43	0.38	30.02	27.30	3.01	0.00	97.73
This Study	CM2	ColdBokkeveld_G06	7.80	11.78	0.71	0.62	51.86	0.23	24.83	22.08	3.06	0.03	98.16
This Study	CM2	ColdBokkeveld_G07	3.31	1.99	0.78	0.46	54.53	0.25	34.98	28.54	7.15	0.02	97.03
This Study	CM2	ColdBokkeveld_G08	4.41	9.12	0.94	0.57	51.84	0.22	29.84	26.97	3.19	0.01	97.27
This Study	CM2	Murray17b_G02	5.37	20.29	1.08	0.80	37.36	0.21	29.83	27.67	2.39	0.01	95.20
This Study	CM2	Murray17b_G03	6.06	12.91	0.93	0.61	48.73	0.24	27.19	24.75	2.71	0.02	96.95
This Study	CM2	Murray17b_G04	4.69	11.71	0.80	0.65	50.16	0.22	29.17	26.87	2.56	0.02	97.68
This Study	CM2	Murray17b_G05	8.38	15.61	0.75	0.65	49.12	0.17	23.87	22.05	2.03	0.01	98.78
This Study	CM2	Murray17b_G06	8.32	15.70	0.70	0.61	48.37	0.16	24.37	22.02	2.60	0.01	98.49

Johnson and Prinz, 1991	CR2 -C	Renazzo (C29)	1.98	1.54	1.54	0.69	58.52	0.55	34.68	30.15	5.04	0.00	100.01
Johnson and Prinz, 1991	CR2 -C	Renazzo (C73)	5.54	10.71	2.04	1.25	49.99	0.28	29.77	26.78	3.32	0.04	99.95
Johnson and Prinz, 1991	CR2 -C	MAC87320 (C8)	1.44	0.05	1.70	0.88	62.62	0.51	32.58	30.88	1.88	0.00	99.97
This Study	CR2	GRA95227_G01	13.73	20.91	0.54	0.25	44.67	2.06	12.67	12.51	0.18	0.01	94.86
This Study	CR2	GRA95227_G03	7.17	7.36	1.57	0.73	54.52	0.31	25.08	22.84	2.50	0.00	97.00
This Study	CR2	GRA95227_G04	16.19	24.43	0.44	0.20	42.99	1.78	9.73	9.73	0.00	0.02	95.77
This Study	CR2	GRA95227_G05	15.04	23.84	0.46	0.21	42.40	1.73	10.24	9.98	0.29	0.01	93.96
This Study	CR2	GRA95227_G06	3.85	1.48	1.83	0.81	59.63	0.74	29.08	26.87	2.47	0.00	97.66
This Study	CR2	GRA95227_G07	4.16	0.20	3.87	0.98	58.07	0.81	29.13	27.88	1.40	0.00	97.36
This Study	CR2	GRA95227_G08	6.36	8.01	1.53	0.65	54.11	0.38	26.17	24.16	2.23	0.01	97.44
This Study	CR6	NWA 7317	3.05	12.70	1.53	0.64	50.43	0.27	30.11	30.09	0.03	0.01	98.75
Johnson and Prinz, 1991	CV3-C	Allende,4311 (C1)	2.95	11.86	1.12	0.73	48.72	0.17	34.09	30.27	4.24	0.04	100.10
Johnson and Prinz, 1991	CV3-C	Allende,4314 (C5)	1.16	6.20	1.56	0.87	52.52	0.23	36.96	32.41	5.06	0.11	100.14
Johnson and Prinz, 1991	CV3-C	Leoville (C1)	2.93	6.21	1.85	0.85	52.75	0.20	34.86	30.11	5.28	0.00	100.19
Johnson and Prinz, 1991	CV3-C	Vigarano,-5 (C1)	4.36	13.71	0.71	0.55	47.93	0.14	32.23	28.08	4.61	0.04	100.14
Johnson and Prinz, 1991	CV3-C	Vigarano,-6 (C1)	1.26	5.80	1.82	0.91	52.68	0.17	36.72	32.48	4.71	0.04	99.86
Johnson and Prinz, 1991	CV3-C	Vigarano,-7 (C1)	6.50	10.61	1.42	0.78	51.06	0.25	28.88	24.82	4.51	0.00	99.95
Johnson and Prinz, 1991	CV3-C	ALH84037 (C1)	4.83	10.01	1.17	0.80	51.32	0.21	31.16	27.09	4.52	0.00	99.95
Johnson and Prinz, 1991	CV3-C	ALH84037 (C2)	5.94	8.43	1.09	0.69	53.26	0.21	30.06	25.18	5.42	0.00	100.22
Johnson and Prinz, 1991	CO3.2 -C	Kainsaz (C26)	3.22	12.49	1.36	0.77	47.02	0.28	34.51	30.12	4.88	0.00	100.14
Johnson and Prinz, 1991	CO3.2 -C	Kainsaz (C27)	5.48	23.05	0.62	0.51	36.77	0.22	32.82	27.67	5.73	0.04	100.08
Johnson and Prinz, 1991	CO3.2 -C	Kainsaz (C30)	3.51	14.32	0.79	0.63	46.61	0.21	33.54	29.43	4.56	0.08	100.13
Johnson and Prinz, 1991	CO3.2 -C	Kainsaz (C33)	4.80	15.91	0.88	0.67	44.19	0.25	32.98	27.88	5.66	0.00	100.24
Johnson and Prinz, 1991	CO3.2 -C	Kainsaz (CF14)	6.69	10.63	0.55	0.45	52.12	0.21	29.06	23.91	5.72	0.00	100.28
Johnson and Prinz, 1991	CO3.4 -C	Ornans (C3)	3.48	21.63	0.89	0.72	36.61	0.32	35.96	30.66	5.90	0.12	100.35
Johnson and Prinz, 1991	CO3.4 -C	Ornans (C5)	1.72	6.73	2.10	0.84	49.40	0.33	38.10	31.93	6.85	0.27	100.18
Johnson and Prinz, 1991	CO3.4 -C	Ornans (C10)	2.32	16.29	0.79	0.63	43.42	0.24	35.93	31.46	4.96	0.24	100.35
Johnson and Prinz, 1991	CO3.4 -C	Ornans (C18)	1.81	11.03	0.80	0.57	49.10	0.31	35.90	31.32	5.09	0.27	100.31
Johnson and Prinz, 1991	CO3.4 -C	Ornans (C20)	1.72	11.68	1.07	0.65	47.13	0.27	36.86	31.82	5.60	0.27	100.21
Johnson and Prinz, 1991	CO3.7 -C	Warrenton (CF2)	1.95	11.39	1.19	0.72	49.28	0.20	34.91	31.24	4.08	0.00	100.05
Johnson and Prinz, 1991	CO3.0 -C	ALH77307 (C1)	7.60	12.61	1.24	0.72	49.81	0.18	27.55	23.43	4.58	0.00	100.16
Johnson and Prinz, 1991	CO3.0 -C	ALH77307 (C2)	4.54	6.71	1.19	0.83	55.17	0.20	30.96	27.07	4.33	0.00	100.03
Johnson and Prinz, 1991	CO3.0 -C	ALH77307 (C3)	6.74	15.73	0.73	0.61	46.30	0.18	29.29	24.75	5.05	0.00	100.08

Johnson and Prinz, 1991	CO3.0 -C	ALH77307 (C4)	3.04	4.61	2.92	0.98	53.96	0.27	33.90	30.53	3.74	0.00	100.06
Johnson and Prinz, 1991	CO3.0 -C	ALH77307 (C5)	4.17	8.11	1.84	0.90	53.01	0.20	31.36	28.41	3.28	0.00	99.92
Johnson and Prinz, 1991	CO3.0 -C	ALH77307 (C6)	6.81	16.86	1.59	0.88	45.56	0.22	27.39	25.36	2.25	0.00	99.52
Johnson and Prinz, 1991	CO3.0 -C	ALH77307 (C7)	5.25	11.64	0.67	0.66	50.87	0.21	30.46	26.34	4.58	0.00	100.22
Johnson and Prinz, 1991	CO3.0 -C	ALH77307 (C8)	5.95	13.40	1.27	0.82	47.22	0.28	30.60	25.98	5.14	0.00	100.07
Johnson and Prinz, 1991	C2-ung-C	Adelaide (C4)	6.30	12.44	2.23	1.31	46.30	0.28	30.69	26.12	5.08	0.04	100.09
Johnson and Prinz, 1991	C2-ung-C	Adelaide (C5)	7.86	16.92	1.19	0.88	43.79	0.18	28.90	23.72	5.76	0.00	100.30
Johnson and Prinz, 1991	C2-ung-C	Adelaide (C9)	7.19	9.40	1.11	0.89	52.67	0.25	28.20	23.39	5.35	0.00	100.24
Johnson and Prinz, 1991	C2-ung-C	Adelaide (C17)	8.11	15.98	1.51	0.92	44.22	0.18	28.70	23.45	5.84	0.00	100.22
Johnson and Prinz, 1991	C2-ung-C	Adelaide (C18)	6.61	11.37	1.83	0.97	48.03	0.28	30.59	25.23	5.96	0.00	100.27
Johnson and Prinz, 1991	C2-ung-C	Adelaide (C20)	6.67	14.97	1.01	0.91	46.54	0.18	29.46	25.03	4.92	0.00	100.22
Johnson and Prinz, 1991	C2-ung-C	Belgica7904 (C4)	6.23	5.71	0.81	0.54	57.66	0.00	28.57	24.10	4.97	0.16	100.18
Johnson and Prinz, 1991	C2-ung-C	Belgica7904 (C7)	9.28	11.23	0.85	0.45	53.37	0.00	24.46	20.38	4.54	0.08	100.18
Johnson and Prinz, 1991	C2-ung-C	Belgica7904 (C10)	7.41	11.38	0.96	0.75	54.11	0.00	25.06	23.26	2.00	0.12	99.99
Johnson and Prinz, 1991	C2-ung-C	Belgica7904 (C12)	6.99	10.82	0.95	0.63	54.62	0.00	25.67	23.84	2.04	0.08	99.97
Johnson and Prinz, 1991	C2-ung-C	Belgica7904 (C16)	5.03	7.82	0.54	0.61	57.55	0.00	28.00	25.92	2.31	0.16	99.94
Johnson and Prinz, 1991	C2-ung-C	Belgica7904 (C17)	3.21	5.62	1.24	0.57	57.58	0.00	31.20	28.97	2.48	0.15	99.82
Bunch et al., 1967	H3	Bremervorde (A)	1.84	5.00	1.51	0.79	60.80	0.69	30.10	30.10	0.00		100.73
Bunch et al., 1967	H3	Bremervorde (B)	1.55	0.20	0.24	0.36	66.80	0.62	30.30	29.39	1.01		100.17
Bunch et al., 1967	H3	Brownfield	2.12	5.30	1.67	0.70	60.30	0.60	30.30	30.30	0.00		100.99
Bunch et al., 1967	H3	Prairie Dog Creek	3.20	2.67	1.57	0.73	59.80	1.10	31.00	28.03	3.30		100.40
Johnson and Prinz, 1991	H3.4 - C1	Sharps	1.33	2.81	2.16	0.79	57.57	0.36	34.50	31.98	2.80	0.04	99.84
Johnson and Prinz, 1991	H3.4 - C2	Sharps	0.59	1.81	2.61	0.85	56.16	0.48	37.04	33.29	4.17	0.07	100.04
Johnson and Prinz, 1991	H3.4 - C5	Sharps	8.01	17.84	0.62	0.69	45.92	0.29	26.29	22.82	3.85	0.13	100.17
Johnson and Prinz, 1991	H3.4 - C6	Sharps	10.38	29.08	0.35	0.25	34.40	0.23	25.12	20.88	4.71	0.09	100.37
Johnson and Prinz, 1991	H3.4 - C7	Sharps	0.71	0.00	0.32	0.51	63.33	0.38	34.44	30.91	3.91	0.04	100.12
Johnson and Prinz, 1991	H3.4 - C8	Sharps	1.00	0.18	2.20	1.02	59.92	0.29	34.86	32.11	3.06	0.15	99.93
Johnson and Prinz, 1991	H3.5 - C2	Frenchman Bay	2.09	3.93	1.89	0.73	56.48	1.02	33.36	29.95	3.79	0.30	100.18
Johnson and Prinz, 1991	H3.5 - C3	Frenchman Bay	2.07	1.94	1.91	0.96	58.05	0.91	33.08	29.57	3.90	0.37	99.70
Wlotzka, 2005	H3.6	Tieschitz	21.60	67.10	0.46	0.12	0.18	0.06	9.16	9.16	0.00	0.36	99.04
Wlotzka, 2005	H3.6	Tieschitz	16.80	62.60	0.21	0.19	2.51	0.11	15.40	15.25	0.17	0.58	98.42
This Study	H3.7	Prairie Dog	1.96	1.95	1.11	0.72	61.34	0.83	29.94	28.87	1.19	0.44	98.42
Johnson and Prinz, 1991	H3.7 - C100	Prairie Dog Ck	2.06	2.37	1.40	0.00	59.86	0.85	32.96	29.44	3.90	0.37	100.25

Johnson and Prinz, 1991	H3.7 - C105	Prairie Dog Ck	2.40	4.20	1.41	0.00	57.89	0.83	32.65	29.16	3.88	0.45	100.22
Wlotzka, 2005	H3.8	Dhajala	17.50	65.70	0.35		1.98		13.70	13.70	0.00		99.23
Wlotzka, 2005	H3.8	Dhajala	2.63	9.02	2.23	0.75	54.30	1.37	29.20	29.20	0.00		99.50
Johnson and Prinz, 1991	H3.8 - C1	Dhajala	2.38	2.64	1.48	0.00	61.39	0.72	30.44	28.99	1.62	0.34	99.55
Johnson and Prinz, 1991	H3.8 - C2	Dhajala	1.96	1.42	0.29	0.00	64.91	0.78	29.99	28.41	1.76	0.37	99.90
Johnson and Prinz, 1991	H3.8 - C3	Dhajala	4.42	12.22	1.25	0.00	50.05	0.63	30.70	27.28	3.80	0.56	100.20
Johnson and Prinz, 1991	H3.8 - C4	Dhajala	2.37	3.26	1.30	0.00	59.75	0.79	31.69	28.89	3.11	0.45	99.92
Johnson and Prinz, 1991	H3.8 - C7	Dhajala	2.19	2.75	1.51	0.00	61.35	0.69	30.86	29.44	1.58	0.38	99.88
Johnson and Prinz, 1991	H3.8 - C8	Dhajala	2.38	4.17	0.96	0.00	60.88	0.86	30.05	28.65	1.55	0.45	99.90
Wlotzka, 2005	H3.9	Clovis No. 1	19.10	67.00	0.25	0.20	0.19	2.00	13.10	11.91	1.33	0.50	102.47
Wlotzka, 2005	H3.9	Clovis No. 1	4.65	17.10	0.88	1.00	48.90	0.88	25.90	25.90	0.00	0.40	99.71
Bunch et al., 1967	H4	Bath	2.48	6.20	2.24	0.70	56.40	0.93	30.50	30.18	0.35		99.49
Bunch et al., 1967	H4	Bushnell	2.47	6.60	1.96	0.77	57.40	0.80	30.90	30.61	0.33		100.93
Bunch et al., 1967	H4	Florence	2.71	5.80	2.71	0.71	56.90	0.88	31.20	30.71	0.54		100.96
Bunch et al., 1967	H4	Kesen	2.89	5.80	1.71	0.65	57.70	1.00	30.90	29.36	1.71		100.82
Bunch et al., 1967	H4	Weston	3.10	7.30	1.96	0.70	57.70	0.70	29.40	29.40	0.00		100.86
Snetsinger et al., 1967	H4	Bath	2.48	6.20	2.24	0.70	56.40	0.93	30.50	30.18	0.35		99.49
Wlotzka, 2005	H4	ALHA77262	15.70	52.20	0.19	0.16	15.01	0.27	16.40	15.78	0.69	0.62	100.62
Wlotzka, 2005	H4	ALHA77262	4.79	8.51	1.84	0.55	56.50	0.75	26.40	26.40	0.00	0.45	99.79
Wlotzka, 2005	H4	Beaver Creek	5.54	6.99	2.30	0.58	57.70	0.75	26.20	26.05	0.17		100.08
Wlotzka, 2005	H4	Beddgelert	3.27	6.66	1.93	0.60	57.70	0.78	28.10	28.10	0.00		99.04
Wlotzka, 2005	H4	Elsinora	3.45	6.65	2.11	0.62	55.60	0.85	29.90	28.50	1.56	0.29	99.63
Wlotzka, 2005	H4	Forest Vale	5.28	6.15	2.18	0.60	58.50	0.77	26.70	26.17	0.59	0.11	100.35
Wlotzka, 2005	H4	Forest Vale	16.50	59.20	0.04	0.14	6.09	0.01	14.40	14.40	0.00	0.22	96.60
Wlotzka, 2005	H4	Forest Vale	6.40	14.20	1.21	0.60	52.20	0.70	25.20	24.98	0.24	0.16	100.69
Wlotzka, 2005	H4	Foster	3.06	5.96	1.46	0.69	59.50	0.83	29.10	28.79	0.34	0.39	101.02
Wlotzka, 2005	H4	Kesen	3.33	6.48	1.66	0.63	57.80	1.03	28.20	28.19	0.01		99.13
This Study	H4	Bushnell	2.94	6.65	1.95	0.70	55.98	0.86	29.23	28.87	0.40	0.31	98.65
This Study	H4	Monroe	2.51	5.23	1.40	0.74	58.08	0.82	29.19	28.68	0.56	0.51	98.54
Bunch et al., 1967	H5	Castalia	2.98	6.10	2.98	0.64	55.80	0.86	31.60	30.64	1.07		101.07
Bunch et al., 1967	H5	Collescipoli	2.43	5.80	1.66	0.72	57.20	1.04	31.40	29.85	1.72		100.42
Bunch et al., 1967	H5	Forest City	2.03	5.70	2.03	0.70	57.70	0.96	31.30	30.89	0.46		100.47
Bunch et al., 1967	H5	Pultusk	2.72	6.00	2.72	0.65	55.90	1.03	30.10	30.01	0.10		99.13

Bunch et al., 1967	H5	Tomhannock Creek	2.77	5.60	2.18	0.69	56.80	1.06	31.60	29.90	1.89		100.89
Snetsinger et al., 1967	H5	Allegan	2.31	6.30	2.08	0.71	56.50	1.05	32.00	30.70	1.44		101.09
Snetsinger et al., 1967	H5	Hessle	2.35	5.90	2.21	0.65	57.00	0.96	31.30	30.58	0.80		100.45
Wlotzka, 2005	H5	DaG 739	3.70	6.83	2.05	0.65	54.90	0.92	29.10	27.70	1.56	0.28	98.59
Wlotzka, 2005	H5	Daraj 020	12.30	34.10	0.34	0.32	30.60	0.54	20.60	17.78	3.14	0.50	99.61
Wlotzka, 2005	H5	Daraj 020	4.93	9.48	1.40	0.65	54.80	0.98	27.10	25.97	1.25	0.25	99.72
Wlotzka, 2005	H5	Ehole	3.47	6.69	2.23	0.64	57.90	0.88	28.90	28.90	0.00	0.33	101.04
Wlotzka, 2005	H5	Guarena	3.44	6.86	2.19	0.65	57.00	0.81	28.70	28.70	0.00	0.30	99.95
Wlotzka, 2005	H5	Laborel	3.44	6.58	2.14	0.63	57.10	0.90	29.10	28.66	0.49	0.33	100.27
Wlotzka, 2005	H5	Morro do Rocio	3.19	7.60	1.36	0.69	56.10	0.93	28.50	27.96	0.60	0.37	98.80
Wlotzka, 2005	H5	Richardton	3.36	5.86	2.00	0.72	57.80	0.93	28.30	28.08	0.25	0.56	99.56
Wlotzka, 2005	H5	Richardton	10.80	33.00	0.47	0.21	34.40	0.49	20.50	20.33	0.19	0.51	100.40
Wlotzka, 2005	H5	Richardton	8.64	26.00	0.56	0.25	40.50	0.59	23.00	22.44	0.62	0.48	100.08
Wlotzka, 2005	H5	Simmern	11.70	36.70	0.27	0.29	30.60	0.84	19.30	19.06	0.27	0.33	100.06
Wlotzka, 2005	H5	Simmern	6.01	11.08	3.36	0.49	50.00	1.05	27.30	26.01	1.44	0.66	100.09
Wlotzka, 2005	H5	Tiffa 005	3.74	6.89	1.83	0.67	57.10	0.93	28.40	27.88	0.57	0.25	99.87
This Study	H5	Forest City	2.84	6.37	2.03	0.68	56.67	0.85	29.05	29.00	0.06	0.29	98.79
This Study	H5	Richardten	2.97	5.68	2.03	0.75	57.18	0.84	28.68	28.47	0.23	0.59	98.75
This Study	H5	Hessle - H5	1.99	6.04	2.42	0.70	54.42	0.65	30.58	30.51	0.09		96.80
Wlotzka, 2005	H5/6	DaG 310	4.48	6.76	2.32	0.65	57.80	0.81	27.60	27.47	0.15	0.40	100.83
Bunch et al., 1967	H6	Butsura	2.84	5.60	2.47	0.66	56.80	0.95	31.40	30.16	1.38		100.86
Bunch et al., 1967	H6	Estacado	3.23	5.70	2.47	0.71	57.90	0.86	29.90	29.66	0.27		100.80
Bunch et al., 1967	H6	Kernouve	2.92	6.00	2.46	0.71	57.00	0.62	31.00	30.40	0.67		100.78
Wlotzka, 2005	H6	DaG 747	3.36	6.57	2.31	0.65	56.70	0.84	29.40	28.99	0.45	0.30	100.18
Wlotzka, 2005	H6	Daraj 016	13.60	44.80	0.18	0.11	22.10	0.49	19.00	17.77	1.36	0.54	100.96
Wlotzka, 2005	H6	Daraj 016	5.35	11.50	1.96	0.67	51.10	0.84	27.70	26.23	1.64	0.26	99.54
Wlotzka, 2005	H6	Daraj 117	3.34	6.68	2.21	0.63	56.80	0.78	29.80	29.16	0.71	0.28	100.59
This Study	H6	Guarena	3.09	6.43	2.19	0.69	56.48	0.73	29.15	29.01	0.15	0.32	99.08
This Study	H6	Kernouve	2.94	6.48	2.22	0.68	57.01	0.78	28.71	28.71	0.00	0.32	99.14
Johnson and Prinz, 1991	L/LL3.4 - C13	Inman	3.33	4.26	2.06	0.77	56.81	0.47	30.90	28.54	2.63	0.23	99.11
Bunch et al., 1967	L3	Khohar	0.84	0.03	0.25	0.41	66.10	0.51	32.20	30.67	1.70		100.51
Bunch et al., 1967	L3	Krymka (A)	0.41	0.10	0.49	0.37	62.70	0.66	35.40	31.44	4.40		100.57
Bunch et al., 1967	L3	Krymka (B)	8.40	12.60	0.60	0.82	53.20	0.59	23.40	21.10	2.56		99.87

Johnson and Prinz, 1991	L3.6 - C27	Khohar	1.99	2.83	1.99	0.83	55.89	0.49	34.75	30.33	4.91	0.38	99.63
Johnson and Prinz, 1991	L3.6 - C29	Khohar	1.57	0.02	0.25	0.88	63.72	0.51	32.39	29.08	3.67	0.37	100.10
Johnson and Prinz, 1991	L3.6 - C30	Khohar	1.55	2.27	2.71	0.93	55.68	0.55	35.35	31.54	4.24	0.41	99.87
Wlotzka, 2005	L3.7	Julesburg	12.50	50.90	0.36	0.10	15.10	0.33	19.40	19.07	0.37	2.45	101.18
Wlotzka, 2005	L3.7	Julesburg	2.88	12.40	1.76	0.78	50.70	0.86	29.70	29.61	0.10	0.76	99.85
Wlotzka, 2005	L3.7	Suwahib (Buwah)	16.60	57.80	0.10	0.13	8.14	0.06	13.60	13.60	0.00	1.10	97.53
Wlotzka, 2005	L3.7	Suwahib (Buwah)	4.38	9.37	0.16	0.39	56.50	0.90	26.20	25.27	1.03	0.29	98.29
Bunch et al., 1967	L4	Atarra	1.43	5.10	1.80	0.72	59.40	0.55	31.90	31.90	0.00		100.90
Bunch et al., 1967	L4	Bald Mountain	1.83	5.50	1.67	0.74	58.10	0.67	32.30	31.27	1.14		100.92
Bunch et al., 1967	L4	Barratta	2.09	2.50	1.50	0.80	59.90	1.00	33.20	30.05	3.50		101.34
Bunch et al., 1967	L4	Goodland	1.64	3.70	1.44	0.81	59.80	0.80	32.80	31.02	1.98		101.19
Bunch et al., 1967	L4	McKinney	2.55	4.00	2.08	0.70	58.70	0.55	32.40	30.50	2.11		101.19
Wlotzka, 2005	L4	Acfer 047	11.20	41.00	0.23	0.17	24.90	0.51	22.60	21.04	1.74	0.47	101.25
Wlotzka, 2005	L4	Acfer 047	4.80	12.50	1.13	0.34	51.80	1.21	27.90	26.25	1.83	0.33	100.19
Wlotzka, 2005	L4	Bjurbˆle	2.18	5.72	2.14	0.67	56.90	0.65	30.70	30.41	0.33	0.33	99.32
Wlotzka, 2005	L4	Bjurbˆle	13.30	59.20	0.19		8.23	0.25	17.70	17.70	0.00	1.15	100.02
Wlotzka, 2005	L4	Bjurbˆle	5.16	18.00	1.29		44.90	0.76	29.00	26.64	2.62	0.93	100.30
Wlotzka, 2005	L4	DaG 323	2.35	6.16	2.04	0.65	57.30	0.74	30.70	30.32	0.42	0.38	100.36
Wlotzka, 2005	L4	HaH 219	5.08	4.45	1.76	0.64	60.50	0.66	26.70	25.80	1.00	0.15	100.04
Wlotzka, 2005	L4	Haxtun	3.49	4.86	1.69	0.63	59.30	0.69	28.40	27.91	0.54	0.23	99.34
Wlotzka, 2005	L4	NWA 767	1.55	5.62	2.62	0.83	56.80	0.74	31.70	31.70	0.00	0.38	100.24
This Study	L4	Bjurbole	1.81	5.61	2.08	0.68	56.87	0.61	30.79	30.73	0.07	0.36	98.83
This Study	L4	McKinney	2.38	4.73	2.24	0.69	57.43	0.60	30.61	29.99	0.69	0.37	99.13
Johnson and Prinz, 1991	L4 - C1	Bjurbole	2.05	5.26	1.60	0.87	55.62	0.63	33.36	30.27	3.44	0.38	100.12
Johnson and Prinz, 1991	L4 - C3	Bjurbole	1.95	4.79	2.23	0.91	55.25	0.59	33.68	30.94	3.05	0.38	100.08
Bunch et al., 1967	L5	Ergheo	2.23	6.30	3.02	0.73	54.80	0.63	33.50	32.18	1.47		101.36
Bunch et al., 1967	L5	Lua	2.19	3.80	2.54	0.71	57.60	1.00	33.00	30.94	2.28		101.07
Bunch et al., 1967	L5	Paragould	4.13	5.30	3.39	0.73	57.00	0.64	30.10	29.44	0.73		101.36
Snetsinger et al., 1967	L5	Sevrukovo	2.02	5.20	3.09	0.70	54.60	0.65	32.60	31.61	1.10		98.97
Wlotzka, 2005	L5	Acfer 307	11.80	47.70	0.17	0.14	17.30	0.38	22.00	20.31	1.88	1.44	101.12
Wlotzka, 2005	L5	Acfer 307	3.51	8.71	0.70	0.76	56.00	1.06	29.70	27.52	2.42	0.56	101.24
Wlotzka, 2005	L5	Baszkówka	2.76	5.99	2.82	0.74	56.20	0.65	30.40	30.37	0.04	0.32	99.88
Wlotzka, 2005	L5	Holbrook	2.61	5.94	3.28	0.62	55.30	0.65	31.30	31.10	0.23	0.24	99.96

This Study	L5	Bluff(a)	4.98	6.00	2.94	0.73	56.91	0.52	27.04	27.03	0.02	0.12	99.23
This Study	L5	Farmington	5.44	6.14	2.54	0.72	57.16	0.48	26.75	26.27	0.53	0.10	99.38
Bunch et al., 1967	L6	Harleton	2.11	5.10	2.88	0.73	56.00	0.57	33.40	31.98	1.58		100.95
Bunch et al., 1967	L6	Kyushu	1.79	5.40	3.13	0.77	55.90	0.76	32.50	32.34	0.18		100.27
Bunch et al., 1967	L6	Modoc 1	1.79	5.20	3.06	0.70	56.50	0.74	31.80	31.80	0.00		99.79
Bunch et al., 1967	L6	New Concord	1.80	5.70	2.09	0.71	56.20	0.60	33.80	31.86	2.16		101.12
Bunch et al., 1967	L6	Walters	2.05	5.50	2.96	0.72	56.00	0.91	32.80	31.89	1.01		101.04
Snetsinger et al., 1967	L6	Kyushu	1.79	5.40	3.13	0.77	55.90	0.76	32.50	32.34	0.18		100.27
Snetsinger et al., 1967	L6	Modoc 1	1.79	5.20	3.06	0.70	56.50	0.74	31.80	31.80	0.00		99.79
Wlotzka, 2005	L6	DaG 952	2.77	6.00	2.98	0.79	55.70	0.56	30.30	30.30	0.00	0.44	99.54
Wlotzka, 2005	L6	Dar al Gani 925	9.37	31.80	0.95	0.12	32.70	0.26	24.30	23.04	1.40	0.28	99.92
Wlotzka, 2005	L6	Dar al Gani 925	4.56	12.12	2.44	0.49	50.90	0.49	28.80	28.62	0.20	0.07	99.89
Wlotzka, 2005	L6	Etter	3.80	5.29	3.05	0.54	58.70	0.66	26.90	26.90	0.00		98.94
Wlotzka, 2005	L6	NWA 848	2.46	5.58	2.76	0.74	54.90	0.83	32.10	30.50	1.78	0.32	99.87
Wlotzka, 2005	L6	Rio Limay	5.53	6.32	2.58	0.64	57.10	0.58	27.10	26.26	0.93	0.11	100.05
This Study	L6	Bruderheim	2.23	5.96	2.63	0.71	55.82	0.65	30.42	30.42	0.01	0.33	98.77
Bunch and Keil, 1971	L6/7	Shaw	2.90	6.80	1.63	0.50	60.40	0.52	27.70	27.70	0.00	0.02	100.47
Bunch et al., 1967	LL3	Ngawai (A)	1.51	6.60	3.66	0.73	52.00	0.50	35.30	33.75	1.72		100.47
Bunch et al., 1967	LL3	Ngawai (B)	0.82	0.03	0.60	0.85	64.60	0.65	33.90	31.28	2.92		101.74
Bunch et al., 1967	LL3	Parnallee	1.35	3.32	1.66	0.45	57.10	0.44	35.80	31.78	4.47		100.57
Wlotzka, 2005	LL3–6	Bhola	1.83	5.55	3.43	0.68	55.90	0.50	31.50	31.50	0.00		99.39
Kimura et al., 2006	LL3.00 - All (avg)	Semarkona	14.20	35.31	0.66	0.40	32.92	0.36	16.27	16.17	0.11		100.13
Kimura et al., 2006	LL3.00 - C	Semarkona	15.87	48.15	0.72	0.12	19.33	0.28	15.28	15.28	0.00		99.75
Kimura et al., 2006	LL3.00 - C	Semarkona	27.82	70.32	0.25	0.32	0.56		0.27	0.27	0.00		99.54
Kimura et al., 2006	LL3.00 - C (avg)	Semarkona	16.07	40.23	0.60	0.34	28.53	0.29	14.07	14.07	0.00		100.13
Kimura et al., 2006	LL3.00 - M	Semarkona	0.29	0.04	0.41	0.69	65.99	0.75	32.30	31.44	0.95		100.57
Kimura et al., 2006	LL3.00 - M/O (avg)	Semarkona	0.86	0.05	1.13	0.84	64.39	0.89	32.02	30.99	1.14		100.29
Kimura et al., 2006	LL3.00 - O	Semarkona	0.17	0.04	0.13	0.89	66.84	1.59	30.88	30.54	0.38		100.58
Johnson and Prinz, 1991	LL3.00 - C1	Semarkona,-1	6.65	4.39	2.69	0.90	57.63	0.38	26.55	24.44	2.35	0.00	99.43
Johnson and Prinz, 1991	LL3.00 - C1	Semarkona,-3	3.24	2.13	1.59	0.90	59.89	0.79	30.91	27.98	3.25	0.08	99.85
Johnson and Prinz, 1991	LL3.00 - C1	Semarkona,-4	5.56	2.71	1.89	0.92	59.91	0.50	27.84	25.05	3.10	0.04	99.68
Johnson and Prinz, 1991	LL3.00 - C111	Semarkona,-2	6.39	5.94	1.85	0.91	57.67	0.38	26.46	24.46	2.23	0.00	99.82
Johnson and Prinz, 1991	LL3.00 - C2	Semarkona,-1	6.74	4.74	2.12	1.01	58.43	0.44	25.87	23.80	2.30	0.04	99.62

Johnson and Prinz, 1991	LL3.00 - C2	Semarkona,-4	6.55	3.69	1.45	0.86	60.42	0.68	25.62	23.09	2.81	0.04	99.59
Johnson and Prinz, 1991	LL3.00 - C200	Semarkona,-2	3.45	0.23	2.06	0.93	62.35	0.72	29.72	27.83	2.10	0.04	99.71
Johnson and Prinz, 1991	LL3.00 - C3	Semarkona,-1	6.16	4.42	1.88	0.93	58.94	0.48	26.55	24.39	2.40	0.04	99.64
Johnson and Prinz, 1991	LL3.00 - C3	Semarkona,-4	0.45	0.18	0.29	0.67	63.28	0.77	33.63	30.73	3.22	0.07	99.67
Johnson and Prinz, 1991	LL3.00 - C4	Semarkona,-4	2.23	0.14	1.20	0.89	62.37	0.84	31.68	28.78	3.22	0.07	99.75
Johnson and Prinz, 1991	LL3.00 - C43	Semarkona,-2	0.47	0.02	0.07	0.47	63.37	0.90	33.36	30.19	3.52	0.04	99.05
Johnson and Prinz, 1991	LL3.00 - C70	Semarkona,-2	6.46	4.45	1.88	0.90	59.92	0.48	25.48	24.01	1.63	0.00	99.73
Bunch et al., 1967	LL3.15	Bishunpur	0.53	0.10	0.43	0.72	63.90	0.58	34.30	31.37	3.25		100.89
Kimura et al., 2006	LL3.15 - All (avg)	Y-74660	4.43	9.80	1.02	0.58	55.09	0.34	27.13	26.80	0.37	0.20	98.63
Kimura et al., 2006	LL3.15 - C	Y-74660	15.62	43.80	0.30	0.18	24.80	0.21	15.20	15.16	0.05		100.11
Kimura et al., 2006	LL3.15 - C	Y-74660	7.81	22.55	0.89	0.27	42.50	0.55	24.00	23.48	0.58		98.63
Kimura et al., 2006	LL3.15 - C (avg)	Y-74660	9.01	21.72	0.89	0.51	44.56	0.32	22.10	21.82	0.31	0.16	99.30
Kimura et al., 2006	LL3.15 - M	Y-74660	0.71	0.17	1.08	0.98	62.46	0.33	32.68	31.11	1.74	0.16	98.74
Kimura et al., 2006	LL3.15 - M/O (avg)	Y-74660	0.71	0.12	1.12	0.65	63.65	0.36	31.21	30.85	0.40	0.23	98.09
Kimura et al., 2006	LL3.15 - O	Y-74660	0.76	0.19	4.05	0.87	58.89	0.32	33.82	33.78	0.04	0.26	99.16
Johnson and Prinz, 1991	LL3.15 - C3	Bishunpur	0.60	0.28	1.33	0.88	62.92	0.58	32.91	31.71	1.34	0.00	99.62
Johnson and Prinz, 1991	LL3.15 - C4	Bishunpur	1.26	0.44	1.34	0.85	60.93	0.51	33.95	30.64	3.67	0.26	99.90
Kimura et al., 2006	LL3.2 - All (avg)	Krymka	10.62	27.50	0.50	0.52	40.01	0.31	20.92	20.43	0.55		100.43
Kimura et al., 2006	LL3.2 - C	Krymka	0.79	1.41	1.45	0.83	62.17	0.31	32.74	31.88	0.95	0.24	100.04
Kimura et al., 2006	LL3.2 - C (avg)	Krymka	12.30	32.00	0.55	0.50	35.52	0.27	19.15	18.62	0.59		100.35
Kimura et al., 2006	LL3.2 - C(R)	Krymka	22.63	64.81	0.22	0.24	4.45		7.50	7.50	0.00	0.13	99.98
Kimura et al., 2006	LL3.2 - M/O (avg)	Krymka	0.33	0.04	0.24	0.67	67.42	0.56	31.73	31.51	0.25	0.11	101.12
Kimura et al., 2006	LL3.2 - O	Krymka	0.34		0.45	0.53	66.95	0.31	31.19	31.19	0.00	0.28	100.05
Kimura et al., 2006	LL3.2 - All (avg)	Y-790448	6.65	17.80	1.03	0.49	46.92	0.32	25.76	24.91	0.95	0.16	99.22
Kimura et al., 2006	LL3.2 - C	Y-790448	9.76	19.99	0.46	0.39	48.20	0.24	21.01	20.49	0.58		100.11
Kimura et al., 2006	LL3.2 - C	Y-790448	3.87	15.41	0.62	0.25	49.74	0.36	28.37	28.23	0.16	0.20	98.84
Kimura et al., 2006	LL3.2 - C (avg)	Y-790448	8.00	22.18	1.21	0.43	42.51	0.29	24.61	23.82	0.88	0.14	99.46
Kimura et al., 2006	LL3.2 - M/O (avg)	Y-790448	0.82	0.50	1.47	0.73	62.14	0.47	32.17	31.07	1.22	0.30	98.72
Kimura et al., 2006	LL3.2 - O	Y-790448	0.52	0.09	2.10	0.76	61.87	0.49	32.56	32.05	0.57	0.27	98.72
Kimura et al., 2006	LL3.3 - All (avg)	Wells	8.62	23.79	0.65	0.44	44.27	0.26	23.10	23.10	0.00	0.16	101.29
Kimura et al., 2006	LL3.3 - C	Wells	8.95	21.88	0.61	0.45	45.97	0.26	22.11	22.11	0.00		100.23
Kimura et al., 2006	LL3.3 - C (avg)	Wells	9.19	25.53	0.62	0.42	42.70	0.25	22.47	22.47	0.00	0.16	101.34
Kimura et al., 2006	LL3.3 - C(R)	Wells	27.58	69.75	0.29	0.17	0.62		1.24	0.98	0.29		99.68

Kimura et al., 2006	LL3.3 - M	Wells	0.31		0.16	0.73	67.32	0.62	31.43	31.33	0.11		100.58
Kimura et al., 2006	LL3.3 - M/O (avg)	Wells	0.85	0.04	1.07	0.70	65.72	0.43	31.66	31.37	0.32	0.20	100.70
Johnson and Prinz, 1991	LL3.4 - C10	Chainpur	1.22	3.40	1.80	0.83	57.76	0.52	33.68	31.55	2.37	0.19	99.63
Johnson and Prinz, 1991	LL3.4 - C11	Chainpur	0.92	2.51	2.33	0.89	57.75	0.49	34.32	32.38	2.15	0.19	99.61
Johnson and Prinz, 1991	LL3.4 - C12	Chainpur	0.75	0.09	1.37	0.98	62.24	0.35	33.44	31.52	2.13	0.22	99.64
Johnson and Prinz, 1991	LL3.4 - C9	Chainpur	1.07	3.20	2.75	0.86	55.65	0.46	35.24	32.69	2.83	0.19	99.70
Kimura et al., 2006	LL3.5 - All (avg)	ALHA77260	3.96	15.00	1.05	0.55	49.24	0.42	28.52	28.22	0.33	0.49	99.26
Kimura et al., 2006	LL3.5 - C	ALHA77260	8.61	29.89	0.36	0.31	37.09	0.26	22.85	22.85	0.00	0.67	100.04
Kimura et al., 2006	LL3.5 - C (avg)	ALHA77260	5.23	20.97	0.95	0.49	43.50	0.38	27.27	27.13	0.16	0.58	99.39
Kimura et al., 2006	LL3.5 - M/O (avg)	ALHA77260	0.97	1.06	1.30	0.70	62.62	0.53	31.44	30.82	0.69	0.28	98.97
Kimura et al., 2006	LL3.5 - O	ALHA77260	0.98	0.36	1.59	0.81	63.75	0.56	31.04	31.04	0.00	0.25	99.34
Kimura et al., 2006	LL3.7 - All (avg)	ALHA77304	1.78	4.55	1.35	0.74	59.67	0.69	30.16	30.00	0.18	0.45	99.41
Kimura et al., 2006	LL3.7 - C	ALHA77304	1.87	4.69	1.11	0.70	59.85	0.61	30.26	29.78	0.53	0.49	99.63
Kimura et al., 2006	LL3.7 - C (avg)	ALHA77304	1.90	5.23	1.28	0.72	59.06	0.67	30.01	29.86	0.17	0.45	99.34
Kimura et al., 2006	LL3.7 - M	ALHA77304	1.58	3.86	1.32	0.76	60.48	0.68	30.00	30.00	0.00	0.44	99.12
Kimura et al., 2006	LL3.7 - M/O (avg)	ALHA77304	1.68	4.02	1.41	0.75	60.13	0.69	30.29	30.14	0.17	0.45	99.44
Kimura et al., 2006	LL3.9 - All (avg)	BoXian	1.98	4.90	1.60	0.82	58.39	0.64	29.85	29.80	0.06	0.42	98.61
Kimura et al., 2006	LL3.9 - C	Bo Xian	1.94	2.87	2.13	0.95	59.88	0.68	30.85	30.36	0.54	0.39	99.74
Kimura et al., 2006	LL3.9 - C (avg)	BoXian	2.63	8.32	1.56	0.78	55.56	0.61	29.39	29.39	0.00	0.44	99.29
Kimura et al., 2006	LL3.9 - M/O (avg)	BoXian	1.59	2.27	1.50	0.80	61.57	0.66	30.00	29.96	0.05	0.39	98.78
Kimura et al., 2006	LL3.9 - O	Bo Xian	1.85	2.52	2.30	0.98	60.99	0.62	30.21	30.21	0.00	0.40	99.87
Bunch et al., 1967	LL4	Hamlet	1.81	1.00	2.73	0.76	59.30	0.58	34.90	31.80	3.45		101.43
Bunch et al., 1967	LL4	Soko Banja	1.55	4.84	2.34	0.78	56.30	0.45	34.30	32.37	2.14		100.77
This Study	LL4	Hamlet	1.63	4.22	2.95	0.71	55.81	0.54	32.65	31.74	1.02	0.36	98.97
This Study	LL4	Soko Banja	1.50	5.85	2.28	0.72	55.51	0.55	31.93	31.53	0.45	0.34	98.73
Kimura et al., 2006	LL4 - All (avg)	Y-74002	1.81	5.82	2.52	0.76	56.58	0.62	31.33	31.33	0.00	0.39	99.83
Kimura et al., 2006	LL4 - M	Y-74002	1.65	5.97	2.05	0.79	57.58	0.63	31.27	31.27	0.00	0.47	100.41
Bunch et al., 1967	LL5	Khanpur	1.70	6.30	2.53	0.75	54.70	0.58	34.30	32.50	2.00		101.06
Bunch et al., 1967	LL5	Oberlin	1.82	5.80	2.45	0.77	54.60	0.74	34.50	31.97	2.81		100.96
Wlotzka, 2005	LL5	Krähenberg	2.09	5.77	3.12	0.80	56.60	0.46	30.60	30.60	0.00		99.44
This Study	LL5	Oberlin	2.06	6.20	2.79	0.73	54.86	0.56	31.55	31.37	0.20	0.26	99.03
Kimura et al., 2006	LL5 - All (avg)	Y-74022	1.89	6.20	2.63	0.75	55.94	0.64	31.17	31.17	0.00	0.29	99.51
Johnson and Prinz, 1991	LL5 - C1	Aldsworth	1.82	5.42	1.86	0.77	55.16	0.66	33.36	30.69	2.96	0.42	99.76

Johnson and Prinz, 1991	LL5 - C2	Aldsworth	1.70	4.87	2.74	0.73	55.18	0.72	33.56	31.66	2.11	0.38	100.10
Johnson and Prinz, 1991	LL5 - C3	Aldsworth	1.80	5.04	2.63	0.77	56.01	0.76	32.63	31.48	1.28	0.30	100.07
Kimura et al., 2006	LL5 - M	Y-74022	1.69	6.63	1.94	0.77	56.69	0.63	31.44	31.43	0.01	0.28	100.07
Bunch et al., 1967	LL6	Cherokee Springs	1.54	5.20	3.98	0.74	54.80	0.68	33.90	33.73	0.19		100.86
Bunch et al., 1967	LL6	Dhurmsala	1.99	5.70	2.89	0.69	55.20	0.75	33.50	32.06	1.60		100.88
Bunch et al., 1967	LL6	Jelica	1.30	5.80	3.71	0.73	53.40	0.50	35.50	34.19	1.46		101.09
Bunch et al., 1967	LL6	Manbhoom	1.39	5.40	3.84	0.69	53.70	0.54	35.40	34.07	1.48		101.11
Snetsinger et al., 1967	LL6	Cherokee Springs	1.54	5.20	3.98	0.74	54.80	0.68	33.90	33.73	0.19		100.86
Wlotzka, 2005	LL6	Vishnupur	1.77	5.31	4.29	0.60	55.00	0.51	31.90	31.90	0.00		99.38
This Study	LL6	Cherokee Springs	1.67	6.15	3.27	0.72	53.94	0.54	32.11	32.10	0.01	0.24	98.65
Kimura et al., 2006	LL6 - All (avg)	Y-790256	1.70	5.91	3.87	0.74	54.28	0.59	32.87	32.87	0.00	0.28	100.24
Johnson and Prinz, 1991	LL6 - C1	Appley Bridge	1.61	5.42	2.45	0.91	55.57	0.46	33.14	31.89	1.39	0.38	100.08
Johnson and Prinz, 1991	LL6 - C2	Appley Bridge	1.74	5.36	2.79	0.91	54.85	0.46	33.41	31.97	1.60	0.38	100.05
Kimura et al., 2006	LL6 - M	Y-790256	1.73	5.52	4.26	0.69	53.81	0.60	32.79	32.79	0.00	0.26	99.66
Wlotzka, 2005	LL7	Uden	1.72	5.44	2.75	0.60	55.70	0.57	32.30	31.79	0.56	0.24	99.38

All FeO: all Fe assigned as FeO
Total does not include All FeO

Table C.2. Oxygen isotope values for modern meteorites, chrome-spinel and bulk.

Reference	Type	Sample	$\delta^{18}O$	*2 SD*	$\delta^{17}O$	*2 SD*	$\Delta^{17}O$	*2 SD*
Clayton and Mayeda, 1996	Shergottite		4.33	*0.70*	2.47	*0.44*	0.27	*0.16*
Clayton and Mayeda, 1996	Nakhlite		4.40	*0.62*	2.59	*0.31*	0.30	*0.13*
Clayton and Mayeda, 1996	Chassignite		3.91		2.33		0.30	
Clayton and Mayeda, 1996	ALH 84001		4.53		2.58		0.22	
Clayton and Mayeda, 1996	Lunar		5.59	*0.40*	2.91	*0.25*	0.01	*0.13*
Clayton and Mayeda, 1996	Eucrite		3.61	*0.38*	1.63	*0.28*	-0.24	*0.13*
This Study	Eucrite	NWA 8365	-7.15	*2.16*	-3.49	*1.28*	0.23	*0.45*
Clayton and Mayeda, 1996	Diogenite		3.32	*0.33*	1.46	*0.26*	-0.27	*0.18*
This Study	Diogenite	NWA 10403	-2.38	*2.21*	-1.37	*1.51*	-0.13	*0.62*
Clayton and Mayeda, 1996	Howardite		3.25	*0.64*	1.43	*0.39*	-0.26	*0.16*
Clayton and Mayeda, 1996	Angrites		3.69	*0.31*	1.77	*0.25*	-0.15	*0.12*
Clayton and Mayeda, 1996	Mesosiderite		3.41	*0.31*	1.53	*0.22*	-0.25	*0.17*
Clayton and Mayeda, 1996	Pallasite		2.47	*3.01*	1.10	*3.42*	-0.63	*2.31*
Clayton and Mayeda, 1996	Iron IIIAB		2.27	*0.59*	0.98	*0.31*	-0.21	*0.11*
Clayton and Mayeda, 1996	Aubrite		5.26	*0.38*	2.75	*0.21*	0.02	*0.07*
Clayton and Mayeda, 1996	Brachinite		3.97	*1.19*	1.81	*0.60*	-0.26	*0.15*
This Study	Brachinite	NWA 3151	-0.97	*2.17*	-0.61	*0.90*	-0.10	*0.51*
Clayton and Mayeda, 1996	Iron IAB		4.82	*0.94*	2.04	*0.49*	-0.48	*0.20*
Clayton and Mayeda, 1996	Iron IIICD		6.06	*3.27*	2.72	*1.87*	-0.43	*0.17*
Clayton and Mayeda, 1996	Winonaite		5.25	*0.97*	2.22	*0.62*	-0.50	*0.21*
Clayton and Mayeda, 1996	Acapulcoite		3.45	*0.96*	0.77	*0.58*	-1.04	*0.24*
This Study	Acapulcoite	NWA 8287	-1.17	*1.15*	-1.79	*0.54*	-1.18	*0.47*
Clayton and Mayeda, 1996	Lodranite		3.38	*0.77*	0.57	*0.41*	-1.18	*0.41*
This Study	Lodranite	NWA 10265	-0.85	*0.65*	-1.92	*0.32*	-1.48	*0.22*
Clayton and Mayeda, 1996	Ureilite		6.93	*1.98*	2.41	*2.07*	-1.20	*1.14*

This Study	Ureilite	NWA 766	10.16	*1.33*	4.00	*0.68*	-1.28	*0.26*
Clayton and Mayeda, 1996	Iron IIE		4.26	*1.13*	2.81	*0.65*	0.59	*0.16*
Clayton and Mayeda, 1996	Iron IVA		4.50	*2.95*	3.51	*1.69*	1.17	*0.22*
Clayton and Mayeda, 1996	Iron Anomalous		2.46	*5.68*	-0.47	*6.21*	-1.75	*3.39*
This Study	CR6	NWA 7317	-3.47	*3.09*	-3.34	*1.66*	-1.53	*0.46*
Meteoritical Bulletin	CR6		3.22	*0.61*	-0.05	*0.28*	-1.73	*0.11*

This study - ion microprobe for chrome-spinel.
Clayton and Mayeda (1996) - bromine pentaflouride (BrF5) oxygen extraction on ground whole-rock.
Meteoritical Bulletin database (www.lpi.usra.edu/meteor/) for NWA7317 (MB 102), NWA2994 (MB 93), NWA3250 (MB 97), NWA6901 (MB 100), and NWA6921 (MB 102) via laser fluorination.

REFERENCES

Alwmark, C., & Schmitz, B. (2009a). Relict silicate inclusions in extraterrestrial chromite and their use in the classification of fossil chondritic material. *Geochimica et Cosmochimica Acta*, *73*(5), 1472-1486.

Alwmark, C., & Schmitz, B. (2009b). The origin of the Brunflo fossil meteorite and extraterrestrial chromite in mid-Ordovician limestone from the Gärde quarry (Jämtland, central Sweden). *Meteoritics & Planetary Science*, *44*(1), 95-106.

Alwmark, C., Schmitz, B., Holm, S., Marone, F., & Stampanoni, M. (2011). A 3-D study of mineral inclusions in chromite from ordinary chondrites using synchrotron radiation X-ray tomographic microscopy—Method and applications. *Meteoritics & Planetary Science*, *46*(8), 1071-1081.

Armstrong, J. T. (1995). Citzaf-a package of correction programs for the quantitative Electron Microbeam X-Ray-Analysis of thick polished materials, thin-films, and particles. *Microbeam Analysis*, 4(3), 177-200.

Barnes, S. J., & Roeder, P. L. (2001). The range of spinel compositions in terrestrial mafic and ultramafic rocks. *Journal of petrology*, *42*(12), 2279-2302.

Barrat, J. A., Jambon, A., Bohn, M., Gillet, P., Sautter, V., Göpel, C., Lesourd, M., & Keller, F. (2002). Petrology and chemistry of the picritic shergottite North West Africa 1068 (NWA 1068). *Geochimica et Cosmochimica Acta*, *66*(19), 3505-3518.

Baumgartner, R. J., Fiorentini, M. L., Baratoux, D., Ferrière, L., Locmelis, M., Tomkins, A., & Sener, K. A. (2017). The variability of ruthenium in chromite from chassignite and olivine-phyric shergottite meteorites: New insights into the behavior of PGE and sulfur in Martian magmatic systems. *Meteoritics & Planetary Science*, *52*(2), 333-350.

Beck, P., Barrat, J. A., Gillet, P., Wadhwa, M., Franchi, I. A., Greenwood, R. C., Bohn, M., Cotton, J., van de Moortèle, B., & Reynard, B. (2006). Petrography and geochemistry of the chassignite Northwest Africa 2737 (NWA 2737). *Geochimica et Cosmochimica Acta*, *70*(8), 2127-2139.

Beckerling, W., & Bischoff, A. (1995). Occurrence and composition of relict minerals in micrometeorites from Greenland and Antarctica—implications for their origins. *Planetary and Space Science*, *43*(3-4), 435-449.

Benedix, G. K., McCoy, T. J., Keil, K., Bogard, D. D., & Garrison, D. H. (1998). A petrologic and isotopic study of winonaites: Evidence for early partial melting, brecciation, and metamorphism. *Geochimica et Cosmochimica Acta*, *62*(14), 2535-2553.

Benninghoven, A. (1987). Secondary Ion Mass Spectrometry. A. Benninghoven, FG Rüdenauer, and HW Werner, editors.

Berkley, J. L., & Boynton, N. J. (1992). Minor/major element variation within and among diogenite and howardite orthopyroxenite groups. *Meteoritics*, *27*(4), 387-394.

Biebe, M. (2009). Spinel group minerals in carbonaceous and ordinary chondrites. (Bachelor thesis, Lund University, Lund, Sweden). Retrieved from https://lup.lub.lu.se/student-papers/search/publication/2301994

Bischoff, A., Geiger, T., Palme, H., Spettel, B., Schultz, L., Scherer, P., Loeken, T., Bland, P., Clayton, R. N., Mayeda, T. K., Herpers, U., Meltzow, B., Michel, R., & Dittrich-Hannen, B. (1994). Acfer 217-A new member of the Rumuruti chondrite group (R). *Meteoritics*, *29*(2), 264-274.

Bischoff, A., Vogel, N., & Roszjar, J. (2011). The Rumuruti chondrite group. *Geochemistry*, 71(2), 101-133.

Bjärnborg, K., & Schmitz, B. (2013). Large spinel grains in a CM chondrite (Acfer 331): implications for reconstructions of ancient meteorite fluxes. *Meteoritics & Planetary Science*, *48*(2), 180-194.

Bottke, W. F., Vokrouhlický, D., & Nesvorný, D. (2007). An asteroid breakup 160 Myr ago as the probable source of the K/T impactor. *Nature*, *449*(7158), 48.

Bowman, L. E., Papike, J. J., & Spilde, M. N. (1999). Diogenites as asteroidal cumulates: Insights from spinel chemistry. *American Mineralogist*, *84*(7-8), 1020-1026.

Bradley, J. P., & Dai, Z. R. (2009). Analytical SuperSTEM for extraterrestrial materials research. *Meteoritics & planetary science*, *44*(10), 1627-1642.

Brearley A. J. and Jones R. H. (1998). Planetary materials. *Reviews in Mineralogy and Geochemistry* 36:3-1.

Bridges, J. C., Schmitz, B., Hutchison, R., Greenwood, R. C., Tassinari, M., & Franchi, I. A. (2007). Petrographic classification of Middle Ordovician fossil meteorites from Sweden. *Meteoritics & Planetary Science*, *42*(10), 1781-1789.

Brownlee, D. E., Bates, B., & Schramm, L. (1997). The elemental composition of stony cosmic spherules. *Meteoritics & Planetary Science*, *32*(2), 157.

Bunch, T. E., Keil, K., & Snetsinger, K. G. (1967). Chromite composition in relation to chemistry and texture of ordinary chondrites. *Geochimica et Cosmochimica Acta*, 31(10), 1569-1582.

Bunch, T. E., Keil, K., & Olsen, E. (1970). Mineralogy and petrology of silicate inclusions in iron meteorites. *Contributions to Mineralogy and Petrology*, *25*(4), 297-340.

Bunch, T. E., & Keil, K. (1971). Chromite and ilmenite in non chondritic meteorites. *American Mineralogist: Journal of Earth and Planetary Materials*, *56*(1-2), 146-157.

Bunch, T. E., Keil, K., & Huss, G. I. (1972). The Landes meteorite. *Meteoritics*, *7*(1), 31-38.

Caplan, C. E., Huss, G.R., Schmitz, B., & Nagashima, K. (2018). Tracking Meteorite Infall Through Time: the Picture of the Jurassic from Remnant Chrome-Spinels. 49th LPSC, Abstract #2701.

Caplan C. E., Huss G. R., Nagashima K., and Schmitz B. (2019). Meteorites of the Jurassic: Populations Determined from Remnant Extraterrestrial Chrome-Spinels in Spanish Limestone (abstract). 82nd Annual Meteoritical Society Meeting: 6050.

Caplan, C. E., Huss, G. R., Ishii, H. A., Bradley, J. P., Schmitz, B., & Nagashima, K. (2020). The classification of relict extraterrestrial chrome-spinels using STEM techniques on silicate inclusions. *Meteoritics & Planetary Science*, accepted.

Ceplecha, Z., Borovička, J., Elford, W. G., ReVelle, D. O., Hawkes, R. L., Porubčan, V., & Šimek, M. (1998). Meteor phenomena and bodies. *Space Science Reviews*, *84*(3-4), 327-471.

Chiba, H., Chacko, T., Clayton, R. N., & Goldsmith, J. R. (1989). Oxygen isotope fractionations involving diopside, forsterite, magnetite, and calcite: Application to geothermometry. *Geochimica et Cosmochimica Acta*, 53(11), 2985-2995.

Chikami, J., Mikouchi, T., Takeda, H., & Miyamoto, M. (1997). Mineralogy and cooling history of the calcium-aluminum-chromium enriched ureilite, Lewis Cliff 88774. *Meteoritics & Planetary Science*, *32*(3), 343-348.

Clayton R. N. (2004) Oxygen isotopes in meteorites. In Treatise on Geochemistry, Volume 1: Meteorites, Comets, and Planets, Davis A. M., editor, pp. 129-142. Elsevier, Oxford.

Clayton, R. N., Mayeda, T. K., Goswami, J. N., & Olsen, E. J. (1991). Oxygen isotope studies of ordinary chondrites. *Geochimica et Cosmochimica Acta*, 55(8), 2317-2337.

Clayton, R. N., & Mayeda, T. K. (1996). Oxygen isotope studies of achondrites. *Geochimica et Cosmochimica Acta*, *60*(11), 1999-2017.

Clayton, R. N., & Mayeda, T. K. (1999). Oxygen isotope studies of carbonaceous chondrites. *Geochimica et Cosmochimica Acta*, 63(13-14), 2089-2104.

Connolly Jr, H. C., & Huss, G. R. (2010). Compositional evolution of the protoplanetary disk: Oxygen isotopes of type-II chondrules from CR2 chondrites. *Geochimica et Cosmochimica Acta*, *74*(8), 2473-2483.

Cronholm, A., and Schmitz, B., (2010). Extraterrestrial chromite distribution across the mid-Ordovician Puxi River section, central China: evidence for a global major spike in flux of L-chondritic matter. *Icarus* 208, 36–48.

Desnoyers, C., Michel-Levy, M. C., Azevedo, I. S., Scorzelli, R. B., Danon, J., & da Silva, E. G. (1985). Mineralogy of the Bocaiuva iron meteorite: A preliminary study. *Meteoritics*, *20*(1), 113-124.

Droop G. T. R. (1987). A general equation for estimating Fe 3+ concentrations in ferromagnesian silicates and oxides from microprobe analyses, using stoichiometric criteria. *Mineralogical magazine*, 51(361), 431-435.

Fahey, A. J. (1998). Measurements of dead time and characterization of ion counting systems for mass spectrometry. Review of scientific instruments, 69(3), 1282-1288.

Fahey, A. J., Goswami, J. N., McKeegan, K. D., & Zinner, E. K. (1987). O-16 excesses in Murchison and Murray hibonites-A case against a late supernova injection origin of isotopic anomalies in O, Mg, Ca, and TI. *The Astrophysical Journal*, *323*, L91-L95.

Folco, L., Franchi, I. A., D'ORAZIO, M., Rocchi, S., & Schultz, L. (2000). A new martian meteorite from the Sahara: The shergottite Dar al Gani 489. *Meteoritics & Planetary Science*, *35*(4), 827-839.

Fuchs, L. H., Olsen, E., & Jensen, K. J. (1973). Mineralogy, mineral-chemistry, and composition of the Murchison (C2) meteorite. *Smithsonian contributions to the earth sciences*.

Gardner-Vandy, K. G., Lauretta, D. S., Greenwood, R. C., McCoy, T. J., Killgore, M., & Franchi, I. A. (2012). The Tafassasset primitive achondrite: Insights into initial stages of planetary differentiation. *Geochimica et Cosmochimica Acta*, *85*, 142-159.

Gardner-Vandy, K. G., Lauretta, D. S., & McCoy, T. J. (2013). A petrologic, thermodynamic and experimental study of brachinites: Partial melt residues of an R chondrite-like precursor. *Geochimica et Cosmochimica Acta*, *122*, 36-57.

Ghisler M. 1977. The Geology, Mineralogy and Geochemistry of the-Pre-Orogenic Archaean Stratiform Chromite Deposits at-Fiskenaesset.

Gladman, B. J., Migliorini, F., Morbidelli, A., Zappalà, V., Michel, P., Cellino, A., Froeschlé, C., Levison, H.F., Bailey, M., Duncan, M. (1997). Dynamical lifetimes of objects injected into asteroid belt resonances. *Science*, 277(5323), 197-201.

Gnaser, H. (2007). Energy and angular distributions of sputtered species. In *Sputtering by particle bombardment* (pp. 231-328). Springer, Berlin, Heidelberg.

Goodrich, C. A., Harlow, G. E., Van Orman, J. A., Sutton, S. R., Jercinovic, M. J., & Mikouchi, T. (2014). Petrology of chromite in ureilites: Deconvolution of primary oxidation states and secondary reduction processes. *Geochimica et Cosmochimica Acta*, *135*, 126-169.

Graham, G. A., Teslich, N. E., Kearsley, A. T., Stadermann, F. J., Stroud, R. M., Dai Z., Ishii H. A., Hutcheon I. D., Bajt S., Snead C. J., Weber P. K., and Bradley J. P. (2008). Applied focused ion beam techniques for sample preparation of astromaterials for integrated nanoanalysis. *Meteoritics & Planetary Science*, *43*(3), 561-569.

Greenwood R. C., Schmitz B., Bridges J. C., Hutchison R., and Franchi I. A. (2007). Disruption of the L chondrite parent body: New oxygen isotope evidence from Ordovician relict chromite grains. *Earth and Planetary Science Letters* 262, 204–213.

Haggerty, S. E., & Meyer, H. O. (1970). Apollo 12: opaque oxides. *Earth and Planetary Science Letters*, *9*(5), 379-387.

Haggerty, S. E. (1972). Luna 16: An opaque mineral study and a systematic examination of compositional variations of spinels from Mare Fecunditatis. *Earth and Planetary Science Letters*, *13*(2), 328-352.

Heck, P. R., Ushikubo, T., Schmitz, B., Kita, N. T., Spicuzza, M. J., & Valley, J. W. (2010). A single asteroidal source for extraterrestrial Ordovician chromite grains from Sweden and China: High-precision oxygen three-isotope SIMS analysis. *Geochimica et Cosmochimica Acta*, *74*(2), 497-509.

Heck, P. R., Schmitz, B., Rout, S. S., Tenner, T., Villalon, K., Cronholm, A., Terfelt, F., & Kita, N. T. (2016). A search for H-chondritic chromite grains in sediments that formed immediately after the breakup of the L-chondrite parent body 470 Ma ago. *Geochimica et Cosmochimica Acta*, *177*, 120-129.

Heck, P. R., Schmitz, B., Bottke, W. F., Rout, S. S., Kita, N. T., Cronholm, A., Defouilloy, C., Dronov, A., & Terfelt, F. (2017). Rare meteorites common in the Ordovician period. *Nature Astronomy*, *1*, 0035.

Huberty J., Kita N. T., Kozdon R., Heck P. R., Fournelle J. H., Spicuzza M. J., Xu H. and Valley J. W. (2010). Crystal orientation effects in δ18O for magnetite and hematite by SIMS. *Chemical Geology*, *276*(3-4), 269-283.

Huss G. R., Rubin A. I. and Grossman J. N. (2006). Thermal metamorphism in chondrites. In *Meteorites and the early solar system II*, edited by Lauretta D. S. and McSween H. Y. Jr. Tucson, Arizona: The University of Arizona Press. pp. 567-586.

Ikeda, Y. (1994). Petrography and petrology of the ALH-77005 shergottite. *Antarctic Meteorite Research*, *7*, 9.

Ishii, H. A., Krot, A. N., Bradley, J. P., Keil, K., Nagashima, K., Teslich N., Jacobsen B., and Yin Q. Z. (2010). Discovery, mineral paragenesis, and origin of wadalite in a meteorite. *American Mineralogist*, *95*(4), 440-448.

Johnson, C. A., & Prinz, M. (1991). Chromite and olivine in type II chondrules in carbonaceous and ordinary chondrites: Implications for thermal histories and group differences. *Geochimica et Cosmochimica Acta*, *55*(3), 893-904.

Kapure, G., Tathavadkar, V., Rao, C. B., Rao, S. M., & Raju, K. S. (2010, June). Coal based direct reduction of preoxidized chromite ore at high temperature. In *Proceedings of the 12th International Ferro-Alloys Congress (INFACON XII)* (pp. 293-301).

Keil, K., & McCoy, T. J. (2018). Acapulcoite-lodranite meteorites: Ultramafic asteroidal partial melt residues. *Geochemistry*, 78(2), 153-203.

Kimura, M., Nakajima, H., Hiyagon, H., & Weisberg, M. K. (2006). Spinel group minerals in LL3. 00–6 chondrites: Indicators of nebular and parent body processes. *Geochimica et Cosmochimica Acta*, *70*(22), 5634-5650.

Kita N.T., Ushikubo T., Fu B., Spicuzza M. J., Valley J. W. (2007). Analytical Developments on Oxygen Three Isotope Analyses Using a New Generation Ion Microprobe ims-1280. 38th LPSC, Abstract # 1981.

Kumar, M., & Patel, N. R. (2007). Clustering data with measurement errors. *Computational Statistics & Data Analysis*, 51(12), 6084-6101.

Lindskog, A., Schmitz, B., Cronholm, A., and Dronov, A., (2012). A Russian record of a Middle Ordovician meteorite shower: extraterrestrial chromite at Lynna River, St. Petersburg region. *Meteoritics & Planetary Science*. 47, 1274–1290.

Lindsley D. H. (Ed.). (2018). *Oxide minerals: petrologic and magnetic significance* (Vol. 25). Walter de Gruyter GmbH & Co KG.

Loferski, P. J., & Lipin, B. R. (1983). Exsolution in metamorphosed chromite from the Red Lodge district, Montana. *American Mineralogist*, *68*(7-8), 777-789.

Longo, D. M., Howe, J. M., & Johnson, W. C. (1999). Experimental method for determining Cliff–Lorimer factors in transmission electron microscopy (TEM) utilizing stepped wedge-shaped specimens prepared by focused ion beam (FIB) thinning. *Ultramicroscopy*, *80*(2), 85-97.

Love, S. G., & Brownlee, D. E. (1993). A direct measurement of the terrestrial mass accretion rate of cosmic dust. *Science*, *262*(5133), 550-553.

Lyon, I. C., Saxton, J. M., & Cornah, S. J. (1998). Isotopic fractionation during secondary ionisation mass spectrometry: crystallographic orientation effects in magnetite. *International Journal of Mass Spectrometry and Ion Processes*, *172*(1-2), 115-122.

Maitland, T., & Sitzman, S. (2007). *Electron backscatter diffraction (EBSD) technique and materials characterization examples* (Vol. 14, p. 522). Berlin: Springer.

Makide, K., Nagashima, K., Krot, A. N., Huss, G. R., Hutcheon, I. D., & Bischoff, A. (2009). Oxygen-and magnesium-isotope compositions of calcium–aluminum-rich inclusions from CR2 carbonaceous chondrites. *Geochimica et Cosmochimica Acta*, 73(17), 5018-5050.Nielsen, F. (2016). "Chapter 8: Hierarchical Clustering". Introduction to HPC with MPI for Data Science. Springer.

Martin, E., Schmitz, B., & Schönlaub, H. P. (2018). From the mid-Ordovician into the Late Silurian: Changes in the micrometeorite flux after the L chondrite parent breakup. *Meteoritics & Planetary Science*, *53*(12), 2541-2557.

Martin, E., Schmitz, B., & Montanari, A. (2019). A record of the micrometeorite flux during an enigmatic extraterrestrial 3He anomaly in the Turonian (Late Cretaceous). In *GSA Special Papers : 250 Million Years of Earth History in Central Italy: Celebrating 25 Years of the Geological Observatory of Coldigioco* (Geological Society of America. Special Papers).

Masiero, J. R., Mainzer, A. K., Grav, T., Bauer, J. M., & Jedicke, R. (2012). Revising the age for the Baptistina asteroid family using WISE/NEOWISE data. *The Astrophysical Journal*, *759*(1), 14.

McCoy, T. J., Corrigan, C. M., Nagashima, K., Reynolds, V. S., Ash, R. D., McDonough, W. F., Yang, J., Goldstein, J. I., & Hilton, C. D. (2019). The Milton pallasite and South Byron Trio irons: Evidence for oxidation and core crystallization. *Geochimica et Cosmochimica Acta*, *259*, 358-370.

Mikouchi, T., Miyamoto, M., & McKay, G. A. (1996). Mineralogical study of angrite Asuka-881371: Its possible relation to angrite LEW87051. *Antarctic Meteorite Research*, *9*, 174.

Mikouchi, T., & Miyamoto, M. (1997). Yamato-793605: A new iherzolitic shergottite from the Japanese Antarctic meteorite collection. *Antarctic Meteorite Research*, *10*, 41.

Mittlefehldt, D. W. (1994). ALH84001, a cumulate orthopyroxenite member of the Martian meteorite clan. *Meteoritics*, *29*(2), 214-221.

Mittlefehldt, D. W., Lindstrom, M. M., Bogard, D. D., Garrison, D. H., & Field, S. W. (1996). Acapulco-and Lodran-like achondrites: Petrology, geochemistry, chronology, and origin. *Geochimica et Cosmochimica Acta*, *60*(5), 867-882.

Mittlefehldt, D. W., Bogard, D. D., Berkley, J. L., & Garrison, D. H. (2003). Brachinites: Igneous rocks from a differentiated asteroid. *Meteoritics & Planetary Science*, *38*(11), 1601-1625.

Mittlefehldt, D. W. (2015). Asteroid (4) Vesta: I. The howardite-eucrite-diogenite (HED) clan of meteorites. *Geochemistry*, *75*(2), 155-183.

Muir, J. E., & Naldrett, A. J. (1973). A natural occurrence of two-phase chromium-bearing spinels. *The Canadian Mineralogist*, *11*(5), 930-939.

Nagashima K., Krot A. N., & Huss G. R. (2015) Oxygen-isotope compositions of chondrule phenocrysts and matrix grains in Kakangari K-grouplet chondrite: Implication to a chondrule-matrix genetic relationship. *Geochimica et Cosmochimica Acta,* 151, 49-67.

Nesvorný, D., Jedicke, R., Whiteley, R. J., & Ivezić, Ž. (2005). Evidence for asteroid space weathering from the Sloan Digital Sky Survey. *Icarus*, 173(1), 132-152.

Nesvorný, D., Brož, M., & Carruba, V. (2015). Identification and dynamical properties of asteroid families. *Asteroids IV*, 297-321.

Nielsen, F. (2016). Hierarchical clustering. In Introduction to HPC with MPI for Data Science (pp. 195-211). Springer, Cham.

Papike, J. J., Shearer, C. K., Spilde, M. N., & Karner, J. M. (2000). Metamorphic diogenite Grosvenor Mountains 95555: Mineral chemistry of orthopyroxene and spinel and comparisons to the diogenite suite. *Meteoritics & Planetary Science*, *35*(4), 875-879.

Patzer, A., Schlüter, J., Schultz, L., Hill, D. H., & Boynton, W. V. (2005). The new polymict eucrite Dar al Gani 983: Petrography, chemical composition, noble gas record, and evolution. *Meteoritics & Planetary Science*, *40*(6), 869-879.

Reddy, V., Sanchez, J. A., Bottke, W. F., Cloutis, E. A., Izawa, M. R., O'Brien, D. P., Mann, P., Cuddy, M., Le Corre, L., Gaffey, M. J., & Fujihara, G. (2014). Chelyabinsk meteorite explains unusual spectral properties of Baptistina Asteroid Family. *Icarus*, *237*, 116-130.

Reolid, M., & Abad, I. (2019). The Middle-Upper Jurassic unconformity in the South Iberian Palaeomargin (Western Tethys): a history of carbonate platform fragmentation, emersion and subsequent drowning. *Journal of Iberian Geology*, 45(1), 87-110.

Rubin, A. E. (1997). Mineralogy of meteorite groups. *Meteoritics & Planetary Science*, *32*(2), 231-247.

Rubin, A. E., & Kallemeyn, G. W. (1994). Pecora Escarpment 91002: A member of the new Rumuruti (R) chondrite group. *Meteoritics*, *29*(2), 255-264.

Rudraswami, N. G., Prasad, M. S., Nagashima, K., & Jones, R. H. (2015). Oxygen isotopic composition of relict olivine grains in cosmic spherules: Links to chondrules from carbonaceous chondrites. *Geochimica et Cosmochimica Acta*, *164*, 53-70.

Rudraswami, N. G., Marrocchi, Y., Shyam Prasad, M., Fernandes, D., Villeneuve, J., & Taylor, S. (2019). Oxygen isotopic and chemical composition of chromites in micrometeorites: Evidence of ordinary chondrite precursors. *Meteoritics & Planetary Science*, *54*(6), 1347-1361.

Schmitz, B. (2013). Extraterrestrial spinels and the astronomical perspective on Earth's geological record and evolution of life. *Geochemistry*, 73(2), 117-145.

Schmitz, B., Lindström, M., Asaro, F., & Tassinari, M. (1996). Geochemistry of meteorite-rich marine limestone strata and fossil meteorites from the lower Ordovician at Kinnekulle, Sweden. Earth and Planetary Science Letters, 145(1-4), 31-48.

Schmitz, B., Peucker-Ehrenbrink, B., Lindström, M., & Tassinari, M. (1997). Accretion rates of meteorites and cosmic dust in the Early Ordovician. Science, 278(5335), 88-90.

Schmitz, B., Tassinari, M., & Peucker-Ehrenbrink, B. (2001). A rain of ordinary chondritic meteorites in the early Ordovician. *Earth and Planetary Science Letters*, *194*(1-2), 1-15.

Schmitz, B., Häggström, T., & Tassinari, M. (2003). Sediment-dispersed extraterrestrial chromite traces a major asteroid disruption event. *Science*, *300*(5621), 961-964.

Schmitz, B., Harper, D. A., Peucker-Ehrenbrink, B., Stouge, S., Alwmark, C., Cronholm, A., Bergström, S. M., Tassinari, M., & Xiaofeng, W. (2008). Asteroid breakup linked to the Great Ordovician biodiversification event. *Nature Geoscience*, *1*(1), 49-53.

Schmitz, B., Huss, G. R., Meier, M. M., Peucker-Ehrenbrink, B., Church, R. P., Cronholm, A., ... & Kristiansson, P. (2014). A fossil winonaite-like meteorite in Ordovician limestone: A piece of the impactor that broke up the L-chondrite parent body?. *Earth and Planetary Science Letters*, *400*, 145-152.

Schmitz, B., Yin, Q. Z., Sanborn, M. E., Tassinari, M., Caplan, C. E., & Huss, G. R. (2016). A new type of solar-system material recovered from Ordovician marine limestone. *Nature communications*, *7*, ncomms11851.

Schmitz, B., Heck, P. R., Alvarez, W., Kita, N. T., Rout, S. S., Cronholm, A., Defouilloy, C., Martin, E., Smit, J., & Terfelt, F. (2017). Meteorite flux to Earth in the Early Cretaceous as reconstructed from sediment-dispersed extraterrestrial spinels. *Geology*, *45*(9), 807-810.

Schmitz, B., Feist, R., Meier, M. M., Martin, E., Heck, P. R., Lenaz, D., Topa, D., Busemann, H., Maden, C., Plant, A. A., & Terfelt, F. (2019). The micrometeorite flux to Earth during the Frasnian–Famennian transition reconstructed in the Coumiac GSSP section, France. *Earth and Planetary Science Letters*, *522*, 234-243.

Schrader, D. L., Connolly, H. C. Jr., Lauretta, D. S., Nagashima, K., Huss, G. R., Davidson, J., Domanik, K. J. (2013). The formation and alteration of the Renazzo-like carbonaceous chondrites II: Linking O-isotope composition and oxidation state of chondrule olivine. *Geochimica et Cosmochimica Acta,* 101, 302–327.

Schrader, D. L., Nagashima, D., Krot, A. N., Ogliore, R. C., & Hellebrand, E. (2014). Variations in the O-isotope composition of gas during the formation of chondrules from CR chondrites. *Geochimica et Cosmochimica Acta,* 132, 50–74.

Schulze, H., Bischoff, A., Palme, H., Spettel, B., Dreibus, G., & Otto, J. (1994). Mineralogy and chemistry of Rumuruti: The first meteorite fall of the new R chondrite group. *Meteoritics*, *29*(2), 275-286.

Snetsinger, K. G., Keil, K., & Bunch, T. E. (1967). Chromite from "equilibrated" chondrites. American Mineralogist: Journal of Earth and Planetary Materials, 52(9-10), 1322-1331.

Steele I. M., Bishop F. C., Smith J. V., and Windley B. F. (1977). The Fiskenaesset Complex, West Greenland, Part III. Grönlands geol. Unders. *Bull*, *124*.

Tenner, T. J., Nakashima, D., Ushikubo, T., Kita, N. T., & Weisberg, M. K. (2015). Oxygen isotope ratios of FeO-poor chondrules in CR3 chondrites: Influence of dust enrichment and H2O during chondrule formation. *Geochimica et Cosmochimica Acta,* 148, 228–250.

Tenner, T. J., Ushikubo, T., Nakashima, D., Schrader, D. L., Weisberg, M. K., Kimura, M., & Kita, N. T. (2018). Oxygen isotope characteristics of chondrules from recent studies by secondary ion mass spectrometry. *Chondrules: Records of Protoplanetary Disk Processes*, 196-246.

Thorslund, P., Wickman, F. E., & Nyström, J. O. (1984). The Ordovician chondrite from Brunflo, central Sweden, I. General description and primary minerals. *Lithos*, *17*, 87-100.

Treiman, A. H. (2005). The nakhlite meteorites: Augite-rich igneous rocks from Mars. *Geochemistry*, *65*(3), 203-270.

Valley, J. W., & Kita, N. T. (2009). In situ oxygen isotope geochemistry by ion microprobe. *MAC short course: secondary ion mass spectrometry in the earth sciences*, *41*, 19-63.

Weisberg, M. K., McCoy, T. J., & Krot, A. N. (2006). Systematics and evaluation of meteorite classification. *Meteorites and the early solar system II*.

Wlotzka, F. (2005). Cr spinel and chromite as petrogenetic indicators in ordinary chondrites: Equilibration temperatures of petrologic types 3.7 to 6. *Meteoritics & Planetary Science*, 40(11), 1673-1702.

Yada, T., Nakamura, T., Noguchi, T., Matsumoto, N., Kusakabe, M., Hiyagon, H., Ushikubo, T., Sugiura, N., Kojima, H., & Takaoka, N. (2005). Oxygen isotopic and chemical compositions of cosmic spherules collected from the Antarctic ice sheet: Implications for their precursor materials. *Geochimica et Cosmochimica Acta*, *69*(24), 5789-5804.

Zappalà, V., Cellino, A., Gladman, B. J., Manley, S., & Migliorini, F. (1998). Asteroid showers on Earth after family breakup events. *Icarus*, 134(1), 176-179.

Zheng, Y. (1991). Calculation of oxygen isotope fractionation in metal oxides. *Geochimica et Cosmochimica Acta*, *55*(8), 2299-2307.